

Krzysztof Wilde

modal diagnostics of civil engineering structures



Gdańsk University of Technology Publishers

Krzysztof Wilde

modal diagnostics of civil engineering structures

Gdańsk 2008

GDAŃSK UNIVERSITY OF TECHNOLOGY PUBLISHERS
CHAIRMAN OF EDITORIAL BOARD
Romuald Szymkiewicz

EDITOR OF SCIENTIFIC PUBLICATIONS
Janusz T. Cieśliński

REVIEWERS
Paweł Kłosowski
Zbigniew Zembaty

Published under the permission
of the Rector of Gdańsk University of Technology

Titles printed by the Gdańsk University of Technology Publishers
can be ordered on-line (ksiegarnia@pg.gda.pl), by fax (+48 58 347 16 18)
or by letter (Wydawnictwo Politechniki Gdańskiej,
ul. G. Narutowicza 11/12, 80-952 Gdańsk)

© Copyright by Gdańsk University of Technology Publishers
Gdańsk 2008

ISBN 978-83-7348-227-2

Contents

LIST OF SYMBOLS AND ABBREVIATIONS	5
PREFACE	9
1. INTRODUCTION	11
1.1. Diagnostics in engineering structures	11
1.2. Diagnostics by vibration based methods	12
1.3. Wavelet transform application in damage detection	14
1.4. Finite element model updating	15
1.5. Arrangement of the text	16
2. FUNDAMENTALS OF MODAL ANALYSIS	17
2.1. Multi degree of freedom systems	17
2.1.1. Natural frequencies and mode shapes of undamped system	20
2.1.2. Natural frequencies and mode shapes of proportionally damped system	29
2.1.3. Natural frequencies and mode shapes of systems with arbitrary viscous damping...	32
2.2. Frequency response functions of MDOF systems	42
2.2.1. Forms of frequency response functions	43
2.2.2. Properties of frequency response functions	44
3. EXPERIMENTAL DERIVATION OF MODE SHAPES	50
3.1. Impulse and sweep tests for mode shapes identification through FRF	50
3.1.1. Procedure of mode shapes identification	50
3.1.2. Experimental examples	55
3.1.2.1. One-dimensional structures	55
3.1.2.2. Two-dimensional structures	58
3.1.2.3. Three-dimensional structures	60
3.1.2.4. Three-dimensional silo structures with filling	63
3.2. Ambient vibration methods for mode shapes identification	70
3.2.1. System Identification with NExT and ERA methods	71
3.2.2. Estimation of modal parameters by Stochastic Subspace Identification method ...	75
3.2.3. Experimental examples	77
3.2.3.1. Steel plate	77
3.2.3.2. Composite bridge in Żukowo.....	84
4. DIAGNOSTICS OF STRUCTURES THROUGH WAVELET ANALYSIS OF MODE SHAPES ..	92
4.1. Basic definitions	93
4.2. Examples of wavelets	96
4.3. Wavelet selection for damage detection	102
4.4. Wavelet damage detection in cantilever beam	105
4.5. Wavelet damage detection in steel plate	107
4.6. Wavelet damage detection in shell structures	111
4.7. Conclusions	115

5. MODE SHAPES IN FEM UPDATING	117
5.1. Sensitivity of mode shapes	117
5.2. Iterative methods using modal pairs	120
5.3. FE model updating in cantilever beam	122
5.3.1. Experimental procedures and measurement results	123
5.3.2. Finite element model of the cantilever beam	125
5.3.3. Updating of the global stiffness and support parameters	126
5.3.4. Search of the each element stiffness on natural frequencies	127
5.3.5. Sequential search of the each element stiffness on modal pairs	129
5.4. Updating of large FE model of cantilever beam	131
5.4.1. FE model updating of each element stiffness for fixed boundary conditions	131
5.4.2. FE model updating with computation of general stiffness and boundary condition parameters	133
5.4.3. FE model updating for boundary condition, undamaged and damaged beam	134
5.4.4. FE model updating by sequential updating procedure	135
5.5. FE model updating in steel plate on numerical data	138
5.5.1. Mass coefficients updating on 16 element FE model	138
5.5.2. Mass coefficients updating on 36 element FE model	143
5.6. FE model updating in plate on experimental data	146
5.7. Conclusions	151
6. MULTILEVEL DAMAGE DETECTION NEURAL SYSTEM ON MODE SHAPES OF PLATE STRUCTURE	152
6.1. Experimental study	153
6.1.1. Ambient vibration test	153
6.1.1. Forced vibration test	154
6.2. Modal parameter identification	155
6.2.1. Ambient vibration test	155
6.2.2. Forced vibration test	155
6.3. Neural network system	156
6.3.1. Backpropagation algorithm	156
6.3.2. Architecture	158
6.4. Results	159
6.5. Conclusions	162
Acknowledgements	163
REFERENCES	164
Appendix A. Finite elements of beam and plate	171
Appendix B. Model reduction methods	175
Appendix C. Signal processing.....	180
Appendix D. Eigenvectors validation criteria	192

List of symbols and abbreviations

Symbols

$\tilde{\Phi}_n$	– experimental mode shapes
\bar{m}_n	– modal mass of the n -th mode
\bar{k}_n	– modal stiffness of the n -th mode
μ	– complex value
λ	– eigenvalue
ρ	– mass density
Φ	– modal matrix
ω	– natural circular frequency
α	– real constant, angle of rotation of the control surface
β	– real constant, angle of rotation of the control surface
Ω	– spectral matrix consisting of λ
Ω_d	– spectral matrix of discrete system
$\xi(t)$	– modal coordinate
Ω^2	– spectral matrix
ω_d	– damped natural circular frequency
ϕ_{ij}	– coefficients of the modal matrix
ξ_k	– damping ratio of the n -th mode
Φ_L	– matrix of left eigenvectors
ϕ_n	– eigenvector, mode shape
ϕ_{ai}	– analytical mode shape
ϕ_{mi}	– mode shape estimated from measurements
Φ_T	– matrix of right eigenvectors
$2b$	– width of the bridge deck with additional surfaces
$2b_c$	– width of the bridge deck
\mathbf{a}	– eigenvector of proportionally damped system, right eigenvector
\mathbf{A}	– system matrix in state space formulation, discrete system matrix
$A_{jk}(\omega)$	– accelerance, frequency response function
\mathbf{b}	– eigenvector of undamped system, left eigenvector
\mathbf{B}	– input matrix, discrete input matrix
B	– width
$\mathbf{B}(s)$	– system matrix in Laplace domain
b_1, b_2	– width of the control surfaces
\mathbf{C}	– damping matrix, output matrix, discrete output matrix
c	– damping coefficient of a single degree of freedom system
\mathbf{D}	– direct coupling matrix, discrete direct coupling matrix
D_1, D_2	– diameters
$D_{jk}(\omega)$	– dynamic stiffness, frequency response function
E	– Young's modulus

$\mathbf{F}(t)$	– stochastic excitation
e_1, e_2	– control surface hinge location
e_{c1}, e_{c2}	– control cable connection to the control surface
EI_k	– stiffness of the k -th element
f	– natural frequency
G_{FF}	– autospectrum of force
G_{FX}	– cross spectrum between response and force
G_{XF}	– cross spectrum between force and response
G_{XX}	– autospectrum of response
H	– height
h	– heaving motion of the bridge deck
$\mathbf{H}(\omega)$	– frequency response matrix
$\mathbf{H}(s)$	– transfer function matrix
$H(\omega)$	– frequency response function
H_1	– distance from a support to a defect along height
$H_1(\omega), H_2(\omega)$	– estimators of frequency response function
$H_{jk}(\omega)$	– frequency response function, receptance
H_r	– height of a defect
\mathbf{I}	– identity matrix
i	– imaginary unit, integer number
\mathbf{K}	– stiffness matrix
k	– integer number
L_1, L_2, L_3	– length of spans of a suspension bridge, damage location
L_r	– length of a defect
\mathbf{M}	– mass matrix
m	– mass of a single degree of freedom system, integer number
$M_\alpha, M_\beta, M_\gamma$	– aerodynamic moments generated on surfaces and bridge deck
$M_{jk}(\omega)$	– mechanical impedance, frequency response function
N	– number of degrees of freedom, integer number
$\mathbf{p}(t)$	– vector of the external forces
$P(\omega)$	– Fourier transform of one-dimensional signal
$P_{jk}(\omega)$	– apparent mass, frequency response function
p_k	– system poles
\mathbf{R}_k	– residue matrix
s	– Laplace variable, scale parameter
T	– natural period
t	– time coordinate
t_k	– scaling factor
U	– wind velocity
$\mathbf{u}(t)$	– vector of displacements
$\mathbf{x}_1, \mathbf{x}_2, \mathbf{x}$	– system states
x_{c1}, x_{c2}	– position of the control cables
$\mathbf{y}(t)$	– vector of output states
$Y_{jk}(\omega)$	– mobility, frequency response function
\mathbf{x}_0	– initial displacements
\mathbf{u}_0	– initial velocities
\mathbf{R}_{xy}	– cross correlation functions
\mathbf{P}_α	– controllability matrix
\mathbf{Q}_β	– observability matrix
$\mathbf{H}(0), \mathbf{H}(k-1)$	– Henkel matrix

\mathbf{S}	– matrix of singular values, sensitivity matrix
\mathbf{U}, \mathbf{V}	– left and right matrix in singular matrix decomposition
$\mathbf{E}_r, \mathbf{E}_m$	– transformation matrices
Δt	– time increment
\mathbf{w}_k	– input noise vector
\mathbf{V}_k	– output noise vector
\mathbf{K}_k	– Kalman filter gain
$\hat{\mathbf{x}}_k$	– estimate of state \mathbf{x}_k
\mathbf{e}_k	– estimation error in Kalman filter
$\psi(x)$	– one-dimensional mother wavelet function
$\psi_{j,k}(x)$	– family of discrete wavelets
$\psi_{u,s}(x)$	– family of wavelets
$\psi^1(x,y)$	– two-dimensional horizontal wavelet function
$\psi^2(x,y)$	– two-dimensional vertical wavelet function
$\psi^3(x,y)$	– two-dimensional diagonal wavelet function
$Wf(u,s)$	– continuous wavelet transform of one-dimensional signal
$Wf(u,v,s)$	– continuous wavelet transform of two-dimensional signal
M	– number of neurons in hidden layer
$Mf(u,v,s)$	– modulus wavelet transform of two-dimensional signal
θ_j	– design parameter
$J(\delta\theta)$	– penalty function
$\mathbf{W}_{ee}, \mathbf{W}_{00}$	– weighting matrices
\mathbf{z}_a	– vector of analytical modal parameters
\mathbf{z}_m	– vector of measured modal parameters
I_D	– damage index
I_{EI}	– relative stiffness change
I_{NMD}	– index based on normalized modal difference
ν	– Poisson ratio
h_{ij}	– coefficients of frequency response matrix
ρ_{ijk}	– peak value of the frequency response function
net	– net function
o	– output of neural network
P	– number of patterns
R	– number of neurons in input layer
w_{km}	– weights of the neural network
\mathbf{M}^e	– mass matrix of the finite element
\mathbf{K}^e	– stiffness matrix of the finite element
$\mathbf{N}(x)$	– matrix of shape functions
\mathbf{K}_{ii}	– sub-block of stiffness matrix
\mathbf{M}_{ii}	– sub-block of mass matrix
\mathbf{T}_s	– transformation matrix
$Sf(u,\zeta)$	– windowed Fourier transform of one-dimensional signal
$g_{u,\zeta}(t)$	– window function

Abbreviations

adj	– adjugate
det	– determinant
$(\cdot)^*$	– complex conjugate
$(\cdot)^T$	– transpose

\dot{u}	– first derivative of u
\ddot{u}	– second derivative of u
CWT	– continuous wavelet transform
DWT	– discrete wavelet transform
FEM	– finite element method
FRF	– frequency response function
FT	– Fourier transform
GPS	– Global Positioning System
NDT	– non-destructive testing
SHM	– structural health monitoring
WFT	– windowed Fourier transform
WT	– wavelet transform
MAC	– modal assurance criteria
MSF	– modal scale factor
NMD	– normalized modal difference
MSV	– modal singular value
NCO	– normalized cross orthogonality

Preface

The book presents a blend of information about the vibrational diagnostics in civil engineering structures, namely, elements of structural dynamics, experimental modal analysis, advanced signal processing and applied optimization theory. The book is oriented towards a practical application of the diagnostics based on measurements of the structure oscillations. Special attention is paid to the civil engineering structures and their experimental examples.

There are many books discussing the problems of modal experimental analysis. The most comprehensive one, to the best of the author's knowledge, is the work by Maia and Silva (1997) entitled "Theoretical and Experimental Modal Analysis". In this book the theory on modal testing methods, modal identification techniques, Finite Element (FE) model updating and nonlinear modal analysis is systematically analyzed. However, the number of the examples on modal analysis on real objects is small. A detailed study on updating the Finite Element models is given by Friswell and Mottershead (1995) in the book "Finite Element Model Updating in Structural Dynamics". The Authors carefully explain the advantages and disadvantages of the direct and iterative methods of dynamic system coefficients updating. The examples are mostly based on the numerically determined input data. The third book that is often cited in the presented work, is "Application of Wavelet Analysis in Damage Detection and Localization" (Rucka and Wilde 2007). In this study a relatively new idea of using the wavelet analysis of damage detection from static and dynamic responses of the structures is discussed.

The aim of this book is to present a state-of-the-art knowledge on modal diagnostics with a special attention on its real application in civil engineering structures. Therefore, the experimental techniques leading to estimations of the structure natural frequencies and mode shapes are discussed in detail. Several examples are given from the author's engineering experience. All of the presented techniques are tested on the data obtained from the experimental studies in the Laboratory of Department of Structural Mechanics and Bridge Structures, Gdansk University of Technology, Poland. One example of mode shape extraction is based on the existing composite bridge, located near Gdańsk. The ambient vibration identifications, not mentioned in the above books, are also formulated and experimentally tested.

The theoretical knowledge on structure dynamics is omitted since many books and papers are available on this topic. Only the derivation of mode shapes for systems with no damping, a proportional damping matrix and arbitrary viscous damping are discussed in detail. For reasons of priority given in the book to the practical aspects, all the structural models are linear. It is assumed that the obtained equations of motion are describing the oscillations of a civil engineering structure around its equilibrium position. Only very small vibration amplitudes are considered. In the case of civil engineering structures the range of frequencies of interest is very low in comparison to the structures in aeronautical or mechanical engineering.

In this book a use of three types of damage detection methods on the experimental modal parameters are studied. To the best of the author's knowledge, there are relatively few publications that refer to the efficiency of damage location on data obtained from the in situ measurements. The first type damage detection methods presented in this book are techniques based on the wavelet analysis. The wavelet analysis, under consideration, do not need any theoretical models of the structure nor information on undamaged structure. Only the experimental mode shapes of structure in the current state are needed. This method belongs to a group of methods that search the crack location from the derivatives of the mode shapes. The wavelets act as a differentiating operator, and therefore, have all the constrains of this type of methods. The method is effective in detecting only relatively large cracks.

The second direction in modal diagnostics, followed in this book, is Finite Element model updating. In this case the mathematical model of the structure dynamics is necessary. It is also necessary to conduct the measurements of the damaged and undamaged structure. Only the updating that uses the reference data can give the correct and practically useful information. There are many papers on updating based on natural frequencies. In this book the updating using both frequencies and experimental mode shapes is discussed. The effective iterative algorithm is searched.

The third type of the modal diagnostics is the proposition of a combination of an artificial neural network with diagnostic data obtained from simple ambient tests and detailed forced vibration tests. In both cases the experimental frequencies and these mode shapes are used as the network input. The proposed strategy assumes a multilevel approach in the sense that cheap ambient tests, that can be easily performed on an existing structure, are conducted to detect the presence of the damage. In doubtful cases about the integrity of the structure, some forced dynamic testes are suggested. Both levels of the structure diagnostics are facilitated by a neural network. This part of the book is rather a presentation of a concept than a systematic study on the neural expert system.

Introduction

1.1. Diagnostics of engineering structures

Engineering structures under their operating conditions like, static and dynamic loading, temperature, wind, vibrations, water, penetration of chemical substances etc. are subjected to corrosion, fatigue, creep and wear. Damage in the structural elements is only a question of time and is a potential threat to proper operation of any civil engineering object. In this book the damage is understood as change to the material or geometric properties of the engineering object, including changes to the boundary conditions and system connectivity. It is assumed that the appearance of the damage adversely affect the current or future performance of the structure. The above definition of damage states that damage is not meaningful without its reference to two different states of the structure, one is called the initial or the undamaged, while the second is referred to as damaged state.

The appearance of damage may lead to significant additional financial losses or even to the losses of human lives. In order to improve the reliability and safety of structures, various damage detection techniques and health monitoring systems have been intensively studied over the last few decades. A simple, quick and non-destructive structural diagnostic system that could facilitate traditional diagnostic procedures is of great importance in solving many maintenance problems of civil engineering structures.

The most common method of the assessment of the structure integrity is a routine visual inspection, mandatory for important structures. The appearance of damage, like, extended cracks in concrete elements usually requires the destructive testing. A sample of material is taken from the structure and tested in the laboratory. The study of the material properties and in situ testing are used as a base for the decision on future operation of the structure and/or the method of rehabilitation. Damage detection can be facilitated by non-destructive testing (NDT) based on the radiography, acoustic emission, ultrasonic testing, magnetic fields methods, eddy current methods, etc. Although such diagnostics can be effectively applied to damage detection in a few known *a priori* areas of damage, they are impractical for search of potential damage through the entire engineering object. Additionally, the mentioned NDT methods are not appropriate for an on-line inspection since they are performed at periodic maintenance checks.

Further development in NDT methods leads to so-called structural health monitoring (SHM). The structural health monitoring is a sub-discipline of structural engineering which is focused on non-destructive techniques related to continuous, automatic and real time *in situ* monitoring of physical parameters and identification of the structure abnormal condition. There are two major types of monitored parameters, i.e. loads (wind, earthquake, temperature, traffic movements, etc.) and structural responses (displacements, accelerations, velocities, stresses, strains, etc.). A typical SHM system includes three major components: a sensor system (seismometers, anemometers, accelerometers, velocity and displacement gauges, Global Positioning Systems, thermometers, etc.), a data processing system (including data acquisition,

transmission and storage) and health evaluating system (including diagnostic algorithms and information management). At present, the SHM techniques are applied mostly to structures of special importance, like, wind turbines (Ghoshal et al. 2000), offshore structures (Nichols 2003), aircraft (Abdelghani et al. 1999) or bridges (Omenzetter et al. 2004).

An extensive literature review on diagnostics of engineering structures has been given by Doebling et al. (1996). He presented the survey of 309 selected references published before 1996. The analyzed diagnostic methods were classified into 133 types according to the following criteria: a) type of the collected data (natural frequency, mode shapes, damping, flexibility, static data, response spectra, time domain responses), b) type of the method scheme (forward, inverse, neural network, direct, interactive), c) types of criteria and/or constrains (frequency change, parameter change, parameter vector, matrix rank, FRF change, connectivity, symmetry, positive definiteness, sparsity), d) properties of results (indication of damage presence, location of damage, global matrix change, element matrix change, element or localized element change, mass change, damping change, stiffness change, hybrid property, crack geometry and location, environmental or operational conditions, nonlinearity). A review of the literature from 1996 to 2001 is given by Sohn et al. (2004) and it discusses 364 papers or books. Since 2001 the number of papers on damage diagnostics has increased. However, successful applications of automatic, reliable systems is still outside the scope of traditional civil engineering and remains mostly within limits of aeronautical and mechanical engineering fields.

1.2. Diagnostics by vibration based methods

The vibration based damage detection methods have been dynamically developed over the last thirty years (Farrar and Doebling 1998). The concept behind the vibrational methods states that damage significantly alters the stiffness, mass or energy dissipation properties of the structure, and this in turn changes the dynamic responses of the tested object. Although, the idea of vibration based diagnostics seems obvious, its practical applications lead to problems. The first one is the dynamic sensitivity of the structure to the damage. A typical crack, flaw, injury etc. are local phenomena, and therefore, they do not significantly influence the global response of the structure. In addition large civil engineering structures, like, long span bridges, have very low natural frequencies falling even below 1 Hz and the local damage is often completely masked in the global response. The higher modes that might be associated with certain segments of the structure are more prone to be affected by local changes in material properties of the elements geometry. However, a very fast development of sensor and precise data acquisition systems with progress in signal processing tools open new possibilities for the application of vibration based methods. In fact, very low input energy levels are sufficient to produce measurable responses. Additionally recently the dynamic measurements on some real structures are simple, quick and relatively cheap.

A successful use of damage detection on modal parameters, like, natural frequencies and mode shapes requires taking into consideration the following points:

1. It is necessary to understand the effects of deterioration and defects on the dynamic characteristics of the structure. Different types of damage in different locations will have different influence on the structure modal parameters.
2. The vibration data must be taken at those points where all the modes, in the frequency range of interest, are well represented. It is usually necessary to conduct a numerical

study prior to the in situ testing. The selection of points where the sum of the magnitudes of the mode shape vectors is maximized is suggested.

3. The effects of the environmental conditions like temperature distribution, humidity, wind speed, interaction with the loads from the surroundings, changes in the boundary conditions must be compensated.
4. The dynamic tests must be performed in two series. The first one on the undamaged structure to be used later as a reference and the second on the damaged object. The measurements in the series must be repeated several times to have a chance to filter out at least part of the noise effects.
5. The testing procedure must be consistent and reliable despite the long time difference between the series of the measurements. The configuration of the data acquisition system and the compatibility of applied sensors must be guaranteed.

The earliest works reported on damage detection by measurements of natural frequencies, to the best of the author's knowledge, have been presented by Cawley and Adams, 1979. They proposed a sensitivity concept in which the ratio of the frequency changes in two modes is only a function of the damage location. The defect is located by the computation of the theoretical frequency shifts and comparison to the measured values. The drawbacks of the method are the need to model the possible damage mechanisms at various sites and the difficulty in defining the method accuracy. Extensive experimental studies on the influence of the damage have been conducted and are selectively presented in this section of the book. Mirza et al. (1990) conducted the dynamic tests on 1/7th scale models of simply supported girder bridges with one and two cell boxes. The results showed that the first natural frequencies decrease with progressive damage. Near the ultimate load the fundamental frequency decreased linearly by about 40% and 75% for the one and two cell bridge, respectively. Findings reported by Salane and Baldwin (1990) as well as Idichandy and Ganapathy (1990) indicated that the damage detection by frequency measurements might be unreliable when the damage was located at regions of low stresses. They argued that a shift in natural frequencies alone might not provide sufficient information for integrity monitoring unless the damage was in an important load bearing member. The importance of higher modes damage localization on experiments on highway bridges has been stressed by Biswas et al. (1990). The study on natural frequency changes in prestressed structures were conducted by Kato and Shimada (1986) on a concrete prestressed bridge during failure. Only small changes were observed while the prestressing wires were in the elastic limit. A sudden decrement of the natural frequencies occurred when the wires entered the plastic region. However, the monitoring based on frequency change was not considered as a promising tool for the damage detection of the prestressed structures since an early warning on damage appearance could not be achieved. There are many other reported studies devoted to damage detection by measurement of the structure natural frequency due to support failure, crack propagation, shear failure, or internal damage due to overload e.g., Zembaty et al. (2006), Mazurek and DeWolf (1978), Savage and Hewlett (1978). The study on diagnostics of the masonry structures has been conducted by Zembaty and Kowalski (2007).

An attempt to use nondestructive damage localization on natural frequencies in geotechnical problems was checked by Sun and Hardy (1992).

The damage detection on natural frequencies can be facilitated by the information stored in mode shapes. This notion was first proposed by West (1984). He used the modal assurance criterion (MAC) to analyze the results of an acoustic environment test for damage location in space shuttle control surfaces. He proposed a procedure for partitioning the measured mode shapes before the computation of the MAC. A comparison was made between several such partitioning schemes. The inconsistencies between the mode shape

partitions before and after damage are used to show how the mode shapes can be used to localize damage. The usefulness of the mode shapes with respect to natural frequencies in the damage detection in cylindrical shells was described by Srinivasen and Kot (1992).

Detection of defects and their locations performed on displacement mode shapes and their derivatives has been studied by, e.g., Yuen (1985), Pandey et al. (1991). This method has been proved to be effective in the case of vibration data obtained from numerical simulations. However, success of the technique is significantly affected by noisy experimental data (Messina 2004). An improved identification method based on modal information has been presented by Kim and Stabbs 2002. The extensive review of previous research in frequency-based methods and mode shape-based methods are given by Kim et al. (2003), Gentile and Messina (2003), and Wang and Deng (1999). Generally speaking, the methods that use the derivatives of the mode shapes can be effective only when very precise displacement modes are available. In the case of even small noise, the numerical differentiation results in large errors in the modes derivatives. Moreover, the experimental modes are determined in limited locations which increases the difficulty in the differentiation. A solution of this problem can be achieved by wavelet transforms used as differential operators. The wavelets possess an inherent smoothing ability.

1.3. Wavelet transform application in damage detection

Wavelet transforms are used in almost all devices surrounding us in everyday life. In recent years most of technological solutions are taking the advantage of wavelet signal processing. Wavelets are used to analyse the variations of values at financial markets (e.g. Struzik, 2001). Electrocardiograms (ECG), used in medical services, are analyzed with help provided by wavelets (Sivannarayana and Reddy 1999) and events like myocardial ischemic can be detected (Ranjith et al. 2003). The Federal Bureau of Investigation (FBI) is intending to apply wavelets for storage of 30 million sets of criminal fingerprints (Strang and Nguyen 1996). The information technology scientists exploit them in image processing like edge recognition, image searching, animation control, image compression. Most of the transient phenomena like processes associated with earthquakes, wind and ocean actions, problems in mechanical engineering (Basu and Gupta 2000, Glabisz 2004, Gurley and Kareem 1999) or dynamic silo flow (Niedostatkiewicz et. al. 2005) are analyzed with use of wavelets. They are also beneficial in problems related to modal parameter identification (Lardies and Gouttebroze 2002, Slavič et. al. 2003).

In the past decade, wavelets have been tested for damage detection (Hou et. al. 2000, Kim and Melhem 2004). The relatively new concept of structural health monitoring (SHM) assumes that the structural parameters can be monitored by a system consisting of online data measurements, analysis and decision making module. The SHM system can detect the damage at the earliest possible stage. This notion becomes an important issue throughout the aircraft, mechanical (Wang and McFadden 1996) and civil engineering communities (Melhem and Kim 2003). A defect in a structure introduces changes or so called singularities to, for example, the mode shapes. These small defects cannot be identified directly from the structure response, but may be extracted with use of the wavelet transforms. Wavelets have time and frequency representation and their major advantage is not only the ability to react to the local abnormalities in the signal, but the possibility to locate the event in time. In case of the damage detection on mode shapes, wavelets help to localize the location of the defect in the structure.

There are many publications on one-dimensional wavelets in engineering problems. Applicability of wavelets in crack detection in beams has been studied by Douka et al. 2003, Loutridis et al. 2004, Quek et al. 2001, Hong et al. 2002, Wang and Deng 1999, Chang and Chen 2003 as well as Gentile and Messina 2003, and Messina 2004. Ovanesova and Suarez 2004 analysed the one-dimensional signals of frame structures. The numerical studies have shown very good accuracy and effectiveness of the wavelet transform but their were lacking the experimental verification. Gentile and Messina 2003, Messina 2004, Chang and Chen 2003 as well as Hong et al. 2002 addressed the importance of taking into account the effect of noise. The theoretical mode shapes have been contaminated by a Gaussian noise and it was shown that the presence of noise can mask the damage.

The experimental researches on plate damage detection have been presented by Rucka and Wilde 2005a. The experimental mode shapes of the cantilever plate have been determined by impulse tests and the defect with the relative depth of 19% was searched. The location of the damage was successfully determined by the one-dimensional Gaussian wavelet. The formulation of the two-dimensional continuous wavelet transform for plate damage detection is presented by Rucka and Wilde 2006b. Mode shapes of a plate with four fixed supports have been analyzed by Reverse Biorthogonal wavelets.

1.4. Finite element model updating

The finite element (FE) model updating based on dynamic testes can be treated as optimization problem of searching for the best fit between the experimental data and analytical prediction. There is a very large number of papers and books on optimization techniques applied to mathematical and numerical models, and therefore, a simple classification is very difficult. A comprehensive survey of 243 references on the FE model updating has been conducted by Mottershead and Friswell (1993). Additional information related to literature on this topic is given, e.g., by Doebling et al. (1996).

The updating methods can be divided according to the philosophy of addressing the parameter actualization problem, i.e., into soft methods and inverse methods. The soft computing techniques take advantage, for example, of the neural systems or statistical pattern recognition methods (Liu and Han 2003). An example of the damage detection system with simple artificial neural network is given by Wilde et al. (2006). The soft computing systems are based on the idea that they store the “experience” on the structure response for many potential scenarios of imperfection location and size. When they are provided with new data they try to match the gathered information with the given measurements. By finding the most appropriate “fit” the information on parameter change is produced. The correctness of the results of the FE model updating by soft computing is given with a certain probability. The results from the neural system can not be considered as strict solutions in a mathematical sense.

The inverse methods aim at reconstruction of the structure model from the measurement data. The problem might have a solution if the number of unknowns was equal to the number of equations constructed from the experimental data and the problem matrix had a full rank. However, in the real engineering problems, the FE models have a lot of parameters whose measurements are limited to some available locations and are usually confined to the translational degrees of freedom. The inverse problems with the number of unknowns larger than number of equations are called ill-conditioned and their treatment is presented, e.g., in the book by Friswell and Mottershead (1995).

The FE updating methods can be divided into direct and iterative techniques. The so called direct methods do not require iterations, and thus, the drawbacks of excessive computational time or divergence are eliminated. The methods are based on minimization of the selected cost function with chosen constraints. Most of them are related to the Lagrange Multiplication Methods (Baruch and Bar-Itzhack 1978, and Baruch 1978). In inverse problems solved by direct methods, it is difficult to impose the physical condition on the updated mass and stiffness matrices, e.g., it is not guaranteed that these matrices are positive definite, even though the model correctly reproduces the experimental data. Many corrections and additional conditions in cost functions have been proposed, e.g., by Berman and Nagy (1983) or Wei (1990).

The most promising, although computationally time consuming, are the iterative methods. The often applied FE updating algorithms are based on sensitivity matrix (Friswell and Mottershead 1995). An improvement of these methods can be obtained by regularization proposed by Link (1993). The regularization can be considered as an application of weighting matrices that stress the importance of the selected set of the design parameters. An alternative method of FE model updating based on harmonic vibrations has proved to be quite effective for frame and beam structures (Kokot and Zembaty 2007). In this book the iterative FE updating methods on modal experimental data are studied in detail.

1.5. Arrangement of the text

The second chapter presents the most important definitions of the dynamics of multi degree of freedom (MDOF) systems. The properties of the MDOF frequency response functions are presented and some detailed information on mode shapes of undamped, proportionally damped and arbitrary viscously damped systems is presented.

The third chapter deals with experimental derivation of the mode shapes and several examples demonstrating the modal estimation procedure and possible results on beam, plate and shell structures. In this chapter a mathematical background, as well as the practical guidance is given on the forced dynamic tests and ambient vibration methods.

The fourth chapter is devoted to damage detection on experimental mode shapes by the use of the wavelet transforms. It is shown, on the experimental models of engineering structures, that the method can locate the damage using one and two dimensional wavelet functions.

The finite element (FE) model updating is presented in chapter five. The FE models of beam and plate structures are derived and updated on the experimentally determined mode shapes. An advantage of using information stored in the mode shapes is discussed.

The sixth chapter is devoted to application of neural network to improve the damage location. The proposed system has two levels of precision. The first, easy to use, detection level is based on ambient vibrations. The second level employs detailed forced dynamic tests and is able to determine the presence of the damage and to give its location.

The basic information in formulating the FE models for beam and plate elements is given in Appendix A. The global degrees of freedom and the aggregation process is not described, since only a simple cantilever beam and a rectangular simply supported plate are considered in this book. The technique of the FE model reduction is presented in Appendix B. The introduction to the Fourier, Windowed Fourier, wavelets and Hilbert-Huang transforms is given in Appendix C. The theory is illustrated by examples of the transforms application on signals from in situ measurements. In Appendix D the criteria of the mode shapes comparison are presented.

Fundamentals of modal analysis

2.1. Multi degree of freedom systems

The dynamic models of engineering structures are constructed with limited number of degrees of freedom, i.e., only selected number of independent coordinates are used to describe their motion. The process of structural modeling and selection of the most appropriate degrees of freedom is explained in many books (e.g., Clough and Penzien 1993, Chopra 2001). The process of modeling simplifications can be summarized as follows:

1. Assumption on homogeneity of the material of structural elements.
2. Linear law of structure materials.
3. Simplifications in modeling of the boundary conditions.
4. Simplifications of geometry of a structure.
5. Selection of structural elements of infinite rigidity.
6. Selection of weightless elements (structural elements that do not generate inertia forces) and assumption on lumped mass that results in neglecting the rotational inertia components.
7. Simplifications of external force models and selection of only the most important factors describing the structure-surrounding environment interaction.
8. Selection of the degrees of freedom corresponding to structural components, like, beams, plates, shells, etc.
9. Reduction of the secondary (not essential) degrees of freedom.

Any dynamic model of an engineering structure, derived through the methods of continuum mechanics have infinite number of degrees of freedom and is described by partial differential equations. Finite Element (FE) models lead to structural models by a set of ordinary differential equations. FE modeling is well established in engineering community and numerical analysis with Finite Element Method (FEM) is commonly used in wide variety of engineering problems. In the examples presented in this book the structural models are obtained through FE modeling. The derivation of the simplified models of civil engineering structures by use of generalized coordinates or through energy principles is given in many sources, e.g., Chopra 2001, Chmielewski and Zembaty (1998), Meirovitch (2001), etc.

In Fig. 2.1 the process of simplifications on an example of a tower is presented. In reality the tower is constructed of different materials of properties that are not constant within the tower volume. For example, its stiffness can be a nonlinear function of many parameters. First two assumptions make it possible to treat the building material as homogeneous and elastic. In many cases the dynamic model can be simplified in terms of structure geometry, its boundary condition (Fig. 2.1c). Also, very rigid elements of the structure can be treated as infinitely stiff, and therefore, can be neglected in model that is derived to capture the global oscillation of the tower. In the analyzed example, the upper part of the tower is considered to be a lumped mass (Fig. 2.1d). The selection of the degree of freedom is con-

ducted through the Finite Element Method and, in most cases, the resulting number of degrees of freedom is very large. The FEM based model of the tower is shown in Fig 2.1e. Together with the discretization of the tower domain, the simplification of the external loading is conducted. Finally, the smallest possible model that can properly describe the dynamic process of interest is obtained (Fig. 2.1f). The basic information on FEM for beams and plates is given in Appendix A.

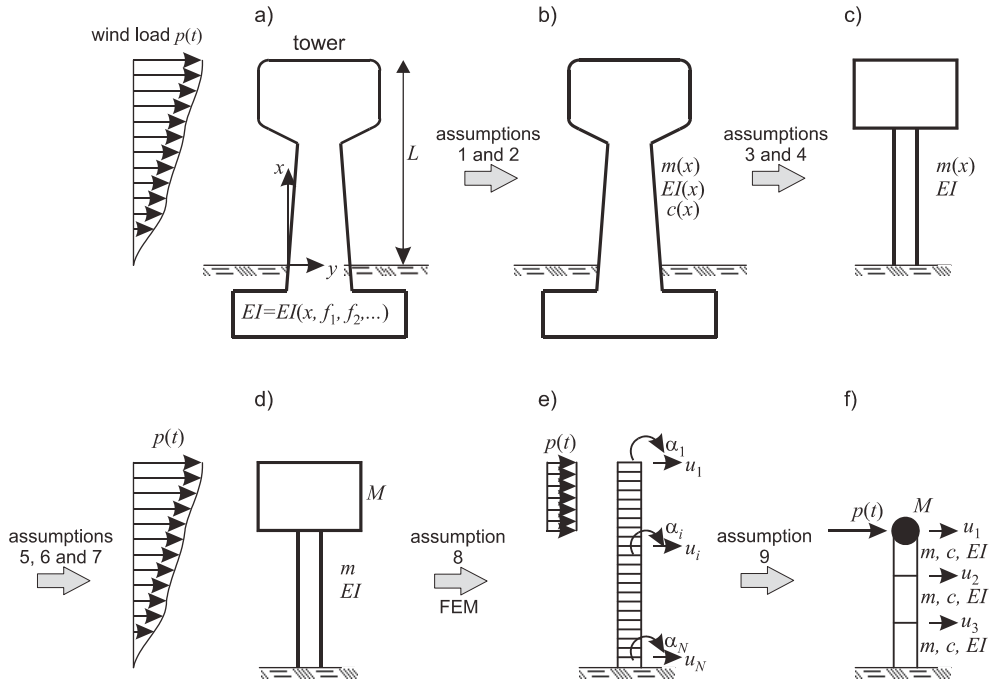


Fig. 2.1. Modeling of tower dynamic model

Any dynamic system modeled by FE models can be graphically presented (Fig. 2.2) by schematic models consisting of spatial masses, m_i (depicted by rectangular car), damping constrains (dashpot), c_i and stiffness elements (springs), k_i . The equation of motion of an engineering structure can be written as

$$\mathbf{M}\ddot{\mathbf{u}}(t) + \mathbf{C}\dot{\mathbf{u}}(t) + \mathbf{K}\mathbf{u}(t) = \mathbf{p}(t) \quad (2.1)$$

where \mathbf{M} is a mass matrix, \mathbf{C} denotes a damping matrix, \mathbf{K} is a stiffness matrix, $\mathbf{p}(t)$ is vector of the external forces and the time varying coordinates describing the motion of the structure are in the system vector $\mathbf{u}(t)$ of size $N \times 1$. The number of the degrees of freedom is denoted by N .

The most common form of the equation of motion for the numerical dynamic analysis is its formulation in the state space. Assuming that the displacements, $\mathbf{u}(t)$, and the velocities of the spatial degrees of freedom, $\dot{\mathbf{u}}(t)$, are selected as variables describing the dynamic state of the system, it is possible to write

$$\begin{aligned} \mathbf{x}_1(t) &= \mathbf{u}(t), \\ \mathbf{x}_2(t) &= \dot{\mathbf{u}}(t). \end{aligned} \quad (2.2)$$

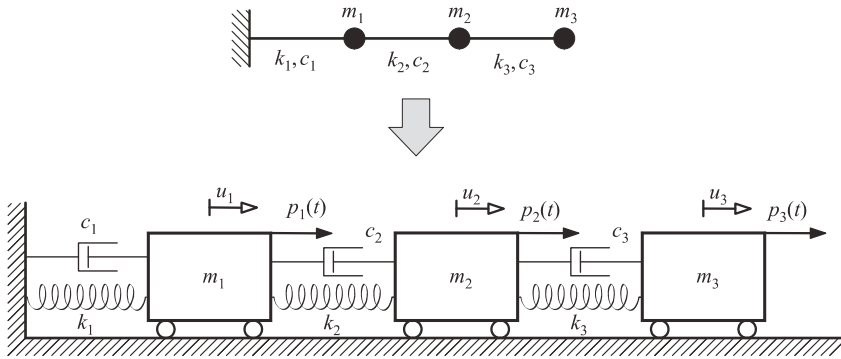


Fig. 2.2. Schematic presentation of the model of a cantilever beam

Substituting (2.2) into (2.1) and regrouping the terms yields

$$\begin{aligned}\dot{\mathbf{x}}_1(t) &= \mathbf{x}_2(t), \\ \dot{\mathbf{x}}_2(t) &= -\mathbf{M}^{-1}\mathbf{C}\mathbf{x}_2(t) - \mathbf{M}^{-1}\mathbf{K}\mathbf{x}_1(t) + \mathbf{M}^{-1}\mathbf{p}(t).\end{aligned}\quad (2.3)$$

Equations (2.3) can be written in standard matrix form as follows

$$\begin{Bmatrix} \dot{\mathbf{x}}_1 \\ \dot{\mathbf{x}}_2 \end{Bmatrix} = \underbrace{\begin{bmatrix} \mathbf{0} & \mathbf{I} \\ -\mathbf{M}^{-1}\mathbf{K} & -\mathbf{M}^{-1}\mathbf{C} \end{bmatrix}}_{\mathbf{A}} \begin{Bmatrix} \mathbf{x}_1 \\ \mathbf{x}_2 \end{Bmatrix} + \underbrace{\begin{bmatrix} \mathbf{0} \\ -\mathbf{M}^{-1} \end{bmatrix}}_{\mathbf{B}} \mathbf{p}(t).\quad (2.4)$$

Matrix \mathbf{A} is called the system matrix and contains all the information on the structure dynamics. Matrix \mathbf{B} is referred to as input matrix. The output equation has the form

$$\mathbf{y}(t) = \mathbf{C}\mathbf{x}(t) + \mathbf{D}\mathbf{p}(t),\quad (2.5)$$

where $\mathbf{y}(t)$ is a vector of the selected outputs, the state vector $\mathbf{x}(t)$ consists of the vectors $\mathbf{x}_1(t)$ and $\mathbf{x}_2(t)$ and the matrices \mathbf{C} and \mathbf{D} describe the influence on outputs from the states and external excitation, respectively. Finally, the equation of motion of the dynamic system in state space is

$$\begin{aligned}\dot{\mathbf{x}}(t) &= \mathbf{A}\mathbf{x}(t) + \mathbf{B}\mathbf{p}(t), \\ \mathbf{y}(t) &= \mathbf{C}\mathbf{x}(t) + \mathbf{D}\mathbf{p}(t).\end{aligned}\quad (2.6)$$

The size of the state vector is $2N$ and the output vector $\mathbf{y}(t)$ is of size $p \times 1$ ($p \leq N$). The advantage of using the state space formulation is the possibility of describing the system by a set of the first order differential equations with constant coefficients and using very well established numerical tools to solve such equations.

The system matrices \mathbf{M} , \mathbf{C} and \mathbf{K} that constitute so called Spatial Model of the structure have certain properties that should be checked after they are derived. The most important constraints on system matrices are:

1. In general matrices \mathbf{M} , \mathbf{C} and \mathbf{K} are not diagonal, i.e., the degrees of freedom are coupled.
2. The mass matrix \mathbf{M} and stiffness matrix \mathbf{K} must be symmetric.

3. The matrix \mathbf{M} is positive definite and its inverse matrix, \mathbf{M}^{-1} , exists. The matrix \mathbf{M} does not satisfy this condition if one or more degrees of freedom have zero inertia due to the simplification assumption. In such a case it is possible to perform the static or dynamic condensation (Appendix B).
4. The stiffness matrix \mathbf{K} is positive definite and its inverse, \mathbf{K}^{-1} , exists. The stiffness matrix \mathbf{K} is singular when a rigid body motion is allowed.
5. The viscous damping matrix \mathbf{C} with coefficients that can assume any values is called an arbitrary viscous damping matrix.
6. If the damping matrix is modeled by a proportional relation to the mass or stiffness matrices, i.e.,

$$\mathbf{C} = \alpha\mathbf{M} + \beta\mathbf{K}, \quad (2.7)$$

the damping is called *proportional*. The coefficients α and β are constants. The proportional damping matrix satisfies the following condition

$$\mathbf{C}\mathbf{M}^{-1}\mathbf{K} = \mathbf{K}\mathbf{M}^{-1}\mathbf{C}. \quad (2.8)$$

In this book the derivation of the mode shapes for the undamped system, system with proportional damping, as well as system with arbitrary viscous damping will be carefully considered.

The solution of the equation of motion of a MDOF system subjected to initial condition and to arbitrary external forces requires the time domain integration. There are many well established numerical time stepping methods, implicit and explicit, that allow the response computation with verified accuracy, convergence and stability. Since most of the problems related to vibrational diagnostics of engineering structures deal with very small amplitudes, it is often possible to treat the structure as linearly elastic and the response can be computed also by the transition matrix (Meirovitch 1990) or through the modal decomposition. There is a very large number of textbooks, books and papers discussing the MDOF response as well as many commercial programs offering the user friendly procedures for time integration. Therefore, this topic is not discussed in this book.

2.1.1. Natural frequencies and mode shapes of undamped system

Multi degree of freedom (MDOF) system subjected to an initial perturbation oscillates around a certain equilibrium position. The MDOF system free vibrations are governed by system natural frequencies and mode shapes.

The equations of motion of an undamped MDOF are given by

$$\mathbf{M}\ddot{\mathbf{u}}(t) + \mathbf{K}\mathbf{u}(t) = \mathbf{0}, \quad (2.9)$$

where $\mathbf{0}$ is a zero vector of size $N \times 1$. The initial conditions are

$$\mathbf{u}(0) = \mathbf{0}, \quad \dot{\mathbf{u}}(0) = \mathbf{0}. \quad (2.10)$$

The N simultaneous equations in (2.9) have a homogeneous solution of the form

$$\mathbf{u}(t) = \boldsymbol{\phi}_n e^{i\omega t} \quad (2.11)$$

where $\boldsymbol{\phi}_n$ is a $N \times 1$ vector of complex time independent amplitudes. The imaginary unit is denoted by i and ω is the circular natural frequency. Substituting equation (2.11) into (2.9) yields

$$(\mathbf{K} - \omega^2 \mathbf{M}) \boldsymbol{\phi}_n e^{i\omega t} = \mathbf{0}. \quad (2.12)$$

Since at time t $e^{i\omega t} \neq 0$, the equation (2.12) becomes

$$(\mathbf{K} - \omega^2 \mathbf{M}) \boldsymbol{\phi}_n = \mathbf{0}. \quad (2.13)$$

Equation (2.13) is called a generalized eigenvalue problem. If the trivial solution of zero amplitudes, $\boldsymbol{\phi}_n = \mathbf{0}$, is neglected, the equation (2.13) is satisfied when

$$\det(\mathbf{K} - \omega^2 \mathbf{M}) = 0, \quad (2.14)$$

where the determinant is denoted by \det . The characteristic equation (2.14) yields N possible positive real solutions $\omega_1^2, \omega_2^2, \dots, \omega_N^2$ called eigenvalues. The square root of eigenvalues provides undamped natural frequencies, i.e., $\omega_1, \omega_2, \dots, \omega_N$. The natural frequencies are usually set in an increasing order. Note that the natural frequencies are fixed unique quantities given for the selected structure.

Substitution of each natural frequency in equation (2.13) and solution of $\boldsymbol{\phi}_n$ yields N possible vectors $\boldsymbol{\phi}_i$ ($i = 1, \dots, N$), known as mode shapes. Vectors $\boldsymbol{\phi}_i$ are eigenvectors of the problem described by (2.13). Each vector $\boldsymbol{\phi}_i$ consists of N elements, ϕ_i , that in the case of undamped system are real numbers. It should be noted that for any constant γ a vector $\gamma \boldsymbol{\phi}_i$ is also an eigenvector satisfying the eigenvalue problem (2.13). Therefore, amplitudes of the synchronic motion of the system degrees of freedom give information on relative motion, and not about their absolute magnitudes.

The set of N mode shapes is often presented in a matrix form as

$$\boldsymbol{\Phi} = [\boldsymbol{\phi}_{jn}] = \begin{bmatrix} \phi_{11} & \phi_{12} & \cdots & \phi_{1N} \\ \phi_{21} & \phi_{22} & \cdots & \phi_{2N} \\ \vdots & \vdots & \ddots & \vdots \\ \phi_{N1} & \phi_{N2} & \cdots & \phi_{NN} \end{bmatrix}. \quad (2.15)$$

The matrix $\boldsymbol{\Phi}$ is called the *modal matrix*. All the natural frequencies can be put together in one diagonal matrix called *spectral matrix* as

$$\boldsymbol{\Omega}^2 = \begin{bmatrix} \omega_1^2 & 0 & \cdots & 0 \\ 0 & \omega_2^2 & \cdots & 0 \\ \vdots & \vdots & \ddots & \vdots \\ 0 & 0 & \cdots & \omega_N^2 \end{bmatrix}. \quad (2.16)$$

Matrices $\boldsymbol{\Omega}^2$ and $\boldsymbol{\Phi}$ constitute a Modal Model of the engineering structure. A pair consisting of a natural frequency, ω , and corresponding mode shape $\boldsymbol{\phi}$, is called a modal pair. The description of a dynamic system through its modal properties (modal pairs) gives a possibility of performing an analysis from different points of view with respect to the description by so called the Spatial Model defined by matrices \mathbf{M} , \mathbf{C} and \mathbf{K} . In practical problems in civil engineering where the number of degrees of freedom is not very large, it is relatively simple to derive the Modal Model from the given Spatial Model. An opposite transformation, however, is not unique and additional data, e.g., on mass distribution, is required.

The mode shape vectors possess the orthogonality properties. Two different modal pairs $\{\omega_r, \phi_r\}$ and $\{\omega_n, \phi_n\}$ satisfy the eigenvalue problem (2.13). Thus,

$$(\mathbf{K} - \omega_r^2 \mathbf{M}) \phi_r = \mathbf{0}, \quad (2.17)$$

and

$$(\mathbf{K} - \omega_n^2 \mathbf{M}) \phi_n = \mathbf{0}. \quad (2.18)$$

Pre-multiplication of the equation (2.17) by ϕ_n^T gives

$$\phi_n^T (\mathbf{K} - \omega_r^2 \mathbf{M}) \phi_r = \mathbf{0}. \quad (2.19)$$

The second equation is derived by transposition of (2.18) with post multiplication by ϕ_r ,

$$\phi_n^T (\mathbf{K}^T - \omega_n^2 \mathbf{M}^T) \phi_r = \mathbf{0}. \quad (2.20)$$

Since the matrices \mathbf{K} and \mathbf{M} are derived through the FEM, they are symmetric and equation (2.20) can be written as

$$\phi_n^T (\mathbf{K} - \omega_n^2 \mathbf{M}) \phi_r = \mathbf{0}. \quad (2.21)$$

Subtraction of equation (2.19) from equation (2.21) yields

$$(\omega_r^2 - \omega_n^2) \phi_n^T \mathbf{M} \phi_r = \mathbf{0}. \quad (2.22)$$

Natural frequencies, according to the initial assumption, are different, and therefore, equation (2.22) can be satisfied only if

$$\phi_n^T \mathbf{M} \phi_r = \mathbf{0} \quad (r \neq n). \quad (2.23)$$

Equation (2.23) represents the orthogonality property of the mode shape vectors. The orthogonality condition does not apply to multiple modes, i.e., modes having the same frequency.

If the same modal vector is considered and the relation $r = n$ is introduced into (2.19), this equation becomes

$$\phi_n^T (\mathbf{K} - \omega_n^2 \mathbf{M}) \phi_n = \mathbf{0}. \quad (2.24)$$

Thus,

$$\phi_n^T \mathbf{K} \phi_n = \omega_n^2 \phi_n^T \mathbf{M} \phi_n. \quad (2.25)$$

Equation (2.25) can be written as

$$\omega_n^2 = \frac{\phi_n^T \mathbf{K} \phi_n}{\phi_n^T \mathbf{M} \phi_n} = \frac{\bar{k}_n}{\bar{m}_n}. \quad (2.26)$$

where \bar{k}_n is a modal stiffness also called the generalized stiffness, and \bar{m}_n is a modal or generalized mass of the n -th structural mode.

Writing the numerator and denominator of equation (2.26) in the matrix form yields

$$\bar{\mathbf{K}} = \Phi^T \mathbf{K} \Phi, \quad (2.27)$$

and

$$\bar{\mathbf{M}} = \mathbf{\Phi}^T \mathbf{M} \mathbf{\Phi}, \quad (2.28)$$

where the modal matrices $\bar{\mathbf{K}}$ and $\bar{\mathbf{M}}$ are of the form

$$\bar{\mathbf{K}} = \begin{bmatrix} \bar{k}_1 & 0 & \cdots & 0 \\ 0 & \bar{k}_2 & \cdots & 0 \\ \vdots & \vdots & \ddots & \vdots \\ 0 & 0 & \cdots & \bar{k}_N \end{bmatrix}, \quad \bar{\mathbf{M}} = \begin{bmatrix} \bar{m}_1 & 0 & \cdots & 0 \\ 0 & \bar{m}_2 & \cdots & 0 \\ \vdots & \vdots & \ddots & \vdots \\ 0 & 0 & \cdots & \bar{m}_N \end{bmatrix}. \quad (2.29)$$

In the experimental modal analysis it is common to normalize the mode shapes derived from the dynamic tests with respect to the largest vector coefficient, i.e.

$$\phi_n = \frac{\tilde{\Phi}_n}{\max |\tilde{\phi}_{jn}|}, \quad (2.30)$$

where $\tilde{\Phi}_n$ is the n -th experimental mode shape and $\tilde{\phi}_{jn}$ is the coefficient of the experimental modal matrix.

Very often the normalization of the mode shapes with respect to mass matrix is used. In this case the formula takes the following form,

$$\phi_n = \frac{\tilde{\Phi}_n}{\sqrt{\tilde{\Phi}_n^T \mathbf{M} \tilde{\Phi}_n}}. \quad (2.31)$$

In the case of normalization (2.31) the transformation of matrices \mathbf{K} and \mathbf{M} yields

$$\mathbf{\Phi}^T \mathbf{K} \mathbf{\Phi} = \mathbf{\Omega}^2, \quad (2.32)$$

and

$$\mathbf{\Phi}^T \mathbf{M} \mathbf{\Phi} = \mathbf{I}, \quad (2.33)$$

where \mathbf{I} is the identity matrix. Equations (2.32) and (2.33) provide easy tests for the verification of the experimentally determined mode shapes.

Modal approach to the engineering system dynamics decomposes the Spatial Model into N independent equations. This is due to the property of mode shape orthogonality. Mode shapes ϕ_n ($n = 1, 2, \dots, N$) are linearly independent and they form a basis for the N dimensional space. The structure response formulated in that space can be expressed as a linear combination of the mode shapes and modal coordinates, $\xi(t)$, being function of time coordinates as

$$\mathbf{u}(t) = \sum_{n=1}^N \phi_n \xi_n(t). \quad (2.34)$$

Equation (2.34) can be written in the matrix form as

$$\mathbf{u}(t) = \mathbf{\Phi} \xi(t), \quad (2.35)$$

where vector $\xi(t)$ consists of the modal coordinates selected to describe the dynamics of the MDOF system.

Example 2.1. The mode shapes are calculated for the undamped cantilever beam with 80 beam elements and 480 degrees of freedom by a commercial code SOFISTIK (see also Appendix A). The beam has a length $L = 480$ mm, width $b = 60$ mm and height $h = 20$ mm. The material properties are: Young modulus $E = 3400$ MPa and density $\rho = 1190 \text{ kg/m}^3$. Five mode shapes are shown in Fig. 2.3. The corresponding natural frequencies are 23.93 Hz, 71.59 Hz, 149.67 Hz, 344.54 Hz, 417.91 Hz. The first, third and fifth modes are called vertical bending modes since the largest displacements in the mode shapes are related to the vertical bending of the beam. The second mode is associated with the horizontal oscillations of the beam and the fourth mode corresponds to torsional response of the beam. The natural frequencies of 23.93 to 417.91 Hz are considered to be high since in the analysis of the dynamics of the existing civil engineering structure the range of interests is in the low frequency range.

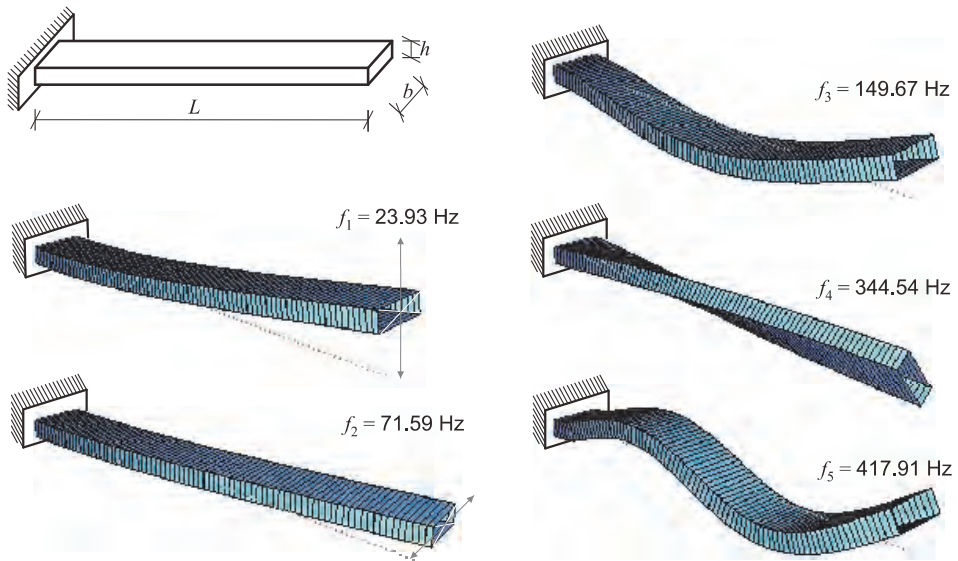
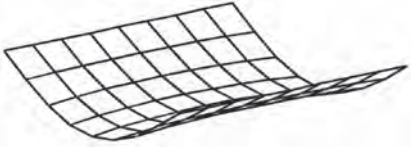
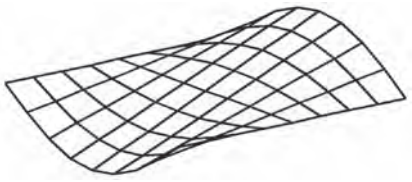
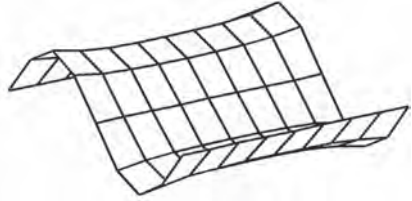
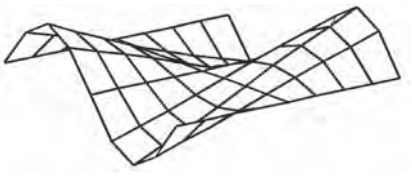
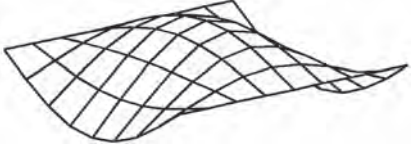
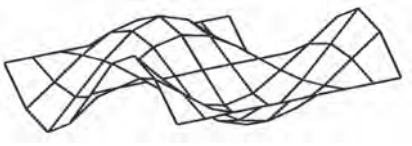


Fig. 2.3. The cantilever beam and its mode shapes

Example 2.2. The steel plate which is simply supported on two edges is shown in Fig. 2.4. The plate has a length of 1500 mm, width of 1200 mm and thickness of 5 mm. The material properties are: $E = 210$ GPa, density $\rho = 7850 \text{ kg/m}^3$ and Poisson's ratio of 0.3. The FEM model of the plate is derived according to the assumptions given in Appendix A. The computations were conducted by code written in MATLAB[®]. The first six mode shapes of the plate are given in Table 2.1 and they can be named according to the similarity to the modes of the cantilever beam. The first and the third modes are called the vertical bending ones. The second and fourth mode can be called torsional and shapes of mode five and six are referred to as plate modes, since they have local minima and maxima characteristic for the plate structures.

Table 2.1

Mode shapes of the steel plate

Mode	Frequency Mode description	Graphical representation
1	$f_1 = 6.19$ Hz – symmetric, – similar to 1 st bending mode of the beam	
2	$f_2 = 11.51$ Hz – antisymmetric, – similar to 1 st torsional mode of the beam	
3	$f_3 = 23.62$ Hz – antisymmetric, – similar to 2 nd bending mode of the beam	
4	$f_4 = 28.60$ Hz – antisymmetric, – similar to 2 nd torsional mode of the beam	
5	$f_5 = 31.89$ Hz – symmetric, – plate mode with one local maximum	
6	$f_6 = 51.59$ Hz – symmetric, – plate mode with several local maxima	

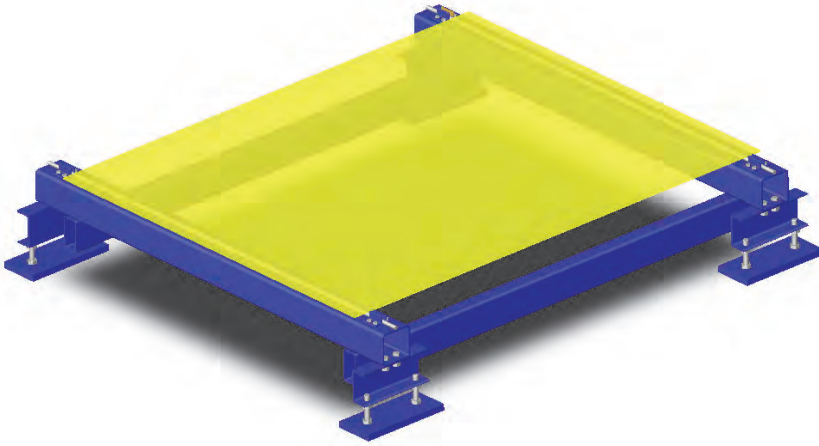


Fig. 2.4. Simply supported steel plate

Example 2.3. The modal analysis is conducted on the FEM model of the cable stayed bridge of the John Paul II bridge over the Vistula River in Gdańsk presented in Fig. 2.5. The bridge has one concrete tower of height 99.89 m and main span is of length 230 m. The deck is a composite structure consisting of two steel girders and concrete plate of 23 cm thickness. There are 30 cables supporting the deck. The FEM model has been derived in commercial program SOFISTIK with beam, plate and cable finite elements available in the code. The linear equations of motion have been defined around the static equilibrium of the structure. The 9 mode shapes of the undamped model are given in Table. 2.2.



Fig. 2.5. Photo of the bridge over the Vistula River in Gdańsk

Table 2.2

Mode shapes of the cable-stayed bridge






Mode	Frequency Mode description	Graphical representation
1	$f_1 = 0.49 \text{ Hz}$ – symmetric, – similar to 1 st bending mode of the main span	
2	$f_2 = 0.77 \text{ Hz}$ – symmetric, – similar to 1 st torsional mode of the main span	
3	$f_3 = 0.80 \text{ Hz}$ – antisymmetric, – similar to 2 nd bending mode of the main span	
5	$f_5 = 1.08 \text{ Hz}$ – symmetric, – similar to 3 rd bending mode of the main span	
6	$f_6 = 1.16 \text{ Hz}$ – antisymmetric, – similar to 2 nd torsional mode of the main span	

Table 2.2 (continued)

Mode	Frequency Mode description	Graphical representation
7	$f_7 = 1.43$ Hz – symmetric, – similar to 3 rd torsional mode of the main span with pylon bending	
8	$f_8 = 1.44$ Hz – antisymmetric, – similar to 4 th bending mode of the main span	
9	$f_9 = 1.50$ Hz – symmetric, – similar to 3 rd torsional mode of the main span	
10	$f_{10} = 1.71$ Hz – antisymmetric, – similar to 5 th bending mode of the main span with pylon lower part bending	

Generally, the modes of the bridge have non zero amplitudes on most of the structural degrees of freedom. However, some of them are very small and the dominant displacements define the properties of the particular mode. The first bridge mode (Table 2.2) of frequency 0.49 Hz corresponds to the first bending mode of the beam. The displacements of the tower and the side span are very small. The second mode of natural frequency 0.77 Hz is torsional. In civil engineering structures, particularly in bridges, it is common that the natural frequencies are closely spaced. In this example the ten structural modes have their natural frequencies in the range from 0 to 1.71 Hz.

2.1.2. Natural frequencies and mode shapes of proportionally damped system

Let the equations of motion of the MDOF dynamic system with damping be of the form

$$\mathbf{M}\ddot{\mathbf{u}}(t) + \mathbf{C}\dot{\mathbf{u}}(t) + \mathbf{K}\mathbf{u}(t) = \mathbf{0}. \quad (2.36)$$

The free response of the system subjected to the initial perturbation on the displacements at time $t = 0$, $\mathbf{u}(0) = \mathbf{0}$, and velocities, $\dot{\mathbf{u}}(0) = \mathbf{0}$, can be assumed as

$$\mathbf{u}(t) = \mathbf{a}e^{\lambda t}, \quad (2.37)$$

where λ is a complex number and \mathbf{a} is a vector of size $N \times 1$. The definition of the proportional damping matrix is given in equation (2.7). In the case of damped systems the exponent λ can have non zero values of its imaginary and real parts. In the previous section, in the solution of the undamped system, the exponent λ is a complex number with zero real part, i.e., purely harmonic motion is considered.

Substitution of equation (2.37) into the equation of motion of the damped system (2.36) yields

$$\left(\lambda^2\mathbf{M} + \lambda\mathbf{C} + \mathbf{K}\right)\mathbf{a}e^{\lambda t} = \mathbf{0}. \quad (2.38)$$

Since exponential term, $\mathbf{a}e^{\lambda t}$, is non zero the eigenvalue problem can be written as follows

$$\left(\lambda^2\mathbf{M} + \lambda\mathbf{C} + \mathbf{K}\right)\mathbf{a} = \mathbf{0}, \quad (2.39)$$

and the eigenvalues are determined from the characteristic equation

$$\det\left(\lambda^2\mathbf{M} + \lambda\mathbf{C} + \mathbf{K}\right) = 0. \quad (2.40)$$

In this section, it will be proved that the eigenvectors of the undamped dynamic system (2.13) are real and that they diagonalize the system matrices \mathbf{M} , \mathbf{C} and \mathbf{K} of the proportionally damped system (2.36), and that the mode shapes of the proportionally damped system are also real. For the sake of clarity, in this section, the mode shapes of the proportionally damped system are denoted by \mathbf{a} , while the mode shapes of the undamped system are denoted by \mathbf{b} . In the first part, it will be shown that natural frequencies and the mode shape of the undamped system are real. In the second part the simultaneous diagonalization of the system matrices by the undamped mode shapes will be discussed.

To show that vectors \mathbf{a} are real a coordinate transformation is introduced,

$$\mathbf{u}(t) = \mathbf{M}^{-\frac{1}{2}}\mathbf{z}(t), \quad (2.41)$$

where vector $\mathbf{z}(t)$ is given by

$$\mathbf{z}(t) = \mathbf{b}e^{\mu t}, \quad (2.42)$$

and the relationship between vectors \mathbf{a} and \mathbf{b} is

$$\mathbf{a} = \mathbf{M}^{-\frac{1}{2}}\mathbf{b}. \quad (2.43)$$

Substitution of equations (2.41), (2.42) and (2.43) into equation (2.13) and premultiplication by $\mathbf{M}^{-1/2}$ yields

$$\left(\mu^2\mathbf{M}^{-\frac{1}{2}}\mathbf{M}\mathbf{M}^{-\frac{1}{2}} + \mathbf{M}^{-\frac{1}{2}}\mathbf{K}\mathbf{M}^{-\frac{1}{2}}\right)\mathbf{b} = \mathbf{0}. \quad (2.44)$$

The matrices in equation (2.44) can be defined as,

$$\mathbf{I} = \mathbf{M}^{-\frac{1}{2}} \mathbf{M} \mathbf{M}^{-\frac{1}{2}}, \quad (2.45)$$

and

$$\hat{\mathbf{A}} = \mathbf{M}^{-\frac{1}{2}} \mathbf{K} \mathbf{M}^{-\frac{1}{2}}, \quad (2.46)$$

where \mathbf{I} is an identity matrix. The eigenvalue problem can be written in the form

$$\left(\mu^2 \mathbf{I} + \hat{\mathbf{A}} \right) \mathbf{b} = \mathbf{0}. \quad (2.47)$$

Equation (2.47) defines the classical eigenvalue problem. Matrix $\hat{\mathbf{A}}$ is real and positive definite since matrix \mathbf{K} is real and positive definite. Thus, the eigenvalues are real and positive and the eigenvectors, \mathbf{b} , are real. Finally, the eigenvalues \mathbf{a} are computed by pre-multiplying the vector \mathbf{b} by a real matrix $\mathbf{M}^{-1/2}$ (2.43). Therefore, the eigenvectors \mathbf{a} are also real, which was to prove.

The discussion on the relation between the mode shapes of the undamped system and the eigenvectors of the damped system starts with the definition of the modal matrix by vectors \mathbf{b} , i.e.,

$$\mathbf{B} = [\mathbf{b}_1, \mathbf{b}_2, \dots, \mathbf{b}_N], \quad (2.48)$$

where eigenvectors \mathbf{b} satisfy the orthogonality condition and diagonalize the system matrix $\hat{\mathbf{A}}$ as follows

$$\mathbf{B}^T \hat{\mathbf{A}} \mathbf{B} = \boldsymbol{\mu}, \quad (2.49)$$

where matrix $\boldsymbol{\mu}$ is a diagonal matrix of the form

$$\boldsymbol{\mu} = \begin{bmatrix} -\mu_1^2 & 0 & \cdots & 0 \\ 0 & -\mu_2^2 & \cdots & 0 \\ \vdots & \vdots & \ddots & \vdots \\ 0 & 0 & \cdots & -\mu_N^2 \end{bmatrix}. \quad (2.50)$$

Introduction of the transformations (2.41), (2.43) and (2.43) into the equation of the proportionally damped eigenvalue problem (2.39) and pre-multiplication by $\mathbf{B}^T \mathbf{M}^{-1/2}$ gives

$$\mathbf{B}^T \left(\lambda^2 \mathbf{I} + \lambda \mathbf{M}^{-\frac{1}{2}} \mathbf{C} \mathbf{M}^{-\frac{1}{2}} + \mathbf{M}^{-\frac{1}{2}} \mathbf{K} \mathbf{M}^{-\frac{1}{2}} \right) \mathbf{B} = \mathbf{0}, \quad (2.51)$$

where the eigenvalue problem (2.51) is formulated in terms of the modal matrix \mathbf{B} and matrix $\mathbf{0}$ is of size $N \times N$. The transformed matrices $\hat{\mathbf{C}}$ and $\hat{\mathbf{K}}$ can be defined as

$$\hat{\mathbf{C}} = \mathbf{M}^{-\frac{1}{2}} \mathbf{C} \mathbf{M}^{-\frac{1}{2}}, \quad (2.52)$$

and

$$\hat{\mathbf{K}} = \mathbf{M}^{-\frac{1}{2}} \mathbf{K} \mathbf{M}^{-\frac{1}{2}}. \quad (2.53)$$

Theorem: Two real symmetric matrices \mathbf{F} and \mathbf{G} are simultaneously diagonalized by a real orthogonal transformation if and only if they commute, i.e., $\mathbf{F} \cdot \mathbf{G} = \mathbf{G} \cdot \mathbf{F}$.

The orthogonal real matrix \mathbf{B} performs a real orthogonal transformation on matrices $\widehat{\mathbf{C}}$ and $\widehat{\mathbf{K}}$. The proportional damping matrix \mathbf{C} is diagonalized if and only if,

$$\left(\mathbf{M}^{-\frac{1}{2}}\mathbf{C}\mathbf{M}^{-\frac{1}{2}}\right) \cdot \left(\mathbf{M}^{-\frac{1}{2}}\mathbf{K}\mathbf{M}^{-\frac{1}{2}}\right) = \left(\mathbf{M}^{-\frac{1}{2}}\mathbf{K}\mathbf{M}^{-\frac{1}{2}}\right) \cdot \left(\mathbf{M}^{-\frac{1}{2}}\mathbf{C}\mathbf{M}^{-\frac{1}{2}}\right). \quad (2.54)$$

The equation (2.54) is true if the following condition is satisfied

$$\mathbf{C}\mathbf{M}^{-1}\mathbf{K} = \mathbf{K}\mathbf{M}^{-1}\mathbf{C}. \quad (2.55)$$

Equity (2.55) is a condition for the simultaneous diagonalization of the system stiffness and damping matrix.

To show that the proportional damping matrix satisfies the condition its definition (2.7) is introduced into equation (2.55) as follows,

$$(\alpha\mathbf{M} + \beta\mathbf{K})\mathbf{M}^{-1}\mathbf{K} = \mathbf{K}\mathbf{M}^{-1}(\alpha\mathbf{M} + \beta\mathbf{K}). \quad (2.56)$$

Thus,

$$\alpha\mathbf{M}\mathbf{M}^{-1}\mathbf{K} + \beta\mathbf{K}\mathbf{M}^{-1}\mathbf{K} = \alpha\mathbf{K}\mathbf{M}^{-1}\mathbf{M} + \beta\mathbf{K}\mathbf{M}^{-1}\mathbf{K}, \quad (2.57)$$

and finally

$$\alpha\mathbf{K} + \beta\mathbf{K}\mathbf{M}^{-1}\mathbf{K} = \alpha\mathbf{K} + \beta\mathbf{K}\mathbf{M}^{-1}\mathbf{K}. \quad (2.58)$$

Equation (2.58) proves that the proportional matrix \mathbf{C} satisfies the condition (2.55).

The modal matrix \mathbf{B} diagonalizes the matrix \mathbf{K} and \mathbf{C} as follows

$$\mathbf{B}^T \left(\mathbf{M}^{-\frac{1}{2}}\mathbf{K}\mathbf{M}^{-\frac{1}{2}} \right) \mathbf{B} = \boldsymbol{\mu}, \quad (2.59)$$

and

$$\mathbf{B}^T \left(\mathbf{M}^{-\frac{1}{2}}\mathbf{C}\mathbf{M}^{-\frac{1}{2}} \right) \mathbf{B} = \mathbf{v}, \quad (2.60)$$

where matrix \mathbf{v} is a diagonal matrix of the form

$$\mathbf{v} = \begin{bmatrix} v_1^2 & 0 & \cdots & 0 \\ 0 & v_2^2 & \cdots & 0 \\ \vdots & \vdots & \ddots & \vdots \\ 0 & 0 & \cdots & v_N^2 \end{bmatrix}. \quad (2.61)$$

The eigenvalues of the damped system computed from the diagonal matrices (2.59) and (2.60) are

$$\lambda_k = \frac{1}{2}v_k^2 \pm i \frac{1}{2}\sqrt{-4\mu_k^2 - v_k^4}. \quad (2.62)$$

The eigenvalues can be also written as

$$\lambda_k = -\xi_k \omega_k \pm i\omega_{d_k}, \quad (2.63)$$

where ξ_k is a damping ratio defined for a single degree of freedom system described by mass m , damping coefficient c , and natural circular frequency ω_k is

$$\xi_k = \frac{c}{2m\omega_k}. \quad (2.64)$$

In this book only the cases of the underdamped systems are considered. The system is underdamped if all the damping ratios of the modes describing the system are smaller than 1, i.e.,

$$\xi_k < 1, \quad k = 1, 2, \dots, N. \quad (2.65)$$

The free response of the underdamped system is described by decaying the harmonic functions. The natural circular frequency of the k -th mode is denoted by ω_k and the damped circular frequency is defined as

$$\omega_{d_k} = \omega_k \sqrt{1 - \xi_k^2}. \quad (2.66)$$

The circular frequency as well as the damped circular frequency is expressed in radians per second [rad/s]. In the following sections the frequency characteristics of the dynamics of an engineering structure will be described also in terms of the natural period, and the natural frequency. The relations between the circular frequency and the natural period, T_k , of the selected mode is

$$T_k = \frac{2\pi}{\omega_k}. \quad (2.67)$$

The natural period is expressed in time units, i.e., seconds. The natural frequency of the k -th mode is

$$f_k = \frac{\omega_k}{2\pi} = \frac{1}{T_k}. \quad (2.68)$$

The units of the natural frequencies, f_k , are Hz.

2.1.3. Natural frequencies and mode shapes of systems with arbitrary viscous damping

In this section the MDOF dynamic system (2.36) with the arbitrary viscous damping matrix \mathbf{C} is considered. In general the damping in an engineering structure is non proportional and relatively small. The damping ratio for the steel structures, usually, does not exceed 2%, while for the concrete structure it might reach about 5%. In the case of very small damping it is possible to neglect all the off diagonal terms without a great loss in accuracy. Regarding small damping of 2–3% the approximation of the damping matrix by a proportional damping model is also acceptable and does not significantly affect the predicted system response. However, in the case of structures with large damping due to damping devices, like, passive or active damping control systems or coupled systems that models interaction of the structure with some surrounding media, e.g., fluid or soil, the neglecting of the off diagonal damping terms or assumption on proportional damping model cannot be applied. In this cases the solution through the state space is applicable.

The modal matrix Φ does not diagonalize the arbitrary damping matrix \mathbf{C} , and thus, the analytical solutions of the free vibration in Spatial Model are not possible. The problem can be solved in the state space (2.6) where the state vector, $\mathbf{x}(t)$, has the length of $2N \times 1$ and is of the form

$$\mathbf{x}(t) = \begin{bmatrix} \mathbf{u}(t) \\ \dot{\mathbf{u}}(t) \end{bmatrix}, \quad (2.69)$$

where $\mathbf{u}(t)$ denotes the displacements and $\dot{\mathbf{u}}(t)$ is the vector of velocities of the system degrees of freedom. Theoretically the state space vector can consist of any of two vectors selected from displacement $\mathbf{u}(t)$, velocity $\dot{\mathbf{u}}(t)$ and acceleration $\ddot{\mathbf{u}}(t)$ vector. The state space equations of motion of the MDOF system for the free vibration case become

$$\dot{\mathbf{x}}(t) = \mathbf{A}\mathbf{x}(t). \quad (2.70)$$

Equation (2.70) is a homogeneous set of the first order ordinary differential equations with constant coefficients and their solution has the form

$$\mathbf{u}(t) = \mathbf{a}e^{\lambda t}, \quad (2.71)$$

where \mathbf{a} is a vector of size $N \times 1$ and λ is complex value. The algebraic eigenvalue problem in its standard form is given by

$$\mathbf{A}\mathbf{a} = \lambda\mathbf{a}. \quad (2.72)$$

In equation (2.72) the state matrix \mathbf{A} of size $2N \times 2N$ has constant coefficients but is non-symmetric. In this case the $2N$ eigenvalues might be complex, and the eigenvectors might be complex as well as it is not sure that they are orthogonal. Because matrix \mathbf{A} is real, if eigenvalue λ_n is a complex value, then the constant $\bar{\lambda}_n$, which is a complex conjugate to λ_n , is also an eigenvalue of problem (2.72). If the values in the eigen pair $\{\lambda_n, \mathbf{a}_n\}$ are complex, the eigenvector $\bar{\mathbf{a}}_n$ belonging to $\bar{\lambda}_n$ is complex conjugate to the eigenvector \mathbf{a}_n . Therefore, the pairs $\{\lambda_n, \mathbf{a}_n\}$ and $\{\bar{\lambda}_n, \bar{\mathbf{a}}_n\}$ have complex conjugate components, respectively.

The eigenvalue problem of the transpose state matrix \mathbf{A} is

$$\mathbf{A}^T \mathbf{b} = \lambda \mathbf{b}. \quad (2.73)$$

Since the determinant of \mathbf{A} is equal to the determinant of \mathbf{A}^T , the characteristic equations for problem \mathbf{A} and \mathbf{A}^T are the same, i.e.,

$$\det(\mathbf{A} - \lambda \mathbf{I}) = \det(\mathbf{A}^T - \lambda \mathbf{I}) = 0. \quad (2.74)$$

Therefore, the eigenvalues of \mathbf{A}^T are the same as the eigenvalues of \mathbf{A} , but eigenvectors \mathbf{a} of the problem \mathbf{A} are not the same as eigenvectors \mathbf{b} of the problem \mathbf{A}^T . The equation (2.73) can be written in the transpose form and is known as the adjoint eigenvalue problem,

$$\mathbf{b}^T \mathbf{A} = \lambda \mathbf{b}^T. \quad (2.75)$$

Because in equation (2.75), the eigenvectors \mathbf{b} are on the left side with respect to matrix \mathbf{A} , they are called the left eigenvectors of \mathbf{A} . Vectors \mathbf{a} in equation (2.72) are on the right side of \mathbf{A} and they are called the right eigenvectors of \mathbf{A} . The right eigenvectors $\mathbf{a}_1, \mathbf{a}_2, \dots, \mathbf{a}_{2N}$, are not mutually orthogonal, and the left eigenvectors $\mathbf{b}_1, \mathbf{b}_2, \dots, \mathbf{b}_{2N}$, are also not mutually orthogonal either. However, the sets of eigenvectors satisfying this condition are called biorthogonal.

Each vector \mathbf{a}_i satisfies the equation (2.72), i.e.,

$$\mathbf{A}\mathbf{a}_i = \lambda_i \mathbf{a}_i, \quad i = 1, 2, \dots, 2N, \quad (2.76)$$

and the vector \mathbf{b}_i , satisfies the equation (2.75) as follows

$$\mathbf{b}_j^T \mathbf{A} = \lambda_j \mathbf{b}_j^T, \quad j = 1, 2, \dots, 2N. \quad (2.77)$$

Pre-multiplication of (2.76) by \mathbf{b}_i^T and post-multiplication of (2.77) by \mathbf{a}_i yields

$$\mathbf{b}_j^T \mathbf{A} \mathbf{a}_i = \lambda_j \mathbf{b}_j^T \mathbf{a}_i \quad (2.78)$$

and

$$\mathbf{b}_j^T \mathbf{A} \mathbf{a}_i = \lambda_i \mathbf{b}_j^T \mathbf{a}_i \quad (2.79)$$

Subtraction of equation (2.79) from equation (2.78) gives

$$(\lambda_i - \lambda_j) \mathbf{b}_j^T \mathbf{a}_i = 0 \quad (2.80)$$

If $\lambda_i \neq \lambda_j$, then equation (2.80) can be satisfied only if

$$\mathbf{b}_j^T \mathbf{a}_i = 0 \quad i = 1, 2, \dots, 2N, \quad j = 1, 2, \dots, 2N. \quad (2.81)$$

Therefore the right eigenvector \mathbf{a}_i is orthogonal to the left eigenvector \mathbf{b}_j for $i \neq j$. It is noted that vectors \mathbf{a} are not orthogonal as in the case of the real and symmetric Spatial Model of the system. The orthogonality holds only between vectors \mathbf{a} and \mathbf{b} .

Insertion of equation (2.81) into equation (2.78) with the condition that $\lambda_i \neq \lambda_j$ gives

$$\mathbf{b}_j^T \mathbf{A} \mathbf{a}_i = 0 \quad i = 1, 2, \dots, 2N, \quad j = 1, 2, \dots, 2N. \quad (2.82)$$

Thus, the right eigenvectors \mathbf{a}_i are also biorthogonal with respect to matrix \mathbf{A} to the left eigenvectors \mathbf{b}_j .

It is convenient to normalize the eigenvectors, as it was shown in the previous sections, so that

$$\mathbf{b}_i^T \mathbf{a}_i = 1 \quad i = 1, 2, \dots, 2N. \quad (2.83)$$

Therefore, it can be written that

$$\mathbf{b}_i^T \mathbf{A} \mathbf{a}_i = \lambda_i \quad i = 1, 2, \dots, 2N. \quad (2.84)$$

The properties of eigenvectors can be presented in a compact matrix form. The matrices of the right and left eigenvectors are

$$\mathbf{\Phi}_R = [\mathbf{a}_1, \mathbf{a}_2, \dots, \mathbf{a}_{2N}], \quad \mathbf{\Phi}_L = [\mathbf{b}_1, \mathbf{b}_2, \dots, \mathbf{b}_{2N}], \quad (2.85)$$

respectively. The diagonal matrix of eigenvalues $\mathbf{\Omega}$ becomes

$$\mathbf{\Omega} = \begin{bmatrix} \lambda_1 & 0 & \cdots & 0 \\ 0 & \lambda_2 & \cdots & 0 \\ \vdots & \vdots & \ddots & \vdots \\ 0 & 0 & \cdots & \lambda_{2N} \end{bmatrix}. \quad (2.86)$$

Then, the equation (2.76) takes the form

$$\mathbf{A} \mathbf{\Phi}_R = \mathbf{\Phi}_R \mathbf{\Omega}, \quad (2.87)$$

and the equation (2.77) is

$$\Phi_L^T \mathbf{A} = \mathbf{\Omega} \Phi_L^T. \quad (2.88)$$

The biorthogonality relation can be recast in the form

$$\Phi_L^T \Phi_R = \mathbf{I}, \quad (2.89)$$

and biorthogonality with respect to matrix \mathbf{A} becomes

$$\Phi_L^T \mathbf{A} \Phi_R = \mathbf{\Omega}, \quad (2.90)$$

Post-multiplication of equation (2.89) by Φ_R^{-1} at the right side yields

$$\Phi_L^T \Phi_R \Phi_R^{-1} = \mathbf{I} \Phi_R^{-1}, \quad (2.91)$$

and

$$\Phi_L^T = \Phi_R^{-1}. \quad (2.92)$$

Thus, the relation between the right eigenvectors modal matrix and left eigenvectors modal matrix becomes

$$\Phi_R \Phi_L^T = \mathbf{I}. \quad (2.93)$$

The decomposition of the state matrix \mathbf{A} is derived from the equation (2.90) and takes the form

$$\mathbf{A} = \Phi_R \mathbf{\Omega} \Phi_L^T. \quad (2.94)$$

The modal analysis of the system with arbitrary viscous damping matrix requires computation or experimental determination of the right and left complex eigenvectors, as well as $2N$ complex eigenvalues.

The right eigenvectors \mathbf{a}_i and the left eigenvectors \mathbf{b}_i of the nonsymmetric matrix \mathbf{A} form the basis for a state space model, and therefore, a response of the dynamic system with arbitrary viscous damping can be written as a linear combination of the right eigenvectors multiplied by modal coordinates $\xi_i(t)$,

$$\mathbf{u}(t) = \sum_{i=1}^{2N} \mathbf{a}_i \xi_i(t). \quad (2.95)$$

Equation (2.95) defines the systems response in a manner similar to the response of the undamped system.

Example 2.4. The case of the system with arbitrary viscous damping is presented on an example of the hypothetical suspension bridge (Wilde 2002) with the main span of 3000 m and side spans of 1000 m (Fig. 2.6). The height of the towers is 310 m and the sag of the main cables is 300 m. The girder is modelled as a continuous three-span beam with fixed horizontal, vertical and torsional displacements at the embankments and towers. The boundary conditions for the main cables are: fixed longitudinal, horizontal and vertical displacements at the anchorage and fixed horizontal and vertical displacements at the towers. The properties of structural elements of the bridge are listed in the book by Wilde (2002). The linear equation of motion has been derived with respect to the bridge static equilibrium position.

The selection of the degrees of freedom for the section of the suspension bridge is given in Fig. 2.7. The longitudinal deformations of the deck are ignored and the hanger cables are considered to be inextensible. Thus, there are two translations and three rotations in the node corresponding to the bridge deck and each node of the cable is described by lateral translation.

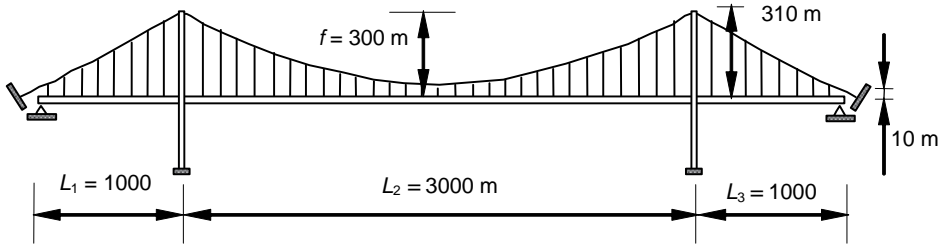


Fig. 2.6. Geometry of the analyzed bridge

The results of modal analysis of the proportionally damped suspension bridge for the wind speed of 0 m/s are given in Table 2.3. The structural elements for deck, towers and cables have their corresponding matrices of proportional viscous damping. The lowest two natural frequencies correspond to the horizontal modes since for very long span bridges the lateral stiffness of the deck is the lowest. The third mode can be named as a vertical anti-symmetric bending and is governed by the suspension cables. The lowest torsional mode has the number 14 but its natural frequency is only of 0.144 Hz. This torsional mode is symmetric and has the largest displacements in the mid span of the bridge. The second torsional mode has the natural frequency of 0.226 Hz and is antisymmetric.

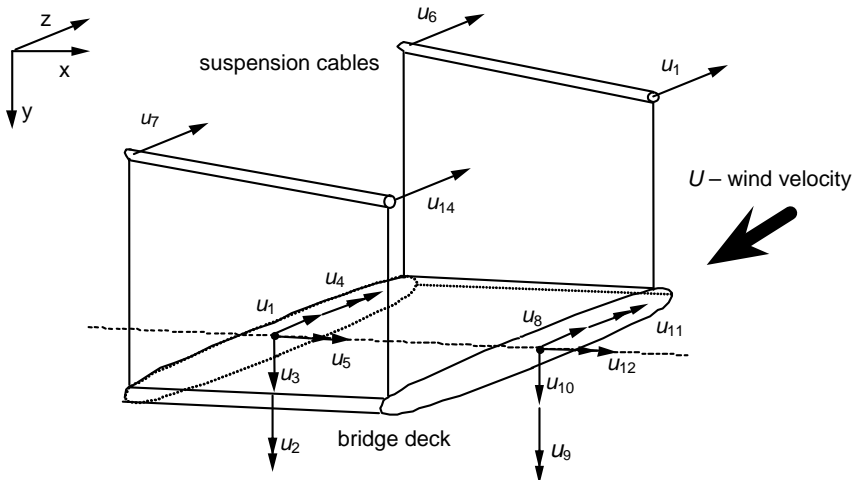


Fig. 2.7. Degrees of freedom for the section of the suspension bridge

Table 2.3

Modes of free vibrations

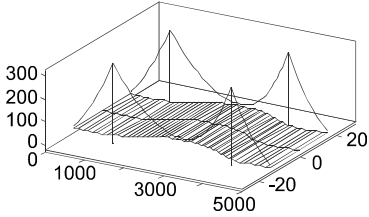
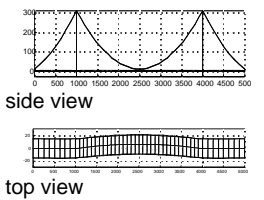
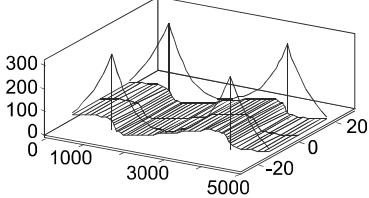
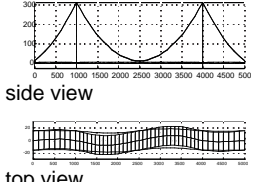
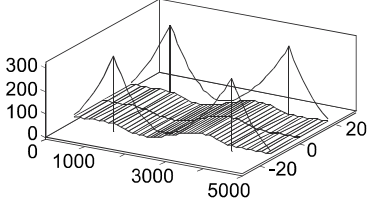
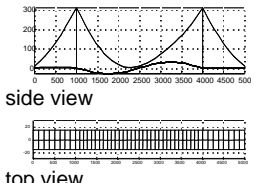
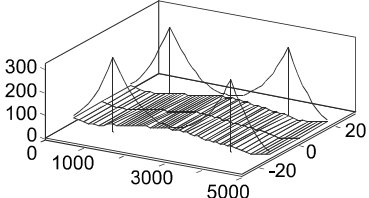
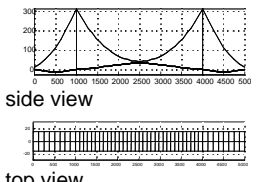
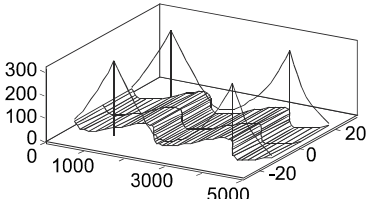
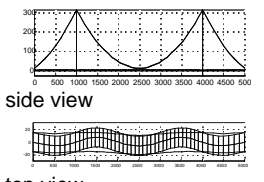
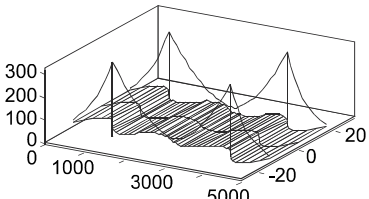
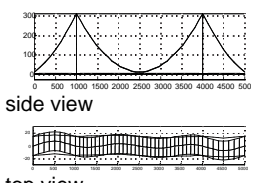
Mode	Frequency Damping ratio Description	Graphical representation of the mode	
1	$f_1 = 0.032$ Hz $\zeta_1 = 0.010$ – horizontal, symmetric, – main span and cables of main span		 <p>side view</p> <p>top view</p>
2	$f_2 = 0.056$ Hz $\zeta_2 = 0.007$ – horizontal, anti-symmetric, – main span and cables of main span		 <p>side view</p> <p>top view</p>
3	$f_3 = 0.066$ Hz $\zeta_3 = 0.010$ – vertical, anti-symmetric, – main span		 <p>side view</p> <p>top view</p>
4	$f_4 = 0.066$ Hz $\zeta_4 = 0.008$ – vertical, symmetric, – main and side spans		 <p>side view</p> <p>top view</p>
5	$f_5 = 0.077$ Hz $\zeta_5 = 0.009$ – horizontal, symmetric, – main and side spans		 <p>side view</p> <p>top view</p>
6	$f_6 = 0.092$ Hz $\zeta_6 = 0.010$ – horizontal, anti-symmetric, – side and main spans		 <p>side view</p> <p>top view</p>

Table 2.3 (continued)

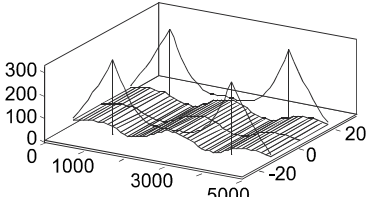
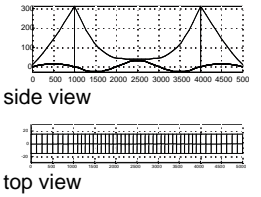
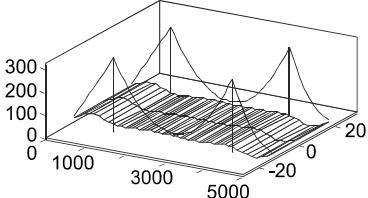
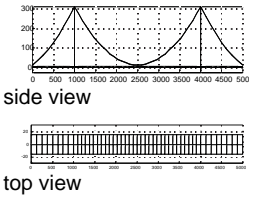
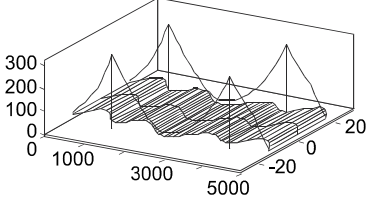
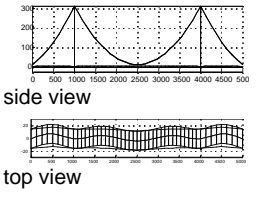
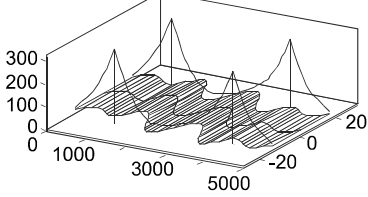
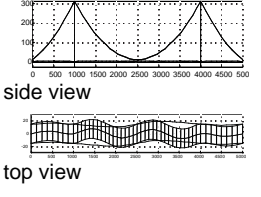
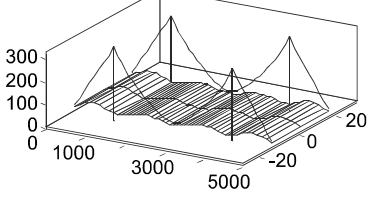
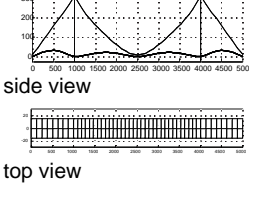
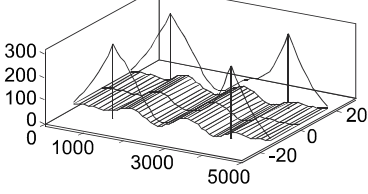
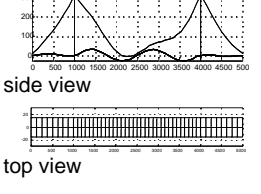
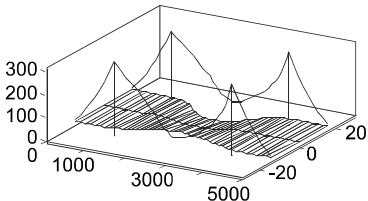
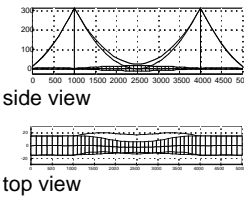
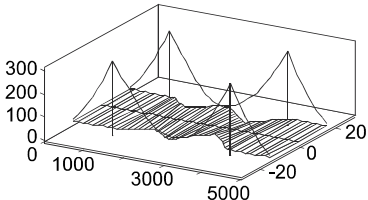
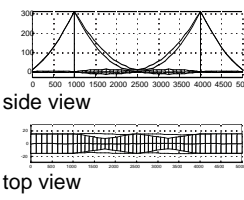
Mode	Frequency Damping ratio Description	Graphical representation of the mode	
7	$f_7 = 0.097$ Hz $\zeta_7 = 0.011$ – vertical, symmetric, – main and side spans		 <p>side view</p> <p>top view</p>
8	$f_8 = 0.100$ Hz $\zeta_8 = 0.011$ – vertical, anti-symmetric, – side spans		 <p>side view</p> <p>top view</p>
9	$f_9 = 0.101$ Hz $\zeta_9 = 0.011$ – horizontal, symmetric, – side and main spans		 <p>side view</p> <p>top view</p>
10	$f_{10} = 0.127$ Hz $\zeta_{10} = 0.016$ – horizontal, anti-symmetric, – main and side spans		 <p>side view</p> <p>top view</p>
11	$f_{11} = 0.130$ Hz $\zeta_{11} = 0.008$ – vertical, symmetric, – side and main spans		 <p>side view</p> <p>top view</p>
12	$f_{12} = 0.133$ Hz $\zeta_{12} = 0.013$ – vertical, anti-symmetric, – main span		 <p>side view</p> <p>top view</p>

Table 2.3 (continued)

Mode	Frequency Damping ratio Description	Graphical representation of the mode	
14	$f_{14} = 0.144$ Hz $\xi_{14} = 0.008$ – torsional, sym- metric, – main span		 <p>side view</p> <p>top view</p>
26	$f_{26} = 0.226$ Hz $\xi_{26} = 0.011$ – torsional, anti- symmetric, – main span		 <p>side view</p> <p>top view</p>

The unsteady aerodynamic forces, i.e. lift and moment, acting on the bridge deck are modeled by the additional degrees of freedom derived through the rational function approximation of the experimental unsteady aerodynamics. The aerodynamic degrees of freedom are governed by the first order differential equations (Wilde et al. 1996, Wilde and Fujino 1998). In addition the different aerodynamic models were assumed for the bridge structural elements, i.e., different damping modes are defined for the aerodynamic damping of cables, towers and deck. To present the effects of the nonproportional damping on mode shapes the case of the bridge deck with structural control under the action of wind will be discussed. The control system consists of some additional flaps connected to the deck by hinges (Omenzetter et al. 2002a, 2002b). The rotation of the flaps is coupled with the rotation of the bridge by additional cables (Fig. 2.8). The rotation of the flaps generates the aerodynamic forces that are also a function of the velocities of state variables. Therefore, the control system adds substantial damping to the structure and prevents the onset of flutter.

The mode shapes of the bridge under the action of wind cannot be presented in terms of displacements since they are complex. The most convenient way to present them is by showing the amplitudes absolute values and the phase shifts. In the case of mode absolute values the information on the relative motion direction is lost since the oscillation amplitudes have only positive values. It must be remembered that the absolute values of eigenvectors, as well as the phases are given only in the relative sense. Thus, only the relative difference between the amplitudes and phases of two selected points on the bridge is meaningful. The complex modes are also eigenvectors when they are multiplied by a constant.

Fig. 2.9 shows the variation of the absolute values of the vertical and torsional components of eigenvector number 11 (Table 2.3). The absolute values of the vertical components are given in Fig. 2.9a. The shape of the mode amplitudes for the lowest wind speed, of $U = 20$ m/s (denoted by square marks) in the main span is similar to letter M. For the assumed wind speed the influence of the unsteady aerodynamics on the structure is limited and the mode is similar to mode 11 shown in Table 2.3. The phases of the vertical component (Fig. 2.9b) for wind of 20 m/s are almost constant for the side spans and are reaching the values of 0.47 rad. The amplitudes of the main span are slowly changing having the

average value of 0.15 rad. Since the motion of the side spans and the main span are in about the same phase, the points of the bridge deck reach the maximum values approximately at the same time.

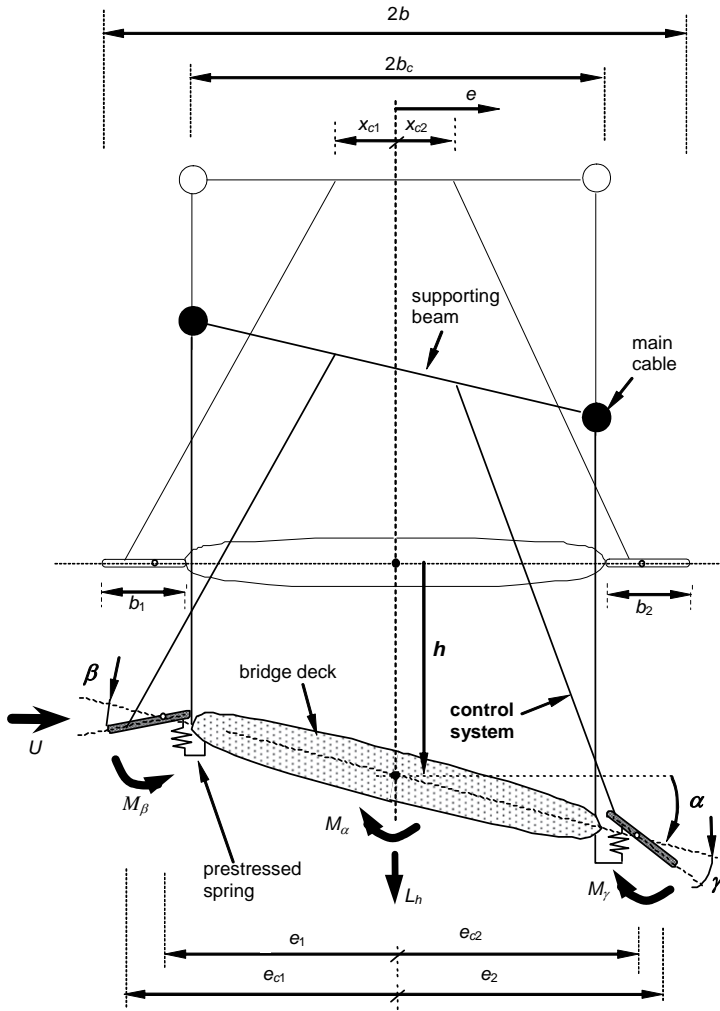


Fig. 2.8. Cross section of passive deck-flaps control system

The changes of the amplitudes of the vertical component at the wind speed of 100m/s are denoted by circles in Fig. 2.9a. The relative amplitudes of the main span are bigger than in the case of the amplitudes at wind speed of 20 m/s. Moreover, at the centre of the main span appears an additional peak of the vertical component. It is because the stabilizing forces generated by the control flaps have the strongest influence at the main span of the bridge and they change the mode amplitudes distribution along the main span. The changes of the mode phases at wind speed of 100 m/s are marked with circles in Fig. 2.9b. Between the point located at a distance of 2000 m from the tower and the mid span of the bridge, the phase difference is $\phi_1 = 1.46$ rad. Therefore, the maximum amplitude of the point at dis-

tance of 2000 m from the tower is reached after the bridge mid span. In this case the maximum amplitudes at different points of the bridge are not reached at the same time.

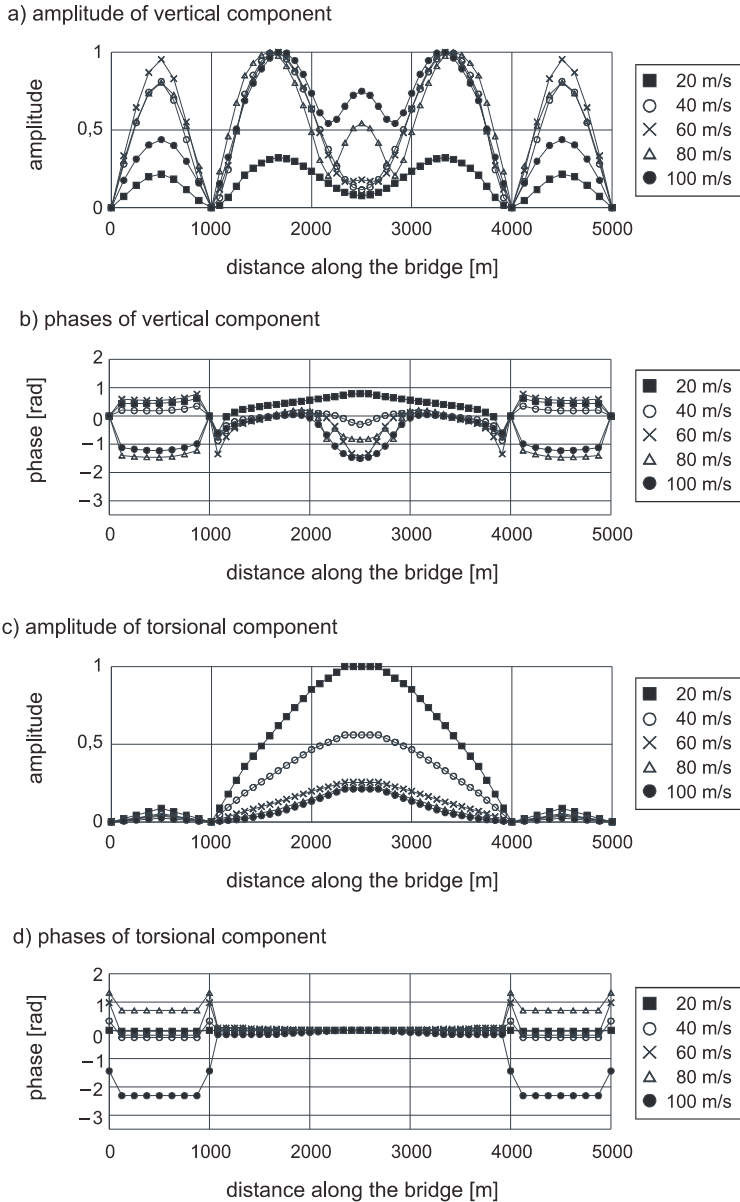


Fig. 2.9. Variation of mode 11 of bridge-flaps control system vs. wind speed

The amplitudes and phases of the torsional component of mode shape 11, along the bridge span, are presented in Fig 2.9c and 2.9d, respectively. The amplitudes of the side and main spans have shapes similar to half sine function, and the influence of wind and control

forces do not affect them significantly. The phases along the main span are approximately zero. It indicates that the torsional component of the mode oscillates in the same phase along the main span.

The analysis of the complex modes of the very long span bridge controlled by the passive system under the action of wind makes it possible to study the influence of the applied control strategy on a particular mode. In this case the consideration of the non proportional viscous damping matrix is necessary.

2.2. Frequency response functions of MDOF systems

The dynamics of engineering structures can be studied from the frequency content point of view. In fact, the analysis in the frequency domain provides a lot of information very helpful in the engineering system design. One way of deriving the frequency response matrix is by means of the Laplace transform method.

The Laplace transform of the equations of motion (2.1) with the initial conditions yields

$$(\mathbf{M}s^2 + \mathbf{C}s + \mathbf{K})\mathbf{U}(s) - \mathbf{M}s\mathbf{U}(0) - \mathbf{M}\dot{\mathbf{U}}(0) - \mathbf{C}\mathbf{U}(0) = \mathbf{P}(s). \quad (2.96)$$

The equation (2.96) can be rewritten under the assumption that the initial conditions are zero,

$$\mathbf{B}(s)\mathbf{X}(s) = \mathbf{P}(s), \quad (2.97)$$

where $\mathbf{B}(s)$ known as a system matrix is given by

$$\mathbf{B}(s) = \mathbf{M}s^2 + \mathbf{C}s + \mathbf{K}. \quad (2.98)$$

The transfer function matrix is defined as follows

$$\mathbf{H}(s) = \mathbf{B}(s)^{-1} = \frac{\text{adj}\mathbf{B}(s)}{\det \mathbf{B}(s)} = \frac{\mathbf{R}(s)}{\det \mathbf{B}(s)}, \quad (2.99)$$

where the matrix $\mathbf{H}(s)$ is of size $N \times N$, $\mathbf{R}(s)$ is called the residue matrix and $\text{adj}\mathbf{B}(s)$ denotes adjugate of matrix $\mathbf{B}(s)$.

Determinant of the adjugate matrix is equal zero and yields the characteristic equation. The roots of the characteristic equation are called poles. They are identical to the eigenvalues of the generalized eigenvalue problem.

The transfer function matrix in the partial fraction expansion form becomes

$$\mathbf{H}(s) = \sum_{k=1}^m \left(\frac{\mathbf{R}_k}{s - p_k} + \frac{\mathbf{R}_k^*}{s - p_k^*} \right), \quad (2.100)$$

where and \mathbf{R}_k is a residue matrix of size $N \times N$ for the k^{th} mode. Residues are related to mode shapes and can be determined the equation of motion written in terms matrix Φ , i.e.,

$$\Phi^T \mathbf{M} \Phi \ddot{\mathbf{q}}(t) + \Phi^T \mathbf{C} \Phi \dot{\mathbf{q}}(t) + \Phi^T \mathbf{K} \Phi \mathbf{q}(t) = \Phi^T \mathbf{p}(t). \quad (2.101)$$

Equation (2.101) represent the system equation of motion transformed by the modal matrix into the modal space. Thus the residue matrix becomes,

$$\mathbf{R}_k = t_k \phi_k \phi_k^T, \quad k = 1, 2, \dots, N, \quad (2.102)$$

where t_k is a scaling factor for the k^{th} mode.

The transfer function matrix described by equation (2.100) computed for $s = i\omega$ gives the *frequency response matrix* given as

$$\mathbf{H}(\omega) = \sum_{k=1}^m \left(\frac{\mathbf{t}_k \boldsymbol{\phi}_k \boldsymbol{\phi}_k^T}{i\omega + \xi\omega_n - i\omega_{d_k}} + \frac{\mathbf{t}_k^* \boldsymbol{\phi}_k^* (\boldsymbol{\phi}_k^*)^T}{i\omega + \xi\omega_n + i\omega_{d_k}} \right). \quad (2.103)$$

The frequency response matrix has coefficients $H_{jk}(\omega)$ which are called *frequency response functions*. Equation (2.103) defines the set of functions that are the ratio between the j -th output variable and the k -th input force.

2.2.1. Forms of frequency response functions

The frequency response functions can be defined by a ratio between different terms of the state space equation of motion. The frequency response function between the displacement response $U_j(\omega)$ and the external force $P_k(\omega)$ is called the *receptance* (Maia and Silva, 1997),

$$H_{jk}(\omega) = \frac{U_j(\omega)}{P_k(\omega)}. \quad (2.104)$$

The frequency function derived by division of velocity response $\dot{U}_j(\omega)$ and the external force, $P_k(\omega)$, is referred to as the *mobility* and is defined as follows

$$Y_{jk}(\omega) = \frac{\dot{U}_j(\omega)}{P_k(\omega)}. \quad (2.105)$$

The frequency response function can also be defined in terms of the acceleration response and the external force

$$A_{jk}(\omega) = \frac{\ddot{U}_j(\omega)}{P_k(\omega)}. \quad (2.106)$$

Equation (2.106) defines the function called the *accelerance*.

It is also possible to define the inverse functions with respect to (2.104), (2.105) and (2.106). In such case the frequency response function relating to the external force and the displacement response becomes

$$D_{jk}(\omega) = \frac{P_k(\omega)}{U_j(\omega)}, \quad (2.107)$$

and is called the *dynamic stiffness*. The inverse function with respect to the mobility is called *mechanical impedance* and is defined as

$$I_{jk}(\omega) = \frac{P_k(\omega)}{\dot{U}_j(\omega)}. \quad (2.108)$$

The frequency response function relating to the acceleration response with the force excitation is called the *apparent mass*, i.e.,

$$P_{jk}(\omega) = \frac{P_k(\omega)}{\ddot{U}_j(\omega)}. \quad (2.109)$$

The most often used frequency response functions, in experimental modal analysis, are the receptance and accelerance. The relationship between the accelerance and the receptance is given by

$$A_{jk}(\omega) = -\omega^2 H_{jk}(\omega). \quad (2.110)$$

The receptance expressed in terms of the accelerations is

$$H_{jk}(\omega) = \frac{-1 \ddot{U}_j(\omega)}{\omega^2 P_k(\omega)}. \quad (2.111)$$

The accelerance is more convenient in the experimental studies since in dynamic test usually the acceleration signals are recorded, whereas the receptance is often used in analytical works.

2.2.2. Properties of frequency response functions

The receptance is a complex function and it can be plotted in terms of three quantities, i.e., frequency, real part and imaginary part. A three-story building shown in Fig. 2.10 is considered as an example to present the FRF properties. The mass and stiffness for the particular stories are: $m_1 = 2000$ kg, $m_2 = 2000$ kg, $m_3 = 4000$ kg, $k_1 = 3400$ kN/m, $k_2 = 2450$ kN/m, $k_3 = 1600$ kN/m. The building is impacted along u_1 degree of freedom by the half sine impulse with amplitude $p_o = 8$ kN and time duration $t_c = 0.05$ s. The damping matrix is assumed as proportional to the mass and stiffness matrix as given below

$$\mathbf{C} = 0.129\mathbf{M} + 0.0029\mathbf{K}. \quad (2.112)$$

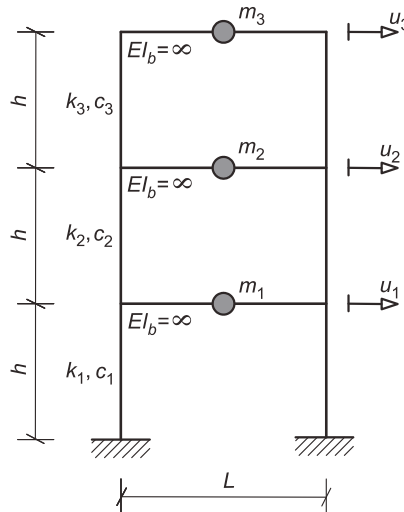


Fig. 2.10. Three-story building

The equation of motion in time domain (Spatial Model) of the building described by three degrees of freedom is given by

$$\begin{aligned}
 \begin{bmatrix} 2 & 0 & 0 \\ 0 & 2 & 0 \\ 0 & 0 & 4 \end{bmatrix} \cdot 10^3 \ddot{\mathbf{u}} + \begin{bmatrix} 17223 & -7105 & 0 \\ -7105 & 12003 & -4640 \\ 0 & -4640 & 5156 \end{bmatrix} \dot{\mathbf{u}} + \\
 + \begin{bmatrix} 5850 & -2450 & 0 \\ -2450 & 4050 & -1600 \\ 0 & -1600 & 1600 \end{bmatrix} \cdot 10^3 \mathbf{u} = \mathbf{p}(t)
 \end{aligned}
 \tag{2.113}$$

A full three dimensional plot of the receptance FRF of the three story building is shown in Fig. 2.11. The plot presents the relation between the $u_2(t)$ and $p_1(t)$, i.e., the response of the second floor and the excitation placed on the first floor. The FRF draws the circles with different radiuses with increasing frequency. The receptance FRF can be plotted on two dimensional plots that are the projections of Fig. 2.11 into the selected plane. Fig. 2.12a shows the real part of the receptance plotted against the frequency. The imaginary part of the receptance is shown in Fig. 2.12b.

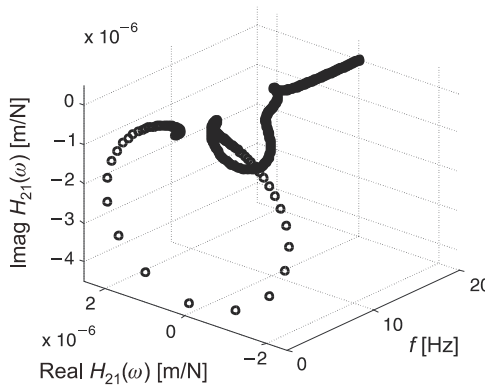


Fig. 2.11. Three dimensional plot of the receptance function

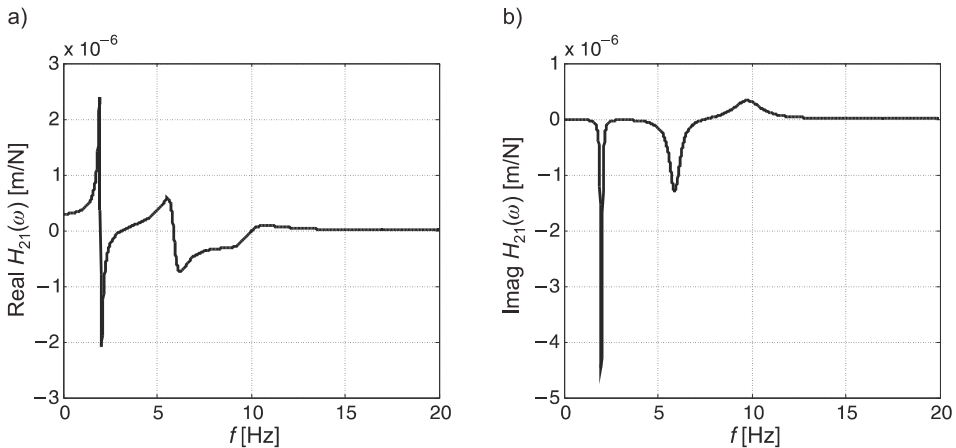


Fig. 2.12. Receptance function (a) Real part; (b) Imaginary part

The real and imaginary parts have visible peaks that correspond to the natural frequencies of the system. The first, the second and the third eigenfrequencies are: 2.0028 Hz, 5.9126 Hz, 9.8258 Hz, respectively. The peaks corresponding to the first natural frequency have the largest values. It indicates that the response in the lower frequency range to the unit harmonic excitation will have larger amplitudes.

The receptance plotted on the real-imaginary plane (complex or Argand plane) is given in Fig. 2.13. Each circle, presented on the plot, corresponds to the natural frequency of the system. This presentation of the FRF is called the Nyquist plot and is very popular in experimental modal analyses.

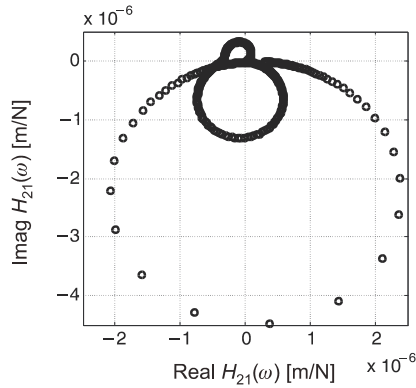


Fig. 2.13. Nyquist plot of the receptance

The most convenient way of graphical presentation of the receptance is the so called Bode diagram. In this case the FRF is plotted as a magnitude and phase vs. frequency, shown in Fig. 2.14. On these plots the system dynamic properties can be easily recognized (Maia and Silva, 1997).

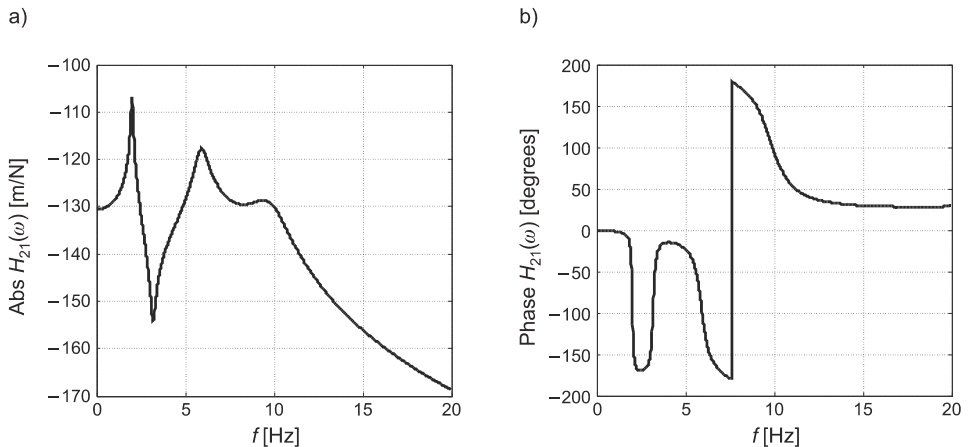


Fig. 2.14. Bode plot: a) Magnitude of the receptance vs. frequency; b) Phase of the receptance vs. frequency

The comparison of the real and imaginary parts of the mobility and accelerance are given in Figs. 2.15 and 2.16. The accelerance FRF is related to the receptance FRF through the term ω^2 , and therefore higher frequencies have relatively bigger values with respect to both receptance and mobility functions. Therefore, it is easier to identify the peaks corresponding to higher frequencies on the accelerance FRF function.

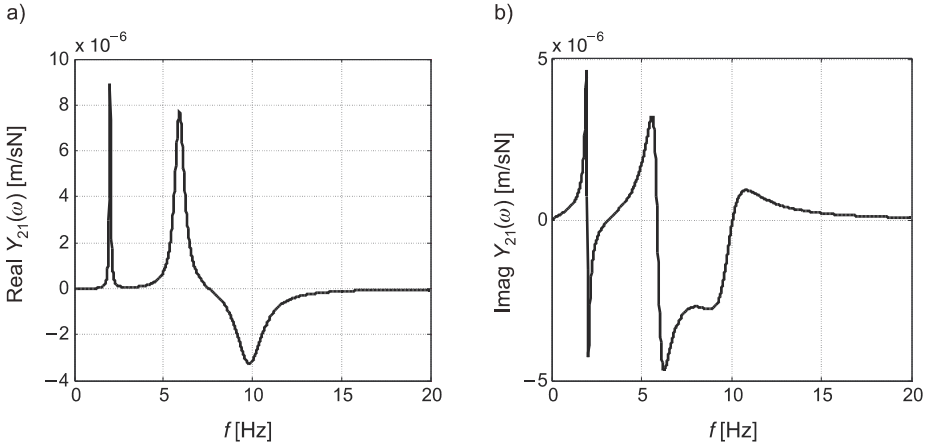


Fig. 2.15. Mobility function (a) Real part; (b) Imaginary part

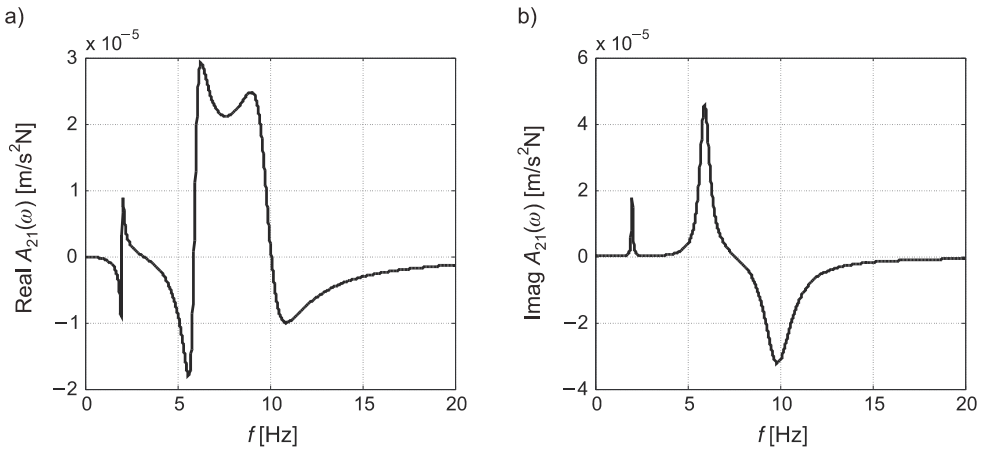


Fig. 2.16. Accelerance function (a) Real part; (b) Imaginary part

The influence of damping on the Nyquist plots is studied on Fig. 2.17. The following damping matrices were applied

- a) very low proportional damping (corresponding to $\xi_1 = 0.5\%$, $\xi_2 = 1\%$)

$$\mathbf{C} = 0.04585\mathbf{M} + 5.05136 \cdot 10^{-4}\mathbf{K}, \tag{2.114}$$

$$\mathbf{C} = \begin{bmatrix} 3046.74477 & -1237.58412 & 0 \\ -1237.58412 & 2137.49929 & -808.21820 \\ 0 & -808.21820 & 991.61213 \end{bmatrix}; \quad (2.115)$$

b) medium proportional damping (corresponding to $\zeta_1 = 2.5\%$, $\zeta_2 = 3\%$)

$$\mathbf{C} = 0.42184\mathbf{M} + 0.0013094\mathbf{K}, \quad (2.116)$$

$$\mathbf{C} = \begin{bmatrix} 8503.76895 & -3208.06955 & 0 \\ -3208.06955 & 6146.81989 & -2095.06583 \\ 0 & -2095.06583 & 3782.43486 \end{bmatrix}; \quad (2.117)$$

c) nonproportional damping

$$\mathbf{C} = \begin{bmatrix} 8503.76895 & -3208.06955 & 0 \\ 6791.93045 & 6146.81989 & -2095.06583 \\ 0 & -2095.06583 & 3782.43486 \end{bmatrix}. \quad (2.118)$$

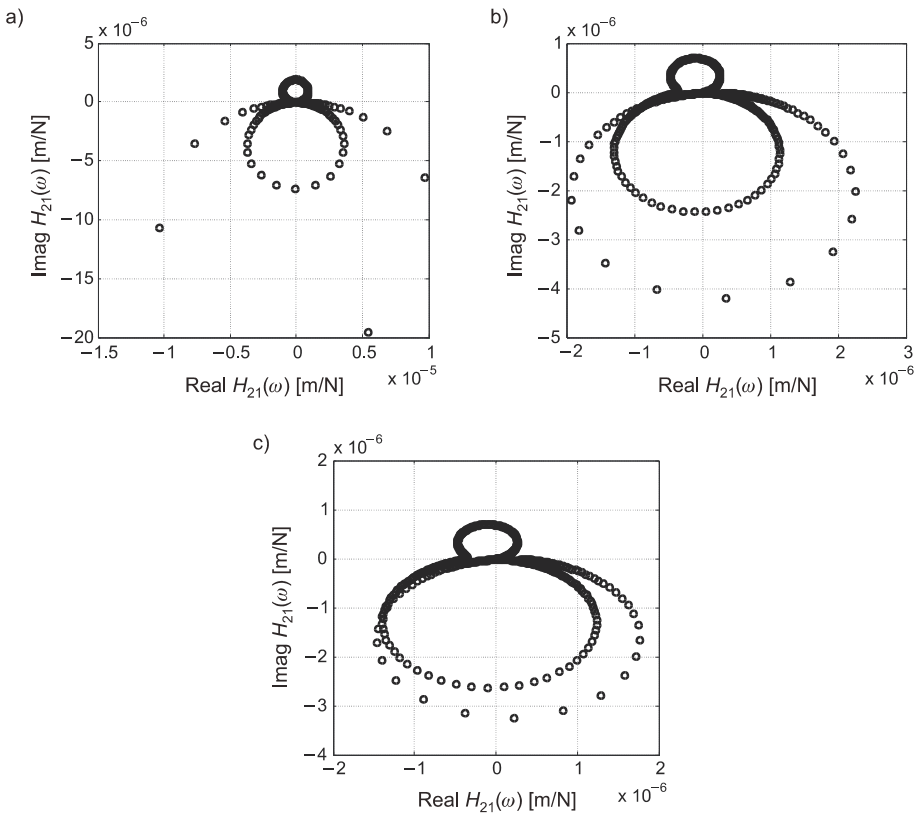


Fig. 2.17. Nyquist plot for the system with (a) very low proportional damping (b) medium proportional damping; (c) nonproportional damping

In all three plots the frequency increment is the same. The plot of the system with small damping (Fig. 2.17a) indicates that the circle corresponding to the fundamental natural frequency is drawn by very few marks. Therefore, the experimental identification of the lowest natural frequencies, from the Nyquist plot, of a very low damped system is usually problematic.

The FRF receptance for the dynamic system with damping representative of the civil engineering structures is plotted in Fig. 2.17b. The circles are clearly visible and one circle corresponding to the third mode has positive values of the imaginary part. All the loops pass through the origin of the coordinate system.

The FRF receptance of the system with the arbitrary damping matrix is given in Fig. 2.17c. In this case the circles drawn at each natural frequency can have centers spread around the complex plane. The circles can have some fragments with positive imaginary parts and some with negative. This is due to the fact that the modal constants for the non-proportionally damped systems are complex quantities, i.e., they have a magnitude and phase. The loops of FRF might not pass through the origin of the complex coordinate system. The damping ratios of the first, the second and the third mode, for the nonproportional damping case, are 0.032388, 0.0279, 0.043594, respectively.

Experimental derivation of mode shapes

The mode shapes can be determined by analysis of the measurement signals of the oscillating structure. The most common dynamic tests for the experimental determination of the dynamic structure properties are the impulse testing and sweep testing. The impulse testing uses the modal hammer (McConnell 1995) to generate a short time duration force. This method is simple and is often used in the experimental modal analysis. Usually, the measuring accelerometer remains at the same selected point of the structure whereas the points of hammer striking are chosen at many locations on the tested object.

In the sine sweep testing the structure is forced to oscillate with use of the vibration generators (Chopra 2001). Usually, the vibration generator remains at the same position whereas an accelerometer or set of accelerometers changes its location. The test with actuators are called harmonic (or sweep tests) when the harmonic force is used and its frequency is gradually changed. In order to obtain the particular mode shape the generated excitation must go through the frequencies of interest. Mode shapes can be also extracted from ambient vibration tests depending on natural excitations such as traffic or wind (Brownjohn et al. 1987, 1989).

3.1. Impulse and sweep tests for mode shapes identification through FRF

3.1.1. Procedure of mode shapes identification

The frequency response matrix $\mathbf{H}(\omega)$, of the size $N \times N$, contains the individual frequency response functions (FRFs) $H_{jk}(\omega)$ that can be determined by measurements of the response signal U_j and external force P_k , (2.104). In cases of the impulse tests the modal hammer is used to for impacting at point k and the corresponding acceleration response is taken point j . One row of the FRF matrix $\mathbf{H}(\omega)$ is obtained by the impulse measurement in all points and the acceleration measurement in the same selected location. To determine one column of the FRF matrix $\mathbf{H}(\omega)$, the modal hammer signal is measured in one point, whereas the acceleration signals are collected in all points. In case of the harmonic tests with use of actuators it is common that the external force measurements, P_k , are taken in the same location since the actuation device is not moved and the locations of the accelerometers for U_j covers the considered surface of the structure. Therefore, in case of the sweep tests, usually, one column of the frequency response function is determined. In most cases the acceleration FRF is used. However, the information on mode shapes is stored in all types of the FRF and the transition between them is easy (2.110). The mode shapes are included in each row or column of the residue matrix and the imaginary part of FRF function $H(\omega)$ shows both the amplitude and direction of the synchronous motion describe by the mode shape.

An extraction of the mode shapes by the impulse test and the sweep test from FRF will be shown on the example of a cantilever beam (Fig. 3.1). It has 3 selected measurement points. In the case of impulse test, the accelerometer is attached to the free end of the beam (point no. 3), whereas the modal hammer hits the beam at point no. 1, 2 and 3 (Fig. 3.1a).

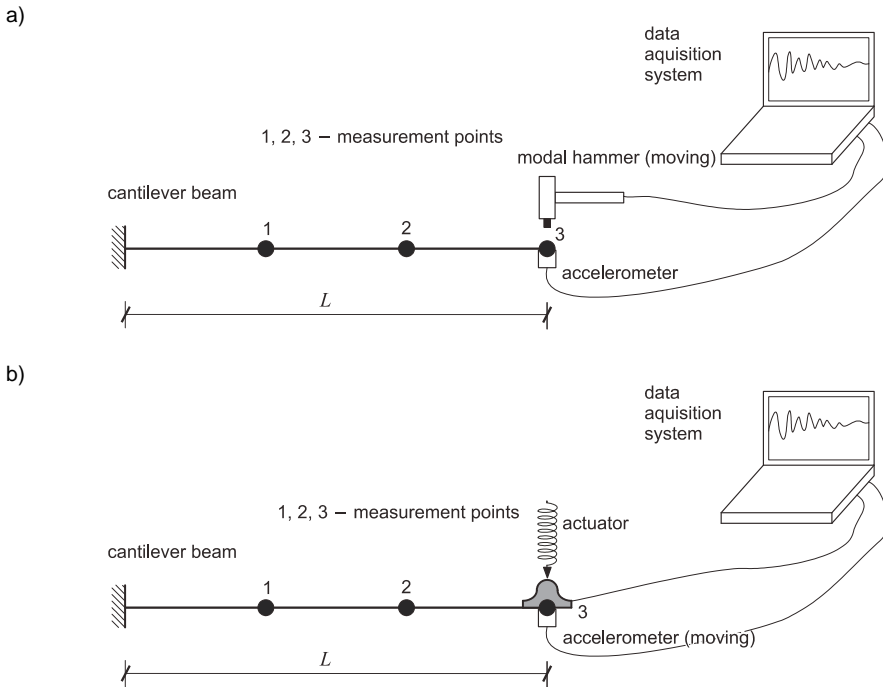


Fig. 3.1. Cantilever beam under dynamic test (a) impulse test (b) sweep test

During the tests the acceleration and force signals are collected. The time signals are transformed into a frequency domain by the Fast Fourier Transform (FFT). Then, the acceleration FRF is computed. The examples of the time signals $f_3(t)$ and $\ddot{u}_3(t)$, as well as their frequency representations $F_3(\omega)$ and $\ddot{U}_3(\omega)$ are given in Fig. 3.2.

The mode shape extraction procedure by the impulse test is presented in Fig. 3.3. From the measurements, the third column of FRF matrix has been obtained (see Fig. 3.3). In order to identify the mode shapes, the imaginary parts of FRF functions are determined. Three imaginary FRFs are plotted next to each other in the middle of Fig. 3.3. To obtain the first mode, the amplitudes corresponding to the frequency of the 1st natural frequency are identified. Then the picked values are treated as the amplitude magnitudes and are plotted on the schematic graph of the structure. In the presented example, all three amplitudes are negative and their value increases for mode 1, 2 and 3. Finally the amplitudes can be connected by a line making a sketch of the first mode shape (Fig. 3.3). The second and the third mode shape are determined by exactly the same procedure. In a more complicated structure the locations of the impact loadings must be carefully selected since these points define the discrete mode shapes. Generally speaking, the diagnostics on mode shapes can be conducted only when the modes are described by as many points as it is possible.

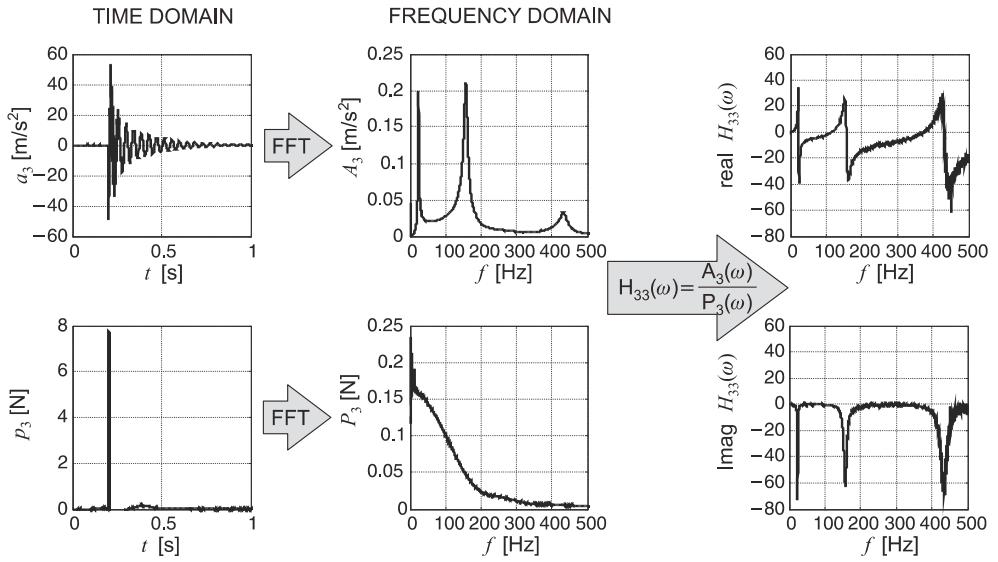


Fig. 3.2. Signals in the time and frequency domain

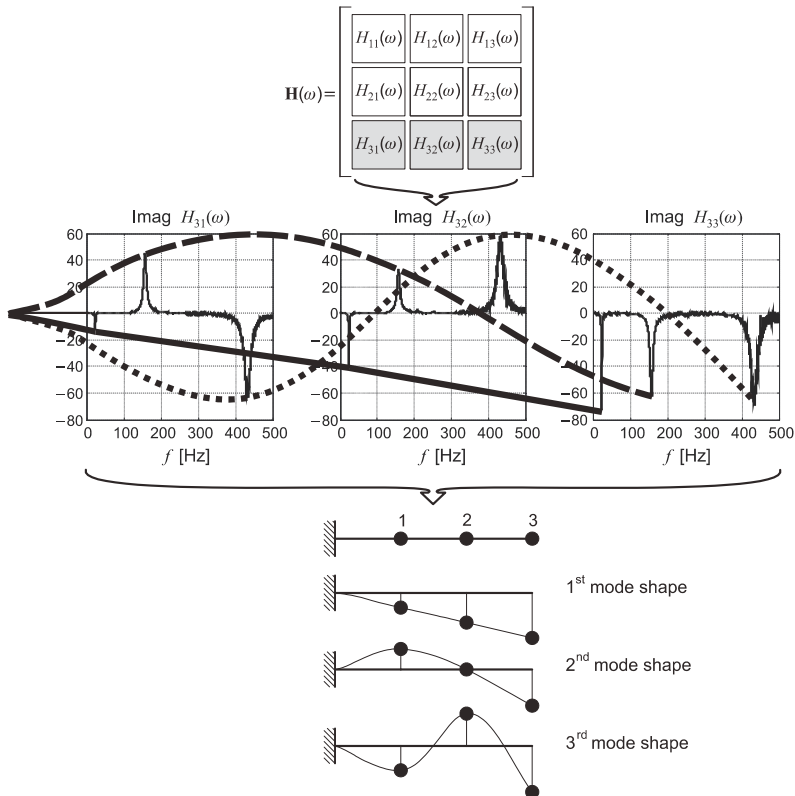


Fig. 3.3. Mode shapes extractions from impact test

Use of the seep tests lead to experimental estimation of one row of the FRF. The extraction of the mode shapes of the cantilever beam is shown in Fig. 3.4. As in the previous example the modes are computed from the imaginary parts of the beam FRFs and are determined through the amplitudes of the FRF corresponding to the particular natural frequency. In most cases the FRF functions, determined by the use of actuators, have better quality since the relation of the excitation amplitudes to the measurement noise is much better than in the impact test. The generation of the impulses is based on very low energy input to the structure, and moreover, the excitation is generated by a human hand. The way of using modal hammer, gripping it in hand, blocking the wrist during the hit and several other factors influence the quality of the generated impulse. In fact use of modal hammer needs some experience while the action of the actuator is free from direct human errors.

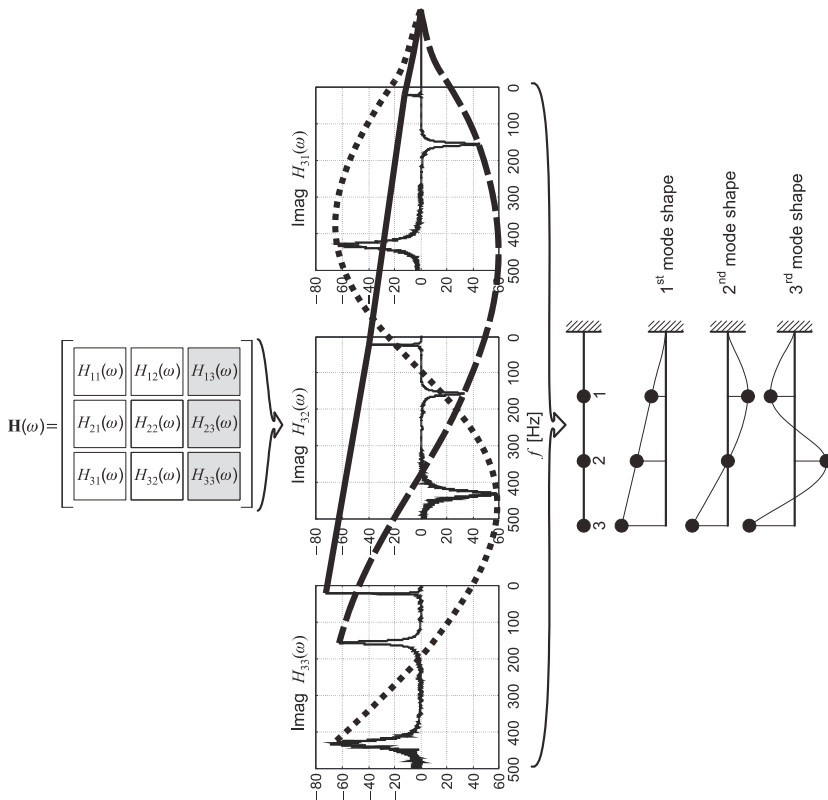


Fig. 3.4. Mode shapes extractions from sweep test

Environmental conditions, temperature, humidity, cable noise, mounting of the transducer, transducer mass, limited instrumentation resolution, etc. (McConnell 1995) introduce errors in measurement signals. Therefore, determination of FRF must be conducted in a way which minimizes a noise in the measured response. Each acceleration and force measurement is repeated several times and data are several times averaged in the frequency domain. Depending on source of noise two estimators are considered i.e., $H_1(\omega)$ estimator is used in the case of noise in the output, whereas $H_2(\omega)$ is used in the case of noise in the input measurements (Maia and Silva, 1997),

$$H_1(\omega) = \frac{G_{PU}(\omega)}{G_{PP}(\omega)}, \quad (3.1)$$

$$H_2(\omega) = \frac{G_{UU}(\omega)}{G_{UP}(\omega)}, \quad (3.2)$$

where: $G_{PU}(\omega)$ is a cross spectrum between the response and the force, $G_{UP}(\omega)$ is a cross spectrum between the force and the response, $G_{UU}(\omega)$ is an autospectrum of the response, $G_{PP}(\omega)$ is an autospectrum of the force. The cross spectra are estimated by the following formula (e.g. Kucharski, 2002 Maia and Silva 1997, McConnell 1995)

$$\begin{aligned} G_{PU}(\omega) &= \lim_{n \rightarrow \infty} \frac{1}{n} \sum_{i=1}^n P_i^*(\omega) U_i(\omega), \\ G_{UP}(\omega) &= \lim_{n \rightarrow \infty} \frac{1}{n} \sum_{i=1}^n U_i^*(\omega) P_i(\omega), \\ G_{UU}(\omega) &= \lim_{n \rightarrow \infty} \frac{1}{n} \sum_{i=1}^n U_i^*(\omega) U_i(\omega), \\ G_{PP}(\omega) &= \lim_{n \rightarrow \infty} \frac{1}{n} \sum_{i=1}^n P_i^*(\omega) P_i(\omega), \end{aligned} \quad (3.3)$$

where $P(\omega)$, $U(\omega)$ are the Fourier transforms of the force $p(t)$ and response $u(t)$, respectively, and $P^*(\omega)$, $U^*(\omega)$ are the complex conjugate to $P(\omega)$ and $U(\omega)$, respectively.

The primary source of noise is related to input measurements (McConnell, 1995). An input signal of the impulse should be zero for over 99 percent of the time range. However, the input signals are contaminated by a cable noise. In addition a ringing phenomenon can occur. Finally, it is very difficult to hit the structured by the modal hammer exactly at the selected point. Therefore, $H_2(\omega)$ estimator is proposed to be used in the impulse vibration tests.

An indicator of the quality of the experimental works is the coherence function defined as the ratio of two estimators (Kucharski, 2002):

$$\gamma^2(\omega) = \frac{H_1(\omega)}{H_2(\omega)} = \frac{|G_{PU}(\omega)|^2}{G_{UU}(\omega)G_{PP}(\omega)}. \quad (3.4)$$

The coherence shows the degree of linearity between output and input in the frequency domain. It can reach the values between zero and one. The coherence equal one means no noise in the measurements whereas coherence equals zero means pure noise.

The usefulness of estimators is shown on the example of the cantilever beam presented in Fig. 3.1. The impact tests are repeated 6 times. The case of the impulse put at the end of the beam (point 3) and the acceleration measurements taken at the same point are considered. The estimator $H_2(\omega)$ computed for this data is given in Fig. 3.5. In the same figure six repeated FRF functions are plotted. The $H_2(\omega)$ estimator has considerably less noise particularly in the frequency range from 10 to 300 Hz. The coherence function is plotted in Fig. 3.6. The value of the coherence is close to 1 proving a good quality of the

conducted dynamic tests. Some “noise” on the coherence function is visible only for the range of higher frequencies.

It is often necessary to compare the experimental mode shapes with the modes determined from the numerical analysis. There are several criteria used to validate the modes shapes. The most common one is the modal assurance criterion called MAC (Maia and Silva, 1997) that gives values between 0 and 1. The relative difference expressed in percentage can be calculated by the Normalized Modal Difference (NMD). Sometimes it is convenient to use the criterion called the Normalised Cross Orthogonality (NCO) that is analogical to MAC with addition of normalization with respect to mass matrix. The comparison of the experimental modes with numerical ones without taking the caution of the 180 degree phase shifts can be obtained by the Modal Scale Factor (MSF). The description, formulas and comments on the presented criteria are given in Appendix D.

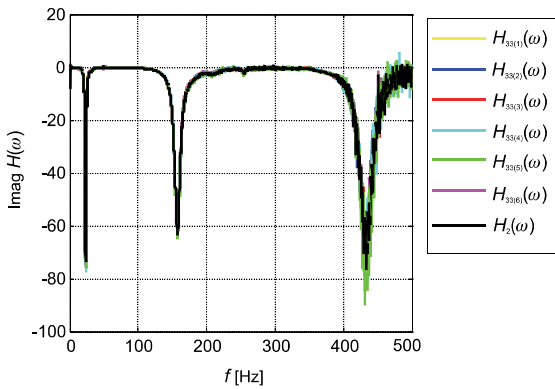


Fig. 3.5. Imaginary part of FRF estimator $H_2(\omega)$

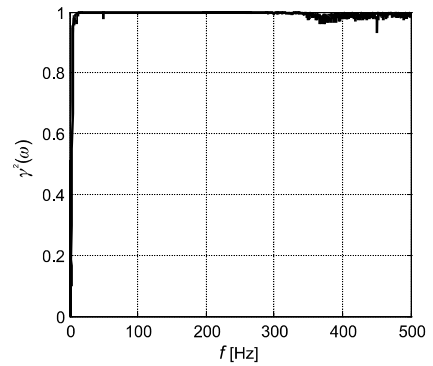


Fig. 3.6. Coherence function

3.1.2. Experimental examples

3.1.2.1. One-dimensional structures

As an example of a one dimensional structure a cantilever beam in bending is considered. The beam is made of Polymethyl Methacrylate (PMMA) also called Plexiglass. The beam, shown in Fig. 3.7 has length $L = 480$ mm, height $H = 20$ mm and width $B = 60$ mm. The experimentally determined material properties are: Young modulus $E = 3420$ MPa, Poisson ratio $\nu = 0.32$ and mass density is $\rho = 1187$ kg/m³. The damaged beam has one open crack of length $L_r = 2$ mm, and height $a = 7$ mm at a distance $L_1 = 120$ mm from the clamped end. The details on the experimental setup and procedures adopted are given by Rucka and Wilde (2007).

The impulse tests were conducted by the application of impulse loads perpendicularly to the beam axis. The black dots, plotted in Fig. 3.7a, show the loading points. The measurements were made using one accelerometer attached to the free end of the beam, i.e. at point no. 48 (see Fig. 3.7b). The dynamic impulse load was induced by the modal hammer PCB 086C03 at 48 points on the beam. The data were collected by the data acquisition system of Bruel&Kjaer (Pulse type 3650C).

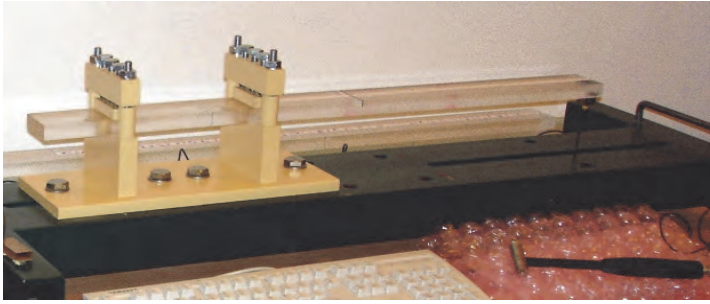
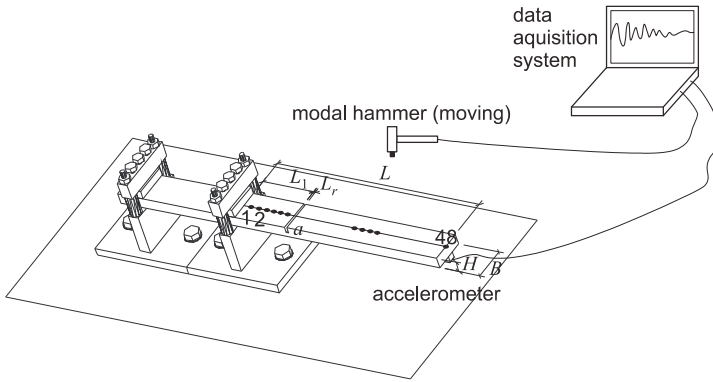


Fig. 3.7. Experimental setup for the beam

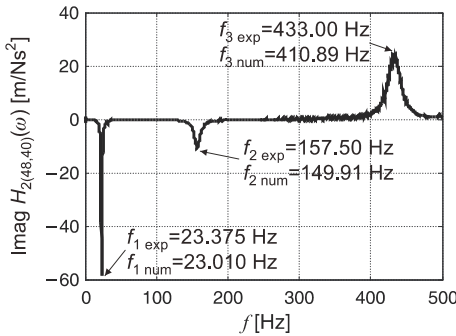
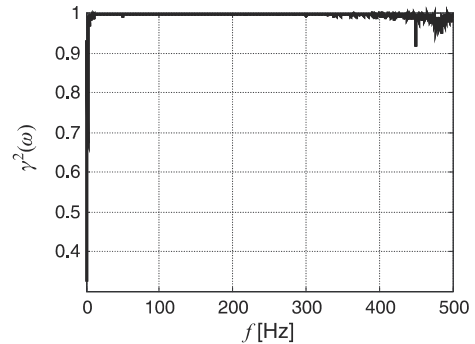
Fig. 3.8. Imaginary part of FRF estimator $H_2(\omega)$ 

Fig. 3.9. Coherence function

The points from 1 to 48 were, one by one, hit by the modal hammer. The accelerometer was attached all the time at the point no. 48. Therefore, the experimentally measured FRFs determine row no. 48th of the FRF matrix $\mathbf{H}(\omega)$. During impact at each point, the acceleration and force signals were measured, transformed into a frequency domain by the Fourier transform and $H_2(\omega)$ estimator was computed. Each acceleration and force measurement was repeated five times and data were averaged in the frequency domain. The imaginary part of frequency response function estimator $H_{2(48,40)}(\omega)$ is shown in Fig. 3.8. The imaginary part of the frequency response function $H_{2(48,40)}(\omega)$ obtained by impact at the

point no. 40 and measurement of response at the point 48. The coherence function is shown in Fig. 3.9. The coherence is close to one, which means low level of noise in the measurements. Experimentally determined first, second and third mode shapes are presented in Fig. 3.10.

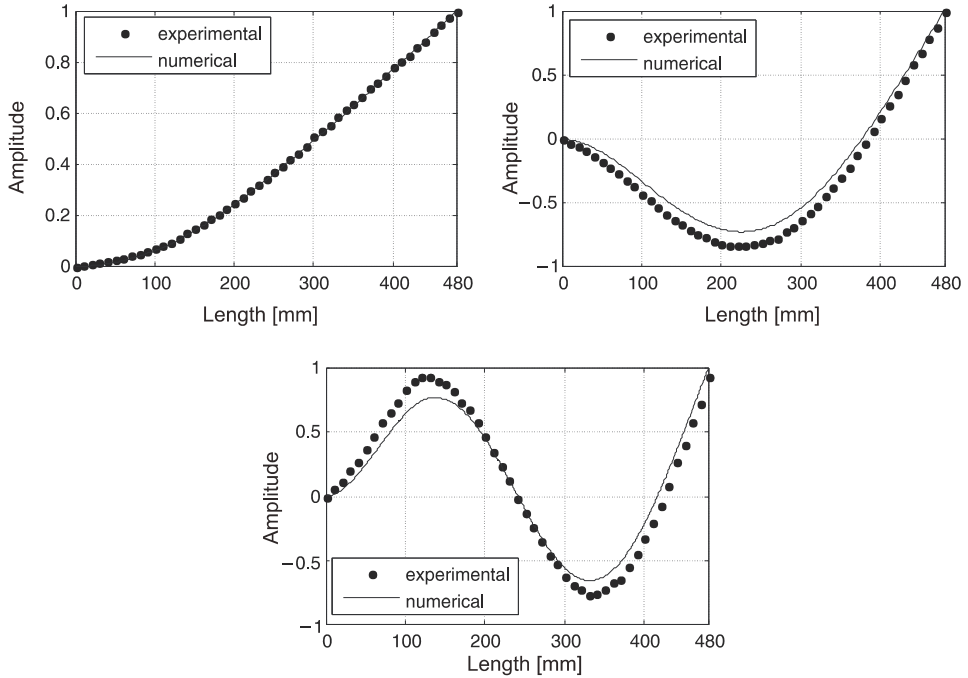


Fig. 3.10. Mode shapes for the beam

Table 3.1

Comparison of numerical and experimental frequencies and modes

Number of mode	Experimental frequency [Hz]	Numerical frequency [Hz]	MAC
1	23.375	23.01	0.9998
2	157.50	149.91	0.9891
3	433.00	410.89	0.9775

The numerical mode shapes for the beam were computed by the FEM program SOFiSTiK by the use of a solid six-sided element with eight nodes. The frequencies for the beam are $f_1 = 23.010$ Hz, $f_2 = 149.91$ Hz, $f_3 = 410.89$ Hz (numerical) and $f_1 = 23.375$ Hz, $f_2 = 157.5$ Hz, $f_3 = 433.00$ Hz (experimental). The numerical and the experimental mode shapes are compared in Fig. 3.10. The differences between the numerical and experimental first mode shape and frequencies are small. However, there is a noticeable difference between the second and third numerical and experimental mode shapes. The beam experimental first mode shapes are slightly underestimated in the region near the support. These discrepancies are due to the difficulties in obtaining an ideal fixed support of the

beam. The second mode shape is more underestimated than the first one also due to the boundary conditions. For example, the experimental modes of the beam show some rotation on the support while the numerical model assumes an ideal cantilever beam. Nevertheless, the MAC values range from 0.7411 to 0.9998 (Table 3.1) indicating a very good agreement.

3.1.2.2. Two-dimensional structures

The example of the two-dimensional structure is a steel plate of the length $L = 560$ mm, width $B = 480$ mm and height $H = 2$ mm. The material properties were determined experimentally and are found to be: Young's modulus $E = 192$ G Pa, Poisson ratio $\nu = 0.25$ and mass density $\rho = 7430$ kg/m³. The plate (Fig. 3.11) contains a rectangular defect, induced by a high precision saw, of length $L_r = 80$ mm, width $B_r = 80$ mm and depth $a = 0.5$ mm. The distances from the defect left-down corner to the plate left-down corner in the horizontal and vertical direction are: $L_l = 200$ mm and $B_l = 200$ mm, respectively. The area of the damage is 2.4 % of the plate area and the depth of the flaw is 25 % of the plate height (Rucka and Wilde 2007).

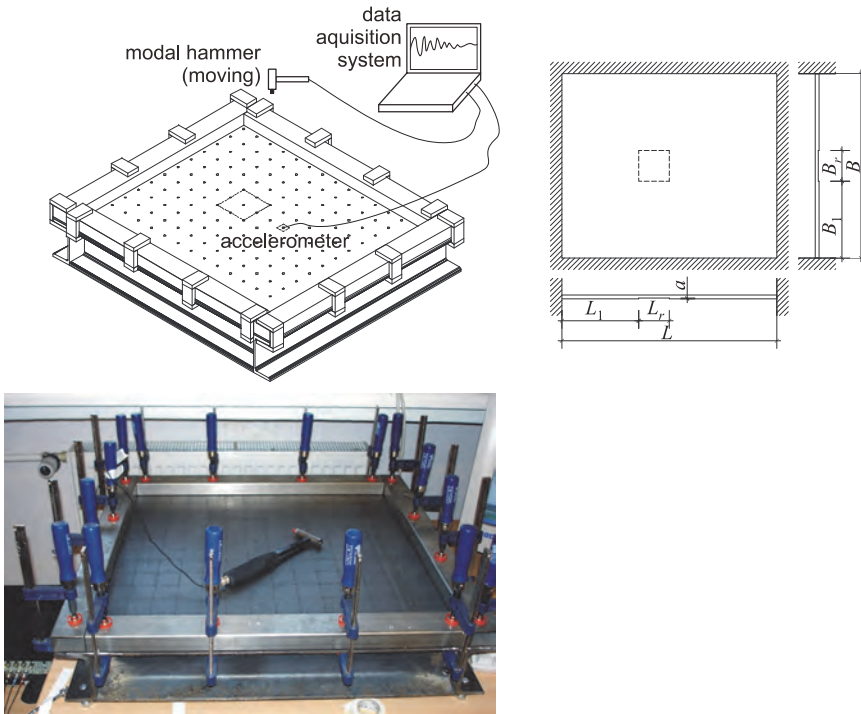


Fig. 3.11. Experimental setup for the plate

The force impulses induced by the modal hammer PCB 086C03 were applied to 143 regularly spaced locations. The points of load application are marked by black dots in Fig. 3.11. The vibration responses were recorded using one accelerometer attached to the plate at point no. 74 on the plate bottom. The data acquisition system Pulse type 3650C was used for data measurements. Additional information on the experiment setup is presented by Rucka and Wilde (2007).

At each point, from 1 to 143 the force signals were measured. The responses were recorded at point no. 74, and so the 74th row of the FRF matrix was measured.

Each recording of the acceleration and force was repeated five times and the results were five times averaged in the frequency domain. The estimation of the mode shapes was conducted through the $H_2(\omega)$ estimator. In Fig. 3.12 the imaginary part of the FRF estimator $H_{2(74,60)}(\omega)$, obtained by impact at point 60 and the measurement of the response at point no. 74, is shown. The coherence function (Fig. 3.13), is close to one in the considered frequency range. However, at several frequencies, e.g., 100 Hz, it reaches smaller values. The coherence function indicates the points of weak relationship between the input and the output due to noise in the output or due to non-linear behaviour at the resonance point.

The experimentally determined mode shapes are illustrated in Fig. 3.14. The plate mode shapes were computed by FEM program SOFiSTiK using the mesh of 40×40 mm plane elements. The frequencies for the plate obtained in the numerical simulations were $f_1 = 65.100$ Hz, $f_2 = 120.00.100$ Hz, $f_3 = 207.09.100$ Hz and they were very similar to the frequencies obtained experimentally $f_1 = 64.875$ Hz, $f_2 = 114.875$ Hz, $f_3 = 195.25$ Hz. The experimental and the numerical mode shapes of the plate are presented in Fig. 3.14. The black dots indicate the measurements while the black lines show the numerical modes. The MAC values range from 0.9693 to 0.9967 (Table 3.2) indicating a very good agreement.

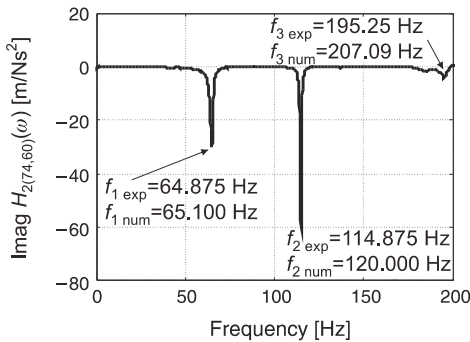


Fig. 3.12. Imaginary part of FRF estimator $H_2(\omega)$

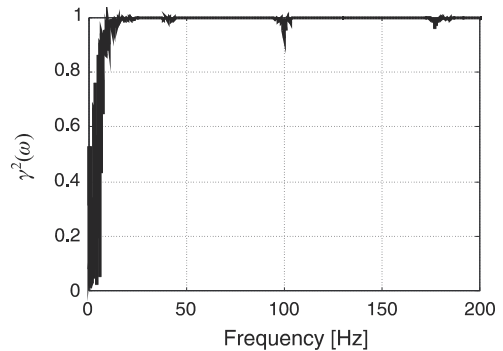


Fig. 3.13. Coherence function

Table 3.2

Comparison of numerical and experimental frequencies and modes

Number of mode	Experimental frequency [Hz]	Numerical frequency [Hz]	MAC
1	64.875	65.100	0.9967
2	114.875	120.000	0.9907
3	195.250	207.09	0.9693

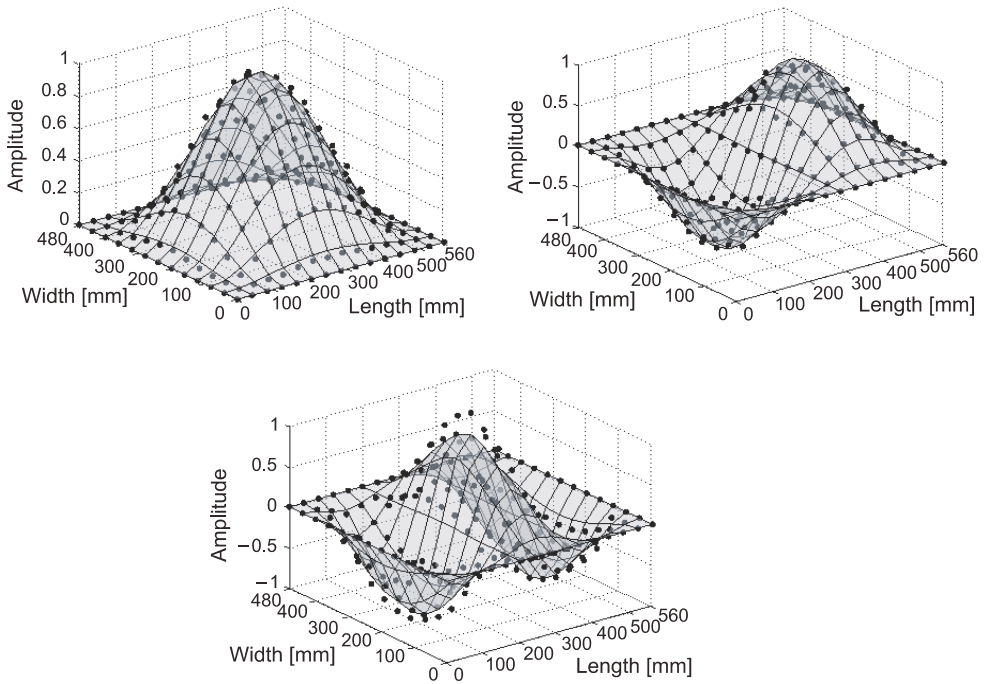


Fig. 3.14. Mode shapes for the plate

3.1.2.3. Three dimensional structure-steel plate

In this section a shell structure imitating a gasoline tank and the silo model is experimentally tested. The tank model is subjected to impulse testes while the silo model will be excited with the modal hammer and actuator.

The first structure consists of a bottom plate with a steel cylindrical shell of height $H = 180$ mm, thickness $t_c = 3.4$ mm and external diameter $D_2 = 300$ mm. It is assumed that Young modulus is $E = 190$ G Pa, Poisson ratio is $\nu = 0.25$ and mass density $\rho = 7850$ kg/m³. The cylindrical shell is welded to a steel plate. The damage is introduced on the inside surface by a high precision saw in the form of a rectangular flaw. It has length $L_r = 5$ mm, height $H_r = 60$ mm and depth $a = 1$ mm. The distances from the flaw left-down corner to the shell left-down corner in the horizontal and vertical directions are $L_1 = 285$ mm and $H_1 = 60$ mm, respectively (Fig. 3.15). The area of the damage is 0.2 % of surface area and the depth of the flaw is about 30 % of the shell thickness. More data on this experiment can be found in publication by Rucka and Wilde (2007).

The impulse tests were conducted by the modal hammer PCB 086C03 at the selected points spread along the central ring of the shell. The black dots, plotted on Fig. 3.15, show the points where the impulses were imposed. The motion of the hammer was controlled in such a way that the dynamic forces were applied perpendicularly to the shell surface. The total number of signal recordings was 62. The vibration responses were recorded using one accelerometer attached outside the shell at point no. 43. The data were collected by the data acquisition system Pulse type 3650C.

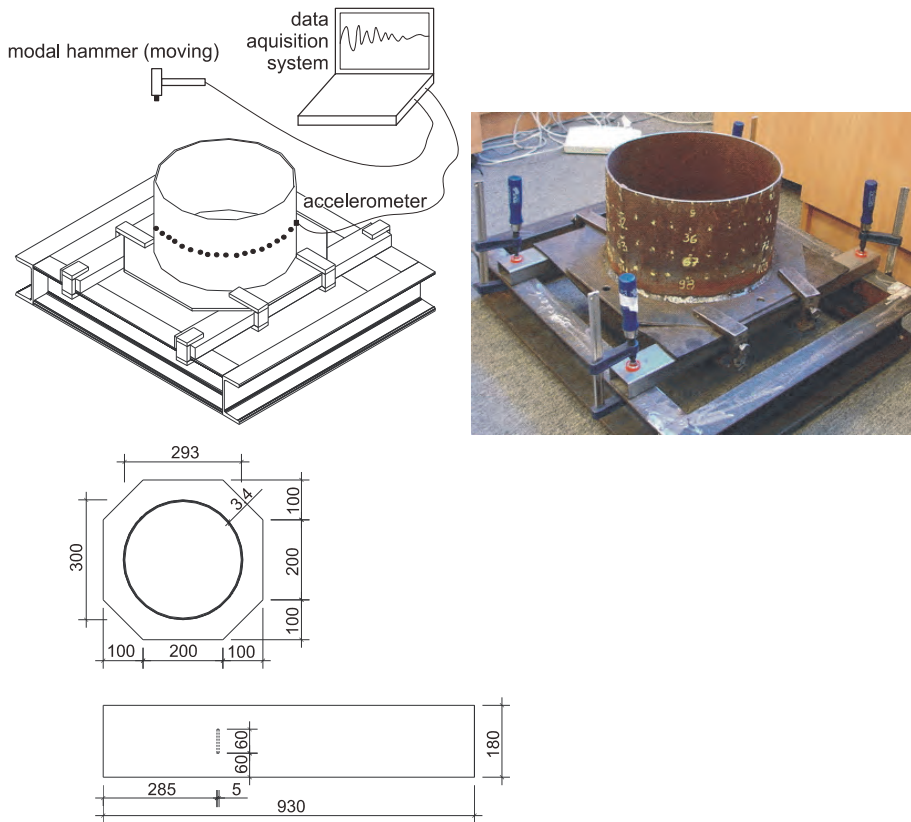


Fig. 3.15. Experimental setup for the shell

The 43rd row of the FRF matrix was estimated. Then, the $H_2(\omega)$ estimator was used to calculate the mode shape estimations. Fig. 3.16 shows the imaginary part of the frequency response function estimator $H_{2(11,43)}(\omega)$ for the cylindrical shell. The coherence function is shown in Fig. 3.17. The coherence is almost one with exception of one point where it becomes 0.67. At the corresponding frequency the considerable noise was added or an unexpected structure response occurred. However, the coherence near the first three frequencies, namely $f_1 = 295.4$ Hz, $f_2 = 575.8$ Hz and $f_3 = 887.2$ Hz is close to one.

The experimentally determined mode shapes are given in Fig. 3.18. The experimental data are denoted by black dots while the numerical modes are drawn by a grey lines. The mode shapes for the damaged cylindrical shell were computed by the FEM program SOFiSTiK. The shell element has a size of 5×5 mm. Although, some differences between the experimental and numerical modes are visible, the agreement is quite good. The reason for the discrepancies might be due to complicated geometry of the cylindrical structure, material and geometrical imperfections, undefined boundary conditions, presence of rust and others. The differences occur also in the numerical and experimental frequencies (Table 3.3). The first measured frequency for the shell was found to be $f_1 = 295.4$ Hz and the calculated one was $f_1 = 337.3$ Hz. The second measured frequency was $f_2 = 575.8$ Hz and the calculated $f_2 = 614.6$ Hz. The third frequency determined from the experiment was $f_3 = 887.2$ Hz and the calculated $f_3 = 928.9$ Hz. The differences between the measured

frequencies relative to the calculated frequencies range from 12.4% to 4.5%. A comparison between the numerical and the experimental mode shapes is given in Fig. 3.18. However, the MAC values range from 0.7411 to 0.9557 (Table 3.3).

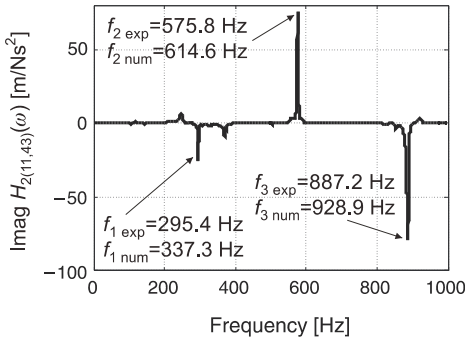


Fig. 3.16. Imaginary part of FRF estimator $H_2(\omega)$ (after Rucka and Wilde 2007)

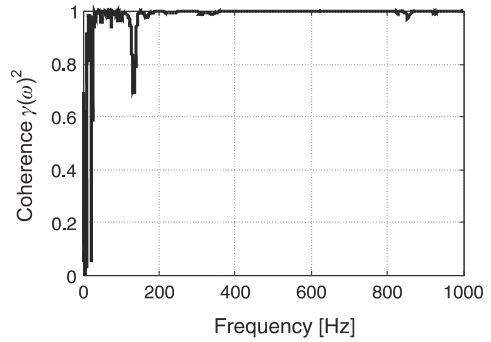


Fig. 3.17. Coherence function (after Rucka and Wilde 2007)

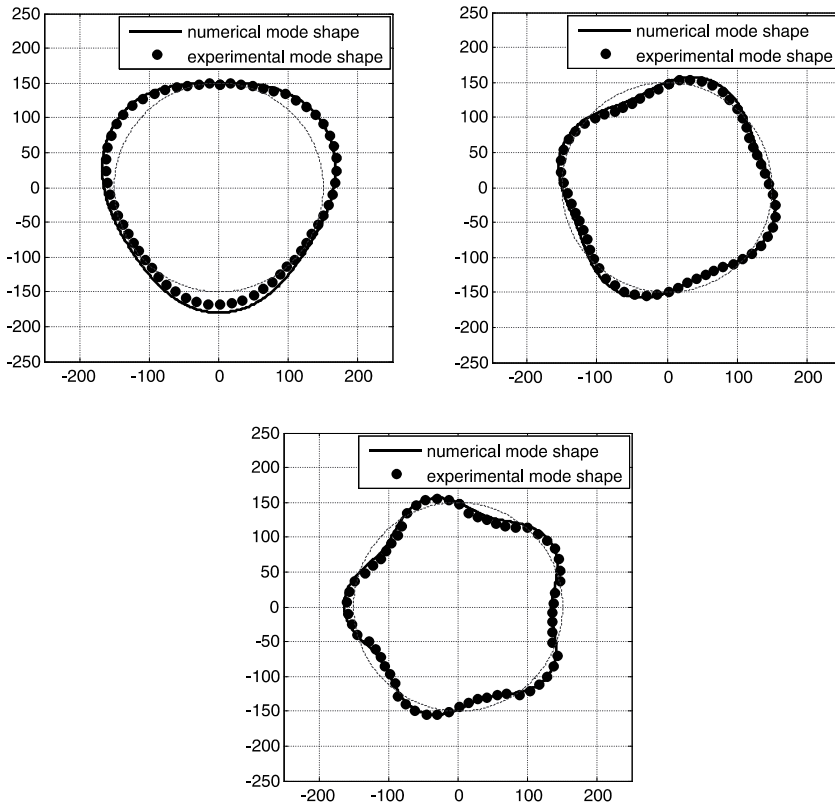


Fig. 3.18. Mode shapes for the shell (after Rucka and Wilde 2007)

Table 3.3

Comparison of numerical and experimental frequencies and modes

Number of mode	Experimental frequency [Hz]	Numerical frequency [Hz]	MAC
1	295.4	337.3	0.7411
2	575.8	614.6	0.9557
3	887.2	928.9	0.9348

3.1.2.4. Three-dimensional silo-structure with filling

The second example of mode shapes estimation in a three-dimensional object concerns the silo structures. The silo model (Fig. 3.19) was made of Polymethyl Methacrylate (PMMA) with 190 cm in height, an outside diameter of 20 cm and a wall thickness 0.4 cm (Tejchman 1998, Niedostatkiewicz and Tejchman 2003). The silo had a symmetric outlet of a diameter 8 cm in the flat bottom to induce the discharging process due to gravity. The silo was fixed at the bottom (it was supported by a steel rigid frame structure) and free at the top. The material properties of PMMA were as follows: Young modulus $E = 3500$ MPa, Poisson ratio $\nu = 0.32$ and mass density $\rho = 1019$ kg/m³. As a filling substance, initially medium dense dry sand with rough grains was used (with a mean grain diameter of $d_{50} = 0.5$ mm). The silo was filled up to different levels varying between 19 cm and 190 cm above the bottom. The measurements were made using the triaxial piezoelectric accelerometers (Delta Tron[®] 4506) fixed at selected points on the silo structure. The PULSE[™] system (type 3560-C Brüel & Kjær Sound & Vibration Measurement A/S) was used for the data acquisition. The silo was excited by a modal hammer, linear motor actuator and flowing sand while emptying, when the silo music was created (Niedostatkiewicz and Tejchman 2003).

The aim of the silo modal testing was an experimental identification of the evolution of mode shapes for different levels of the granular material in the cylindrical silo. The impulse and harmonic tests were performed.

The dynamic pulse loads were applied using a modal hammer (PCB Piezotronics type 086C03). The silo was subjected to an impulse load applied in the selected points spread along four rings at a distance of 3 cm. The vertical positions of the measurement rings were: 37, 94, 147 and 190 cm measured from the bottom (the black dots in Fig. 3.20b indicate the points of the load application). The dynamic pulse loads were perpendicular to the shell surface. The total number of the considered measurement points was 84. The vibration responses were recorded using one accelerometer attached outside the silo at point '85' placed at a distance of 10 cm from the top. The accelerations, as well as impulse loads were measured in a radial direction. Five tests were performed – with an empty silo and a silo containing sand at four different levels: 37, 94, 147 and 190 cm above the bottom. The levels were chosen in such way that the sand had a large influence on the silo mode shapes.

The complementary modal testing was conducted by a linear motor actuator used to generate harmonic forces of different frequencies. The actuator was placed at the distance of 10 cm from the top edge (point '86') through a horizontal cantilever beam in a radial direction. The excitation frequency changed from 0 to 256 Hz with the step of 1 Hz each second. The acceleration measurements were conducted at 8 points (Fig.3.20c). In each point, the accelerations were measured in a radial (x) as well as in a vertical (z) direction. In the case of the harmonic testing, 11 experiments were performed with an empty silo and a silo at different levels of filling varying from 19 up to 190 cm (with the step of 19 cm). The following results are taken after the paper Wilde et al. 2007.

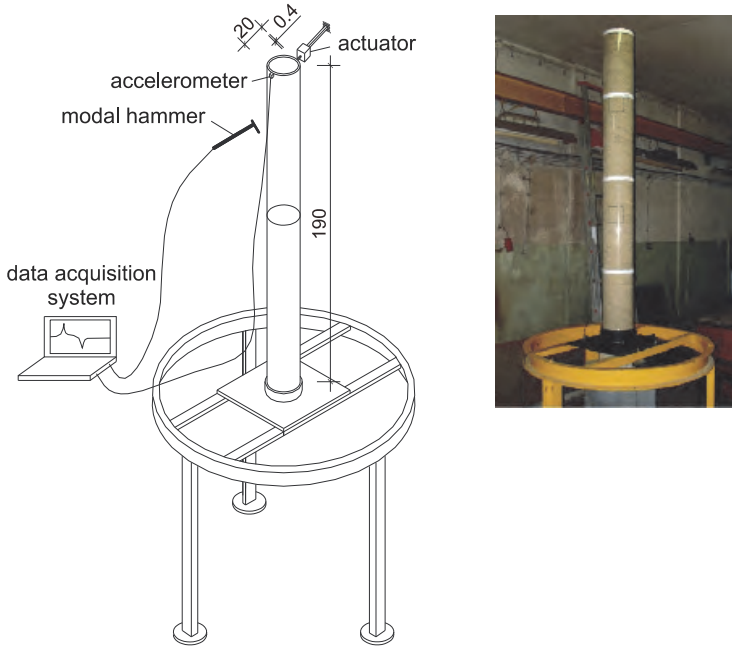


Fig. 3.19. Experimental set-up

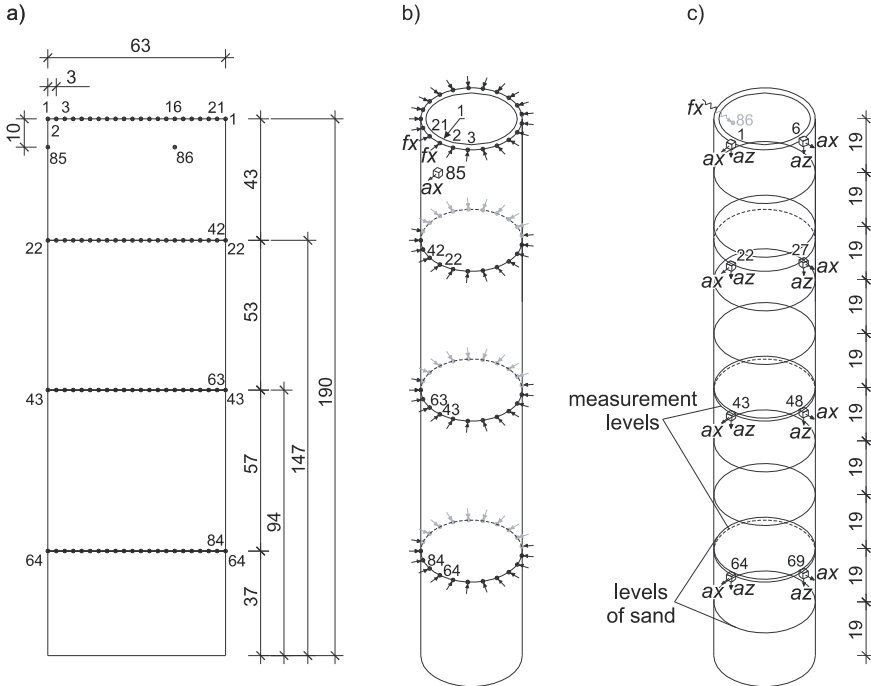


Fig. 3.20. Silo location of measurement points (a) impulse test (b) harmonic test (c)

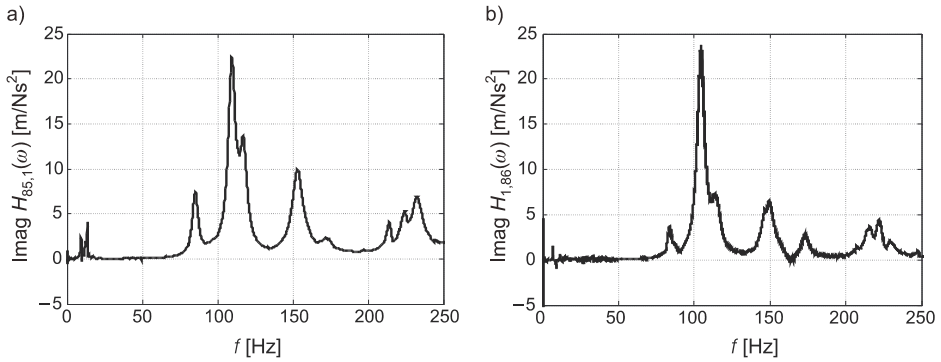


Fig. 3.21. Imaginary part of FRF for an empty silo (a) impulse testing; (b) harmonic testing

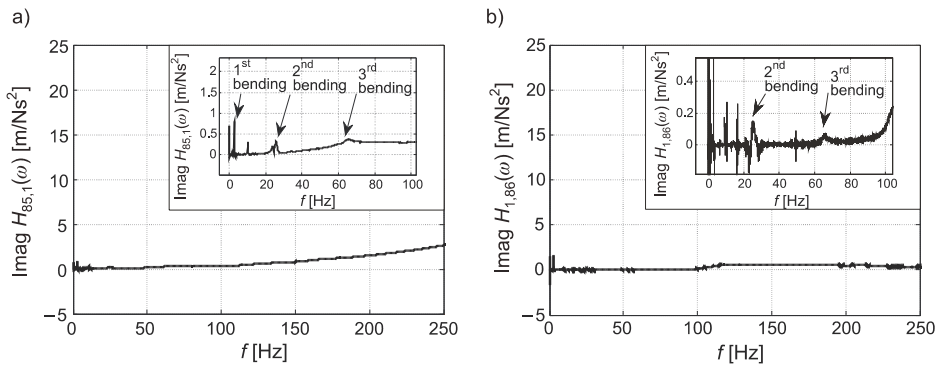


Fig. 3.22. Imaginary part of FRF for a silo with sand (a) impulse testing; (b) harmonic testing

In the performed impact test, the modal hammer signal was measured in all 84 points, whereas the acceleration at the same point '85'. Therefore only one row of the FRF matrix was determined. During the harmonic test, the excitation force was applied to point '86', whereas the accelerations were recorded at 8 points making it possible to obtain one column of the FRF matrix. The examples of the imaginary part of FRF for the impulse test and the harmonic test for an empty silo are presented in Fig. 3.21, and for the silo filled with sand are given in Fig. 3.22. The natural frequencies up to 250 Hz for an empty silo and up to 65 Hz for a silo with sand could be detected.

The identified mode shapes divided with respect to the dominant vibration types (bending or ovaling) for different levels of sand are given in Table 3.4. In the experiments the identification involved only 3 modes for the silo containing sand up to 190 cm (Fig. 3.23) since the inertia of the filling was very large and the energy transmitted to the structure through the modal hammer and actuator was not sufficient to excite higher modes. Therefore, only three bending modes could be extracted and the frequency of the highest one was 65 Hz. In the case of an empty silo, 9 mode shapes were identified (Fig. 3.24). Three lowest modes were bending ones and for higher modes – ovaling ones (i.e. the radial displacements dominated the shape of the modes). Generally, the natural frequencies associated with the bending modes changed significantly with the sand level since the filling mass experienced motion towards the outlet. The frequency of the second bending mode changed from 26 Hz for a filled silo up to 83.6 Hz in the case of an empty silo. In turn, the frequencies of ovaling modes (Table 3.4) were not much affected by the sand

level. The frequency of the first ovalling mode decreased from 113 Hz for the sand level of 152 cm down to 104.5 Hz in the case of the an empty silo. The ovalling modes are less sensitive to the sand level than the bending ones. The silo mode shapes for different levels of sand are plotted in Fig. 3.25, 3.26 and 3.27.

Table 3.4

Mode shapes for different levels of silo fill

Level of sand [cm]	Type of excitation	Frequency [Hz] and mode shapes								
		bending			ovalling					
		1 st	2 nd	3 rd	1 st	2 nd	3 rd	4 th		
190	imp.	2.6	26.0	65.0	–	–	–	–	–	–
190	harm.	–	25.2	64.1	–	–	–	–	–	–
171	harm.	–	29.7	75.0	–	–	–	–	–	–
152	harm.	–	33.2	84.2	113.0	–	–	–	–	–
147	imp.	4.1	36.6	86.0	123.0	–	–	–	–	–
133	harm.	–	39.8	88.5	109.0	–	–	–	–	–
114	harm.	–	42.6	88.6	106.0	–	–	–	–	–
95	harm.	–	43.6	93.0	105.0	–	–	–	–	–
94	imp.	12.5	43.7	95.0	110.80	161.0	–	–	–	–
76	harm.	–	44.0	–	104.0	132.5	–	–	–	–
57	harm.	13.1	47.6	–	104.4	123.8	–	–	–	–
38	harm.	13.2	58.0	148.5	104.3	118.4	–	–	–	–
37	imp.	14.2	58.5	148.0	109.80	122.5	185.0	–	–	–
19	harm.	13.3	73.0	152.0	104.5	115.0	182.5	–	–	–
0	imp.	13.6	85.2	173.50	109.5	117.0	153.0	214.0	224.5	232.5
0	harm.	13.9	83.6	173.0	104.5	114.0	149.5	216.0	222.0	229.5

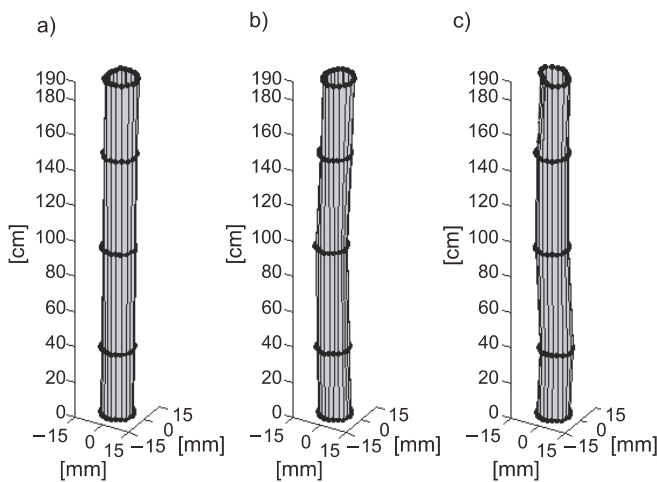


Fig. 3.23. Mode shapes of silo with filling level of 190 cm: a) 1st bending mode, b) 2nd bending mode, c) 3rd bending mode

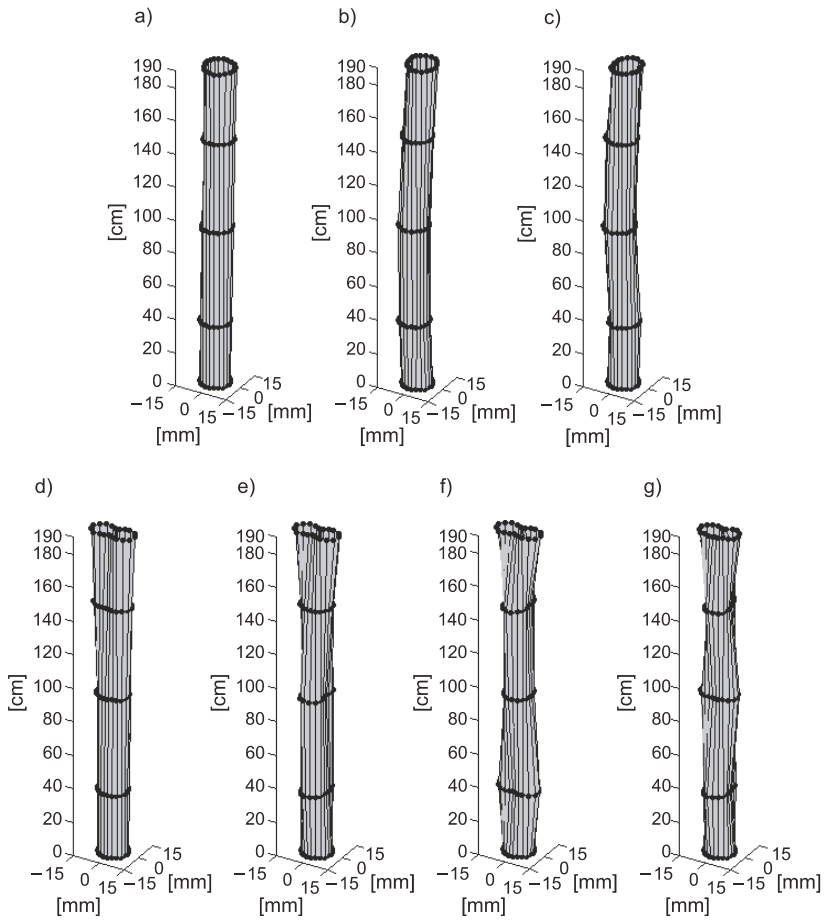
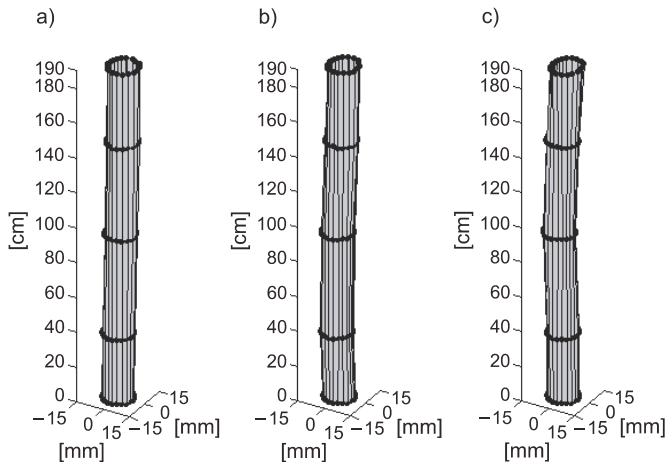


Fig. 3.24. Mode shapes of empty silo: a) 1st bending mode, b) 2nd bending mode, c) 3rd bending mode, d) 1st ovalling mode, e) 2nd ovalling mode, f) 3rd ovalling mode, g) 4th ovalling mode



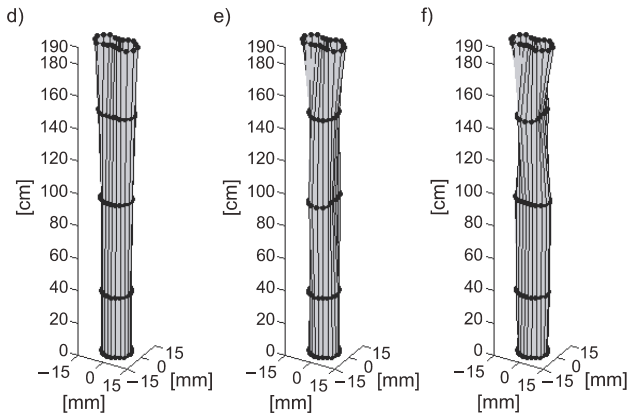


Fig. 3.25. Mode shapes of silo with sand up to 0.37 cm: a) 1st bending mode, b) 2nd bending mode, c) 3rd bending mode, d) 1st ovalling mode, e) 2nd ovalling mode, f) 3rd ovalling mode

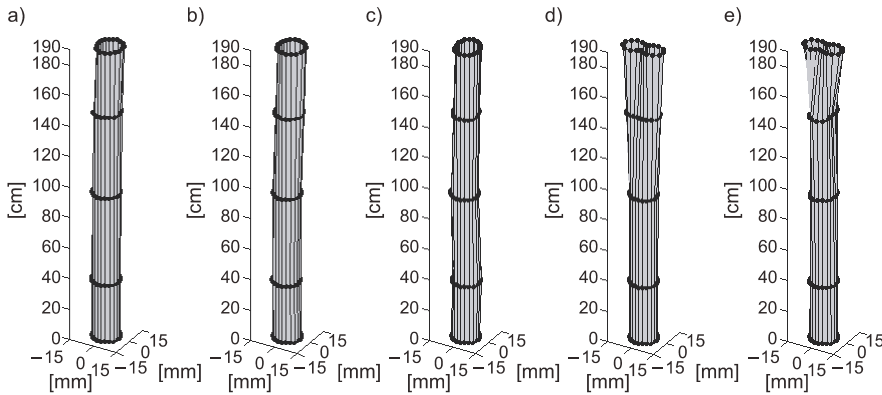


Fig. 3.26. Mode shapes of silo with sand up to 0.94 cm: a) 1st bending mode, b) 2nd bending mode, c) 3rd bending mode, d) 1st ovalling mode, e) 2nd ovalling mode

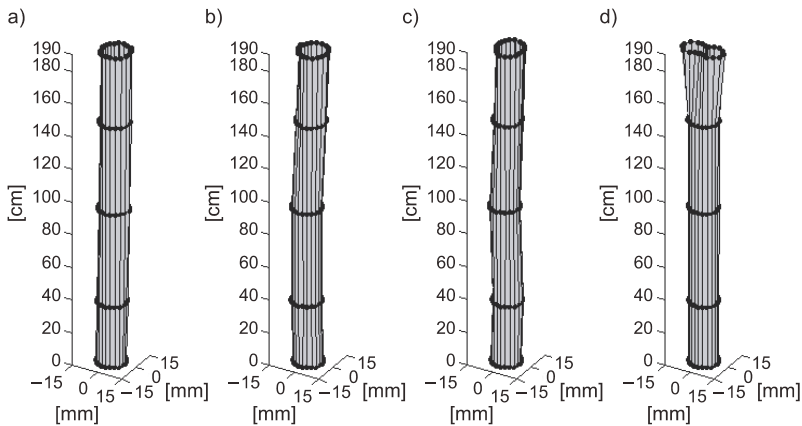


Fig. 3.27. Mode shapes of silo with sand up to 1.47 cm: a) 1st bending mode, b) 2nd bending mode, c) 3rd bending mode, d) 1st ovalling mode

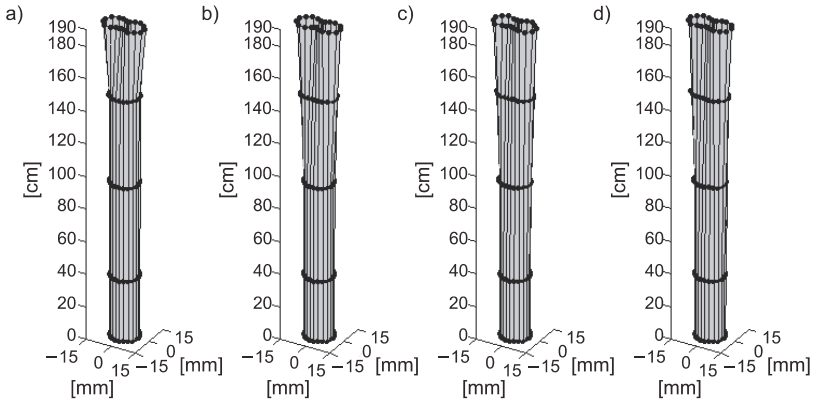


Fig. 3.28. Evolution of the 1st ovalling mode shape: a) sand level at 147 cm, b) sand level at 94 cm, c) sand level at 37 cm, d) empty silo

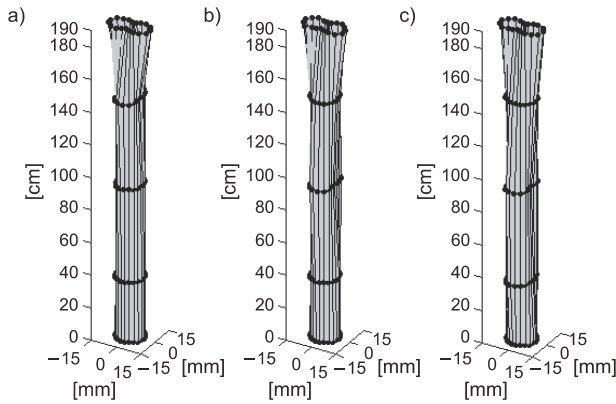


Fig. 3.29. Evolution of the 2nd ovalling mode shape: a) sand level at 94 cm, b) sand level at 37 cm, c) empty silo

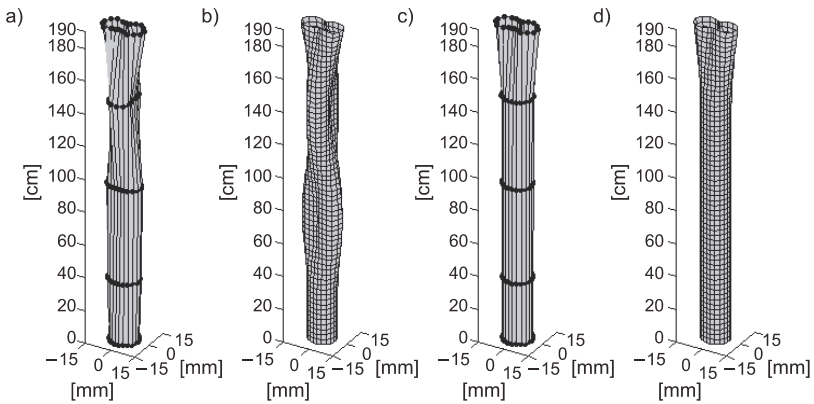


Fig. 3.30. Mode shapes of silo model: a) experimental 3rd ovalling mode (level of sand at 37 cm) 185 Hz, b) numerical 3rd ovalling mode (level of sand at 37 cm) 178.40 Hz, c) experimental 1st ovalling mode (level of sand at 147 cm) 123 Hz, d) numerical 1st ovalling mode (level of sand at 147 cm) 134.72 Hz

The evolution of the first and second ovaling mode at sand levels of 147, 94 and 37 cm heights and an empty silo is given in Figs. 3.28 and 3.29, respectively. The height of the oscillating silo walls changed with the sand level. Thus, for this experimental set-up, the sand in the silo acted as a full support. Oscillations were conducted by the silo walls that had no contact with the fill.

The experimental mode shapes of the silo with sand were compared with the mode shapes determined numerically using the commercial FEM program SOFiSTiK. The shell wall element of the size 3.0×3.015 mm was used for the silo. The silo was fixed quarterly at four points according to geometry of the experimental model. The sand was modelled with solid elements. The material parameters for sand were: Young modulus $E = 80$ MPa, Poisson ratio $\nu = 0.25$ and mass density $\rho = 1700$ kg/m³. On the boundary between the silo and the sand, the shell and solid elements had common nodes and degrees of freedom. The effect of the mesh discretization was negligible.

The numerical ovaling frequencies of the empty silo are found to be 102.3, 109.4, 144.5, 204.5, 213.0, 220.9 Hz. The relative errors between the numerical and experimental modal frequencies are very small and do not exceed 7.7%. The first longitudinal mode, i.e., mode with dominant vertical components has a frequency of 221.4 Hz. This mode has not been experimentally determined. Generally speaking, the differences between the measured frequencies relative to the calculated ones ranged from 0% to 26%. A comparison between the selected experimental and numerical mode shapes is given in Fig. 3.30. To provide a measure of consistency between the experimental and numerical mode shapes, the function of a modal assurance criterion MAC was applied. They ranged from 0.978 to 0.598 for bending modes and from 0.986 to 0.829 for ovaling modes. Only the third bending mode shape for a silo containing sand, which in fact was an assembly of a bending and ovaling mode, had the MAC value equal only to 0.3422.

3.2. Ambient vibration methods for mode shapes identification

The estimation of the experimental mode shapes in ambient vibration is very attractive from the practical point of view since the dynamic tests do not need any additional external excitations. The structure oscillations are generated by environmental loadings like action of wind, human or traffic vibrations or any other types of dynamic excitation coming from interaction with the surroundings.

The methods of mode shape extraction are based on random processes satisfying the Markov properties. The Markov chain is a discrete-time stochastic process, usually described in state space, fulfilling the condition that the future states are independent of the past states. Alternatively stated, the present state description fully captures all the information that can influence the future evolution of the process. Thus, given the present, the future is conditionally independent of the past.

The equation of motion in the state space (2.6) can be written in a discrete form as

$$\begin{aligned} \mathbf{x}_{k+1} &= \mathbf{A}\mathbf{x}_k + \mathbf{B}\mathbf{u}_k, \\ \mathbf{y}_k &= \mathbf{C}\mathbf{x}_k + \mathbf{D}\mathbf{u}_k, \end{aligned} \quad (3.5)$$

where \mathbf{x}_{k+1} is a vector of the states at time step $k + 1$ and vector \mathbf{x}_k consists of states at step k . The output vector and input vector are denoted by \mathbf{y}_k and \mathbf{u}_k , respectively. The matrix \mathbf{A} is called a transition matrix. The discrete system matrices \mathbf{A} , \mathbf{B} , \mathbf{C} and \mathbf{D} are

different from the matrices of the continuous system (2.6). A computation of the discrete system matrices is given, e.g., by Meirovitch 1990. The initial condition at step $k = 0$ is \mathbf{x}_0 .

For the system excited by the impulse response, $\mathbf{u}_0 = 1$, the states at step $k = 0$ become,

$$\begin{aligned}\mathbf{x}_0 &= \mathbf{0}, \\ \mathbf{y}_0 &= \mathbf{C}\mathbf{x}_0 + \mathbf{D}\mathbf{u}_0 = \mathbf{D},\end{aligned}\tag{3.6}$$

and for the time step $k = 1$ the states are

$$\begin{aligned}\mathbf{x}_1 &= \mathbf{A}\mathbf{x}_0 + \mathbf{B}\mathbf{u}_0 = \mathbf{B}, \\ \mathbf{y}_1 &= \mathbf{C}\mathbf{B}.\end{aligned}\tag{3.7}$$

The response for the step $k = 2$ is,

$$\begin{aligned}\mathbf{x}_2 &= \mathbf{A}\mathbf{x}_1 + \mathbf{B}\mathbf{u}_1 = \mathbf{A}\mathbf{B}, \\ \mathbf{y}_2 &= \mathbf{C}\mathbf{x}_2 + \mathbf{D}\mathbf{u}_2 = \mathbf{C}\mathbf{A}\mathbf{B}.\end{aligned}\tag{3.8}$$

By analogy the discrete response system for the unit impulse excitation at the time step $k = n$ can be written as

$$\begin{aligned}\mathbf{x}_n &= \mathbf{A}\mathbf{x}_{n-1} + \mathbf{B}\mathbf{u}_{n-1} = \mathbf{A}^{n-1}\mathbf{B}, \\ \mathbf{y}_n &= \mathbf{C}\mathbf{x}_n + \mathbf{D}\mathbf{u}_n = \mathbf{C}\mathbf{A}^{n-1}\mathbf{B}.\end{aligned}\tag{3.9}$$

Therefore, the outputs of the impulse response of the system can be written in a general form as

$$\mathbf{y}_n = \begin{cases} \mathbf{D} & , \quad n = 0 \\ \mathbf{C}\mathbf{A}^{n-1}\mathbf{B} & , \quad n > 0 \end{cases}\tag{3.10}$$

The discrete time samples \mathbf{y}_n are called Markov parameters. The coefficients of matrix $\mathbf{C}\mathbf{A}^{n-1}\mathbf{B}$ contain information on the whole system dynamics. The aim of the identification methods based on ambient vibration is the estimation of the coefficients of state space matrices solely on the measurements of the system response, i.e., without a knowledge on the external excitation.

There are several successful applications of the ambient vibration methods to large bridges. The dynamic properties of the Vincent Thomas suspension bridge have been determined by Abdel-Ghaffar and Housner (1978). The ambient vibration test was conducted on the Golden Gate suspension bridge (Abdel-Ghaffar, 1985), the Commodore Barry Bridge (Catbas. et al. 1999), the Vasco da Gama cable – stayed bridge (Cunha et al. 2001), the Hakucho suspension bridge (Siringoringo and Fujino 2008) and many others (Szymczak and Tomaszewska 2007).

3.2.1. System Identification with NExT and ERA methods

The estimation of the state matrices of the dynamic system is divided in two stages which will be discussed in this section. The first stage is aimed at computation of the system impulse responses from the ambient signal measurements obtained by Natural Excitation Technique (NExT). The second stage is the reconstruction of the state space model of the system. In this section the Eigensystem Realization Algorithm (ERA) is considered. The combination of NExT and ERA leads to the identification of the system

matrices, and therefore, to computation of the system modal parameters. Methods NExT and ERA can be considered as independent from each other.

Farrar and James (1997) have shown that the cross-correlation of two measurement responses due to random excitation have the form of decaying sinusoids, and therefore, have the same characteristics as the impulse response functions. This method is referred to as NExT. In this book the property of the cross-correlation will be obtained by derivation from the system equation of motion. The displacement response of the dynamics system defined by equation (2.1) can be regarded as a stochastic process vector $X(t)$ induced by the stochastic excitation $F(t)$. Thus, equation (2.1) can be written as

$$\mathbf{M}\ddot{X}(t) + \mathbf{C}\dot{X}(t) + \mathbf{K}X(t) = \mathbf{F}(t). \quad (3.11)$$

It is assumed that $F(t)$ is a random white noise function and matrices \mathbf{M} , \mathbf{C} , \mathbf{K} are deterministic. Post-multiplication of equation (3.11) by reference response $x_i(t + \tau)$ yields,

$$\mathbf{M}\ddot{X}(t)x_i(t + \tau) + \mathbf{C}\dot{X}(t)x_i(t + \tau) + \mathbf{K}X(t)x_i(t + \tau) = \mathbf{F}(t)x_i(t + \tau). \quad (3.12)$$

Taking the expectations denoted by E in equation (3.12) gives

$$\mathbf{M}E[\ddot{X}(t)x_i(t + \tau)] + \mathbf{C}E[\dot{X}(t)x_i(t + \tau)] + \mathbf{K}E[X(t)x_i(t + \tau)] = E[\mathbf{F}(t)x_i(t + \tau)]. \quad (3.13)$$

Equation (3.13) can be expressed in terms of the correlation functions as

$$\mathbf{M}\mathbf{R}_{\ddot{X}X_i}(t, t + \tau) + \mathbf{C}\mathbf{R}_{\dot{X}X_i}(t, t + \tau) + \mathbf{K}\mathbf{R}_{XX_i}(t, t + \tau) = \mathbf{R}_{FX_i}(t, t + \tau), \quad (3.14)$$

or in short

$$\mathbf{M}\mathbf{R}_{\ddot{X}X_i}(\tau) + \mathbf{C}\mathbf{R}_{\dot{X}X_i}(\tau) + \mathbf{K}\mathbf{R}_{XX_i}(\tau) = \mathbf{R}_{FX_i}(\tau). \quad (3.15)$$

where the correlation and cross correlation functions are denoted by \mathbf{R} . Since it is assumed that the external excitation process and the displacement random process are not correlated, equation (3.15) becomes

$$\mathbf{M}\ddot{\mathbf{R}}_{XX_i}(\tau) + \mathbf{C}\dot{\mathbf{R}}_{XX_i}(\tau) + \mathbf{K}\mathbf{R}_{XX_i}(\tau) = \mathbf{0}. \quad (3.16)$$

Vector $\mathbf{R}_{XX_i}(\tau)$ satisfies the system equation of motion (3.16) that are represented by the set of ordinary differential equations with no external excitation. Therefore, vector $\mathbf{R}_{XX_i}(\tau)$ can be interpreted as the free response of the system.

The ERA method is a time domain identification method aimed at a search of the minimum state space system model through the analysis of the system impulse responses. The foundations for the ERA have been given by Ho and Kalman (1996). They combined the Markov parameters in the form of the Hankel matrix and performed its decomposition. The Hankel matrix has the form

$$\mathbf{H}(0) = \begin{bmatrix} \mathbf{y}_1 & \mathbf{y}_2 & \cdots & \mathbf{y}_{\beta-1} \\ \mathbf{y}_2 & \vdots & & \vdots \\ \cdots & & & \\ \mathbf{y}_{\alpha-1} & & & \mathbf{y}_{\alpha+\beta-2} \end{bmatrix}. \quad (3.17)$$

where vector \mathbf{y}_k of the system response at time step k at N system measurement points, i.e.,

$$\mathbf{y}_k = \begin{bmatrix} y_k^1 \\ y_k^2 \\ \vdots \\ y_k^n \end{bmatrix}. \quad (3.18)$$

The scalar value y_r^2 is a single measurement at the structural point r . The rank of the Hankel matrix is N , if $\alpha \geq N$ and $\beta \geq N$. The Hankel matrix can be written in terms of the observability, \mathbf{P}_α , and controllability, \mathbf{Q}_β , matrix as,

$$\mathbf{H}(0) = \mathbf{P}_\alpha \mathbf{Q}_\beta, \quad (3.19)$$

where

$$\mathbf{P}_\alpha = \begin{bmatrix} \mathbf{C} \\ \mathbf{CA} \\ \mathbf{CA}^2 \\ \dots \\ \mathbf{CA}^{\alpha-1} \end{bmatrix}, \quad (3.20)$$

and

$$\mathbf{Q}_\beta = [\mathbf{B} \quad \mathbf{AB} \quad \mathbf{A}^2\mathbf{B} \quad \dots \quad \mathbf{A}^{\beta-1}\mathbf{B}]. \quad (3.21)$$

The solution of the problem of the minimum realization is solved by decomposition of the Hankel matrix by the inverse \mathbf{H}^\dagger in the sense of the Moore-Penrose definition.

The results presented by Ho and Kalman are derived for the noise free and infinite impulse time response. The extension of this method to the problems with noise was given by Kung (1978). The decomposition $\mathbf{H}(k-1)$ is contacted through the singular matrix decomposition (SVD) as,

$$\mathbf{H}(k-1) = \mathbf{USV}^T. \quad (3.22)$$

where the Hankel matrix written in terms of the state space matrices is,

$$\mathbf{H}(k-1) = \begin{bmatrix} \mathbf{CA}^{k-1}\mathbf{B} & \mathbf{CA}^k\mathbf{B} & \mathbf{CA}^{k+1}\mathbf{B} & \dots & \mathbf{CA}^{k+\beta-1}\mathbf{B} \\ \mathbf{CA}^k\mathbf{B} & \mathbf{CA}^{k+1}\mathbf{B} & & & \\ \mathbf{CA}^{k+1}\mathbf{B} & & \dots & & \\ \dots & & & \dots & \\ \mathbf{CA}^{k+\alpha-1}\mathbf{B} & & & & \mathbf{CA}^{k+\alpha+\beta-2}\mathbf{B} \end{bmatrix}. \quad (3.23)$$

Matrix \mathbf{S} is a rectangular diagonal matrix consisting of singular values and matrices \mathbf{U} and \mathbf{V} satisfy the orthonormality condition. The singular values are inserted in matrix \mathbf{S} in a decreasing order. The very low singular values are neglected. Then, the Kung method employs the procedures presented by Ho and Kalman (1996) to compute the state spaces matrices.

The ERA was proposed by Juang and Papa in 1985. The search for the system minimum realization follows the Kung's procedure with new formulas for the state space matrices of the discrete dynamic system, i.e.,

$$\mathbf{A} = \mathbf{S}^{-1/2} \mathbf{U}^T \mathbf{H}(1) \mathbf{V} \mathbf{S}^{-1/2}, \quad (3.24)$$

$$\mathbf{B} = \mathbf{S}^{1/2} \mathbf{V}^T \mathbf{E}_r, \quad (3.25)$$

$$\mathbf{C} = \mathbf{E}_m^T \mathbf{U} \mathbf{S}^{1/2}. \quad (3.26)$$

where matrices \mathbf{E}_r and \mathbf{E}_m are

$$\mathbf{E}_m^T = [\mathbf{I}_m \quad \mathbf{0}_m \quad \dots \quad \mathbf{0}_m], \quad \mathbf{E}_r = \begin{bmatrix} \mathbf{I}_r \\ \mathbf{0}_r \\ \vdots \\ \mathbf{0}_r \end{bmatrix}. \quad (3.27)$$

Matrices \mathbf{I}_k and $\mathbf{0}_k$ denote the identity matrix and the zero matrix of size $r \times r$. The modal parameters can be computed from the state matrices \mathbf{A} , \mathbf{B} , and \mathbf{C} by the solution of the eigenvalue problem. It is assumed that in the state space model of the engineering structure matrix \mathbf{D} has zero coefficients since in these structures there is no direct link between the external excitation and the system outputs. Such relations are possible, e.g., in electrical circuits. The matrix of the discrete eigenvectors, $\mathbf{\Phi}_d$, decomposes the discrete system matrix \mathbf{A} as follows (2.87),

$$\mathbf{A} = \mathbf{\Phi}_d \mathbf{\Omega}_d \mathbf{\Phi}_d^T, \quad (3.28)$$

where $\mathbf{\Omega}_d$ is the diagonal matrix of complex coefficients. The matrices in equations (3.28) are not the same as in the continuous formulation presented in Chapter 2 and are denoted by index d . The transformation between the discrete $\mathbf{\Omega}_d$ and continuous $\mathbf{\Omega}$ is

$$\mathbf{\Omega} = \frac{\ln(\mathbf{\Omega}_d)}{2\pi\Delta t}. \quad (3.29)$$

The coefficients in the diagonal of matrix $\mathbf{\Omega}$ are given as complex conjugate pairs as

$$\lambda_i^c, \lambda_i^{c*} = -\xi_i \omega_i \pm i \sqrt{1 - \xi_i^2} \omega_i. \quad (3.30)$$

Then, the natural circular frequency of the system is

$$\omega_i = |\lambda_i^c|, \quad (3.31)$$

and the damping ratio can be calculated from

$$\xi_i = \frac{\text{Re}(\lambda_i^c)}{\omega_i}. \quad (3.32)$$

The mode shapes are determined from matrix $\hat{\mathbf{C}}$ computed for the case of measurements of displacements

$$\hat{\mathbf{C}} = \mathbf{C} \mathbf{\Phi}_d, \quad (3.33)$$

for the case of measurements of velocities

$$\hat{\mathbf{C}} = \mathbf{C} \mathbf{\Phi}_d \mathbf{\Omega}_d^{-1}, \quad (3.34)$$

and for acceleration signals

$$\hat{\mathbf{C}} = \mathbf{C}\Phi_d\mathbf{\Omega}_d^{-2}. \quad (3.35)$$

The mode shapes are the columns of the matrix $\hat{\mathbf{C}}$ multiplied by the signs of the real parts of $\hat{\mathbf{C}}$ coefficients, i.e.,

$$\boldsymbol{\varphi}_m = \left| \hat{\mathbf{C}}_m \right| \cdot \text{sign} \left[\text{Re}(\hat{\mathbf{C}}_m) \right]. \quad (3.36)$$

where m denotes the m -th column of $\hat{\mathbf{C}}$.

The procedure of the NExT and ERA ambient vibration methods requires:

1. Measurements of the accelerations at several locations of the structure.
2. The computation of the cross-correlations with respect to the chosen referenced signal.
3. Computation of the system impulse responses.
4. Computation of the Hankel matrix.
5. Singular Value decomposition of the Hankel matrix.
6. Computation of discrete state matrices \mathbf{A} , \mathbf{B} and \mathbf{C} .
7. Computation of the natural frequencies, damping ratios and mode shapes.

There are several methods based on NExT and ERA that improve the performance of the presented technique, e.g., ERA with data correlation (Juang 1994) or ERA-FD ERA conducted in frequency domain (Maia and Silva 1997).

3.2.2. Estimation of modal parameters by Stochastic Subspace Identification method

The Stochastic Subspace Identification (SSI) method became well known after the work was published in 1996 by Overschee and DeMoor. They have identified state-space models from output data by taking advantage of the Kalman filter prediction (Kalman, 1960), the robust numerical QR factorization (or SVD) and the least squares method. On the contrary to the methods falling into the category of the NExT/ERA methods, called covariance-driven, where the computation of the covariance functions between the outputs is necessary, in SSI there is no need to compute the time impulse responses through the covariance between the outputs.

It is assumed that the states $\mathbf{x}(t)$ represent the stochastic process having the following properties:

1. The process is stationary.
2. The mean value is zero, i.e., $E[\mathbf{x}(t)] = 0$.
3. The covariance matrix is independent of states, i.e., $\boldsymbol{\Sigma} = E[\mathbf{x}(t)\mathbf{x}(t)^T]$.
4. The noise vectors \mathbf{w} and \mathbf{v} are independent of the state at time t , $E[\mathbf{x}(t)\mathbf{w}(t)^T] = 0$, $E[\mathbf{x}(t)\mathbf{v}(t)^T] = 0$.

The discrete model of a dynamic system with the input and measurement white noise \mathbf{w} and \mathbf{v} are given by,

$$\begin{aligned} \mathbf{x}_{k+1} &= \mathbf{A}\mathbf{x}_k + \mathbf{w}_k \\ \mathbf{y}_k &= \mathbf{C}\mathbf{x}_k + \mathbf{v}_k \end{aligned} \quad (3.37)$$

The optimal prediction of the state at time step $k + 1$, $\hat{\mathbf{x}}_{k+1}$, can be expressed in terms of the Kalman filter equation as

$$\hat{\mathbf{x}}_{k+1} = \mathbf{A}\hat{\mathbf{x}}_k + \mathbf{K}_k \mathbf{e}_k. \quad (3.38)$$

where \mathbf{K}_k is the Kalman filter gain and the estimation error is,

$$\mathbf{e}_k = \mathbf{y}_k - \mathbf{C}\hat{\mathbf{x}}_k . \quad (3.39)$$

Then, equation (3.37) becomes,

$$\begin{aligned} \hat{\mathbf{x}}_{k+1} &= \mathbf{A}\hat{\mathbf{x}}_k + \mathbf{K}_k \mathbf{e}_k \\ \mathbf{y}_k &= \mathbf{C}\hat{\mathbf{x}}_k + \mathbf{e}_k \end{aligned} \quad (3.40)$$

In equation (3.40) the state vector is replaced by the state estimation vector, $\hat{\mathbf{x}}_k$. Using the assumption of the Kalman filter theory the equation (3.40) written in terms of the conditional expectation form can simplified to the form

$$\begin{aligned} \hat{\mathbf{x}}_{k+1} &= \mathbf{A}\hat{\mathbf{x}}_k \\ \hat{\mathbf{y}}_k &= \mathbf{C}\hat{\mathbf{x}}_k \end{aligned} \quad (3.41)$$

where the variable $\hat{\mathbf{y}}_k$ denotes the response prediction without any noise. Equation (3.41) can be written in the matrix form as

$$\hat{\mathbf{Y}}_k = \mathbf{P}_i \hat{\mathbf{X}}_k . \quad (3.42)$$

where matrix \mathbf{P}_i is the extended observation matrix. Computation of the states and output estimates allows us to determine the state matrices \mathbf{A} and \mathbf{C} .

The numerical solution of the state matrices is based on the orthogonal projection of the selected subspace on the given space. The projection of matrix \mathbf{Y} on matrix \mathbf{X} is denoted by \mathbf{Y}/\mathbf{X} . It can be computed by the use of the commonly known LQ decomposition or with Singular Value Decomposition.

Procedure of the SSI method is:

1. Creation of a matrix consisting of vectors of the responses at a given time step of the form

$$\mathbf{Y}_{02i-1} = \begin{bmatrix} \mathbf{y}_0 & \mathbf{y}_1 & \cdots & \mathbf{y}_{j-1} \\ \mathbf{y}_1 & \mathbf{y}_2 & \cdots & \mathbf{y}_j \\ \vdots & \vdots & \ddots & \vdots \\ \mathbf{y}_{i-1} & \mathbf{y}_i & \cdots & \mathbf{y}_{i+j-2} \\ \mathbf{y}_i & \mathbf{y}_{i+1} & \cdots & \mathbf{y}_{i+j-1} \\ \mathbf{y}_{i+1} & \mathbf{y}_{i+2} & \cdots & \mathbf{y}_{i+j} \\ \vdots & \vdots & \ddots & \vdots \\ \mathbf{y}_{2i-1} & \mathbf{y}_{2i} & \cdots & \mathbf{y}_{2i+j-2} \end{bmatrix} = \begin{bmatrix} \mathbf{Y}_{0j-1} \\ \mathbf{Y}_{i2i-1} \end{bmatrix} = \begin{bmatrix} \mathbf{Y}_p \\ \mathbf{Y}_f \end{bmatrix} = \begin{bmatrix} \mathbf{y}_0 & \mathbf{y}_1 & \cdots & \mathbf{y}_{j-1} \\ \mathbf{y}_1 & \mathbf{y}_2 & \cdots & \mathbf{y}_j \\ \vdots & \vdots & \ddots & \vdots \\ \mathbf{y}_{i-1} & \mathbf{y}_i & \cdots & \mathbf{y}_{i+j-2} \\ \mathbf{y}_i & \mathbf{y}_{i+1} & \cdots & \mathbf{y}_{i+j-1} \\ \mathbf{y}_{i+1} & \mathbf{y}_{i+2} & \cdots & \mathbf{y}_{i+j} \\ \vdots & \vdots & \ddots & \vdots \\ \mathbf{y}_{2i-1} & \mathbf{y}_{2i} & \cdots & \mathbf{y}_{2i+j-2} \end{bmatrix} = \begin{bmatrix} \mathbf{Y}_{0i} \\ \mathbf{Y}_{i+1|2i-1} \end{bmatrix} = \begin{bmatrix} \mathbf{Y}_p^+ \\ \mathbf{Y}_f^- \end{bmatrix} . \quad (3.43)$$

where the line divides the elements denoted as \mathbf{Y}_p as the data from the ‘‘past’’ and \mathbf{Y}_f is date from the future.

2. Computation of the projection of the future data onto the past data according to the formula

$$\hat{\mathbf{Y}}_i = \mathbf{Y}_f / \mathbf{Y}_p = \mathbf{Y}_f \mathbf{Y}_p^T (\mathbf{Y}_p \mathbf{Y}_p^T)^{\dagger} \mathbf{Y}_p . \quad (3.44)$$

3. Computation of the SV decomposition of the matrix $\hat{\mathbf{Y}} = \mathbf{USV}^T$. The algorithm by the use of the LQ decomposition follows slightly different steps.
4. Computation of the extended observability matrix $\mathbf{P} = \mathbf{US}^{1/2}$.
5. Extraction the discrete equation of motion state matrix from the observability matrix.
6. Computation the natural frequencies, damping ratios and mode shapes of the system.

3.2.3. Experimental examples

3.2.3.1. Steel plate

The steel plate is shown in example 2.2 in chapter 2 (Fig. 2.4). The numbering of the points used in the ambient vibration tests is given in Fig. 3.31.

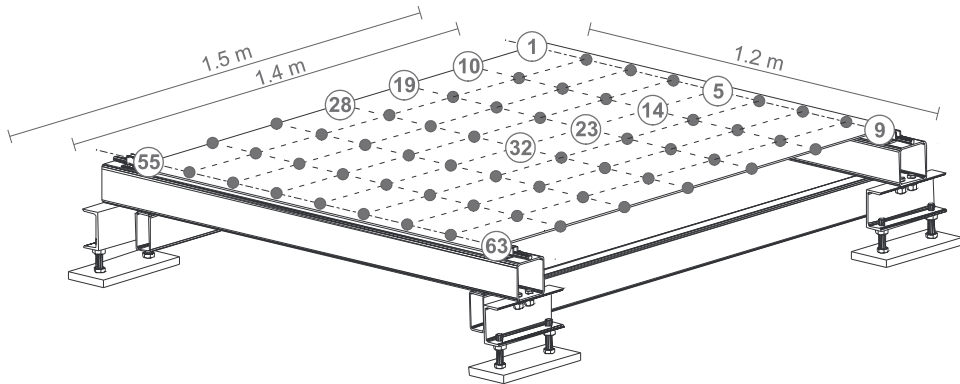


Fig. 3.31. The numbering of points on the experimental plate setup

The measurements have been conducted with the data acquisition system described in section 3.1.2.2. The accelerometers were placed at the locations denoted by numbers from 1 to 63 (Fig. 3.31). The experiments were conducted with 11 accelerometers and the 6 series were completed. Table. 3.5 presents the location of the accelerometers in each series. The sampling frequency was 1024 Hz and each series lasted for 256 seconds.

The plate vibrations were induced by the vibrations transmitted from the university road passing near the university, by people walking near the university and by people moving within the laboratory. The example of the acceleration time response at point 3 is given in Fig. 3.32. The peak acceleration responses reached 2.7 m/s^2 . The mean value of the measured signal is zero. The selected results, given in this section, are after Dudek 2008.

First the identification by NExT/ERA was conducted. The chosen reference points were: 1, 3, 4, 6, 7 and 9. In all series the best selection of the reference point was at the location on the plate free support. The time acceleration responses from the points, theoretically, on the support were not zero. The reason is that it is practically impossible to place the sensor perfectly on the support. In fact, the experiments showed that the steel plate in several locations was not attached to the free support due to the plate and supports imperfections, and therefore, some oscillations were observed.

Table 3.5

Measurement points in each series

Measurement series no.	Measurement point number
1	1, 10, 19, 28, 37, 46, 55, 2, 11, 20, 29
2	29, 38, 47, 56, 3, 12, 21, 30, 39, 48, 57
3	4, 13, 22, 31, 40, 49, 58, 5, 14, 23, 32
4	32, 41, 50, 59, 6, 15, 24, 33, 42, 51, 60
5	7, 16, 25, 34, 43, 52, 61, 62, 53, 44, 35
6	35, 26, 17, 8, 9, 18, 27, 36, 45, 54, 63

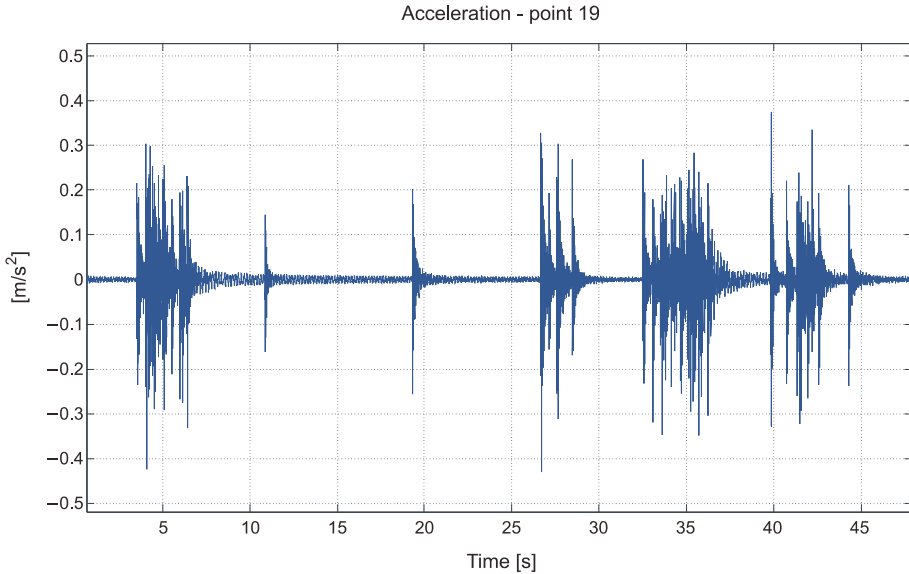


Fig. 3.32. The acceleration response at point 19

The size of the Hankel matrix has been selected as 1280×480 . The number of rows and columns were selected after numerous simulations. The power spectral density functions of each measurement signal were computed using the Fast Fourier Transform.

The averaged normalized power spectral density (ANPSD) function is shown in Fig. 3.33. This function is obtained from the Fourier transform of the cross-power spectra between the random responses at the reference channels and some other random responses. The ANPSD function is normalized to one and averaged over the available PSD functions. The peaks at the ANPSD function can correspond to the plate natural frequencies. The inverse Fourier transform of the ANPSD provides the time domain responses that are treated as the impulse response of the plate. The selected time responses are given in Fig. 3.34.

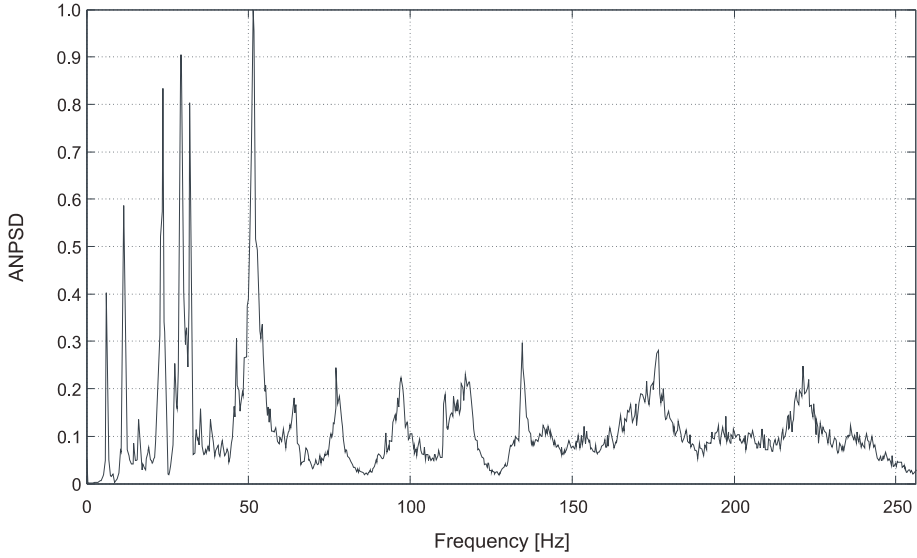


Fig. 3.33. The averaged normalized power spectra density function (NExT)

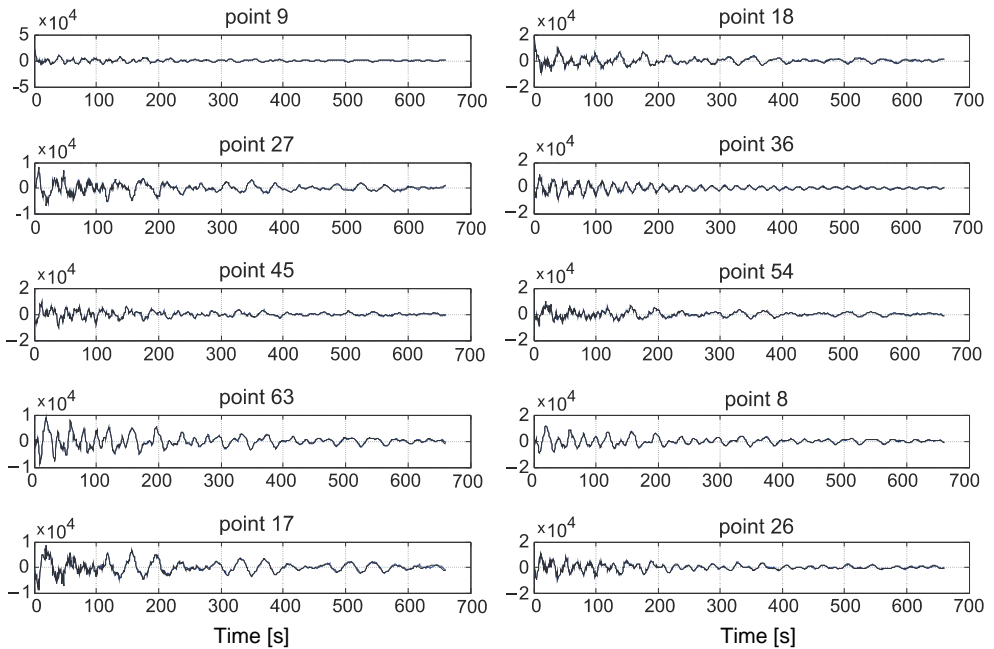


Fig. 3.34. The impulse response functions obtained from NExT

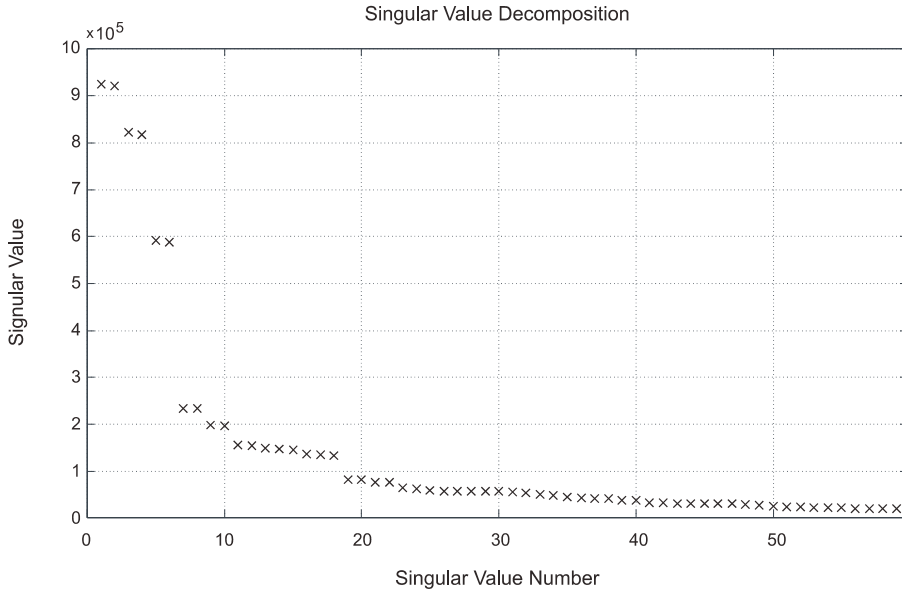


Fig. 3.35. The singular values of the Hankel matrix for steel plate

The decomposition of the Hankel matrix has been conducted by the SVD procedure. The first 60 singular values of the plate are shown in Fig. 3.35. Practically the number of the selected singular values should not exceed the number of the measurement points selected in the experiment. It is assumed that the selection of the points is made so that the most important degrees of freedom are captured. Simulations on the plate, showed that the singular values smaller than 0.1 caused appearance of a fake and computational modes. The selection of the model order were conducted for the numbers of the singular values from 20 to 60. Additional criteria, evaluated at each step, were chosen as follows,

$$MAC \geq 0.99, \quad (3.45)$$

and

$$MSV \geq 0.20, \quad (3.46)$$

where MAC denotes the modal assurance criteria and MSV is modal singular value criteria (Appendix D). The averaged size of the model computed in each series was found to be 34. The stabilization diagram for the series that satisfies the conditions (3.45) and (3.46) is given in Fig. 3.36.

The selection of the physical modes needs additional conditions. It is proposed to trace the variations of the system natural frequencies and the damping ratios. It is assumed that the real physical modes do not jump on the stabilization diagram. Thus, they should satisfy the inequities,

$$\Delta\omega = \omega_{i+1} - \omega_i < 0.01, \quad (3.47)$$

and

$$\Delta\xi = \xi_{i+1} - \xi_i < 0.03. \quad (3.48)$$

The critical values of 1% and 3% in equations (3.47) and (3.48) are selected from the experience gained in the numerical simulations. A stabilization diagram for the plate with the conditions of frequency and the damping variations are given in Fig. 3.37.

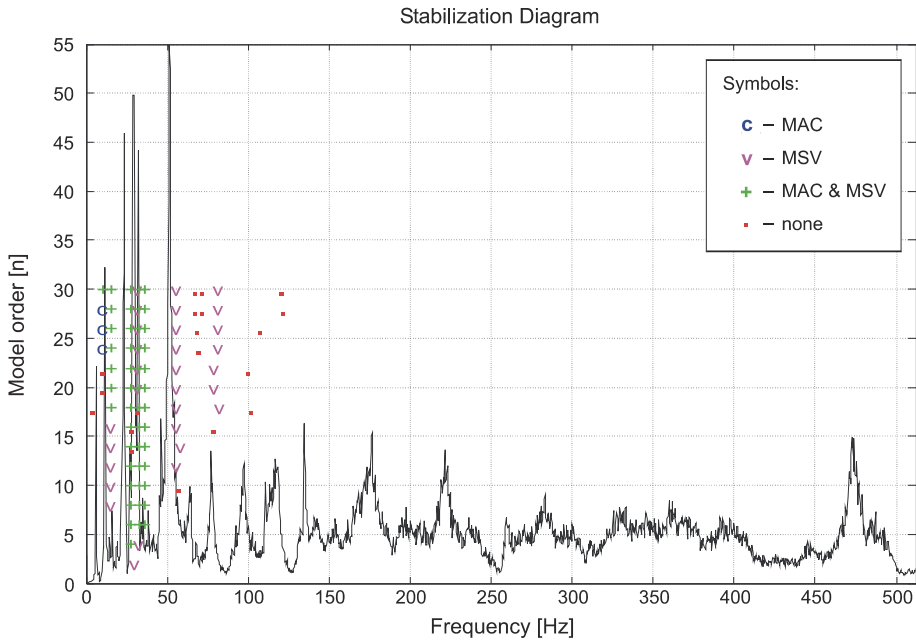


Fig. 3.36. The stabilization diagram for the plate physical mode selection with MAC and MSV criteria

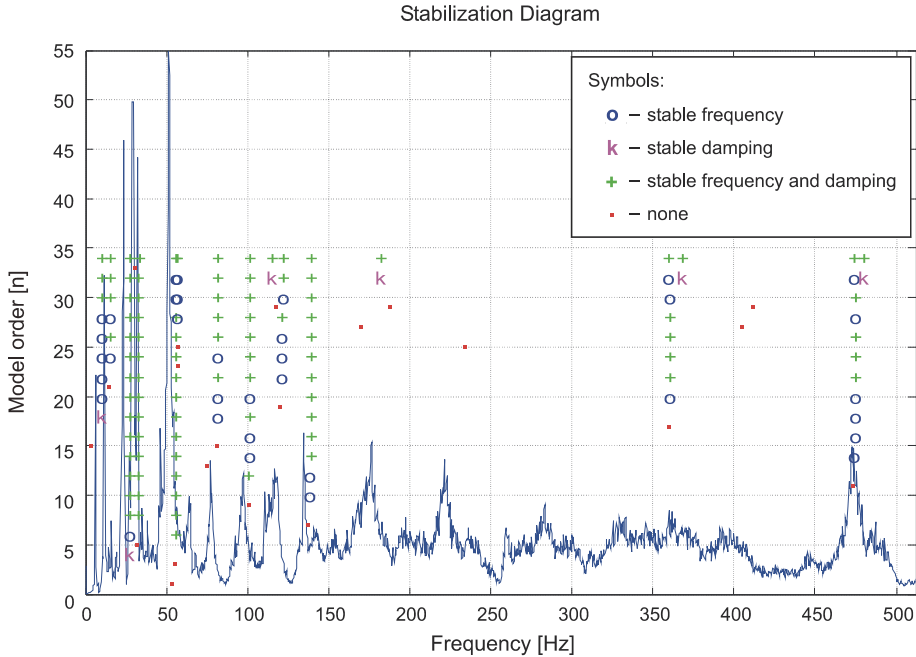


Fig. 3.37. The stabilization diagram for the plate physical mode selection with addition conditions on frequency and damping

The crosses denote the modes which satisfy both conditions (3.47) and (3.48). Finally, it has been found that 8 frequencies correspond to the possible real plate modes. The results of the identified averaged natural frequencies are given in Table. 3.6. Figs. 3.39, 3.40 and 3.41 show the cross section of the mode shapes determined by NExT/ERA method.

The identification of the modal parameters by the Stochastic Subspace Identification method conducted by data matrix of the size 260×5200 . The LQ decomposition was used to reduce the data matrix and the selection of the system minimum realization conducted by the singular value decomposition. In the case of the SSI method the criteria for the search of the stable modes were,

$$\Delta\omega = \omega_{i+1} - \omega_i < 0.01, \quad (3.49)$$

and

$$\Delta\xi = \xi_{i+1} - \xi_i < 0.03. \quad (3.50)$$

The stabilizing diagram of for the SSI method is given in Fig. 3.38.

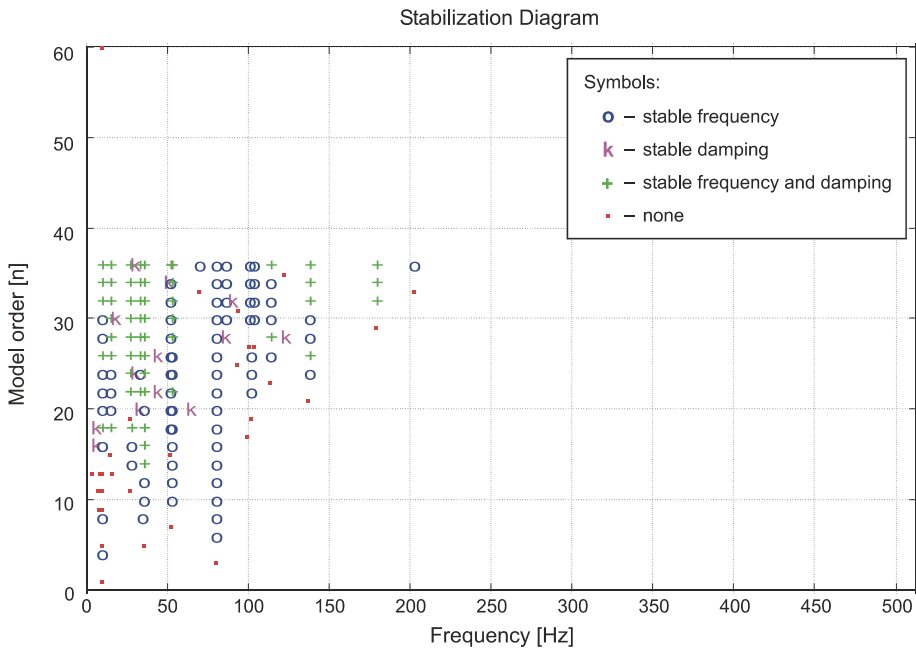


Fig. 3.38. The stabilization diagram for SSI method applied to plate using criteria on frequency and damping variation

The results of the frequency and damping identification are given in Table 3.6. The identified modes are presented in Figs. 3.39, 3.40 and 3.41. The comparison of different methods of ambient vibrations shows quite good agreement with the results of the numerical simulations.

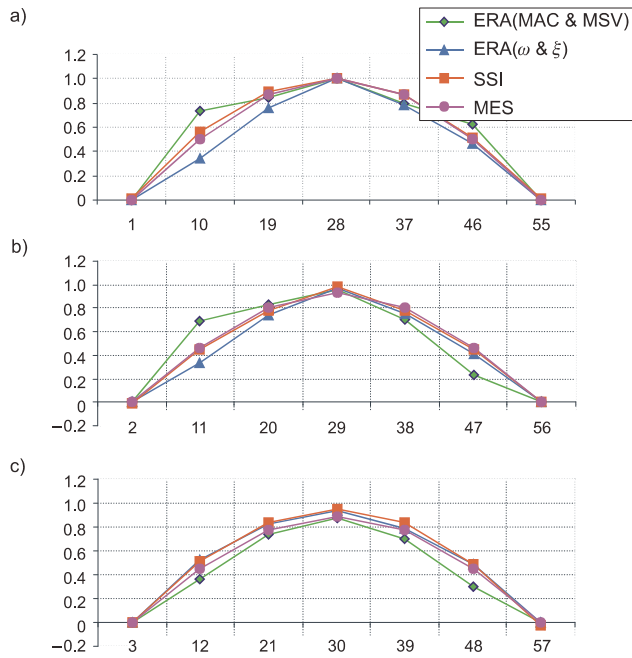


Fig. 3.39. First mode of the plate a) cross section at the free edge of the plate b) cross section 13.33 cm from the free edge c) cross section 26.66 cm from the free edge

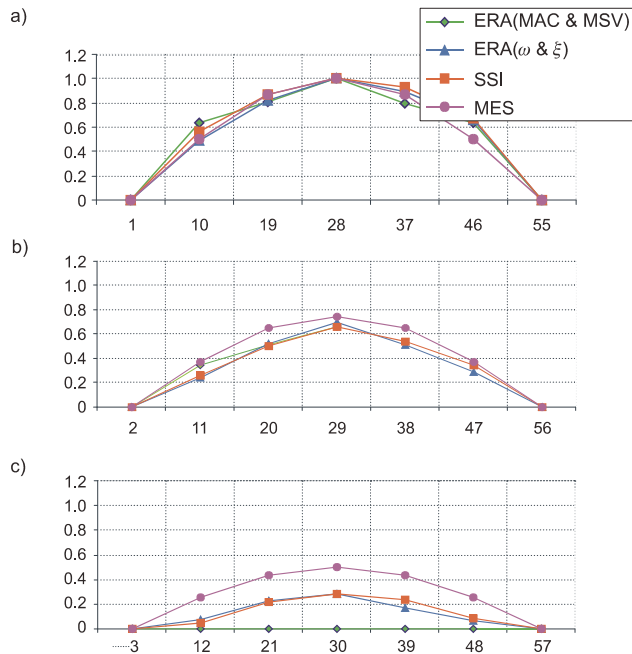


Fig. 3.40. Second mode of the plate a) cross section at the free edge of the plate b) cross section 13.33 cm from the free edge c) cross section 26.66 cm from the free edge

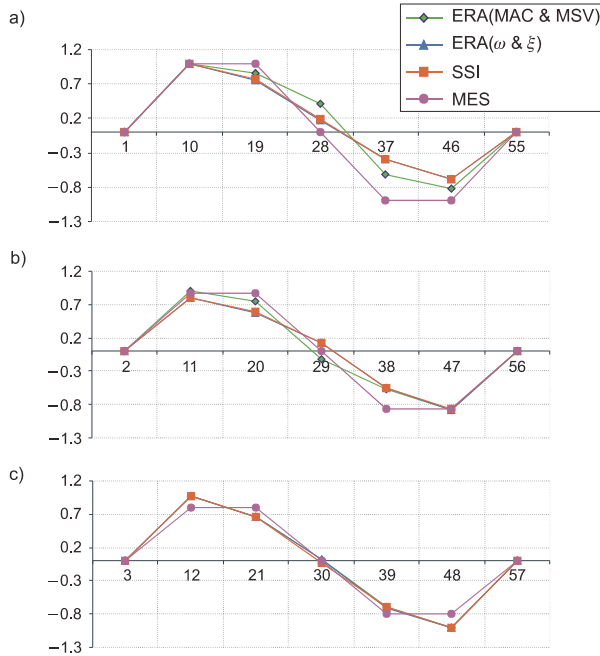


Fig. 3.41. Third mode of the plate a) cross section at the free edge of the plate b) cross section 13.33 cm from the free edge c) cross section 26.66 cm from the free edge

Table 3.6

Comparison of the identified natural frequencies and damping ratios

No.	MES f [Hz]	ERA (MAC & MSV)		ERA (ω & ξ)		SSI (ω & ξ)	
		f [Hz]	ξ	f [Hz]	ξ	f [Hz]	ξ
1	6.17	6.19	0.0122690	6.20	0.0099684	6.180	0.0024316
2	11.04	11.49	0.0160434	11.53	0.0093412	11.650	0.0059012
3	25.42	23.55	0.0163940	23.47	0.0151930	23.530	0.0086427
4	27.11	29.22	0.0107769	29.31	0.0107449	29.350	0.0081792
5	30.86	32.19	0.0064220	32.20	0.0060699	32.299	0.0052074
6	47.52	51.91	0.0141967	51.90	0.0128346	48.650	0.0003712

3.2.3.2. Composite bridge in Żukowo

The ambient vibration identification techniques are tested on a small span bridge in Żukowo near Gdańsk. The bridge is located on the road Kościerzyna – Gdynia. A schematic plan of the bridge is given in Fig. 3.42. The bridge has a single span of length of 27 m. It consists of 4 girders of steel 18G2a and concrete B30 plate of 24 cm thickness. The cross section of the bridge is shown in Fig. 3.43. The view of the bridge is given in Figs. 3.44. and 3.45.

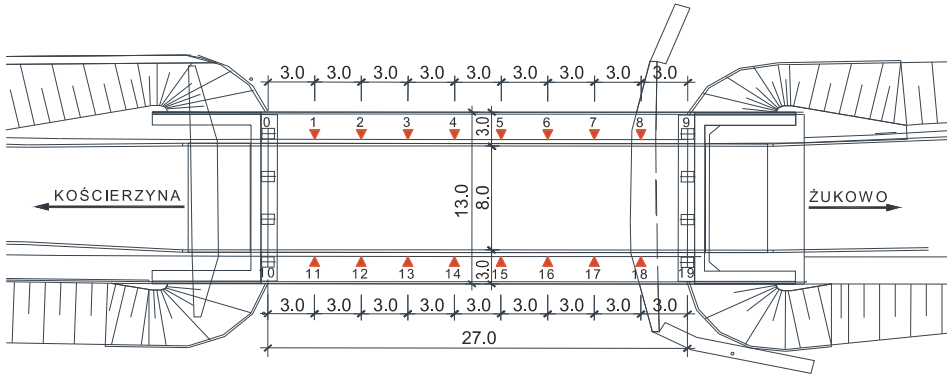


Fig. 3.42. The stabilization diagram for the SSI method applied to plate with criteria on frequency and damping variation

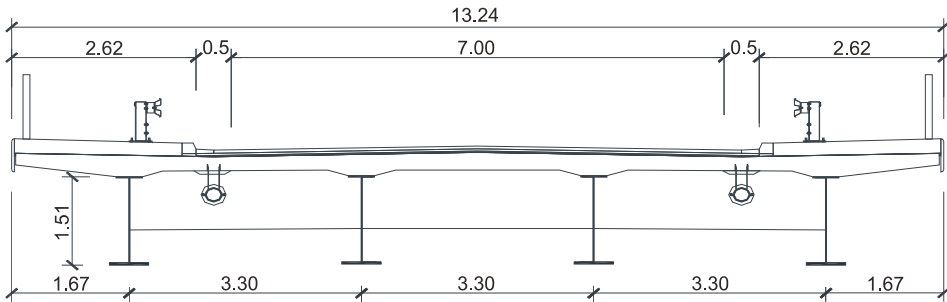


Fig. 3.43. The cross-section of the bridge

The data acquisition station was installed in a car parked under the bridge (Fig. 3.47). The data acquisition system is presented in Fig. 3.48 and the sensor location on one side of the bridge is illustrated in Fig. 3.49. The location of the accelerometers on the bridge is shown in Fig. 3.42 and is marked by red triangles.



Fig. 3.44. General view of the bridge



Fig. 3.45. Side view of the bridge

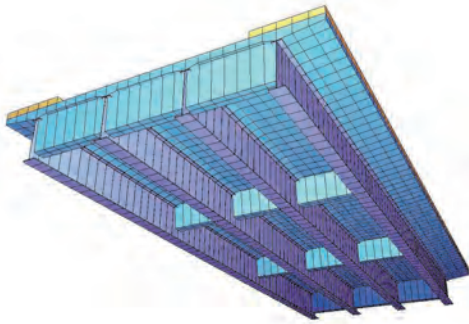


Fig. 3.46. Bridge FEM model



Fig. 3.47. Data acquisition station



Fig. 3.48. Data acquisition system



Fig. 3.49. Location of the accelerometers

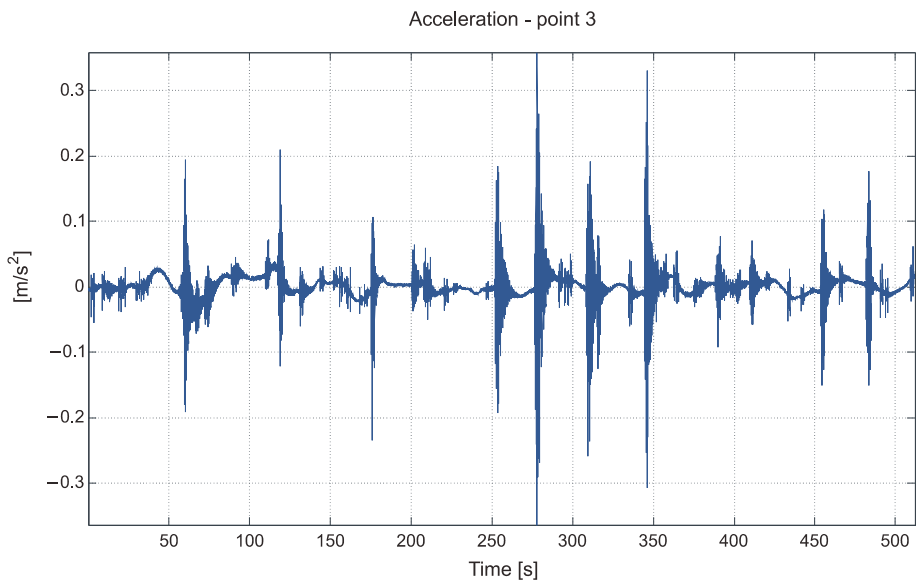
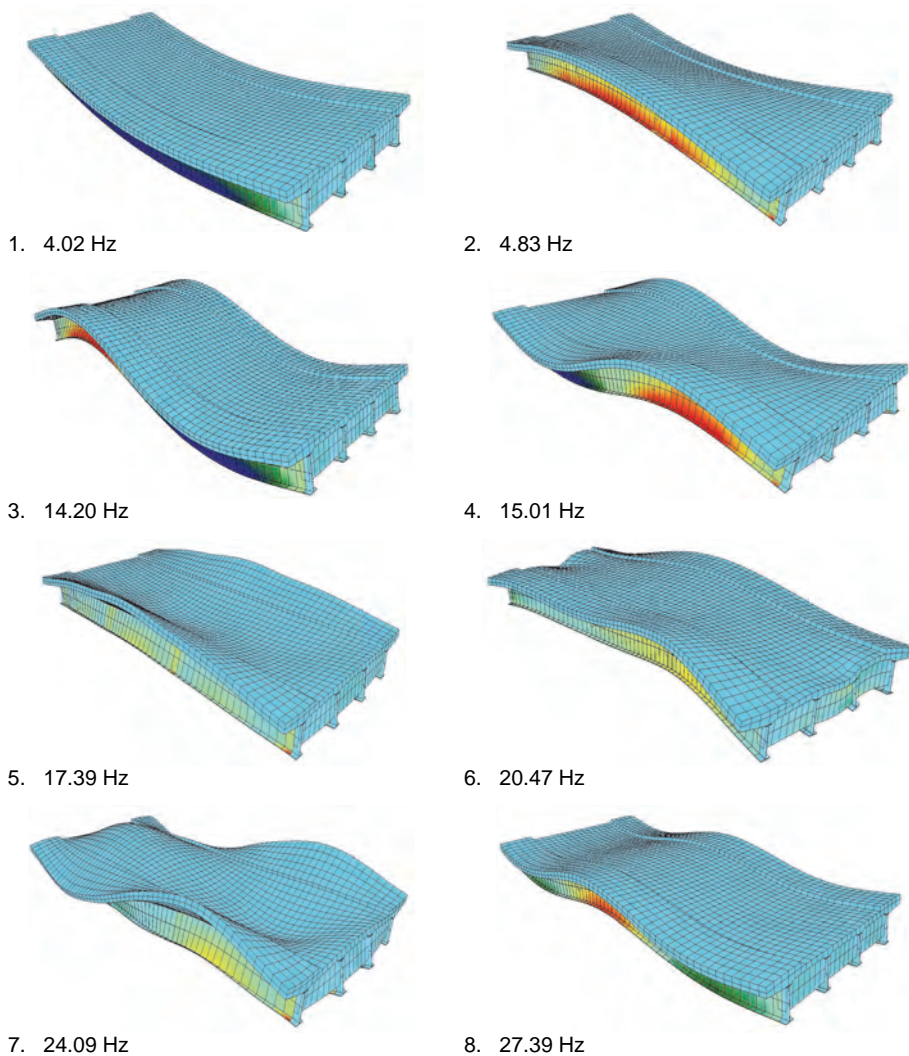


Fig. 3.50. The example of the acceleration record of the bridge ambient vibrations

The FEM model of the bridge is presented in Fig. 3.46. The model was derived in commercial code SOFISTIK with plate and beam elements. The visualization of the computed first 8 mode shapes is given in Table 3.7.

Table 3.7

Numerical mode shapes of the composite bridge



The ambient measurements were conducted in two stages using 10 accelerometers in each series. The bridge was excited mainly by the passing cars of the different sizes and weight and wind of small velocity and accidental gusts. Occasionally the bridge was also crossed by pedestrians. An example of the time history of the acceleration is shown in Fig. 3.50. The sampling frequency was set to 512 Hz and the signals were recorded for the time durations of 256 seconds.

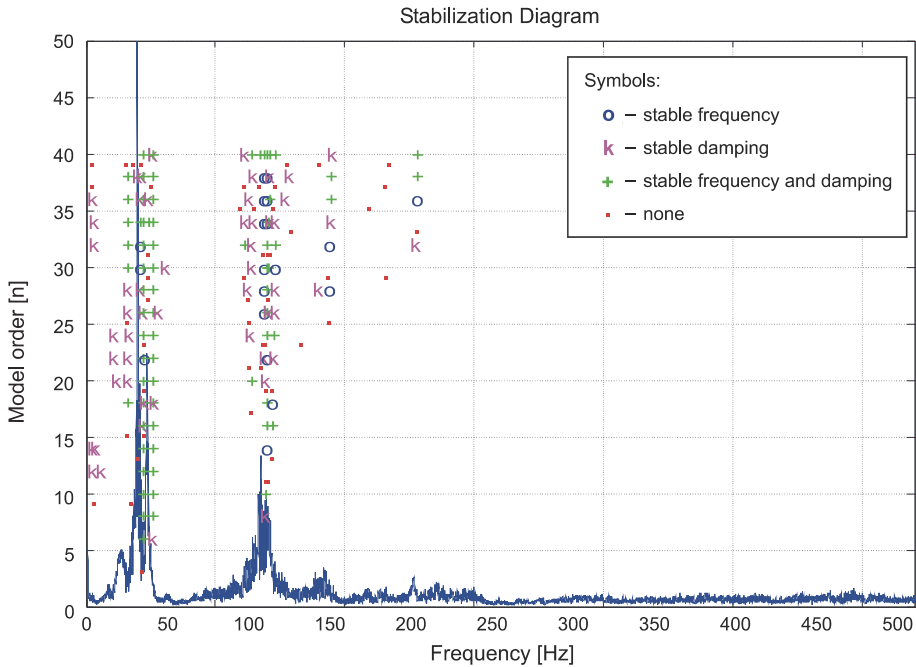


Fig. 3.51. The stabilization diagram of NExT/ERA method

The NExT/ERA identification procedure was conducted for the referenced points selected at locations 1 and 8 (Fig. 3.42). The stabilization diagram with the additional conditions of

$$\Delta\omega = \omega_{i+1} - \omega_i < 0.0025, \quad (3.51)$$

and

$$\Delta\xi = \xi_{i+1} - \xi_i < 0.075, \quad (3.52)$$

is shown in Fig. 3.51. The number of the 30 first singular values was selected for the further computations. Six natural frequencies and mode shapes were successfully identified. The natural frequencies of the bridge are given in Table 3.8 and Table 3.9 for series 1 and 2, respectively. The identified mode shapes are presented in Figs. 3.52, 3.53, 3.54 and 3.55. Two cases of the ERA and SSI identifications are considered. In the first case the computations are conducted directly on the measured data. In the second case the combination of the Empirical Modal Decomposition (Appendix C) is used. The results obtained with the EMD are denoted as ERA EMD and SSI EMD, respectively.

The SSI method was applied to the bridge model defined by 30 singular values with the additional condition for search of the physical modes given by (3.51) and (3.52). The results of the natural frequencies identification are presented in Table 3.9 and the mode shapes are plotted in Figs. 3.51, 3.52, 3.54 and 3.55.

By using ERA and SSI with and without the Empirical Modal Decomposition first four modes could be identified. The comparison of the ambient mode with the numerical results shows a very good agreement. Application of the EMD improves the shape of the experimental modes. However, it was impossible to identify the higher modes of the bridge.

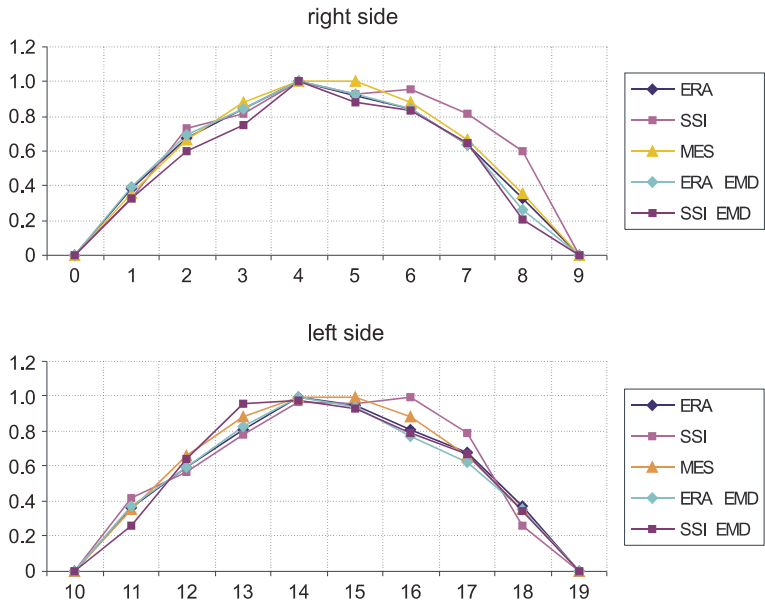


Fig. 3.52. First mode shape (bending, 3.96 Hz) identified on the left and right side of the bridge (measurements series 1 and 2)

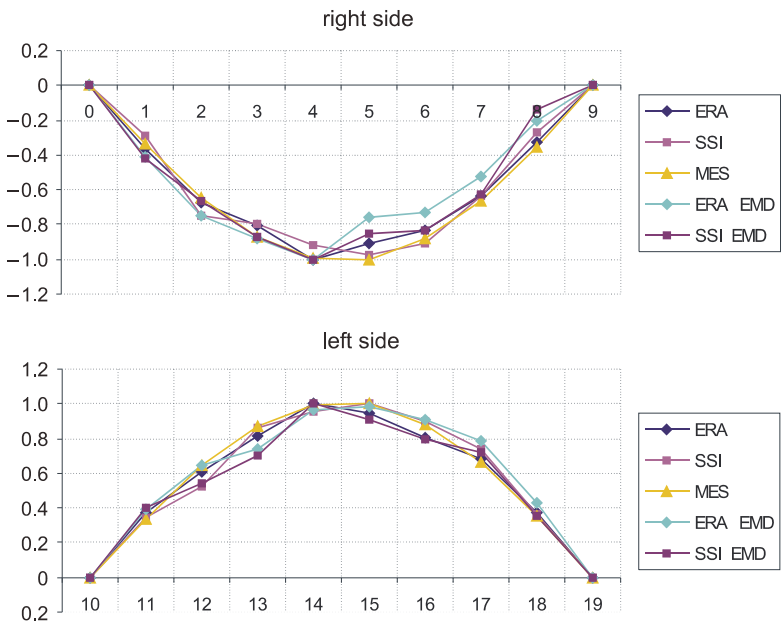


Fig. 3.53. Second mode shape (torsional, 4.69 Hz) identified on the left and right side of the bridge (measurements series 1 and 2)

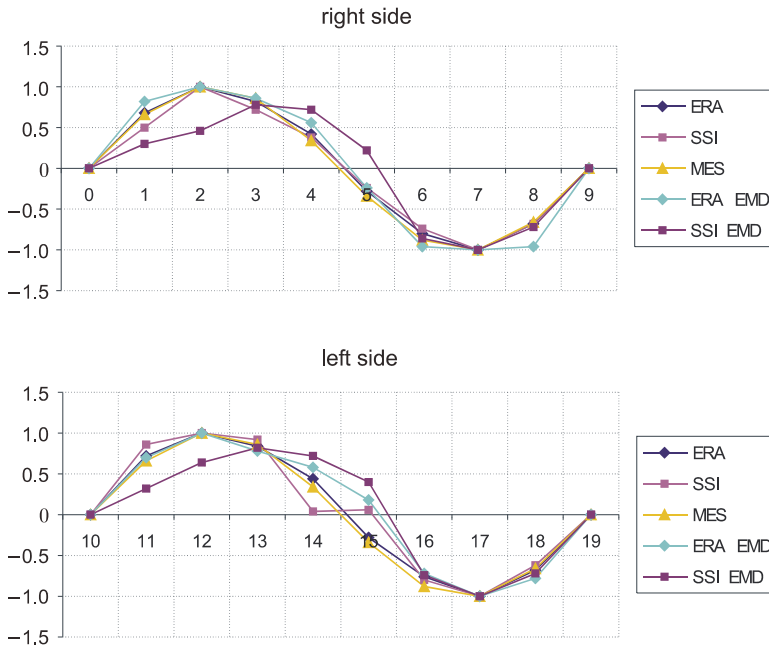


Fig. 3.54. Third mode shape (second bending, 13,34 Hz) identified on the left and right side of the bridge (measurements series 1 and 2)

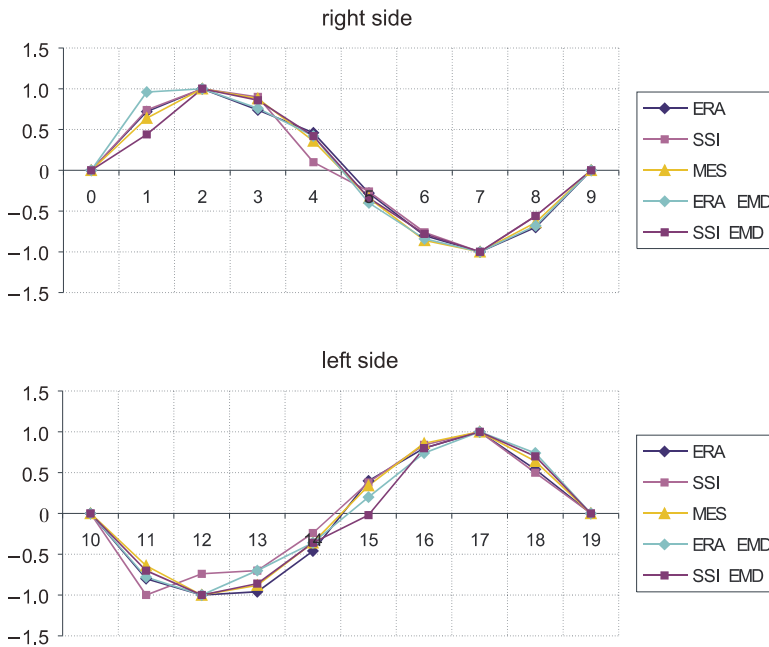


Fig. 3.55. Forth mode shape (second torsional, 14,19 Hz) identified on the left and right side of the bridge (measurements series 1 and 2)

Table 3.8

Natural frequencies damping ratios of the bridge by different methods (series 1)

Serie 1	FEM	ERA		SSI		ERA EMD		SSI EMD	
	f [Hz]	f [Hz]	ξ	f [Hz]	ξ	f [Hz]	ξ	f [Hz]	ξ
	4.02	3.9605	0.089195	3.9864	0.012792	3.9684	0.010325	3.9820	0.000672
	4.83	4.6892	0.013586	4.6830	0.000992	4.6657	0.018416	4.6646	0.001546
	14.20	13.3100	0.022295	13.3990	0.001007	13.3950	0.001445	13.1280	8.63E-04
	15.01	14.1270	0.013567	14.1210	0.000752	14.0470	0.000723	14.1330	0.000139
	17.39	–	–	18.2240	0.000308	18.4430	0.011828	18.3320	0.001036
	20.47	–	–	–	–	–	–	–	–
	24.09	25.1630	0.013567	–	–	–	–	–	–
	27.39	–	–	–	–	–	–	–	–

Table 3.9

Natural frequencies damping ratios of the bridge by different methods (series 2)

Serie 2	FEM	ERA		SSI		ERA EMD		SSI EMD	
	f [Hz]	f [Hz]	ξ	f [Hz]	ξ	f [Hz]	ξ	f [Hz]	ξ
	4.02	3.9616	0.014040	3.9595	0.016489	3.9836	0.010848	3.9435	0.002378
	4.83	4.6911	0.015480	4.6815	0.016107	4.7285	0.019393	4.6928	0.001668
	14.20	13.2880	0.010489	13.4140	0.000795	13.3620	0.005075	13.4400	0.000587
	15.01	14.3070	0.012379	13.8090	0.001687	13.9800	0.007538	14.3220	0.000469
	17.39	18.2940	0.011379	–	–	18.2610	0.008704	18.2180	0.000172
	20.47	–	–	–	–	–	–	–	–
	24.09	–	–	–	–	–	–	–	–
	27.39	26.7080	0.008721	26.9890	0.000785	–	–	27.1740	0.000157

Diagnostics of structures through wavelet analysis of mode shapes

A practical application of the damage detection methods based on wavelet techniques requires conducting the research on experimental data. It is well known that the applicability of the wavelet damage detection techniques depends on the measurement precision and the sampling distances. Pai and Young, 2001 used a scanning laser vibrometer for non-contact measurements of the beams velocities. This method allowed the simultaneous measurements of up to 400 equally spaced points. Hong et al., 2002 and Douka et al., 2003 showed that the distance between the measurement points is the most important factor influencing the effectiveness of the method. They conducted experiments on cantilever beam locating the accelerometer at the fixed reference point and 39 measurement points along the beam. The mode shapes were extracted from the transforms of the acceleration records. Before conducting the wavelet analysis the signals were oversampled to 390 points by a cubic spline interpolation. Other approach directed towards reduction of the measurement sampling distance has been proposed by Rucka and Wilde, 2006a. They used the photogrammetric displacement measurement technique that allowed the high precision measurements simultaneously in 81 points.

The numerical study on a two-dimensional damage detection problem by a Haar wavelet was addressed by Wang and Deng, 1999. They analyzed a numerical data determined from the example of a steel plate with an elliptical hole subjected to uniform tensile loading. The wavelet damage detection study on a rectangular plate with a crack running parallel to one side of the plate has been successfully conducted by Douka et al., 2004. The cracks had relative depth from 10% to 50%. The input data has been determined numerically. Chang and Chen, 2004 and Rucka and Wilde, 2004 also studied the plates on the numerically computed mode shapes. In most of the cases the two-dimensional plate problems (Chang and Chen, 2004, Douka et al., 2004, Rucka and Wilde, 2004) were treated by one-dimensional wavelets. It was assumed that the two dimensional data can be treated as a set of one-dimensional data lines.

To the best authors knowledge there are only few publications addressing the wavelet damage detection on experimental data. The experimental research on plate damage detection has been presented by Rucka and Wilde (2005a). The mode shapes of the cantilever plate with a rectangular defect of 19% with respect to the plate thickness, have been extracted through the frequency response matrix constructed from acceleration signals. The location of the defect was determined through the analysis by Gaussian wavelet with 4 vanishing moments. The two-dimensional formulation of the wavelet transform for plate damage detection is presented by, e.g., Rucka and Wilde in 2006b.

4.1. Basic definitions

The function $\psi(x)$ is said to be a wavelet if and only if its Fourier transform $\Psi(\omega)$ satisfies the wavelet admissibility condition (Mallat 1998)

$$\int_0^{+\infty} \frac{|\Psi(\omega)|^2}{\omega} d\omega < +\infty. \quad (4.1)$$

The wavelet might be a complex function $\psi(x) \in \mathbf{L}^2(\mathbb{R})$ of finite length. $\mathbf{L}^2(\mathbb{R})$ denotes the Hilbert space of measurable, square-integrable one-dimensional functions. The wavelet must have zero average value, i.e.,

$$\int_{-\infty}^{+\infty} \psi(x) dx = 0. \quad (4.2)$$

To guarantee that the integral (4.1) is finite, the Fourier transform of the wavelet function at $\omega = 0$ must be zero, i.e.,

$$\Psi(0) = 0. \quad (4.3)$$

Equation (4.3) explains why wavelet functions must have a zero average value. The function $\psi(x)$ is a base for creation of a family of wavelets $\psi_{u,s}(x)$ of the form

$$\psi_{u,s}(x) = \frac{1}{\sqrt{s}} \psi\left(\frac{x-u}{s}\right), \quad (4.4)$$

where the real numbers s and u denote the scale and translation parameters, respectively. The family of wavelet functions is derived by a shift performed by u parameter and a stretching conducted by s on the mother wavelet $\psi(x)$.

In this study only real wavelets $\psi(x)$ are considered and are formulated in the space domain of a civil engineering structure. Therefore, the variable x is assumed to be a spatial coordinate.

The Continuous Wavelet Transform (CWT), for a given signal $f(x)$, is an inner product of the signal function with the wavelet functions (e.g., Mallat 1998, Meyer 1993, Misiti et al. 2000, Strang and Nguyen 1996)

$$Wf(u, s) = \langle f, \psi_{u,s} \rangle = \frac{1}{\sqrt{s}} \int_{-\infty}^{+\infty} f(x) \psi\left(\frac{x-u}{s}\right) dx. \quad (4.5)$$

$Wf(u, s)$ is called a wavelet coefficient for the wavelet $\psi_{u,s}(x)$ and it measures the variation of the signal in the vicinity of u which size is proportional to s . The correlation between the signal and the wavelet is in the sense of frequency content. If the signal contains a spectral component corresponding to the current value of s , the product of the wavelet with the signal gives large values. Strang and Nguyen, 1996 suggested normalizing the wavelet coefficients by a factor $1/\sqrt{s}$ so that the rescale wavelets have equal energy, i.e.,

$$\|\psi_{u,s}\| = \|\psi\| = 1. \quad (4.6)$$

The convolution form of the integral product in equation (4.5) is of the form

$$Wf(u, s) = \frac{1}{\sqrt{s}} f * \psi \left(\frac{-u}{s} \right) = f * \bar{\psi}_s(u), \quad (4.7)$$

where $\bar{\psi}_s(x)$ is given by the formula

$$\bar{\psi}_s(x) = \frac{1}{\sqrt{s}} \psi \left(\frac{x}{s} \right). \quad (4.8)$$

The computation of the wavelet coefficients given by equation (4.7) can be implemented in any computer code, which guarantees a shorter calculation time than computations by the use of equation (4.5).

The two-dimensional wavelet transforms are also considered for the civil structures modelled by two dimensional elements. Since there are two spatial coordinates, two functions for computation of the wavelet coefficients can be defined (Mallat 1998). The first one is called the horizontal wavelet and is denoted by $\psi^1(x, y)$. It can be constructed by the separable products of a one-dimensional scaling function $\phi(x)$ and a one-dimensional wavelet function $\psi(x)$ in the following form

$$\psi^1(x, y) = \phi(x)\psi(y). \quad (4.9)$$

By analogy the vertical wavelet is defined by a product of the $\psi(x)$ function of the spatial coordinate x , and the scaling function $\phi(y)$ based on the coordinate y . The formula for the vertical wavelet $\psi^2(x, y)$ becomes

$$\psi^2(x, y) = \psi(x)\phi(y). \quad (4.10)$$

In the two dimensional case a family of wavelets can be written as

$$\psi_{u,v,s}^i = \frac{1}{s} \psi^i \left(\frac{x-u}{s}, \frac{y-v}{s} \right), \quad i = 1, 2. \quad (4.11)$$

Let the function $f(x, y)$ be a signal belonging to the Hilbert $L^2(\mathbb{R}^2)$ space of measurable, square-integrable two-dimensional functions. The wavelet transforms of the function $f(x, y)$ defined with respect to each of the wavelets given by equations (4.9) and (4.10) are formulated as follows

$$\begin{aligned} W^i f(u, v, s) &= \langle f, \psi_{u,v,s}^i \rangle = \frac{1}{s} \int_{-\infty}^{\infty} \int_{-\infty}^{\infty} f(x, y) \psi^i \left(\frac{x-u}{s}, \frac{y-v}{s} \right) dx dy = \\ &= \frac{1}{s} f * \psi^i \left(\frac{-u}{s}, \frac{-v}{s} \right) = f * \bar{\psi}_s^i(u, v) \quad i = 1, 2. \end{aligned} \quad (4.12)$$

Two wavelets $\psi^1(x, y)$ and $\psi^2(x, y)$ can be defined as the partial derivatives of the smoothing function $\theta(x, y)$ with respect to coordinates x and y

$$\psi^1(x, y) = \frac{\partial^n \theta(x, y)}{\partial x^n}, \quad \psi^2(x, y) = \frac{\partial^n \theta(x, y)}{\partial y^n}, \quad (4.13)$$

where indices 1 and 2 denote horizontal and vertical directions, respectively, and n is the number of vanishing moments. Two scaled wavelets can be rewritten in the form

$$\begin{aligned}\psi_s^1(x, y) &= \frac{\partial^n \theta_s(x, y)}{\partial x} = s^n \frac{\partial \theta(x, y)}{\partial x}, \\ \psi_s^2(x, y) &= \frac{\partial^n \theta_s(x, y)}{\partial y} = s^n \frac{\partial \theta(x, y)}{\partial y}\end{aligned}\quad (4.14)$$

where the scaled smoothing function $\theta(x, y)$ is defined as

$$\theta_{u,v,s}(x, y) = \frac{1}{s} \theta\left(\frac{x-u}{s}, \frac{y-v}{s}\right). \quad (4.15)$$

Thus, the derivative form of the wavelet transform can be expressed as

$$\begin{aligned}\begin{pmatrix} W^1 f(u, v, s) \\ W^2 f(u, v, s) \end{pmatrix} &= \begin{pmatrix} f^* \bar{\psi}_s^1(u, v) \\ f^* \bar{\psi}_s^2(u, v) \end{pmatrix} = \begin{pmatrix} f^* s^n \frac{\partial \bar{\theta}_s}{\partial u}(u, v) \\ f^* s^n \frac{\partial \bar{\theta}_s}{\partial v}(u, v) \end{pmatrix} = \\ &= s^n \begin{pmatrix} \frac{\partial}{\partial u} (f^* \bar{\theta}_s)(u, v) \\ \frac{\partial}{\partial v} (f^* \bar{\theta}_s)(u, v) \end{pmatrix} = s^n \bar{\nabla} (f^* \bar{\theta}_s)(u, v),\end{aligned}\quad (4.16)$$

where $\bar{\theta}_{u,v,s} = \theta_{u,v,s}(-x, -y)$. It is noted that the wavelet transform components of the derivative form given by equation (4.16) can be interpreted as the coordinates of a gradient vector of $f(x, y)$ smoothed by $\bar{\theta}_s(x, y)$. The name horizontal and vertical wavelet has its origin in the transformation of the video signal. The wavelet component $W^1 f(u, v, s)$ indicates horizontal edges, while the component $W^2 f(u, v, s)$ indicates the vertical edges.

The modulus of the wavelet transform can be defined as

$$Mf(u, v, s) = \sqrt{|W^1 f(u, v, s)|^2 + |W^2 f(u, v, s)|^2}. \quad (4.17)$$

The modulus at the scale s is proportional to the modulus of the gradient vector $\bar{\nabla} (f^* \bar{\theta}_s)(x, y)$. The local minima of the modulus $Mf(u, v, s)$ are in the direction of the gradient given by angle between the vertical and horizontal wavelets as

$$Af(u, v, s) = \tan^{-1} \left(\frac{W^2 f(u, v, s)}{W^1 f(u, v, s)} \right). \quad (4.18)$$

The modulus (4.17) gives the information about the absolute values of the horizontal and vertical components. The largest modulus indicates the locations where the potential damaged could occur. The angle (4.18) indicates the direction in which the signal has the sharpest variation locally (Mallat and Hwang, 1992). The large angles indicate the vicinity of the potential damage location.

In the case of the three dimensional (3D) structures, where the 3D spatial distribution of the selected structural parameters is considered the presented formulation can be further extended. However, in this book the 3D structures, like, shells are treated by one-, or possibly, two-dimensional wavelets.

4.2. Examples of wavelets

Historically the first wavelet has been known since 1910 (Daubechies 1992) and is called the Haar wavelet (Fig. 4.1a). It has an explicit form and is given by

$$\psi(x) = \begin{cases} 1 & 0 \leq x < 0.5 \\ -1 & 0.5 \leq x < 1. \\ 0 & \text{otherwise} \end{cases} \quad (4.19)$$

Other wavelets used in damage detection are: Gaussian, Morlet, Mexican hat and Meyer wavelets.

A family of the Gaussian wavelet is shown in Fig. 4.2. It can be built by taking its a^{th} derivative of Gaussian function, $g(x)$,

$$g(x) = C_a e^{-x^2}. \quad (4.20)$$

The integer value a is a parameter of this family and C_a is a constant such that

$$\|g^{(p)}\|^2 = 1. \quad (4.21)$$

where $g^{(p)}$ is the a^{th} derivative of $g(x)$ (Misiti et al. 2000). The first four wavelets from the Gaussian family have the following forms (Gentile and Messina 2003)

$$\begin{aligned} \text{gaus1} \quad \psi(x) &= (-1)^1 2\sqrt{2/\pi} x e^{-x^2}, \\ \text{gaus2} \quad \psi(x) &= (-1)^2 \frac{2\sqrt{2/\pi}}{\sqrt{3}} (1-2x^2) e^{-x^2}, \\ \text{gaus3} \quad \psi(x) &= (-1)^3 \frac{4\sqrt{2/\pi}}{\sqrt{15}} (3x-2x^3) e^{-x^2}, \\ \text{gaus4} \quad \psi(x) &= (-1)^4 \frac{4\sqrt{2/\pi}}{\sqrt{105}} (3-2x^2+4x^4) e^{-x^2}. \end{aligned} \quad (4.22)$$

The Mexican hat (Fig. 4.1b) is the wavelet equal to the second derivative of the Gaussian function $e^{-x^2/2}$. If it is normalized so that its L^2 -norm is equal to 1 and $\psi(0) > 0$. Daubechies (1992) derived the closed form formula as

$$\psi(x) = \frac{2}{\pi^{1/4} \sqrt{3}} (1-x^2) \exp\left(-\frac{x^2}{2}\right). \quad (4.23)$$

In damage detection a Morlet wavelet shown in Fig. 4.1c is also applied. It is defined by the following formula

$$\psi(x) = e^{-x^2/2} \cos(5x). \quad (4.24)$$

This wavelet does not satisfy exactly the admissibility condition (Misiti et al. 2000).

The Meyer wavelet (Fig. 4.1d) is defined in the frequency domain (Misiti et al. 2000)

$$\Psi(\omega) = \begin{cases} (2\pi)^{-1/2} e^{i\omega/2} \sin\left(\frac{\pi}{2} \nu\left(\frac{3}{2\pi}|\omega|-1\right)\right) & \text{if } \frac{2\pi}{3} \leq |\omega| \leq \frac{4\pi}{3} \\ (2\pi)^{-1/2} e^{i\omega/2} \cos\left(\frac{\pi}{2} \nu\left(\frac{3}{4\pi}|\omega|-1\right)\right) & \text{if } \frac{4\pi}{3} \leq |\omega| \leq \frac{8\pi}{3} \\ 0 & \text{otherwise} \end{cases} \quad (4.25)$$

where $\nu(a) = a^4(35 - 84a + 70a^2 - 20a^3)$, $a \in \langle 0,1 \rangle$.

Some wavelets cannot be written in an explicit form. The conjugated mirror filters are the origin of, for example, the Daubechies, Coiflets, and Symlets wavelets. They do not have explicit analytical formula and they are not symmetric. The symmetry and regularity is a desired feature for the wavelet used in damage detection. The following plots of the wavelet examples are taken after Rucka and Wilde 2007.

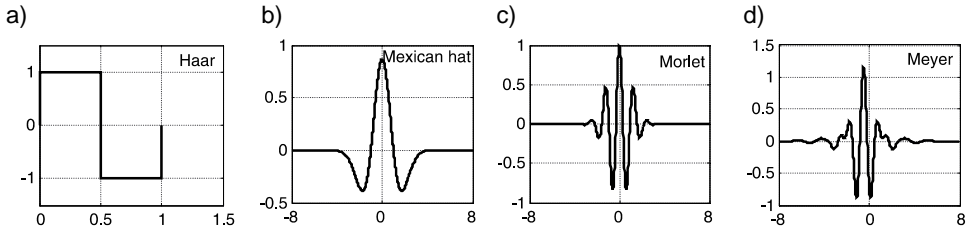


Fig. 4.1. Types of wavelet functions: a) Haar; b) Mexican hat; c) Morlet; d) Meyer

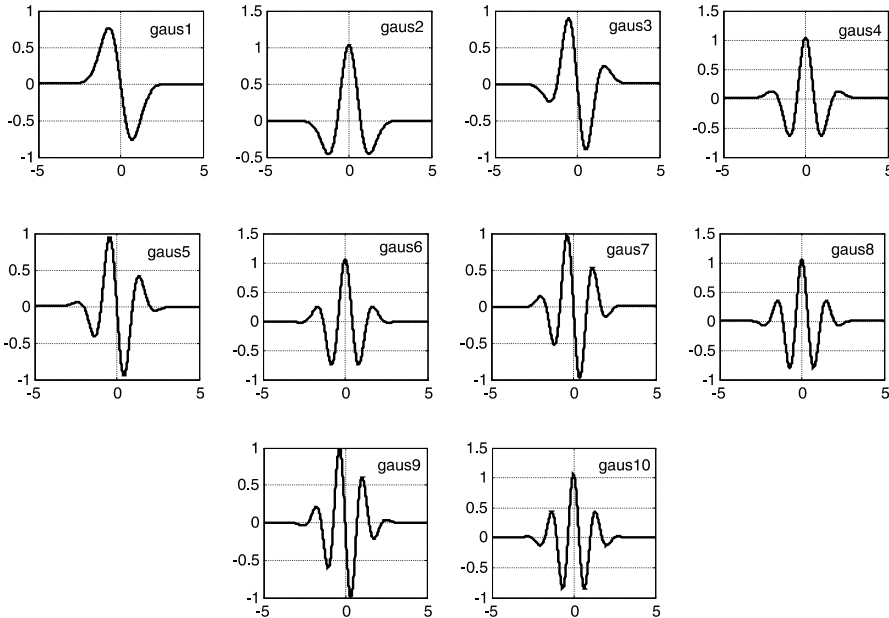


Fig. 4.2. Gaussian family of wavelet functions

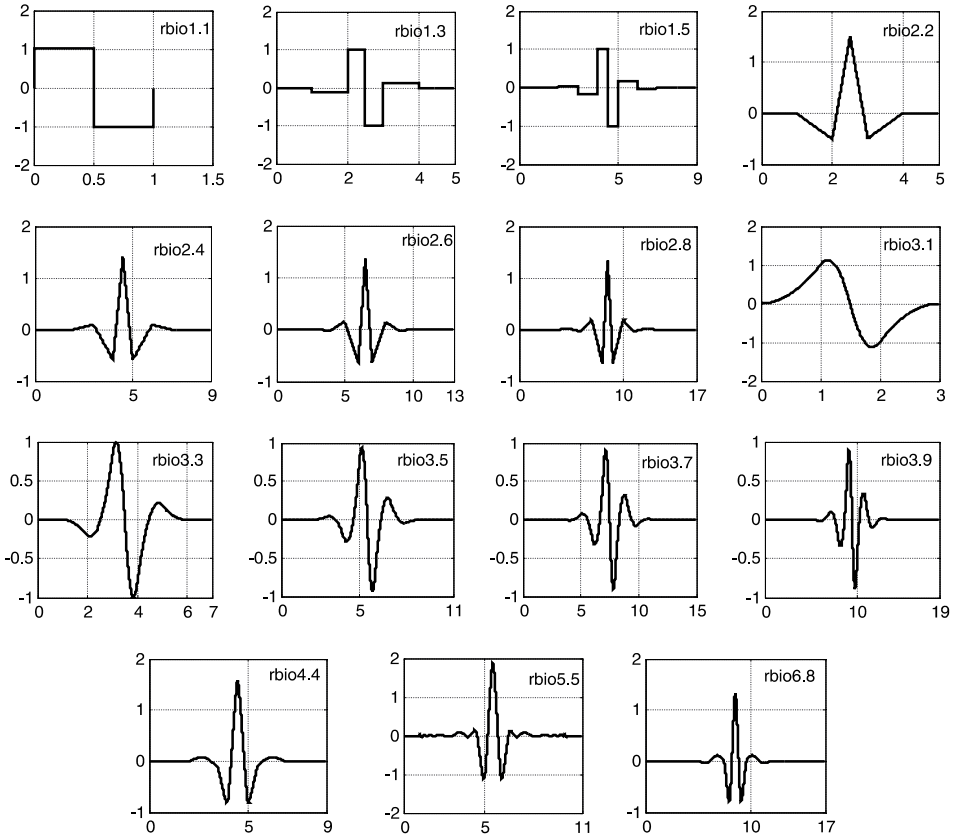


Fig. 4.3. Biorthogonal family of wavelets functions

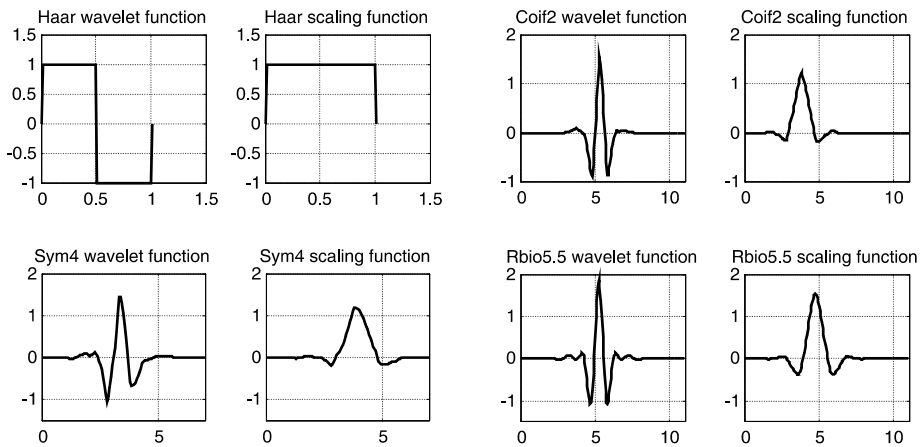


Fig. 4.4. Wavelet and scaling functions for Haar, Coiflet, Symlet and Reverse Biorthogonal families

Table 4.1

Characteristics of selected real wavelets

Wavelet family name	Orthogonal	Biorthogonal	Order N Order N_r, N_d	No. of vanishing moments	Symmetry	Support width	CWT
Haar	yes	yes	–	1	yes	1	yes
Daubechies N	yes	yes	$N = 1, 2, \dots$	N	far from	$2N - 1$	yes
Symlet N	yes	yes	$N = 2, 3, \dots$	N	near from	$2N - 1$	yes
Coiflet N	yes	yes	$N = 1, 2, 3, 4, 5$	$2N$	near from	$6N - 1$	yes
Biorthogonal N_r, N_d	no	yes	$N_r = 1, N_d = 1, 3, 5$ $N_r = 2, N_d = 2, 4, 6, 8$ $N_r = 3, N_d = 1, 3, 5, 7, 9$ $N_r = 4, N_d = 4$ $N_r = 5, N_d = 5$ $N_r = 6, N_d = 8$	$N_r - 1$	yes ($N_r = 1, 3$) asymmetry ($N_r = 2, 4, 5, 6$)	$2N_d + 1$	yes
Reverse Biorthogonal N_d, N_r	no	yes	$N_d = 1, N_r = 1, 3, 5$ $N_d = 2, N_r = 2, 4, 6, 8$ $N_d = 3, N_r = 1, 3, 5, 7, 9$ $N_d = 4, N_r = 4$ $N_d = 5, N_r = 5$ $N_d = 6, N_r = 8$	$N_d - 1$	yes ($N_d = 1, 3$) asymmetry ($N_d = 2, 4, 5, 6$)	$2N_r + 1$	yes
Gaussian N	no	no	$N = 1, 2, \dots$	N	yes (N even) asymmetry (N odd)	10	yes
Meyer	yes	yes	–	–	yes	16	yes
Mexican hat	no	no	–	2	yes	16	yes
Morlet	no	no	–	–	yes	16	yes

The Biorthogonal and Reverse Biorthogonal (Fig. 4.3) wavelets come from biorthogonal filters. The real wavelet characteristics are given in Table 4.1 (after Rucka and Wilde, 2007).

The two dimensional Morlet, Mexican hat and the Gaussian wavelets cannot be computed according to the formulas (4.9) and (4.10) since they do not have scaling functions. Therefore, they cannot be used in two-dimensional wavelet damage detection analysis. The one-dimensional plots of Haar, Coiflet, Symlet and Reverse Biorthogonal wavelet are given in Fig. 4.4. The two-dimensional plots of wavelets and scaling functions are given in Fig. 4.5, Fig. 4.6, Fig. 4.7 and Fig. 4.8 (after Rucka and Wilde 2007).

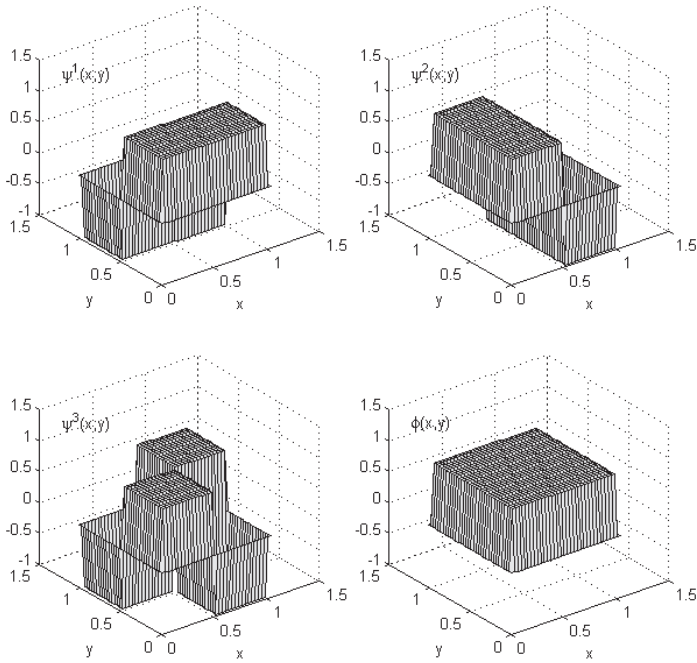


Fig. 4.5. Wavelet functions $\psi^1(x, y)$, $\psi^2(x, y)$, $\psi^3(x, y)$ and scaling function $\phi(x, y)$ for Haar

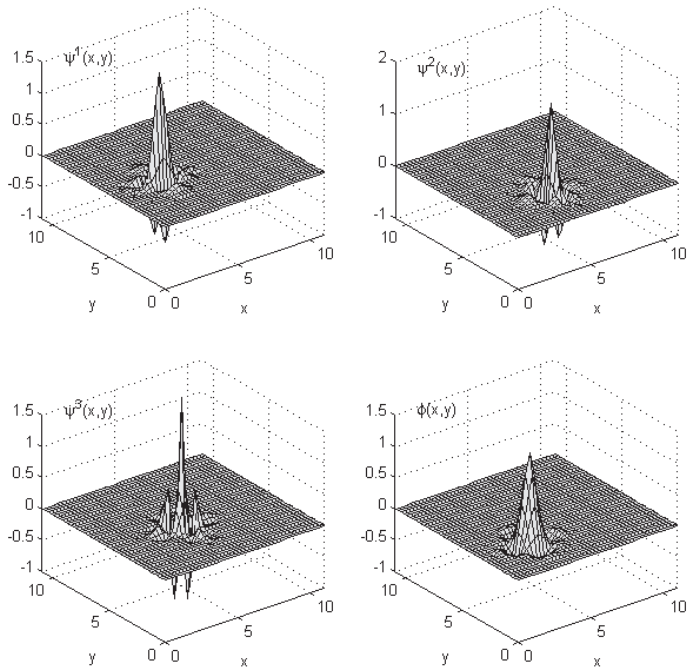


Fig. 4.6. Wavelet functions $\psi^1(x, y)$, $\psi^2(x, y)$, $\psi^3(x, y)$ and scaling function $\phi(x, y)$ for coif2

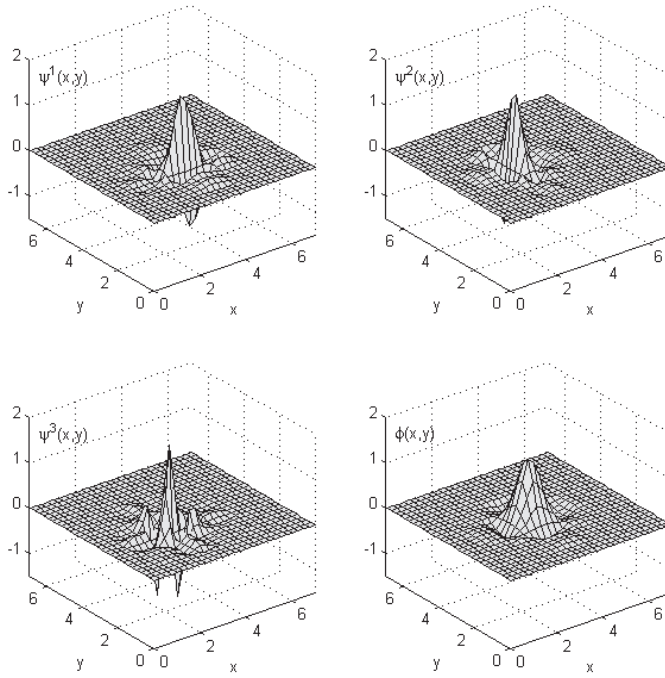


Fig. 4.7. Wavelet functions $\psi^1(x, y)$, $\psi^2(x, y)$, $\psi^3(x, y)$ and scaling function $\phi(x, y)$ for sym4

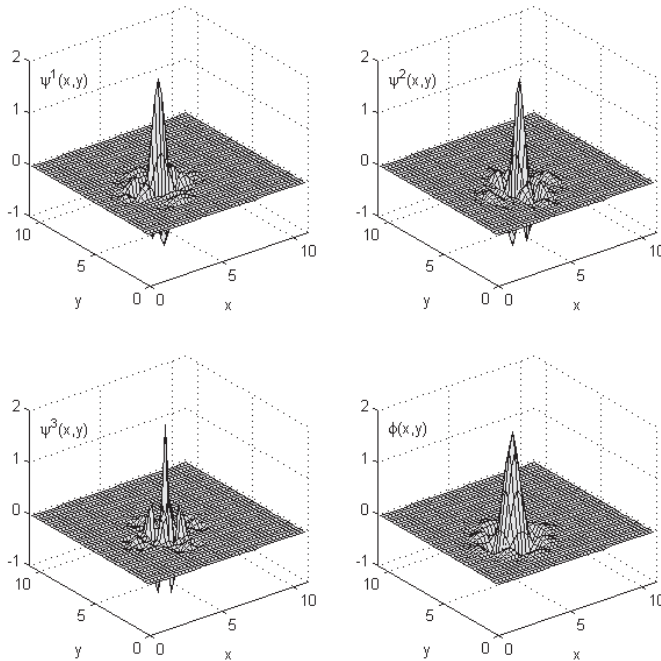


Fig. 4.8. Wavelet functions $\psi^1(x, y)$, $\psi^2(x, y)$, $\psi^3(x, y)$ and scaling function $\phi(x, y)$ for rbio5.5

4.3. Wavelet selection for damage detection

An important property of wavelets is their ability to react to subtle changes, breakdown points or discontinuities contained in a signal. The important role in detection of the signal abnormalities is placed on so called vanishing moments.

A wavelet has n vanishing moments if the following integral equation is satisfied

$$\int_{-\infty}^{+\infty} x^n \psi(x) dx = 0, \quad n = 0, 1, 2, \dots, k-1. \quad (4.26)$$

The equation (4.26) stands that the wavelet having n vanishing moments is orthogonal to polynomials up to degree $k-1$.

The number of vanishing moments can be related to differential operation. Mallat (1998) has proved that a wavelet with n vanishing moments can be treated as the n^{th} order derivative of function $\theta(x)$. Thus, the wavelet transform can be expressed in terms of a multiscale differential operator as

$$\begin{aligned} Wf(u, s) &= \frac{s^n}{\sqrt{s}} \int_{-\infty}^{+\infty} f(x) \frac{d^n}{dx^n} \theta\left(\frac{x-u}{s}\right) dx = \frac{s^n}{\sqrt{s}} \frac{d^n}{dx^n} \int_{-\infty}^{+\infty} f(x) \theta\left(\frac{-(u-x)}{s}\right) dx = \\ &= \frac{s^n}{\sqrt{s}} \frac{d^n}{du^n} f * \theta\left(\frac{-u}{s}\right) = s^n \frac{d^n}{du^n} (f * \bar{\theta}_s)(u), \quad \bar{\theta}_s(x) = \frac{1}{\sqrt{s}} \theta\left(\frac{-x}{s}\right), \end{aligned} \quad (4.27)$$

where $f * \bar{\theta}$ denotes the convolution of functions. The fast decaying function $\theta(x)$ is defined as follows (Mallat and Zhong, 1992)

$$\psi(x) = \frac{d^n \theta(x)}{dx^n}, \quad \int_{-\infty}^{+\infty} \theta(x) dx \neq 0 \quad (4.28)$$

For $n = 1$ the function $\theta(x)$ is the integral of the wavelet function $\psi(x)$ over $(-\infty, x)$ for each value of x , i.e.,

$$\theta(x) = \int_{-\infty}^x \psi(u) du = \int_x^{\infty} \psi(u) du. \quad (4.29)$$

Formula (4.28) brings some important consequences in the field of wavelet damage detection. Many detection methods are based on the numerically determined derivatives of selected parameter. Here it is stated that the wavelet transform is the n^{th} derivative of the signal $f(x)$ smoothed by a function $\bar{\theta}_s(x)$ at the scale s . Therefore, if the signal has a singularity at a certain point, it is not differentiable and the CWT coefficients will have relatively large values. When the scale is large, the convolution with $\bar{\theta}_s(x)$ removes small signal fluctuation. In this case the detection of the small variations in the signal is not possible (Mallat and Zhong, 1992).

The selection of the number of wavelet vanishing moments is an important factor in wavelet selection. Hong et al. (2002) proved that in the case of beams the number of the vanishing moments is related to the function describing the deflection line and should be at least 2. Although, it has been stated by several researchers that the wavelet having higher number of vanishing moments provides more stable performance (e.g., Douka, 2003), there are limitations in this approach. Since the deflection line or mode shape can be approximated by polynomial function it is clear that very high derivative with smoothing

function will result in zero values. Moreover, wavelets with large number of vanishing moments have longer supports and their spatial resolution become limited. The applicability of Haar, Gabor, Mexican hat, Symlet, Coiflet and Gaussian wavelets has been studied (e.g., Misiti et al, 2000, Quek et al, 2001, Wang and Deng, 1999, Hong et al, 2002, Misiti et al, 2000, Douka et al, 2003, Douka et al. 2004, Misiti et al, 2000, Gentile and Messina, 2003, Messina, 2004, Rucka and Wilde, 2005b, Rucka and Wilde, 2006a).

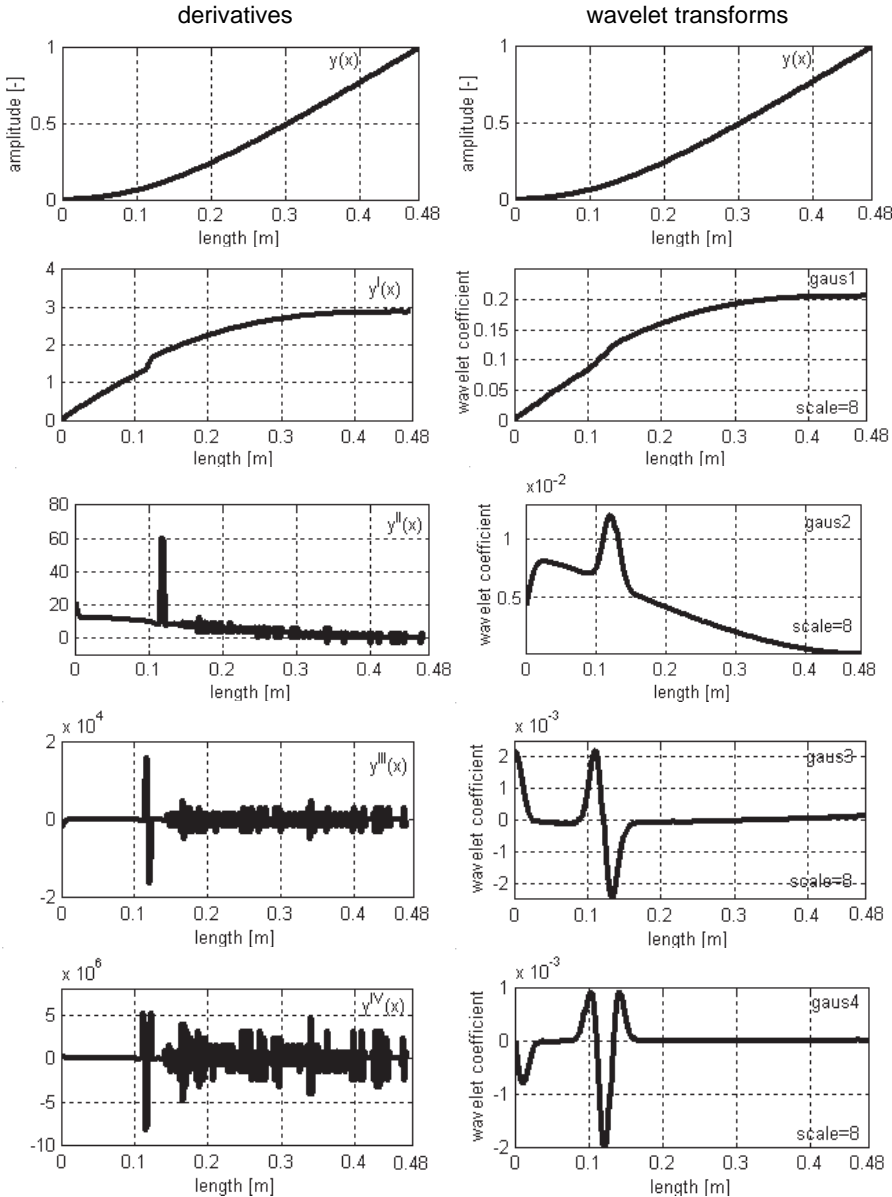


Fig. 4.9. Derivatives and wavelet transforms of the 1st mode shape of beam (after Rucka and Wilde 2007)

The comparison between the derivatives and the wavelet transforms acting on the mode shape cantilever beam with a crack is presented in Fig. 4.9. The left column shows the mode shape computed on FEM model (Rucka and Wilde 2007) and its numerically computed derivatives up to fifth order. The location of the crack is not visible directly on the mode shape. The first derivative indicates the defect location by a change of the curvature slope. However, the precise position of the defect can be obtained from the second derivative of the mode. Higher derivatives, despite very high computation precision, are contaminated with noise. The noise level in the fourth order derivative reaches the values of the peak corresponding to the crack.

The right column in Fig. 4.9 shows the mode shape and the wavelet transform coefficients computed by Gaussian wavelet with 1, 2, 3 and 4 vanishing moments. The wavelet coefficients from *gaus1* do not expose the damage position. However, the wavelet transforms from *gaus2*, *gaus3* and *gaus4* clearly indicate the location of the crack. The smoothing action of the wavelet, filters out the noise and the curves obtained by wavelet with higher number of vanishing moments are without the noise. Use of the wavelet transform instead of differentiation might provide the noise-free results even in the case of noisy data.

The comparison between the wavelets with two and four vanishing moments is given in Fig. 4.10 and Fig. 4.11. The wavelets with 2 vanishing moments have shorter support length than wavelets with 4 moments. Although there are no explicit formula relating the number of vanishing moments and the support size, there is the constrain imposed on the orthogonal wavelets stating that the wavelet with n vanishing moments has the support of at least $2n-1$ (Mallat, 1998). The wavelet coefficients computed by Gaussian wavelets with 3 and 4 vanishing moments are close to zero in the regions free from signal abnormalities.

After extensive numerical experimentations (Rucka 2005, Rucka and Wilde 2007) the Gaussian wavelet (*gaus4*) was chosen as the best wave form to damage detection with the one-dimensional continuous wavelet transform. For the structural responses that are similar to polynomial of higher order than 4, the use of wavelets with higher number of vanishing moments is necessary (*gaus6* or higher).

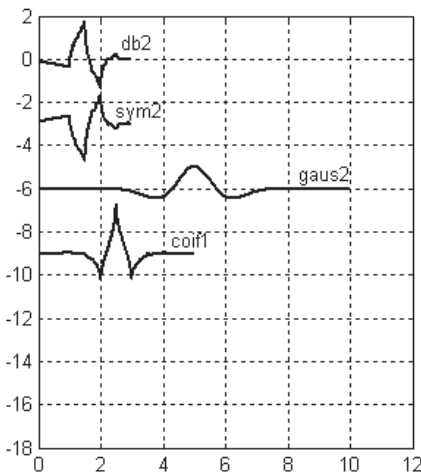


Fig. 4.10. Wavelets having two vanishing moments

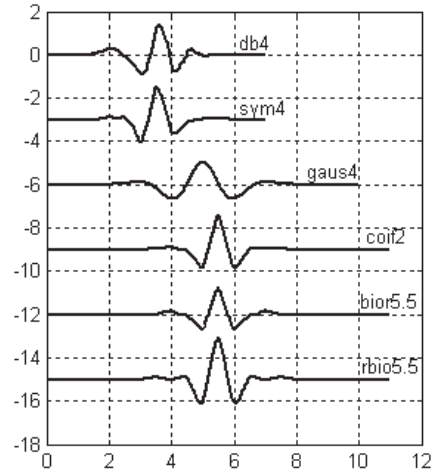


Fig. 4.11. Wavelets having four vanishing moments

For the two-dimensional cases the Reverse Biorthogonal wavelet (rbio5.5) with four vanishing moments (Rucka and Wilde 2007) was chosen as the best wavelet (Fig. 4.8). The Reverse Biorthogonal wavelet is symmetric and regular.

4.4. Wavelet damage detection in cantilever beam

The experimental setup and procedures of the cantilever beam impulse tests are given in section 3.1.2.1. The beam is presented in Fig. 3.7. The experimentally estimated mode shapes of the beam with the crack are given in Fig. 3.10.

The first and second mode shape of the beam are considered as input signals for Gaussian wavelets. The wavelets with 4 and 6 vanishing moments are considered. In case of the first mode, its shape can be well approximated by the polynomial of 4th order, and therefore, the Gaussian wavelet with 4 vanishing moments is used. The second mode shape has more complicated shape and wavelets with 4 and 6 moments are applied. The presented results are taken after Rucka and Wilde, 2007.

The results of the wavelet transforms on the first mode are given in Fig. 4.12. The numerical (Fig. 4.12a) and experimental (Fig. 4.12b) mode shapes are used for wavelet coefficient computations for scales $s = 1 \div 30$. The plot shows the modulus of the wavelet coefficients. In the case of the results on the numerical data, only one clear maximum is visible. The wavelet coefficient modulus grow with an increase of the scale and precisely indicates the crack position at a distance of 121 mm from the clamped end. Some additional peaks are visible in the region near to the clamped end. However, these perturbations are due to the numerical representation of the boundary conditions (Rucka and Wilde 2007).

Fig. 4.12b shows the modulus of the wavelet coefficients computed from the experimental data. The results have a large, in comparison to the numerical transforms, number of additional maxima lines. Nevertheless, the dominant maxima lines, corresponding to the crack positions, increase monotonically and for larger scales they achieve the largest values. The crack location can be easily recognised. The position of defects determined by the wavelet analysis is 132 mm. The relative error of the damage position prediction is 9.1%. Comparing to the numerical case, the wavelet technique on the experimental mode indicates the crack location for the scales above 40, whereas in the case of the numerical data the crack positions can be determined from the scale $s = 2$. Significantly different are the values of the wavelet coefficients for the numerical and experimental wavelet transforms.

The wavelet transform modulus of the second numerical mode shape for the gaus4 wavelet is presented in Fig. 4.13a. The results of the transform by gaus6 wavelet are given in Fig. 4.14a. In both cases the damage location is precisely indicated by the maxima line of the coefficient modulus. However, the wavelet with 6 vanishing moments has its maxima only in the damage region, while the gaus4 wavelet has relatively large maximum resulting from the effect of the boundary condition modelling. The maxima values of the transform calculated using the gaus4 are larger than the maximum value calculated using the gaus6 wavelet. Application of the wavelet with a higher number of vanishing moments results in decreasing of the maximum value of the wavelet transform. However, in this example only one crack is searched and the wavelet with a longer support can be used. The selection of the most appropriate wavelet must be decided individually for each problem.

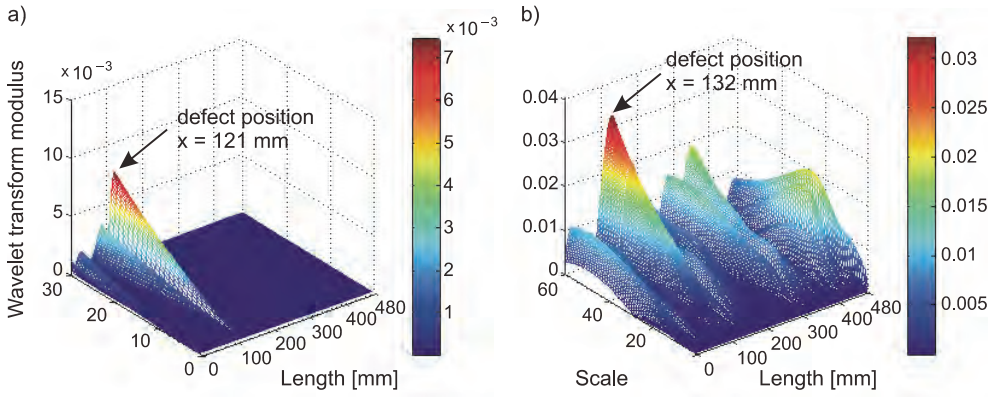


Fig. 4.12. Wavelet transform modulus of first mode shape using gauss4 wavelet: a) numerical; b) experimental

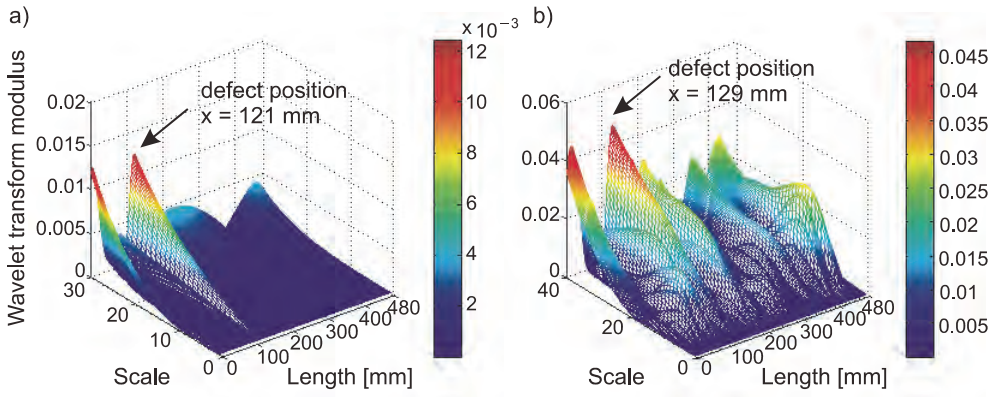


Fig. 4.13. Wavelet transform modulus of second mode shape using gauss4 wavelet: a) numerical; b) experimental

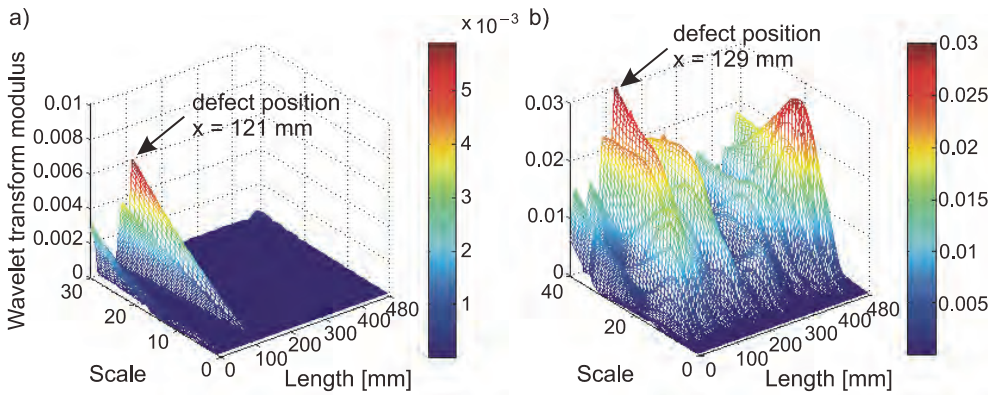


Fig. 4.14. Wavelet transform modulus of second mode shape using gauss6 wavelet: a) numerical; b) experimental

The results based on the experimental second mode shapes by Gaussian wavelet with 4 and 6 vanishing moments are given in Fig. 4.13b and Fig. 4.14b. It is visible that the wavelet coefficients contain noise. However, the detection of the cracks is possible. Both the gaus4 and gaus6 wavelets clearly indicate the defect position at the location of 129 mm. The largest relative error between the actual and predicted damage location is 6.6%. As in the case of the numerical case, in the experimental data the maximum value of the wavelet transform decreases with the increase of the number of vanishing moments. Thus, the use of a wavelet with a higher number of vanishing moments than essential might not be appropriate

4.5. Wavelet damage detection in steel plate

The description of the clamped steel plate and the rectangular flaw is given in section 3.1.2.2. The experimental setup is presented in Fig. 3.11 and the experimentally determined mode shapes of the plate, together with the numerical modes, are shown in Fig. 3.14.

The results of the wavelet transform of the plate fundamental mode shape are given in Fig. 4.15 and Fig. 4.16. The horizontal coefficients $W^1f(u, \nu, s)$, the vertical coefficients $W^2f(u, \nu, s)$ and the wavelet transform moduli $Mf(u, \nu, s)$ for the numerical and experimental data are presented. The wavelet coefficients are computed for scales from 1 to 60 but only the results for the scale $s = 40$ are shown. The rbio5.5 (Reverse Biorthogonal) has been chosen after extensive numerical analysis. The $W^1f(u, \nu, s)$ wavelet component indicates the signal abnormalities along the width of the plate, i.e., along the y coordinate while the $W^2f(u, \nu, s)$ component indicates the abnormalities along the length of the plate. The coefficient $W^1f(u, \nu, s)$ presented in the first row of Fig. 4.15 is computed for the two-dimensional approach and the coefficient lines along the y coordinate resemble the shape of the wavelet function $\psi(y)$. By analogy, the lines of the vertical coefficient along the x coordinate resemble the $\psi(x)$ function. The distribution of the horizontal and vertical coefficients in x and y directions is similar, which suggests that the shape of the flaw has similar dimensions in both directions. The third row of Fig. 4.15 presents the modulus of the 2D wavelet coefficients.

The modulus peaks computed on the numerical (Fig. 4.15) as well as the experimental data (Fig. 4.16) clearly indicate the defect position and its shape. In the case of the experimental data, the local maxima are larger than in the numerical data. However, the one peak corresponding to the flaw is clearly visible. The maximum of the modulus $Mf(u, \nu, s)$ based on the experimental data is in the distance of $x = 240$ mm and $y = 243$ mm from the left-down plate corner. The actual location of defect is $x = 240$ mm and $y = 240$ mm from the left-down plate corner. The position of the damage location is also correctly predicted by the wavelet transform determined on the numerical data.

The maximum value of the experimental wavelet transform modulus $Mf(u, \nu, s)$ is about four times larger than the corresponding numerical modulus.

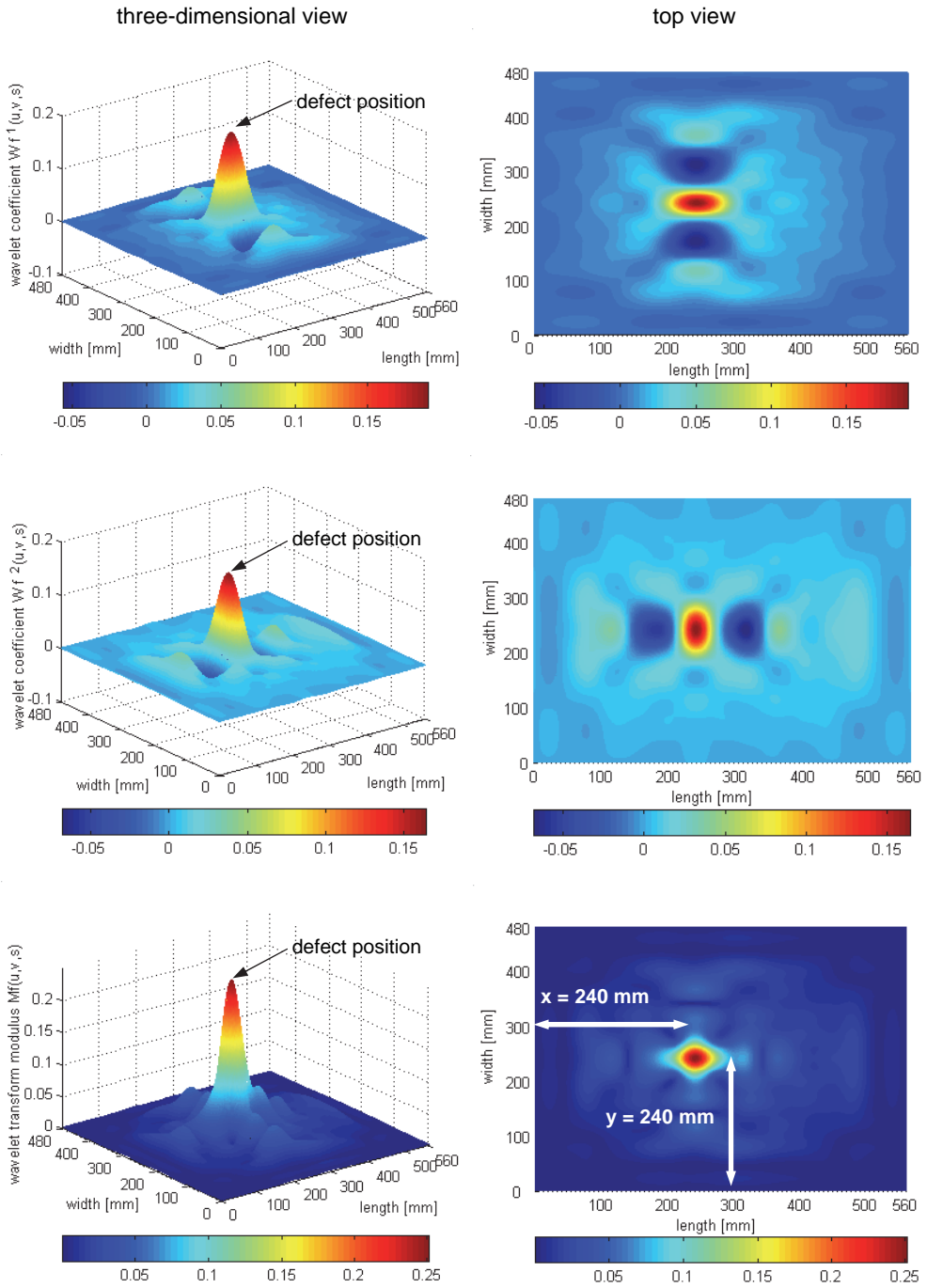


Fig. 4.15. Wavelet coefficients and wavelet transform modulus for the plate using rbio5.5 wavelet based on numerical data (after Rucka and Wilde 2007)

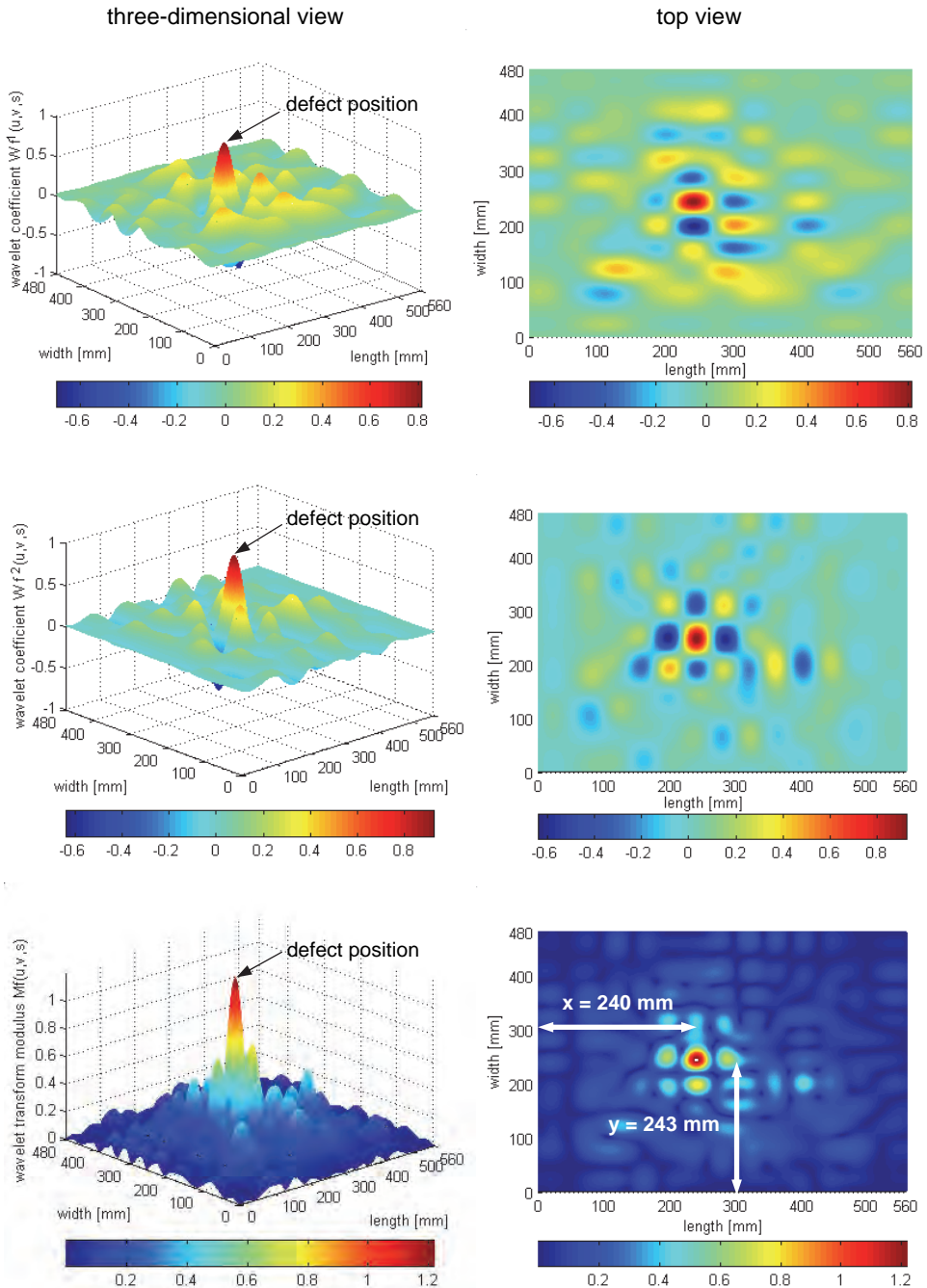


Fig. 4.16. Wavelet coefficients and wavelet transform modulus for the plate using $rbio5.5$ wavelet based on experimental data (after Rucka and Wilde 2007)

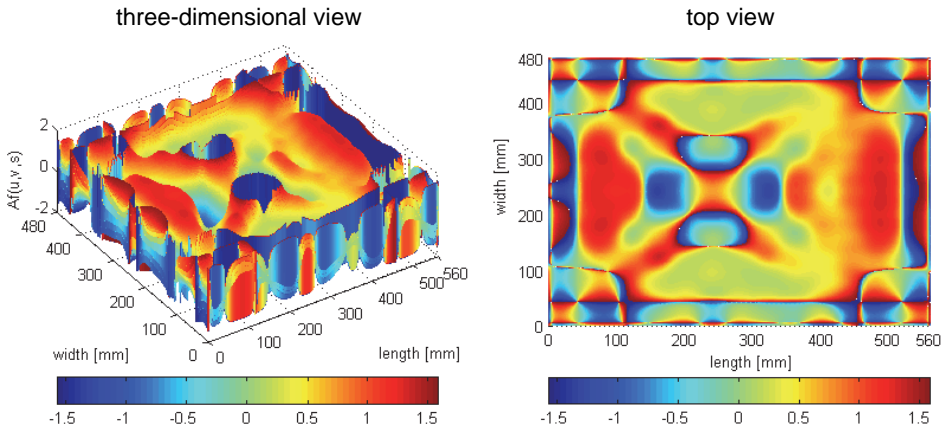


Fig. 4.17. Angle of the wavelet transform vector using rbio5.5 wavelet based on numerical data (after Rucka and Wilde 2007)

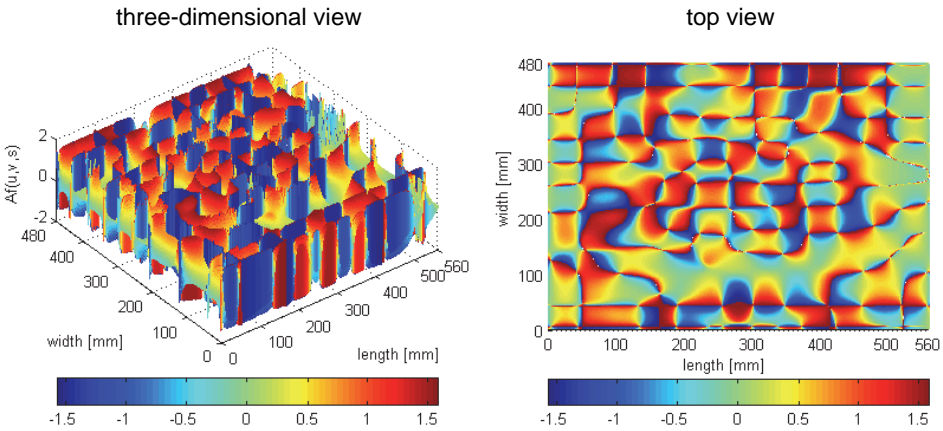


Fig. 4.18. Angle of the wavelet transform vector using rbio5.5 wavelet based on experimental data (after Rucka and Wilde 2007)

Theoretically, the defects can be located also from the analysis of the angle $Af(u, v, s)$. However, in the case of the experimental data the noise corrupts the information contained in the angle plot. The angle is computed as the ratio between the vertical and horizontal wavelet and is sensitive to the coefficient values of the wavelets. The coefficients $W^1 f(u, v, s)$ and $W^2 f(u, v, s)$ often change signs, and therefore, the angle of the gradient vector $\bar{\nabla}(f * \bar{\theta}_s)(x, y)$ quickly changes values (Fig. 4.18). The angles computed from the experimental mode shape do not indicate the damage location. The position of the flaw can be found on the top plot presented in Fig. 4.17. The angles computed for the numerical mode have visible peaks in the region of the damage. However, large peaks are also present near the boundaries of the plate. In the case of data obtained from the measurements the analysis of the angles $Af(u, v, s)$ might not be useful for damage detection purposes.

4.6. Wavelet damage detection in shell structures

As an example of the 3D object, the steel shell structure presented in section 3.1.2.3 is considered. Fig. 3.15 shows a photo of the shell mounted on a steel base frame. The shell structure consisted of steel base plate and the steel cylinder (Fig. 3.15) and has been described in section 3.1.2.3. The damage has the shape of short length crack induced by a high precision saw. The experimental mode shapes and numerical eigenvectors are given in Fig. 3.18. The modes were determined for one ring of points located in the middle of the cylinder.

The wavelet analysis is conducted by the Gaussian one-dimensional wavelets. The wavelets with 4, 6, 8 and 10 vanishing moments are used. The need to use higher order Gaussian wavelets results from a more complicated shape of the shell modes that cannot be modelled by polynomials of low order. The wavelet coefficients are computed for scales from 1 to 10.

In the beginning the study on the numerical mode shapes is conducted. The results of the wavelet coefficients computed from the first, second and third mode are given in Fig. 4.19, Fig. 4.20 and Fig. 4.21, respectively. The application of the Gaussian wavelet with 4, 6, 8 and 10 vanishing moments gives correct prediction of the damage detection in all considered modes. The position of the crack is found to be 288 mm from the measurement base. Some difficulties in selecting the correct modulus maxima line are encountered in the case of the third mode shape and analysis with the gaus4 wavelet. In this case the largest maxima of CWT correspond to the location near the clamped end. The maxima lines are, however, due to the problems with modelling the boundary conditions for the computation of the continuous wavelets. The value of modulus maximum decreases with increase of the number of vanishing moments so using the wavelet with the number of vanishing moments higher than a certain value characteristic for a given problem is not appropriate.

The results of the CWT by Gaussian wavelets with 4, 6, 8 and 10 vanishing moments on the experimental third mode are shown in Fig. 4.23. The damage location can be determined despite the presence of some additional maxima lines resulting from the measurement noise. The maxima lines corresponding to the crack location increase monotonically and for larger scales they achieve the largest values. The wavelet modulus computed by the gaus4 wavelet (Fig. 4.23a) provides the maximum line at 299 mm from the reference point, whereas the real location of the crack centre is 287.5 mm. The wavelet modulus computed by the use of the gaus6 points the damage location at 298 mm from the weld, and the wavelet modulus computed by both the gaus8 and gaus10 gives defect position at 297 mm from the start point. The relative errors between the location determined by wavelet analysis and actual ones varies from 3.3% to 4%. The figures presented in this section are after Rucka and Wilde, 2007.

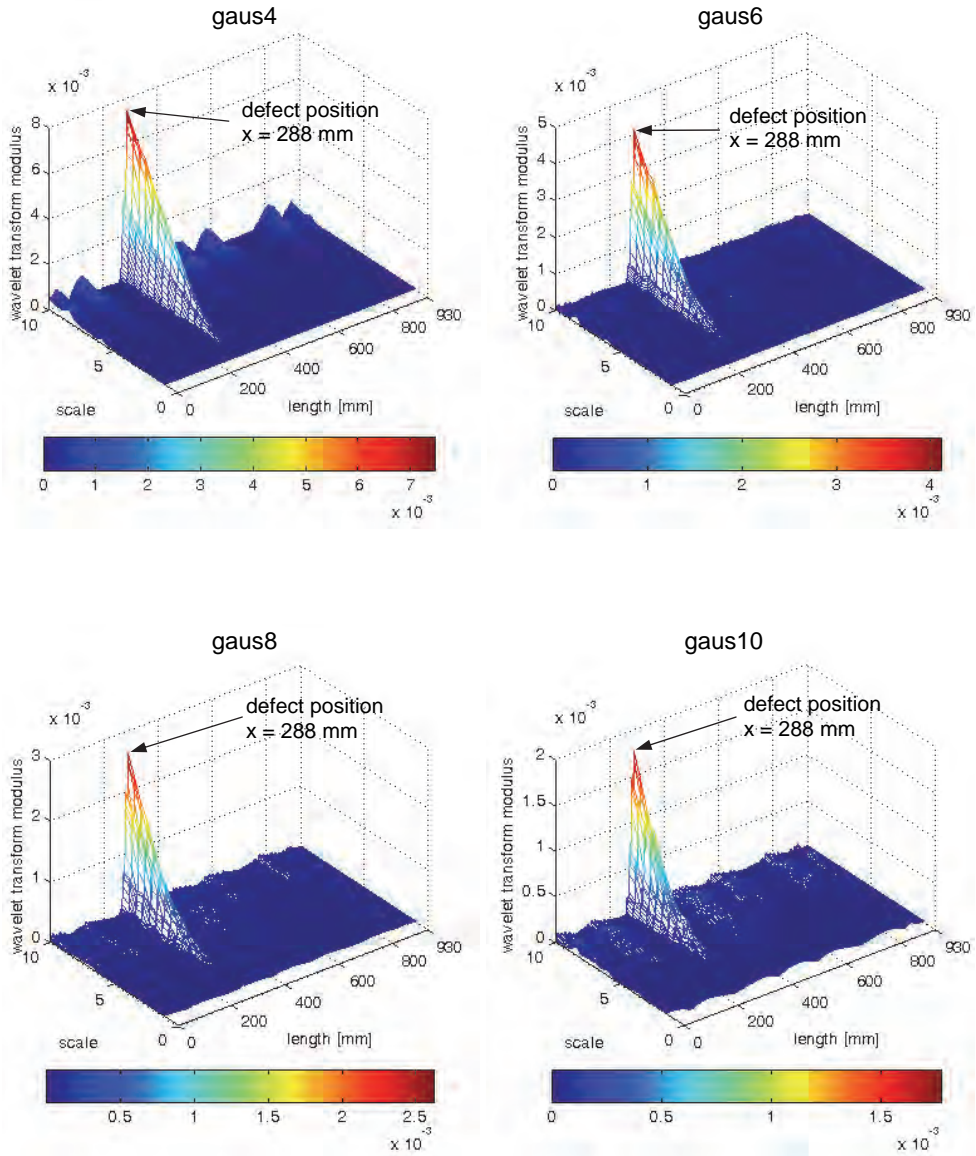


Fig. 4.19. Wavelet transform modulus of numerical first mode shape using Gaussian wavelet family

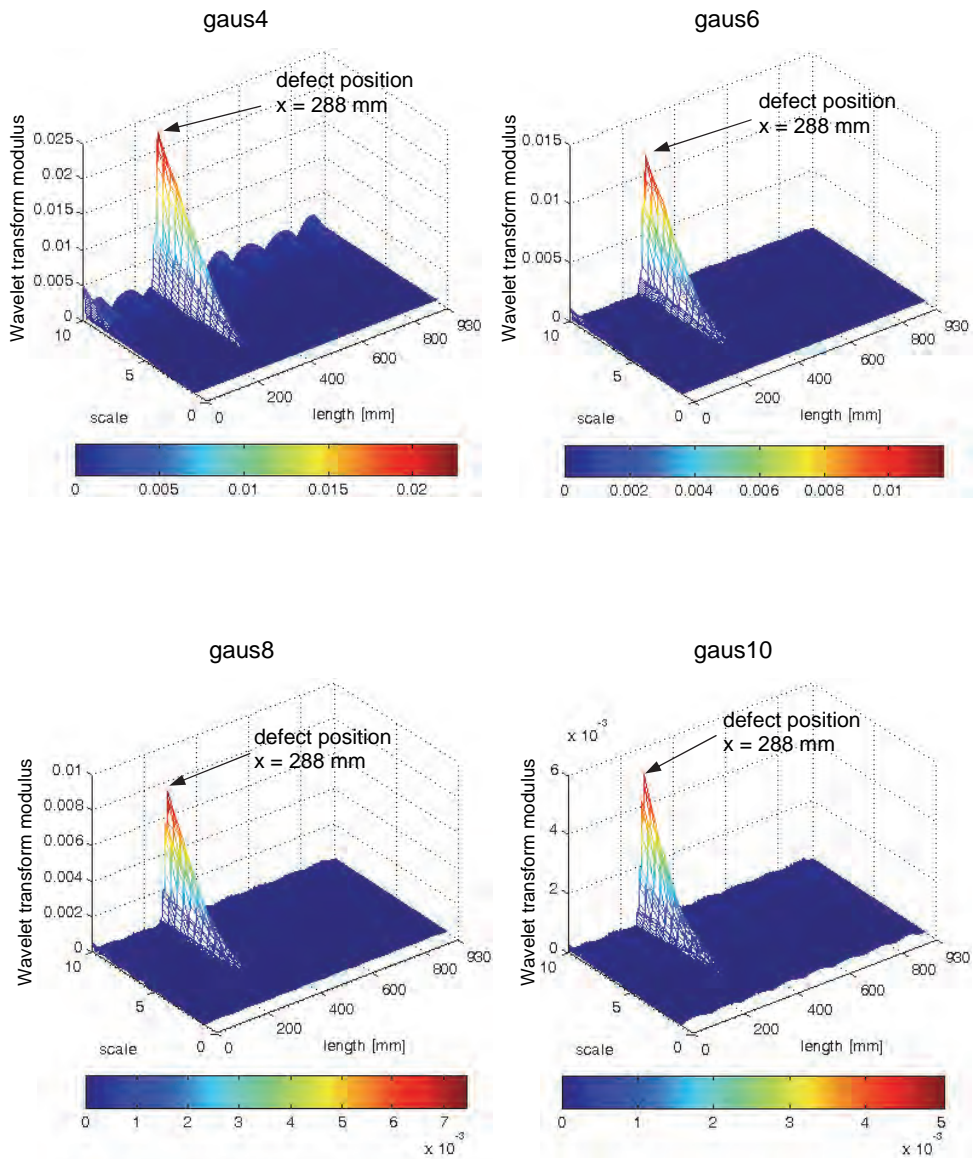


Fig. 4.20. Wavelet transform modulus of numerical second mode shape using Gaussian wavelet family

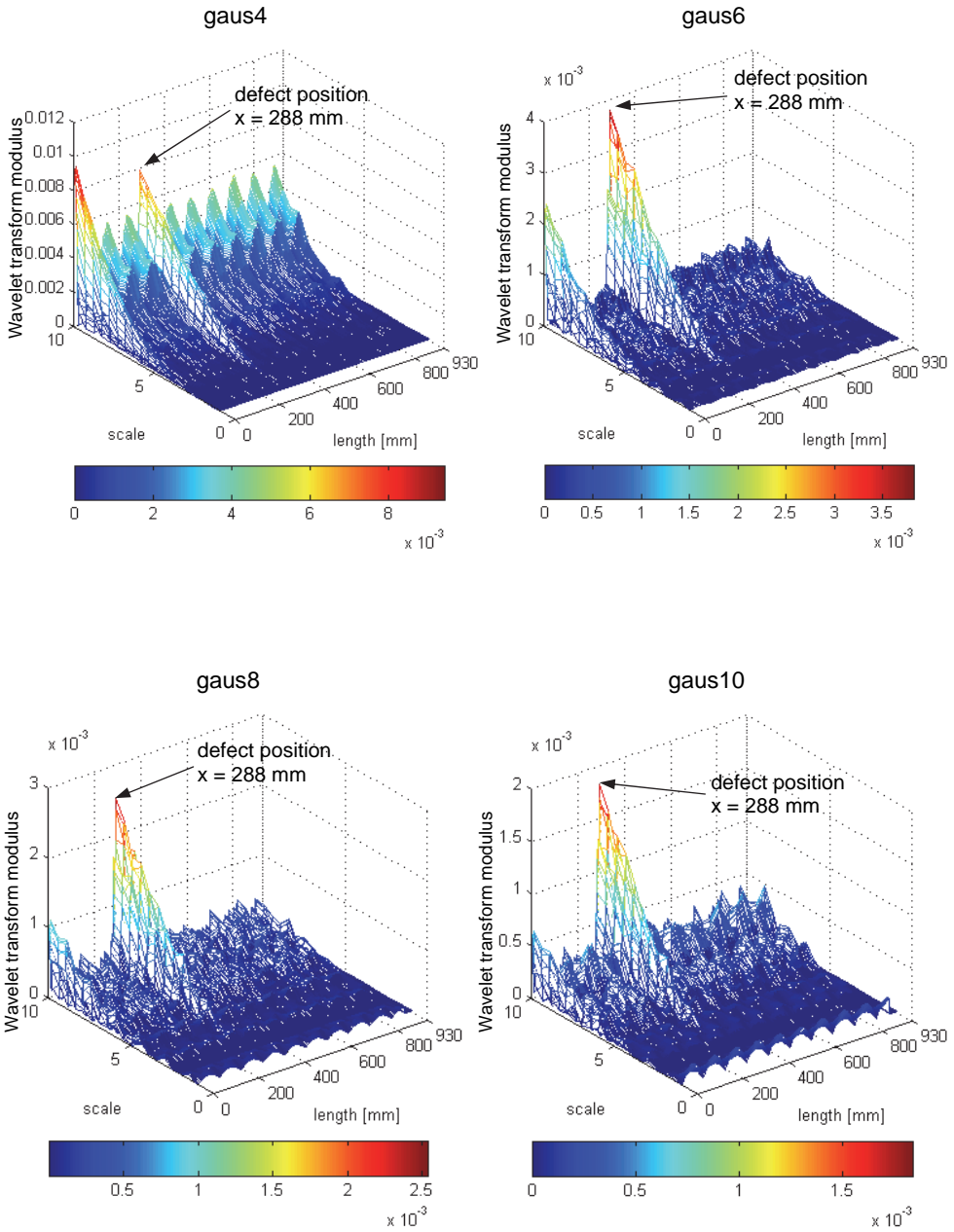


Fig. 4.21. Wavelet transform modulus of numerical third mode shape using Gaussian wavelet family

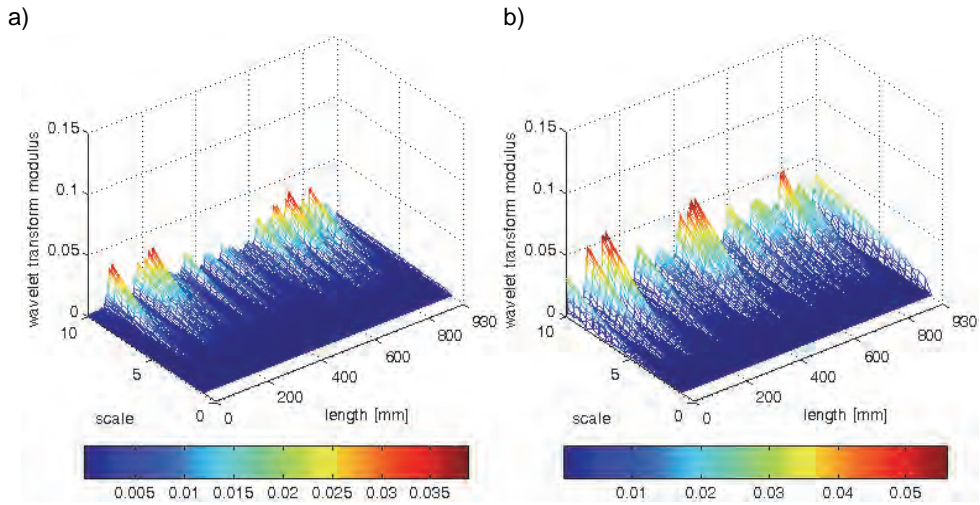


Fig. 4.22. Wavelet transform modulus of experimental mode shapes using gau6:
a) first mode shape; b) second mode shape

4.7. Conclusion

In this chapter the wavelet transforms are considered as differential operators and are applied for the analysis of the mode shape spatial signals. The damage location is determined by the largest peak of the wavelet coefficients. The differentiating action of the wavelets is governed by the number of vanishing moments. Comparison between the derivatives and wavelets shows that the number of vanishing moments corresponds to the order of the derivative. However, in the case of the wavelet transforms the smoothing action filters out the noise and low level signal abnormalities. The computation of derivatives on experimental signals results in large computational noise for higher order derivatives.

The conclusions from the conducted wavelet damage detection study on the experimental data of the beam, plate and shell structure can be stated as follows:

1. It is beneficial to use wavelets with number of vanishing moments at least 4.
2. The best effectiveness in damage detection has been obtained by Gaussian wavelet and Reverse Biorthogonal.
3. Use of modulus of wavelet coefficients is a good index for damage localization in case of one and two-dimensional problems. In case of 2D analysis the computation of the angle between the horizontal and vertical wavelet component is not effective due to sensitivity to noise.
4. The study on the beam showed that the wavelet analysis could locate the crack of the relative height larger than 30%. In general, the narrow crack do not influence the lower modes of the beam.
5. The wavelet analysis of the 3D shell structure showed that the damage detection is more effective on the third mode than on first and second. The method showed that relatively small defect (area 0.2% and wall thickness reduction of 30%) can be correctly localized.

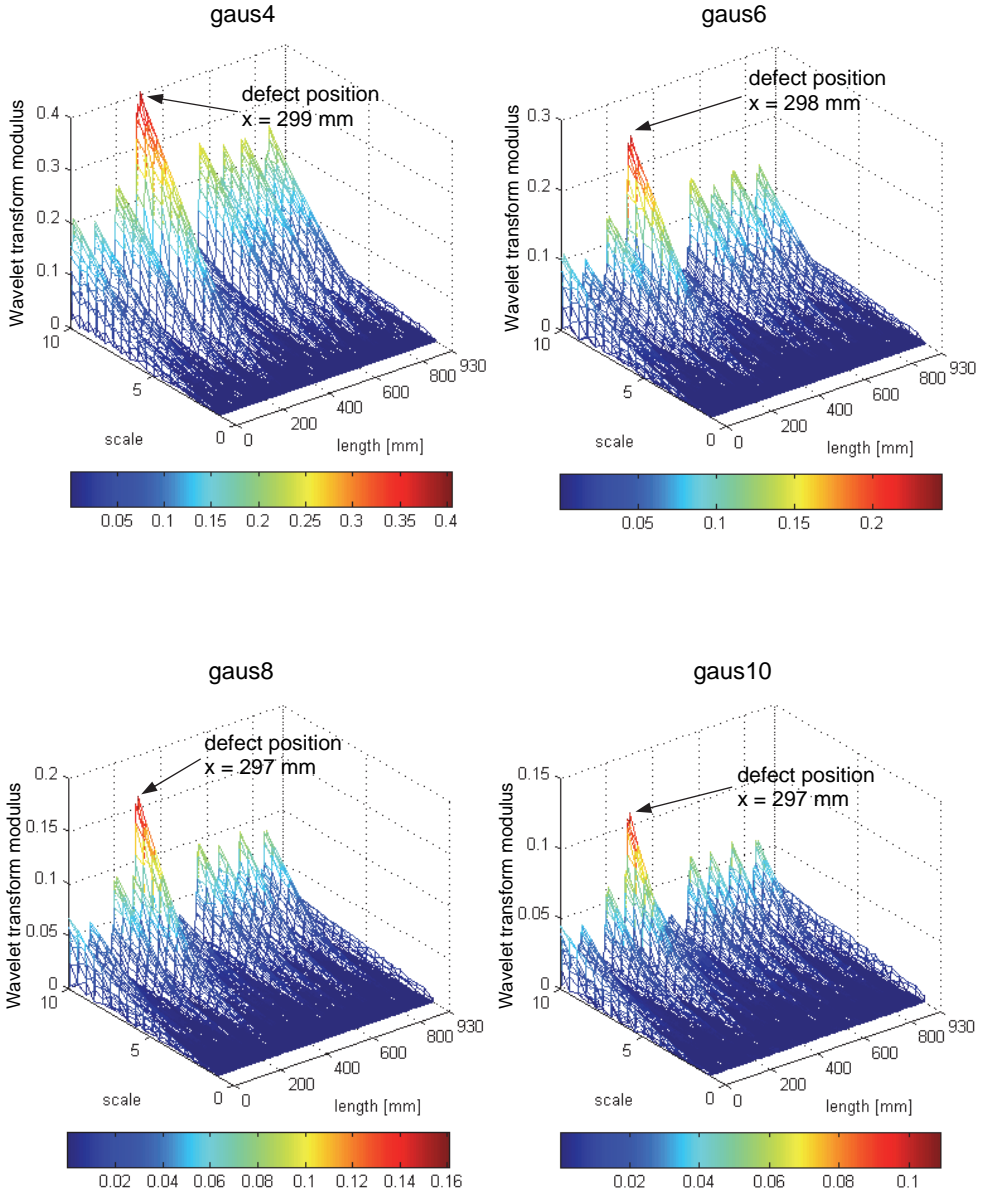


Fig. 4.23. Wavelet transform modulus of experimental third mode shape using Gaussian wavelet family

Mode shapes in FEM updating

The updating of the FE model on the in situ measurements provides detailed information on the location and the severity of the damage since the distribution of the parameters, like, stiffness is known. The FE updating that takes the advantage of the information stored in the experimental mode shapes is presented in this chapter. The properties and limitations of the updating method based on sensitivity matrix are considered.

The FE updating on natural frequencies is limited only to an introductory example. In all cases considered in this book, the parameter identification on the experimental natural frequencies could not provide satisfactory results. The FE updating on modal pairs, i.e., natural frequencies and corresponding mode shapes, is conducted in stages. The first studies, for each example, are conducted for the undamaged structure. Initially the parameters of the boundary conditions are determined by means of the global stiffness parameter. Then, the search for the stiffness or mass changes is analysed using the assumption of independent values of the selected parameters of each finite element. Finally, the new conditions or additional constraints are imposed to obtain the best FE model updating results.

5.1. Sensitivity of mode shapes

The derivation of sensitivity formula with respect to the eigenvectors has been shown by Maia and Silva (1998). If λ_{ai} and ϕ_{ai} are an analytical eigensolution of the eigenvalue problem in an undamped system, then they satisfy the equation:

$$[\mathbf{K} - \lambda_{ai}\mathbf{M}]\phi_{ai} = 0, \quad (5.1)$$

Where $i = 1, 2, \dots, N$ means the number of eigenvalues and eigenvectors.

The measured, obtained through the experimental dynamic tests, eigenpair λ_{mi} and ϕ_{mi} can be calculated using an analytical eigensolution, λ_{ai} and ϕ_{ai} , by a truncated Taylor series expansion in terms of the updating parameters

$$\phi_{mi} = \phi_{ai} + \sum_{j=1}^{N_p} \frac{\partial \phi_{ai}}{\partial \theta_j} \theta_j + \mathbf{O}(\theta_j^2), \quad (5.2)$$

where $\mathbf{O}(\theta_j^2)$ is the remainder of the Taylor series and $j = 1, 2, \dots, N_p$ means the number of unknown updating parameters θ_j .

Assuming that the required changes in the updating parameters are small, the experimental eigenvectors expansion can be linearised and limited to the first two terms:

$$\phi_{mi} = \phi_{ai} + \Delta\phi, \quad (5.3)$$

where

$$\Delta \boldsymbol{\phi} \approx \sum_{j=1}^{N_p} \frac{\partial \boldsymbol{\phi}_{ai}}{\partial \theta_j} \theta_j. \quad (5.4)$$

Partial derivative of the eigenvectors has been proposed by Fox and Kapoor (1968). As the eigenvectors are linearly independent, it is possible to state that their sensitivity with respect to θ_j can be expressed as a linear combination of the eigenvectors themselves:

$$\frac{\partial \boldsymbol{\phi}_{ai}}{\partial \theta_j} = \sum_{k=1}^N \varphi_{ik}^{(j)} \boldsymbol{\phi}_{ak}. \quad (5.5)$$

Although this expression is reasonable, in practice, the number of available modes is often limited and N is usually smaller than the number of the analytical mode shapes.

Differentiation of equation (5.1) yields the formula

$$\frac{\partial [\mathbf{K} - \lambda_{ai} \mathbf{M}]}{\partial \theta_j} \boldsymbol{\phi}_{ai} + [\mathbf{K} - \lambda_{ai} \mathbf{M}] \frac{\partial \boldsymbol{\phi}_{ai}}{\partial \theta_j} = \mathbf{0}, \quad (5.6)$$

which includes the eigenvalues and eigenvectors sensitivities. Unlike the eigenvalues sensitivity (Maia and Silva, 1998) equation (5.6) cannot be directly solved for eigenvectors sensitivity, since $[\mathbf{K} - \lambda_{ai} \mathbf{M}]$ is singular. Substitution of equation (5.5) into (5.6) gives,

$$\frac{\partial [\mathbf{K} - \lambda_{ai} \mathbf{M}]}{\partial \theta_j} \boldsymbol{\phi}_{ai} + [\mathbf{K} - \lambda_{ai} \mathbf{M}] \sum_{k=1}^N \varphi_{ik}^{(j)} \boldsymbol{\phi}_{ak} = \mathbf{0}, \quad (5.7)$$

or

$$\sum_{k=1}^N \varphi_{ik}^{(j)} [\mathbf{K} - \lambda_{ai} \mathbf{M}] \boldsymbol{\phi}_{ak} = - \frac{\partial [\mathbf{K} - \lambda_{ai} \mathbf{M}]}{\partial \theta_j} \boldsymbol{\phi}_{ai}. \quad (5.8)$$

Pre-multiplication of equation (5.8) by the mass normalized $\boldsymbol{\phi}_{as}^T$, on the assumption of $s \neq i$, leads to

$$\sum_{k=1}^N \varphi_{ik}^{(j)} \boldsymbol{\phi}_{as}^T [\mathbf{K} - \lambda_{ai} \mathbf{M}] \boldsymbol{\phi}_{ak} = - \boldsymbol{\phi}_{as}^T \frac{\partial [\mathbf{K} - \lambda_{ai} \mathbf{M}]}{\partial \theta_j} \boldsymbol{\phi}_{ai}. \quad (5.9)$$

Due to the orthogonality properties of the eigenvectors, the left hand side of equation (5.9) is equal to zero, except for $k = s$. Thus,

$$\varphi_{ik}^{(j)} (\lambda_{ak} - \lambda_{ai}) = - \boldsymbol{\phi}_{ak}^T \frac{\partial [\mathbf{K} - \lambda_{ai} \mathbf{M}]}{\partial \theta_j} \boldsymbol{\phi}_{ai} \quad k \neq i. \quad (5.10)$$

Evaluation of the right hand side of equation (5.10) gives,

$$\varphi_{ik}^{(j)} (\lambda_{ak} - \lambda_{ai}) = - \boldsymbol{\phi}_{ak}^T \frac{\partial \mathbf{K}}{\partial \theta_j} \boldsymbol{\phi}_{ai} + \frac{\partial \lambda_{ai}}{\partial \theta_j} \boldsymbol{\phi}_{ak}^T \mathbf{M} \boldsymbol{\phi}_{ai} + \lambda_{ai} \boldsymbol{\phi}_{ak}^T \frac{\partial \mathbf{M}}{\partial \theta_j} \boldsymbol{\phi}_{ai}. \quad (5.11)$$

Since $k \neq i$, the second term on the right hand side of equation (5.11) is zero so that,

$$\varphi_{ik}^{(j)} = \frac{1}{(\lambda_{ak} - \lambda_{ai})} \boldsymbol{\phi}_{ak}^T \left[\frac{\partial \mathbf{K}}{\partial \theta_j} - \lambda_{ai} \frac{\partial \mathbf{M}}{\partial \theta_j} \right] \boldsymbol{\phi}_{ai} \quad k \neq i. \quad (5.12)$$

For $k=i$ coefficients $\varphi_{ik}^{(j)}$ have to be calculated separately. Differentiating $\boldsymbol{\phi}_{ai}^T \mathbf{M} \boldsymbol{\phi}_{ai} = 1$ with respect to design parameters, yields

$$2\boldsymbol{\phi}_{ai}^T \mathbf{M} \frac{\partial \boldsymbol{\phi}_{ai}}{\partial \theta_j} = -\boldsymbol{\phi}_{ai}^T \frac{\partial \mathbf{M}}{\partial \theta_j} \boldsymbol{\phi}_{ai}. \quad (5.13)$$

Then, substitution of equation (5.5) into (5.13) gives,

$$2\boldsymbol{\phi}_{ai}^T \mathbf{M} \sum_{k=1}^N \varphi_{ik}^{(j)} \boldsymbol{\phi}_{ak} = -\boldsymbol{\phi}_{ai}^T \frac{\partial \mathbf{M}}{\partial \theta_j} \boldsymbol{\phi}_{ai} \quad (5.14)$$

or

$$2 \sum_{k=1}^N \varphi_{ik}^{(j)} \boldsymbol{\phi}_{ai}^T \mathbf{M} \boldsymbol{\phi}_{ak} = -\boldsymbol{\phi}_{ai}^T \frac{\partial \mathbf{M}}{\partial \theta_j} \boldsymbol{\phi}_{ai} \quad (5.15)$$

and due to the orthogonality properties,

$$\varphi_{ii}^{(j)} = -\frac{1}{2} \boldsymbol{\phi}_{ai}^T \frac{\partial \mathbf{M}}{\partial \theta_j} \boldsymbol{\phi}_{ai}. \quad (5.16)$$

Hence from equation (5.12) and (5.16) it can be written

$$\varphi_{ik}^{(j)} = \begin{cases} \frac{1}{(\lambda_{ak} - \lambda_{ai})} \boldsymbol{\phi}_{ak}^T \left[\frac{\partial \mathbf{K}}{\partial \theta_j} - \lambda_{ai} \frac{\partial \mathbf{M}}{\partial \theta_j} \right] \boldsymbol{\phi}_{ai}, & \text{for } k \neq i \\ -\frac{1}{2} \boldsymbol{\phi}_{ai}^T \frac{\partial \mathbf{M}}{\partial \theta_j} \boldsymbol{\phi}_{ai}, & \text{for } k = i. \end{cases} \quad (5.17)$$

Combination of equations (5.12) and (5.16) and substitution into (5.5), results in the final formula describing the partial derivative of the mode shape with respect to the design parameters,

$$\frac{\partial \boldsymbol{\phi}_{ai}}{\partial \theta_j} = \sum_{k=1, k \neq i}^N \frac{\boldsymbol{\phi}_{ak} \boldsymbol{\phi}_{ak}^T}{\lambda_{ai} - \lambda_{ak}} \left[\frac{\partial \mathbf{K}}{\partial \theta_j} - \lambda_{ai} \frac{\partial \mathbf{M}}{\partial \theta_j} \right] \boldsymbol{\phi}_{ai} - \frac{1}{2} \boldsymbol{\phi}_{ai} \boldsymbol{\phi}_{ai}^T \frac{\partial \mathbf{M}}{\partial \theta_j} \boldsymbol{\phi}_{ai}. \quad (5.18)$$

Finally the sensitivity matrix of the eigenvalues and eigenvectors can be written as

$$\mathbf{S}_{(N_c \times N_p)} = \begin{bmatrix} \frac{\partial \lambda_{a1}}{\partial \theta_1} & \dots & \frac{\partial \lambda_{a1}}{\partial \theta_{N_p}} \\ \frac{\partial \boldsymbol{\phi}_{a1}}{\partial \theta_1} & \dots & \frac{\partial \boldsymbol{\phi}_{a1}}{\partial \theta_{N_p}} \\ \vdots & & \vdots \\ \frac{\partial \lambda_{ap}}{\partial \theta_1} & \dots & \frac{\partial \lambda_{ap}}{\partial \theta_{N_p}} \\ \frac{\partial \boldsymbol{\phi}_{ap}}{\partial \theta_1} & \dots & \frac{\partial \boldsymbol{\phi}_{ap}}{\partial \theta_{N_p}} \end{bmatrix}, \quad (5.19)$$

where p is the number of modal pairs considered in the updating of the unknown parameters θ_j , and $N_c = p(N + 1)$.

When large discrepancies exist between the experimental and analytical models, the validity of the Taylor series truncations in equation (5.2) is undermined and the iterative computations are prone to divergence. The modification of equation (5.18) has been presented by Lin et al (1995).

This is achieved by using both analytical and experimental modal data in the formulation of the eigensensitivities (Maia and Silva, 1998). Equation (5.18) becomes

$$\frac{\partial \lambda_{ai}}{\partial \theta_j} = \phi_{ai}^T \frac{\partial \mathbf{K}}{\partial \theta_j} \phi_{mi} - \lambda_{mi} \phi_{ai}^T \frac{\partial \mathbf{M}}{\partial \theta_j} \phi_{mi}. \quad (5.20)$$

$$\frac{\partial \phi_{ai}}{\partial \theta_j} = \sum_{k=1; k \neq i}^N \frac{\phi_{ak} \phi_{ak}^T}{\lambda_{mi} - \lambda_{ak}} \left[\frac{\partial \mathbf{K}}{\partial \theta_j} - \lambda_{mi} \frac{\partial \mathbf{M}}{\partial \theta_j} \right] \phi_{mi} - \frac{1}{2} \phi_{ai} \phi_{ai}^T \frac{\partial \mathbf{M}}{\partial \theta_j} \phi_{mi}. \quad (5.21)$$

In equation (5.21) the sensitivities are calculated on the basis of both the experimental and analytical modes, and therefore, the procedure convergence is improved in the case of very large discrepancies between the modes. However, calculation of the experimental eigensensitivities requires measurements of the displacements (or accelerations) in every degree of freedom of the FE model, which is very difficult in the real structures.

5.2. Iterative methods using modal pairs

The computation of the updated design parameters needs to overcome several problems. The first obstacle is limitations on the possible measurement points. It is usually impossible to extract from the in situ signal recordings the number of modal pairs that might be treated in the numerical analysis. It is obvious that the number of experimental modal pairs identified with sufficient precision might be small and in many practical problems in civil engineering it is limited to a few first modes.

Theoretically it is possible to select the degrees of freedom of the numerical model at the same locations as the experimental degrees of freedom. However, if the FEM modeling is used the element degrees of freedom has, e.g., rotational degrees of freedom that are difficult to be measured on the real structure. In that case model reduction techniques can be used (Appendix B).

In many cases the mode shapes in the analytical and experimental tests, even though, have similar frequencies are, not related to the same mode. It is often observed on structures like long span bridges where many modes have natural frequencies of similar values. Mode shape pairing is easily solved using the modal assurance criteria (MAC) or normalized modal difference (NMD). Details on mode shapes validation criteria are given in Appendix D. If the MAC between an experimental and analytical mode is close to 1 and if the NMD is close to 0 then this pair of modes may be used in the updating algorithms. It happens that the measured and analytical mode shapes are in opposite phases (180° out of phase). In this case the experimental mode shape may be scaled to the analytical mode shape by multiplying it by the modal scale factor (MSF).

To start the derivation of the updating algorithm the vector of analytical natural frequencies and mode shapes are expressed as (Friswell and Mottershead 1995),

$$\mathbf{z}_a = [\lambda_{a1}, \boldsymbol{\phi}_{a1}^T, \lambda_{a2}, \boldsymbol{\phi}_{a2}^T, \dots, \lambda_{aN}, \boldsymbol{\phi}_{aN}^T]^T, \quad (5.22)$$

and the vector of measured modal pairs is

$$\mathbf{z}_m = [\lambda_{m1}, \boldsymbol{\phi}_{m1}^T, \lambda_{m2}, \boldsymbol{\phi}_{m2}^T, \dots, \lambda_{mN}, \boldsymbol{\phi}_{mN}^T]^T. \quad (5.23)$$

Since in the experimental derivation of modes, higher modes are usually obtained with larger errors, it is helpful to use a weighting matrix $\mathbf{W}_{\varepsilon\varepsilon}$. The weighting matrix $\mathbf{W}_{\varepsilon\varepsilon}$ is a positive definite and usually diagonal matrix. In practice the components of the weighting matrix are standard deviations of the measured natural frequencies and mode shapes. In the updating algorithm the perturbation in the unknown parameters can be expressed:

$$\delta\theta = [\mathbf{S}^T \mathbf{W}_{\varepsilon\varepsilon} \mathbf{S}]^{-1} \mathbf{S}^T \mathbf{W}_{\varepsilon\varepsilon} (\mathbf{z}_m - \mathbf{z}_{aj}), \quad (5.24)$$

and the updating parameters can be iteratively calculated as

$$\theta_{j+1} = \theta_j + [\mathbf{S}_j^T \mathbf{W}_{\varepsilon\varepsilon} \mathbf{S}_j]^{-1} \mathbf{S}_j^T \mathbf{W}_{\varepsilon\varepsilon} (\mathbf{z}_m - \mathbf{z}_{aj}). \quad (5.25)$$

Another type of weighting can be put in terms of matrix $\mathbf{W}_{\theta\theta}$ (Friswell and Mottershead 1995). This weighting matrix is used to put different weights on the parameters of significantly different nature, like, e.g., Young modulus, the height of the beam. The interactive algorithm with this type of weighting becomes,

$$\delta\theta = \mathbf{W}_{\theta\theta}^{-1} \mathbf{S}^T [\mathbf{S} \mathbf{W}_{\theta\theta}^{-1} \mathbf{S}^T]^{-1} (\mathbf{z}_m - \mathbf{z}_{aj}), \quad (5.26)$$

or in full,

$$\theta_{j+1} = \theta_j + \mathbf{W}_{\theta\theta}^{-1} \mathbf{S}_j^T [\mathbf{S}_j \mathbf{W}_{\theta\theta}^{-1} \mathbf{S}_j^T]^{-1} (\mathbf{z}_m - \mathbf{z}_{aj}). \quad (5.27)$$

The weighting matrix $\mathbf{W}_{\theta\theta}$ is usually a diagonal matrix with the reciprocals of the estimated variances of the corresponding parameters as the diagonal elements. The use of this weighting matrix does not limit the absolute parameter change over many iterations (Friswell and Mottershead 1995).

The perturbation of parameters $\delta\theta$ can also be obtained by minimizing the penalty function with respect to the change in parameters $\delta\theta$:

$$J(\delta\theta) = \varepsilon^T \mathbf{W}_{\varepsilon\varepsilon} \varepsilon + \delta\theta^T \mathbf{W}_{\theta\theta} \delta\theta. \quad (5.28)$$

Substitution of $\varepsilon = \delta\mathbf{z} - \mathbf{S}\delta\theta$ into equation (5.28) and collection of the terms together gives the following formula

$$J(\delta\theta) = \delta\mathbf{z}^T \mathbf{W}_{\varepsilon\varepsilon} \delta\mathbf{z} - 2\delta\theta^T \mathbf{S}^T \mathbf{W}_{\varepsilon\varepsilon} \delta\mathbf{z} + \delta\theta^T [\mathbf{S}^T \mathbf{W}_{\varepsilon\varepsilon} \mathbf{S} + \mathbf{W}_{\theta\theta}] \delta\theta. \quad (5.29)$$

Equation (5.29) contains two weighting matrices, $\mathbf{W}_{\varepsilon\varepsilon}$ and $\mathbf{W}_{\theta\theta}$. Minimization of equation (5.29) with respect to $\delta\theta$ gives changes in parameters as

$$\delta\theta = [\mathbf{S}^T \mathbf{W}_{\varepsilon\varepsilon} \mathbf{S} + \mathbf{W}_{\theta\theta}]^{-1} \mathbf{S}^T \mathbf{W}_{\varepsilon\varepsilon} \delta\mathbf{z}, \quad (5.30)$$

or in terms of the iteration formula

$$\theta_{j+1} = \theta_j + \left[\mathbf{S}_j^T \mathbf{W}_{\varepsilon\varepsilon} \mathbf{S}_j + \mathbf{W}_{\theta\theta} \right]^{-1} \mathbf{S}_j^T \mathbf{W}_{\varepsilon\varepsilon} (\mathbf{z}_m - \mathbf{z}_{aj}). \quad (5.31)$$

Equation (5.30) and (5.31) may be more effective if the weight is given to the initial parameter estimates (Link 1993, Flores-Santiago and Link 1993). The change of parameter from the initial estimated value is more accurate than the parameter change at every iteration. Thus, the new expression is given by

$$\begin{aligned} J(\delta\theta) &= \varepsilon^T \mathbf{W}_{\varepsilon\varepsilon} \varepsilon + \{\theta - \theta_0\}^T \mathbf{W}_{\theta\theta} \{\theta - \theta_0\} \\ &= \varepsilon^T \mathbf{W}_{\varepsilon\varepsilon} \varepsilon + \left\{ \delta\theta + \{\theta_j - \theta_0\} \right\}^T \mathbf{W}_{\theta\theta} \left\{ \delta\theta + \{\theta_j - \theta_0\} \right\} \end{aligned} \quad (5.32)$$

where θ_0 is the initial parameter estimate. Substitution of $\varepsilon = \delta\mathbf{z} - \mathbf{S}\delta\theta$ into the first term of equation (5.32) and expansion of the second term gives the following

$$\begin{aligned} J(\delta\theta) &= \delta\mathbf{z}^T \mathbf{W}_{\varepsilon\varepsilon} \delta\mathbf{z} + \{\theta_j - \theta_0\}^T \mathbf{W}_{\theta\theta} \{\theta_j - \theta_0\} \\ &\quad - 2\delta\theta^T \left\{ \mathbf{S}^T \mathbf{W}_{\varepsilon\varepsilon} \delta\mathbf{z} - \mathbf{W}_{\theta\theta} \{\theta_j - \theta_0\} \right\} + \delta\theta^T \left[\mathbf{S}^T \mathbf{W}_{\varepsilon\varepsilon} \mathbf{S} + \mathbf{W}_{\theta\theta} \right] \delta\theta. \end{aligned} \quad (5.33)$$

Minimization of the penalty function (5.33) with respect to the parameters gives the change of parameters as

$$\delta\theta = \left[\mathbf{S}^T \mathbf{W}_{\varepsilon\varepsilon} \mathbf{S} + \mathbf{W}_{\theta\theta} \right]^{-1} \left\{ \mathbf{S}^T \mathbf{W}_{\varepsilon\varepsilon} \delta\mathbf{z} - \mathbf{W}_{\theta\theta} \{\theta_j - \theta_0\} \right\}. \quad (5.34)$$

Finally, the formula for the iterative search of the design parameters based on the changes in the natural frequencies and mode shapes becomes (Friswell and Mottershead 1995)

$$\theta_{j+1} = \theta_j + \left[\mathbf{S}_j^T \mathbf{W}_{\varepsilon\varepsilon} \mathbf{S}_j + \mathbf{W}_{\theta\theta} \right]^{-1} \left\{ \mathbf{S}_j^T \mathbf{W}_{\varepsilon\varepsilon} (\mathbf{z}_m - \mathbf{z}_{aj}) - \mathbf{W}_{\theta\theta} \{\theta_j - \theta_0\} \right\}. \quad (5.35)$$

The update of the design parameters θ_{j+1} is determined on the previous step parameters θ_j altered by the term consisting of the sensitivity matrices and weighting matrices, and is based on the difference between the experimental and analytical modal pairs as well as error between the initial and actual design parameters.

5.3. FE model updating of the cantilever beam

In this section three methods of the FE model updating of the cantilever beam are discussed. It should be noted that the computations are conducted for the modal data obtained through the experimental dynamic tests. The first method is performed for the undamaged beam and assumes that the stiffness of all finite elements is the same and that the experimental support can be modeled by a vertical and torsional spring. The second method, conducted for beam with and without the damage, independently updates the stiffness of each finite element and the third method is conducted using the proposed sequential updating procedure. The selected results, given in this section, are after Hirsz 2008.

5.3.1. Experimental procedures and measurement results

The experimental setup is shown in Fig. 3.7. However, in this case the cantilever beam has a length of 500 mm. The data on the beam material properties and the data acquisition system are described in section 3.1.2.1. The damaged beam consists of one imperfection of length $L_r = 20$ mm and height $a = 2$ mm, located at distance $L_I = 170$ mm from the clamped end. For the FE model updating purpose the impact loading was placed at 25 equally spaced points on the upper surface of the beam. the location of the points is given in Fig. 5.1. The measurement at one impulse location was repeated five times and the experimental mode shapes were determined through the H_2 estimator (chapter 3).

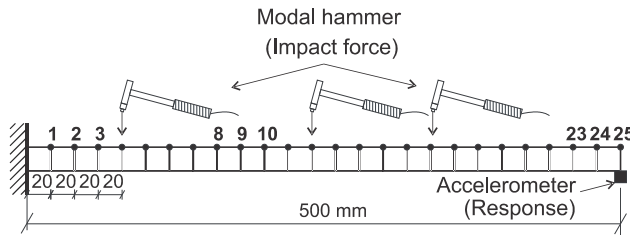


Fig. 5.1. Locations of impulse loads on the cantilever beam

An example of the time histories of the impulse force with the beam tip response is given in Fig. 5.2. The maximum amplitude of the impulse force is reaching up to 127 N. The maximum acceleration of the beam is 312 m/s^2 .

The magnitude of the Fourier transforms of the time responses is shown in Fig. 5.3. The Fourier spectrum of the impulse force is gradually decreasing over the considered frequency range and its magnitude at frequency 1000 Hz is 0.072. Therefore, the applied impulse could effectively excite the frequencies up to 1000 Hz. Four peaks, visible in Fig. 5.3, corresponds to four natural frequencies of the beam. The measured modal frequencies are: 22.50, 149.35, 425.30 and 807.1 Hz.

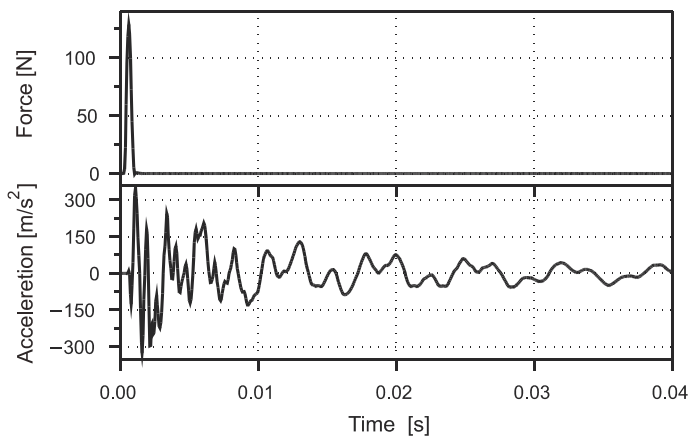


Fig. 5.2. Impact force and beam response in time domain

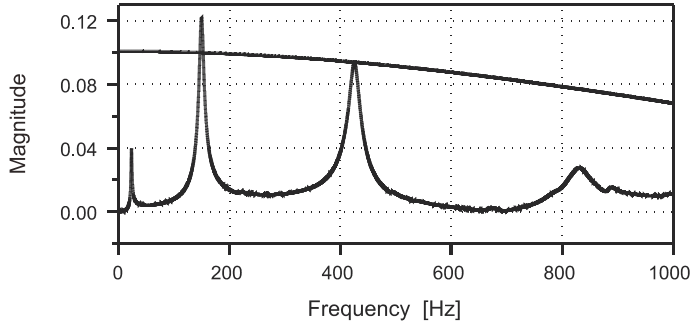


Fig. 5.3. Impact force and response in frequency domain

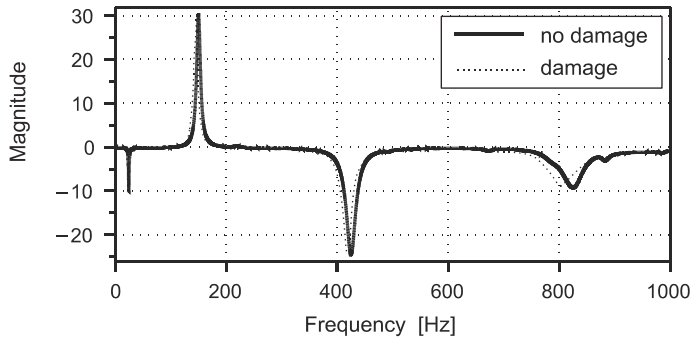


Fig. 5.4. Frequency response function from point 10 to 25

Fig. 5.4 depicts the accelerance FRF obtained from the measurement at point 25 and the impulse placed at point 10 (Fig. 5.1). The FRF has four peaks at the modal frequencies. The no damage case is denoted by solid line, while the FRF for the damaged beam is plotted by a dotted line. The presence of the crack lowers the beam stiffness and lowers the natural frequencies of the beam. It is particularly visible for higher modal frequencies.

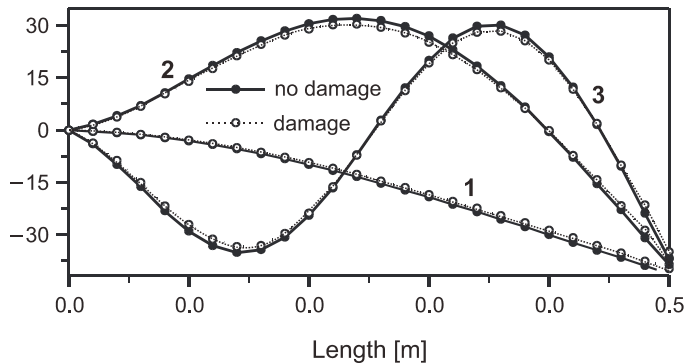


Fig. 5.5. Experimental mode shapes

The extraction of the experimental mode shapes is conducted via an analysis of the imaginary part of the beam FRF (section 2.2). The first free experimentally determined

beam mode shapes for the undamaged and damaged case are presented in Fig. 5.5. Generally speaking, the presence of the crack does not significantly affect the mode shapes if the crack depth is small with respect to the beam height.

There are no visible differences between the undamaged and damaged mode shapes. The position of the crack cannot be determined by visual examination of the extracted mode shape. It seems that the mode shapes do not have the zero derivative at the support, and thus, most likely the experimental support allows some small rotation and possibly translation at the point of the support.

5.3.2. Finite element model of the cantilever beam

The FE cantilever beam model consists of ten Bernoulli beam elements and has 22 degrees of freedom (Fig. 5.6). The details on the FE model matrices are given in Appendix A. The model has been reduced to 10 translational degrees of freedom by eliminating angles of rotations by SEREP method (Appendix B). The support system is modelled by a vertical and rotational springs denoted as k_r , k_t , respectively. The computed from FEM model eigenfrequencies of the undamaged beam are presented in Table 5.1 together with the corresponding experimental values. The initial values used for the simulations are given in Table 5.1. The numerical modal frequencies are lower than the experimental ones. The relative error of the third natural frequency is 16.5%. The numerical and experimental three modes of the beam are plotted in Fig. 5.7. Generally speaking, the agreement between the numerical and experimental results is very good. Some discrepancies are visible in the middle part of the first and second mode.

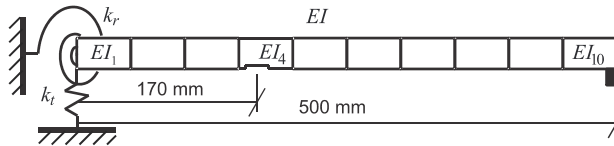


Fig. 5.6. Model of the cantilever beam with imperfection

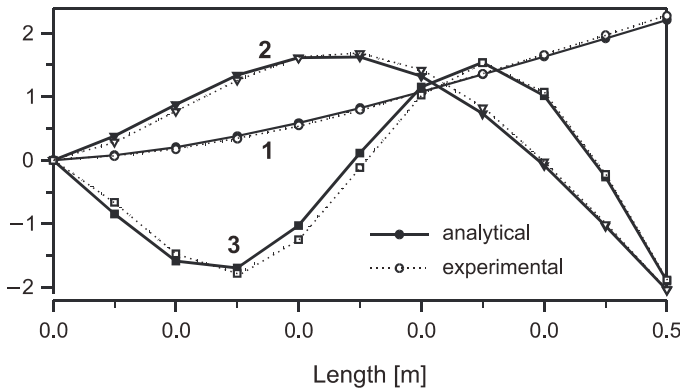


Fig. 5.7. Analytical and experimental mode shapes before updating

Table 5.1

Analytical and experimental values

Initial values		FEM solution		Measured values	
				No imperfe.	Imperfe.
EI	132 Nm ²	f_1	20.07	23.12	22.501
k_t	5.00×10 ⁷ Nm ⁻¹	f_2	126.38	149.35	146.540
k_r	2.00×10 ⁴ Nm rad ⁻¹	f_3	355.00	425.30	416.600
		f_4	697.40	826.40	807.100

The search for the best FE model to represent the experimental data is limited to the optimal selection of stiffness of the finite elements and the support system. In the case of the damaged beam modeled by 10 finite elements the area of the imperfection is within the 4th element. Thus, the stiffness EI_4 of the damaged structure should be smaller than the stiffness of other elements.

5.3.3. Updating of the global stiffness and support parameters

The FE updating of the undamaged beam is preformed by iterative procedure (5.35) only on the natural frequencies, i.e., by neglecting the presence of the mode shapes in equation (5.20). The weighting matrices are considered as unity matrices, and thus, none of the element stiffness is exposed over the others in the simulations. The design parameters are selected as: global stiffness, EI , translational spring stiffness, k_t , and torsional spring for modeling the support rotation, k_r . The results of the FE updating with the corresponding eigenvalues are presented in Table 5.2. In the first column the numbers from 1 to 4 refer to the number of the natural frequencies used in the updating algorithm. The stiffness of the beam is significantly larger than the assumed initial value (Table 5.1) and varies from 178 to 219 Nm². The updated value of the vertical supporting spring is very large and does not depend on number of frequencies taken in the updating. The large value of the supporting spring indicates that the beam support is relatively rigid. The updated values of the rotational spring provides the best fit for experimental modal frequencies in the case of first and second frequency used in the updating procedure (second row of Table 5.2).

The convergence of the frequencies versus the iteration number for the updating on first modal frequency is plotted in Fig. 5.8. The first frequency reaches the target value after the first iteration. However, the remaining updated frequencies are computed with significant errors and the discrepancies are kept constant with an increase of the iteration number. The convergence of FE updating on first two natural frequencies (Fig. 5.9) shows good fit of all considered beam frequencies. The values of the support system determined for this section are used in the following simulations. The value of the global stiffness is used as an initial condition for the FE updating methods within section 5.3. The updating on only a few natural frequencies is simple and provides fast convergence, and therefore, is suitable for the selection of the starting values for some more complex algorithms.

Table 5.2

Results of the updating of global stiffness and boundary conditions

No.	Updated parameters			Calculated eigenvalues			
	EI [Nm ²]	k_t [Nm ⁻¹]	k_r [Nm rad ⁻¹]	f_1 [Hz]	f_2 [Hz]	f_3 [Hz]	f_4 [Hz]
1	178	5×10^7	20000	23.12	145.68	409.3	803.9
2	219	5×10^7	5491	23.13	149.35	426.4	847.7
3	215	5×10^7	6175	23.23	149.35	425.3	844.1
4	186	5×10^7	29097	23.83	150.03	421.2	826.5

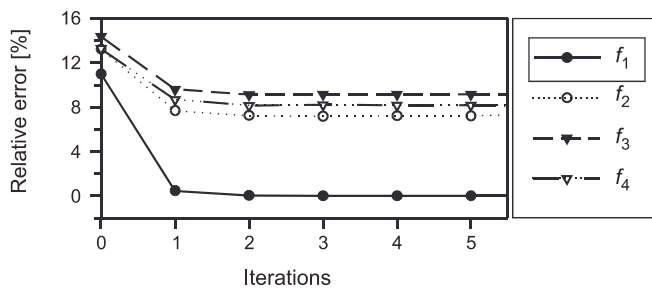


Fig. 5.8. Convergence of eigenfrequencies (the 1st natural frequency is used in the updating algorithm)

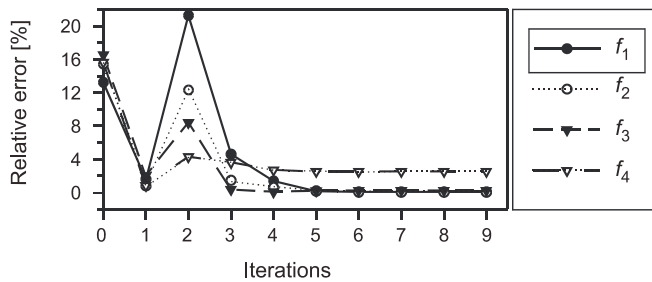


Fig. 5.9. Convergence of eigenfrequencies (the 1st and 2nd natural frequency are used in the updating algorithm)

5.3.4. Search for each element stiffness on natural frequencies

The parameters EI , k_t and k_r determined in the previous section are used as the initial values for simulations to follow. The stiffness of each element is computed for the beam with and without a crack. The weighting matrices are identity matrices. The updating is computed for four combinations of the experimental modal frequencies. The relative change of stiffness between the beam with crack and the stiffness of the undamaged beam indicates the damage i.e., the zero error means no change in the stiffness and non zero error points out the stiffness variation and its location. The FE updating results based on combinations

of 4 eigenfrequencies are given in Fig. 5.10. Although, the method provides very good fit to the experimental frequencies and mode shapes, the procedure does not indicate the location of the damage. Moreover, the damage is imposed in the 4th element and in the case of the FE updating on all four natural frequencies (Fig. 5.10d) the relative change of stiffness is almost zero proving no damage.

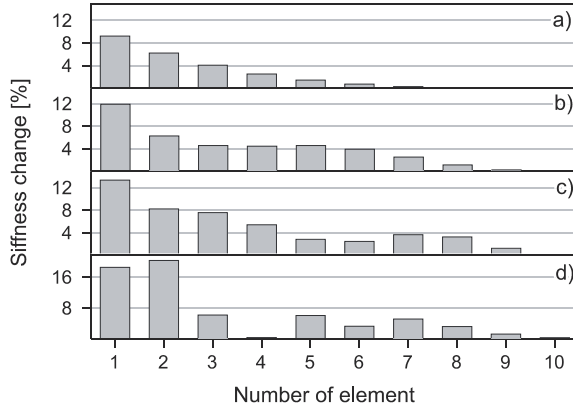


Fig. 5.10. Relative change in elements' stiffness for: a) the 1st natural frequency used in the updating algorithm, b) 1st and 2nd, c) 1st, 2nd and 3rd, d) 1st, 2nd, 3rd and 4th

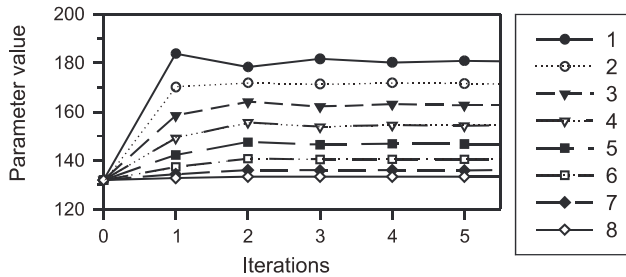


Fig. 5.11. Convergence of stiffness for the 1st natural frequency used in the updating algorithm

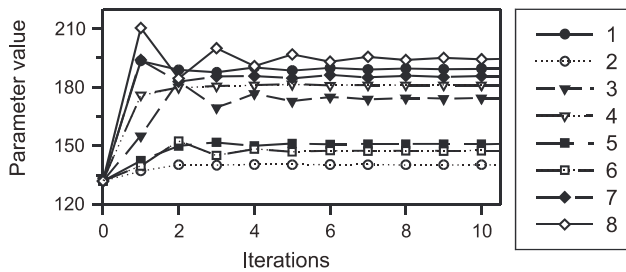


Fig. 5.12. Convergence of stiffness for the first four natural frequencies used in the updating algorithm

The convergence of the stiffness parameters for updating on 1st modal pair is given in Fig. 5.11. The elements stiffness is not updated since only one element stiffness should have smaller value (due to presence of the crack). It is noted that after the first iteration the errors in the parameter identification are kept constant. Fig. 5.12 shows a convergence computed on four natural frequencies. In this case the updated values of the parameters are also incorrect.

5.3.5. Sequential search of each element stiffness on modal pairs

The third method is based on FE updating on modal pairs. The sensitivity matrix is computed according to the formulas (5.19), (5.20) and (5.21). The updating algorithm is defined in equation (5.35). A new modification of the updating method is proposed. Each parameter is iteratively searched independently from each other, i.e., the value in the weighting matrices corresponding to the particular parameter is chosen so that the procedure, in fact, tries to fit only one element stiffness in to the experimental data. Then, the iterative procedure is repeated for the next design parameters. Using this method the computational time is considerably increased but the possibility of location of the damaged element is gained. This method will be referred to as sequential updating algorithm.

The results of the updating by the use of the sequential updating algorithm based on the first experimental modal pair (natural frequency and mode shape), first and second, as well as first, second and third are shown in Fig. 5.13. The relative changes in the elements' stiffness for updating conducted on two and three eigen pairs are the biggest for the 4th element and they correctly indicate the location of the damage. Nevertheless, the results show the relative changes of stiffness also in the elements that are not damaged.

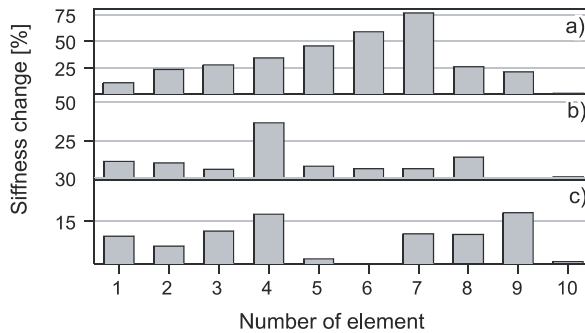


Fig. 5.13. Relative change in element's stiffness for: a) the 1st eigen pair used in the updating algorithm, b) 1st and 2nd, c) 1st, 2nd and 3rd

Fig. 5.14 shows the normalized modal difference criterion (NMD) values for the damaged beam between the numerical and experimental mode shapes. The description of the NMD modal validation criteria is given in Appendix D. The values of the NMD are calculated during updating of the stiffness of the individual element. In the presented case the agreement between the numerical and the experimental results is very good and the NMD values slightly exceed 2%.

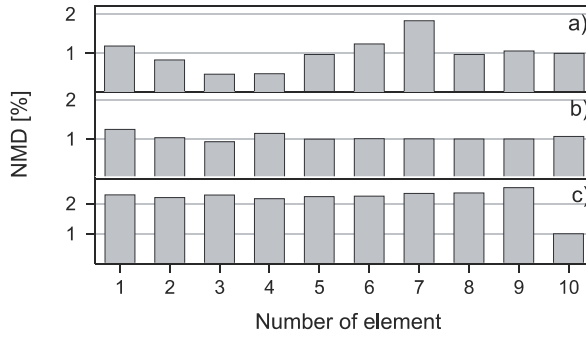


Fig. 5.14. Normalised modal difference (NMD): a) the 1st modal pair is used in the updating algorithm and similarly b) 1st and 2nd, c) 1st, 2nd and 3rd

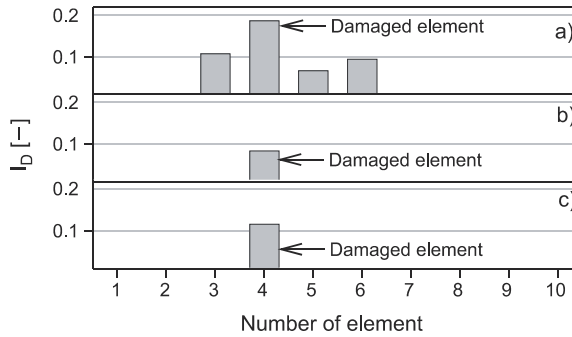


Fig. 5.15. Damage index for sequential procedure: a) the 1st eigen pair used in the updating algorithm, b) 1st and 2nd, c) 1st, 2nd and 3rd

To extract the maximum information from the updating algorithm a damage index, I_D , computed during one updating sequence of the i -th element is proposed to be

$$I_D^i = I_{EI}^i - I_{NMD}^i, \quad (5.36)$$

where

$$I_{EI}^i = \frac{\Delta EI_i}{\max(\Delta EI)}, \quad (5.37)$$

and

$$I_{NMD}^i = \frac{\Delta NMD_i}{\max(\Delta NMD)}. \quad (5.38)$$

The terms I_{EI}^i and I_{NMD}^i take values from 0 to 1. The first term in equation (5.36) becomes 1 for the largest stiffness change. The second term in equation (5.36) becomes 0 when the numerical mode shapes are identical with the experimental ones. Therefore, when the damage index, I_D , equals 1, it indicates that the finite element with the largest change in stiffness and perfectly fitting of the numerical modes into the experimental data.

The results of the damage index (5.36) for the sequential algorithm based on first, first and second, as well as three eigen pairs are given in Fig. 5.15. In the case of simulations based on only the first natural frequency and related mode shape, the four elements have

positive values of the damage index. However, in the case of two and three eigen pairs only one element is indicated as damaged, i.e., element number 4.

The model updating based on information stored in natural frequencies and mode shapes makes the detection of the damaged element possible. The tested algorithm called the sequential updating algorithm could correctly localize the position of the crack of relative size of 10% with respect to the cantilever beam height.

5.4. Updating of large FE model of cantilever beam

The FE model of the cantilever beam described in section 5.2 is modelled by 25 finite elements (Fig. 5.16) according to the formulas presented in Appendix A. The 52 unknowns are reduced by System Equivalent Reduction Expansion Process (SEREP) into a problem defined by 25 translational degrees of freedom (Appendix B). Each finite element has a length of 20 mm. The imperfection of the length of 20 mm is located in the whole 9th element. Therefore, perfect results of FE updating should indicate the damage only in stiffness EI_9 .

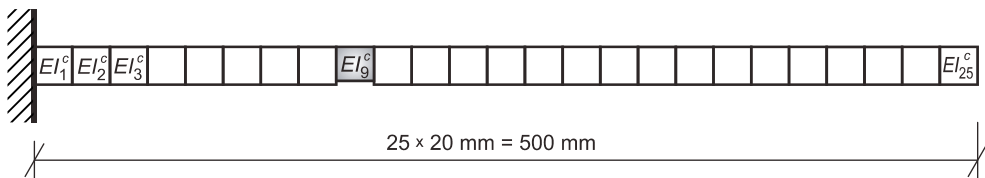


Fig. 5.16. The cantilever beam modelled with 25 finite elements

The experimental natural frequencies are given in Table 5.1 and the beam mode shapes are plotted in Fig. 5.7. Three procedures are considered. The first one assumes that the boundary conditions are perfect, and thus, there is no rotation nor translation on the beam fixed end and the global stiffness EI is computed. The second procedure assumes that the boundary conditions and general stiffness, EI , are optimized and then the search for the stiffness of each element of the damaged beam, EI_i^c is evaluated. The updated elements of stiffness, EI_i^c , of the damaged beam are compared to the general stiffness of the undamaged beam EI . The third method is the most general one. It assumes that the boundary conditions are updated. Then the variation of the stiffness of each element of the undamaged beam, EI_i^u is determined and finally the updated stiffness of the damaged beam, EI_i^c , is referred to the corresponding EI_i^u .

5.4.1. FE model updating of each element stiffness for fixed boundary conditions

In this section it is assumed that the boundary conditions are modeled by an ideal fixed support. Thus, the vector of the design parameters consists of all 25 element stiffness. The updating procedure is conducted according to (5.35) and in each iteration all the parameters are simultaneously updated. The FE updating is done for the damaged and undamaged beam. In each beam two cases of the input data are considered. First the updating is performed on single modal pair, i.e., the first one only, then separately the second and

finally the third one. Further, the design parameters search is conducted on three combinations, i.e., the first pair only, the first and the second together and the first, second and third pairs as one set of the input data. The coefficients of the weighting matrices are set to one.

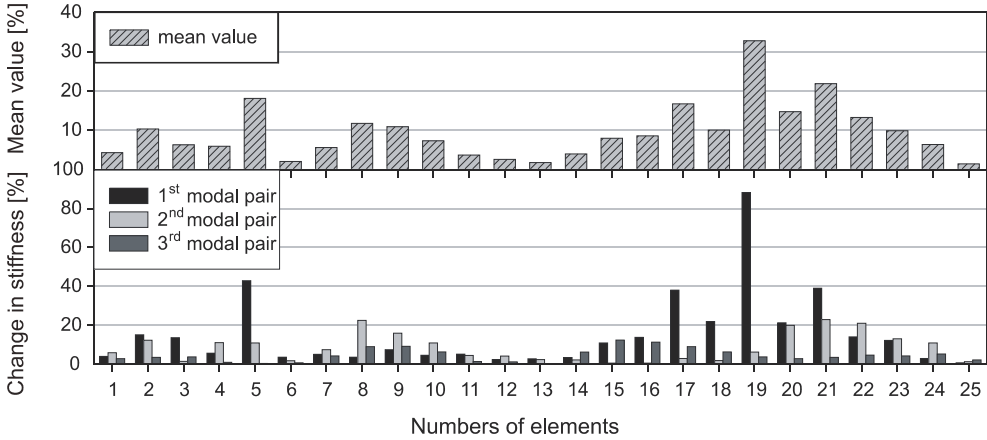


Fig. 5.17. Element stiffness updating results on single modal pairs

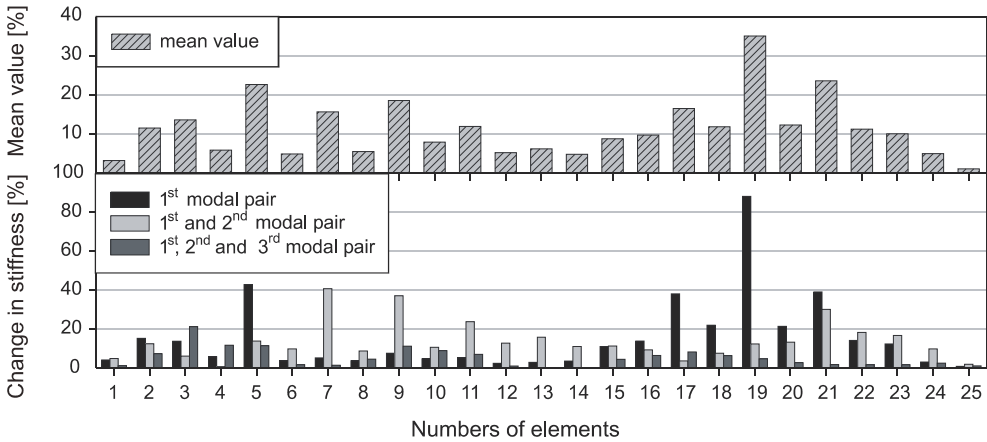


Fig. 5.18. Element stiffness updating results on combinations of modal pairs

The results of the relative change of the element stiffness between the cracked case, EI_i^c , and the undamaged stiffness EI_i^u for optimization on single modal pair and the combinations of the modal pairs are given in Fig. 5.17 and Fig. 5.18. The graph with three bars corresponding to a certain element number presents the stiffness changes for each input data. The second graph in the figure shows the values of the damage index (5.36) of the stiffness variations for all three input cases. The results presented in Fig. 5.17 and 5.18 show that the method is not able to find the damage location in the element number 9. In fact the values of I_D^i in elements 19th and 21st are larger than the bar indicating the real damage location.

5.4.2. FE model updating with computation of general stiffness and boundary condition parameters

It is assumed that the boundary condition parameters, k_t and k_r , as well as the general stiffness, EI_g , are first updated on the undamaged beam. The assumption states that the undamaged beam has constant values of all element stiffness, EI_i^u . Then, the obtained values are used for the updating of each element stiffness of the damaged beam EI_i^c . The relative change of stiffness is given in terms of the relative error between EI_g and EI_i^c . In addition, the damage index values of the set of solutions for three inputs are computed. Two cases of input data are considered, i.e., computations on single modal pairs and updating on three combinations of modal pairs as described in the previous section.

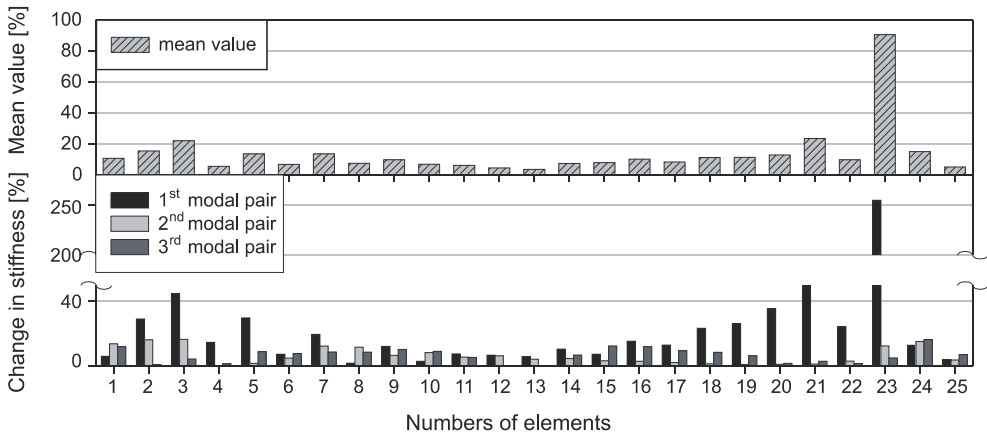


Fig. 5.19. Element stiffness updating results on single modal pairs

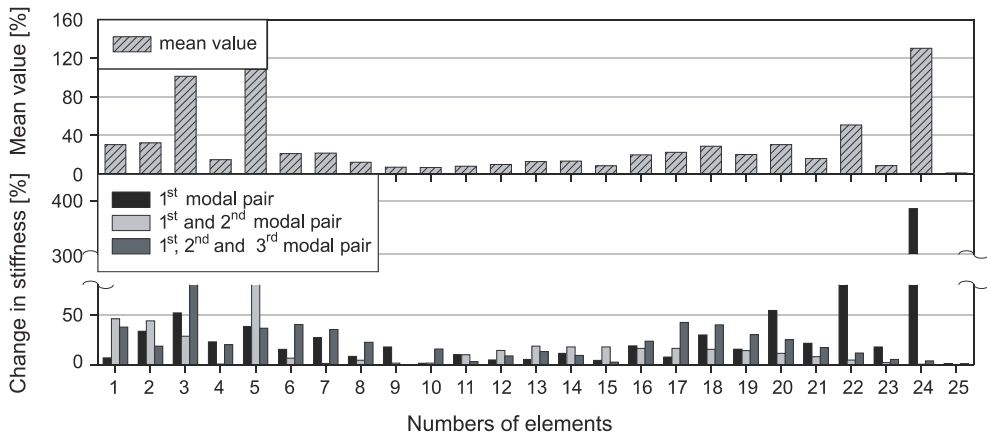


Fig. 5.20. Element stiffness updating results on combinations of modal pairs

Fig. 5.19 presents the stiffness changes computed independently on each single modal pair. The results for the 1st modal pair in the element 23 is over 250% indicating very large

damage of this element. The relative change in element number 9 is very low even though this element is the only one with the damage.

The results of the updating on the combinations of modal pairs (Fig. 5.20) are also incorrect. The largest stiffness changes occur around the elements number 3, 5 and 24. The updating conducted in this case does not indicate the real damage location.

The results shoes that the assumption that undamaged beam has the uniform stiffness distribution might not be correct. In fact in the real structure there are some variations of the Young modulus as well as the geometry of the beam. The changes in the height of the PMMA beam, tested in the experiment, were of the order of 1 mm, i.e., of about 5% with respect to the beam nominal height. The study on the distribution of Young modulus in the beam volume was not conducted.

5.4.3. FE model updating for boundary condition, undamaged and damaged beam

The previous results indicate that the most general approach should be used. First the boundary conditions, k_l and k_r , and the general stiffness, EI_g , should be determined for the undamaged beam. The support springs are used as the boundary conditions for the next updating stages, while the general stiffness is used as the initial conditions. The second step is the computation of the stiffness distribution in the undamaged beam, EI_i^u . Then, the simulations on the elements stiffness in the damaged beam are calculated, EI_i^c . The relative change of stiffness, that indicates the damage position, is obtained by the relative errors between EI_i^u and EI_i^c .

Figs. 5.21 and 5.22 show the relative changes of the element stiffness. As in the previous sections the indication of the damaged element is not correct. The incorrect values are particularly visible near the free end of the beam. The analysis of the mode sensitivity to the particular element stiffness indicates that the first mode of the cantilever beam is not sensitive to the stiffness of elements 22, 23 and 24. Therefore, the importance of the particular element during the updating should be taken into account. The drawback of direct a application of the procedure (5.35) is that it updates all the design parameters simultaneously (at once) trying to fit them all into the experimental data.

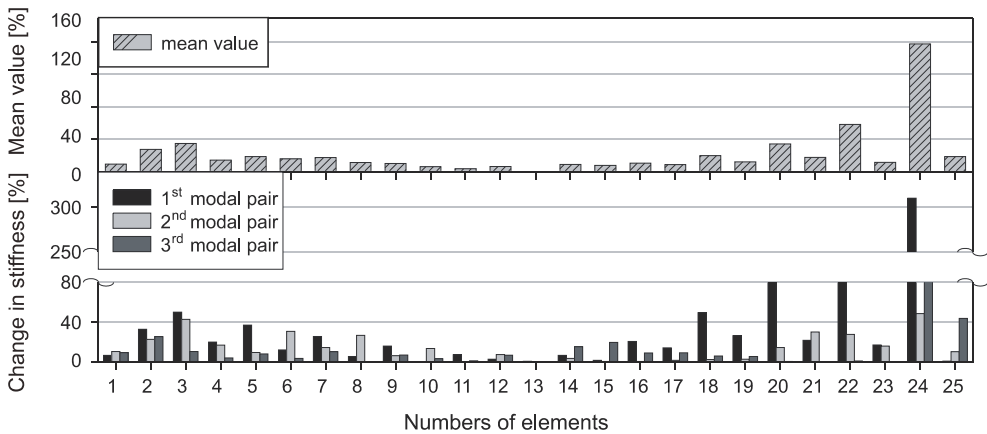


Fig. 5.21. Element stiffness updating results on single modal pairs

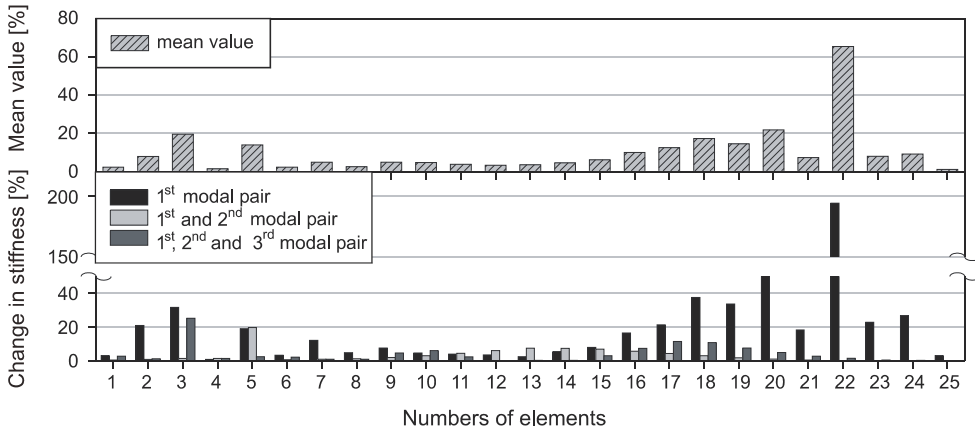


Fig. 5.22. Element stiffness updating results on combinations of modal pairs

5.4.4. FE model updating by sequential updating procedure

The negative experience lead to a proposal of some sequential computations of the elements stiffness. The proposed notion states that the optimization, at one step, is trying to find the best stiffness of only one element that yields the lowest value of the cost function. Then, the procedure is repeated for each element of the FE model. The selection of the particular element is obtained by a selection of the corresponding coefficients in the weighting matrices. The sequential updating procedure is applied to the cases described in section 5.4.1, 5.4.2 and 5.4.3.

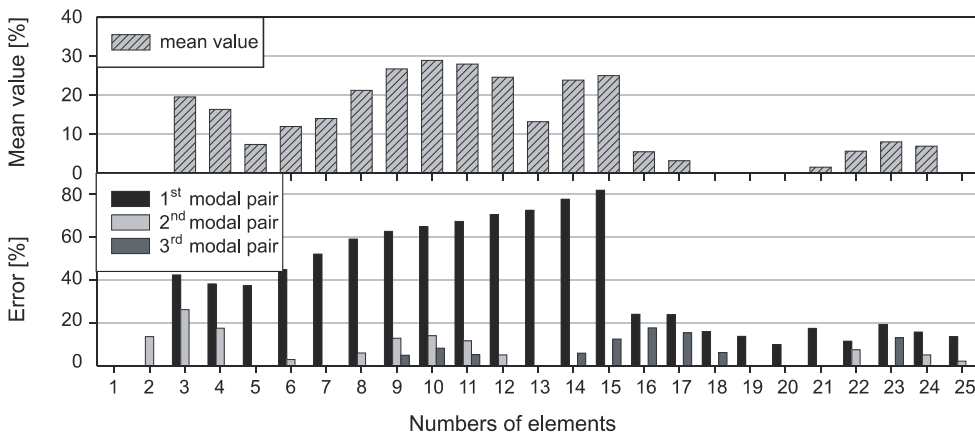


Fig. 5.23. Element stiffness updating results on single modal pairs

The results of the updating for the FE model with fixed boundary conditions (section 5.4.1) on single modal pair and combinations of modal pairs are given in Fig. 5.23 and Fig. 5.24. The results computed for the first modal pair have the largest values in the vicinity of the damaged element number 9. The stiffness changes indicated for the second and third mode also have peaks at element 9. The damage index I_d^i has the largest value in element 9. The damage index has non zero values in all the elements between 3 and 15.

The results on the sequential updating procedure on the combination of modal pairs is given in Fig. 5.24. The main contribution to the results given in terms of the damage index I_d^i is coming from the first modal pair. The positive value of the index points out three elements with damage, namely, element number 8, 9 and 10. These results correctly present the damaged element and the neighboring region. Although the results do not indicate only one damaged element, it is commonly accepted that modal properties spread the local damage information on a certain region of the structure.

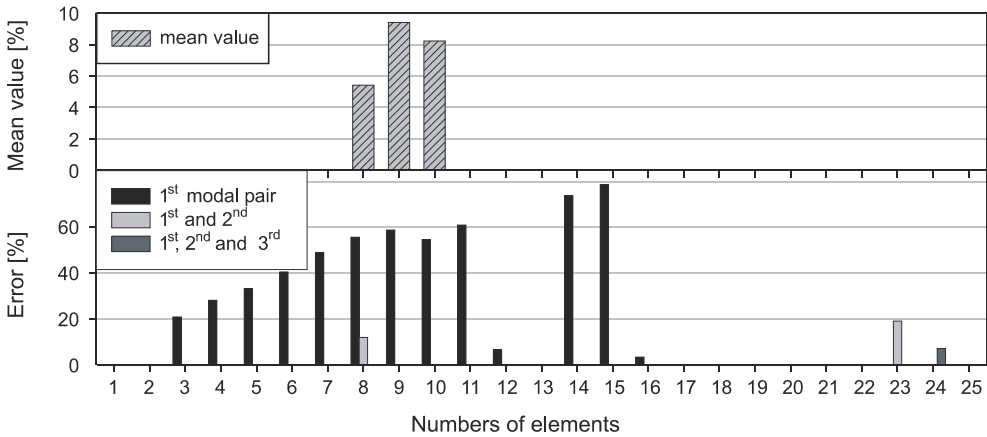


Fig. 5.24. Element stiffness updating results on combinations of modal pairs

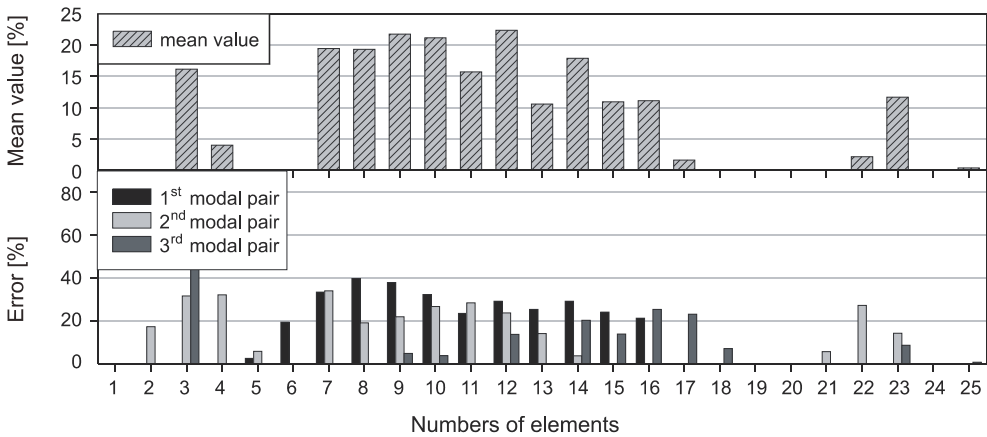


Fig. 5.25. Element stiffness updating results on single modal pairs

The results of the updating for the FE model with updating of the boundary conditions and general stiffness and then computation of the stiffness of the damaged beam (section 5.4.2) are presented in Fig. 5.25 and 5.26 for the case of the single modal pairs and the combinations of pairs, respectively. The results on the single pairs (Fig. 5.25) show that 10 elements have large values of the damage index I_d^i in the region near element 9. The largest value of the index corresponds to element 12.

The damage index computed for the combination of the modal pairs is positive only for two elements (Fig. 5.26), namely, number 8 and 9. The largest value appointed to element 9 correctly indicates the damage location.

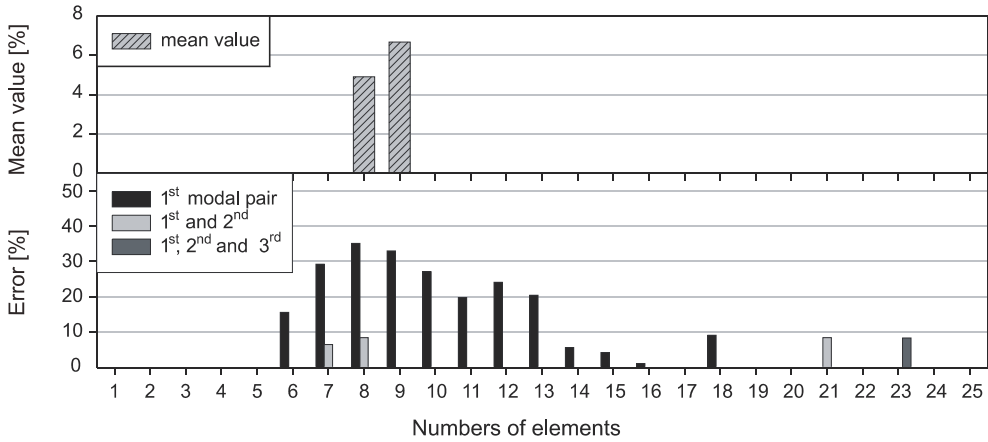


Fig. 5.26. Element stiffness updating results on combinations of modal pairs

The third case described in section 5.4.2 gives the updating of the boundary conditions, stiffness of the undamaged elements and finally stiffness of the damaged elements. The results of the sequential updating procedure are given in Figs. 5.27 and 5.28. The optimization on the single modal pair results in precise indication of the damage region with the maximum damage index value for the 9th element. However, there are two additional regions, near the support and around element 16, where the presence of the damage is indicated (Fig. 5.27).

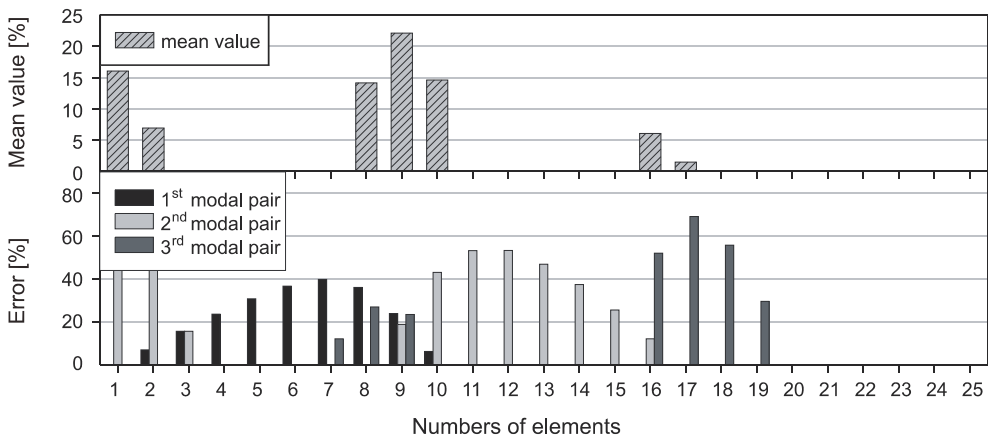


Fig. 5.27. Element stiffness updating results on single modal pairs

The damage index on the combination of the modal pairs correctly points out to the damage in the 9th element (Fig. 5.28). The positive values of the index I_d^i are found for four elements. It is noted that the main contribution to the index results comes from the

optimization on the first modal pair and the combination of the first and the second one. Both these inputs provide large stiffness changes of the elements in the vicinity of the 9th element.

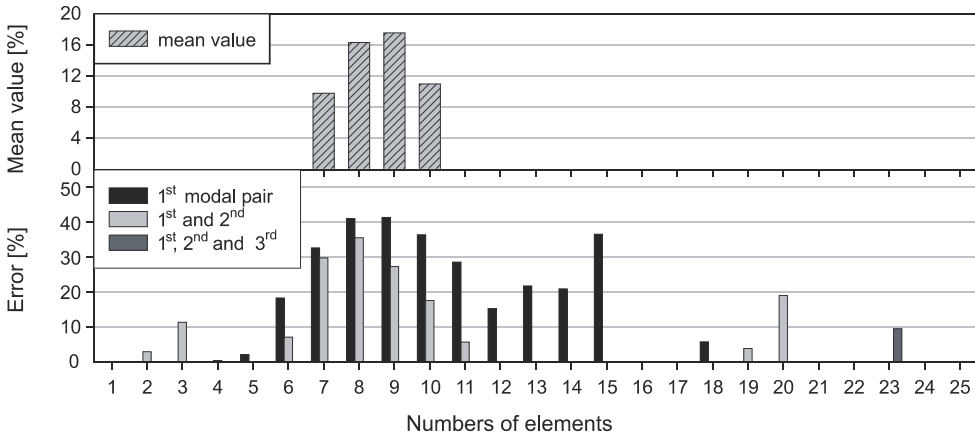


Fig. 5.28. Element stiffness updating results on combinations of modal pairs

5.5. FE model updating in steel plate on numerical data

The study is conducted on the numerically determined mode shapes and natural frequencies. The damage is simulated by a change in the element mass density. The FE updating design parameters are the element masses, and therefore, the number of updated parameters is equal to the number of elements. The consistent mass element, \mathbf{M}^e , has a full element matrix and the term ρt describing the material density is a multiplier (Appendix A).

5.5.1. Mass coefficients updating on 16 element FE model

The FE model of the plate simply supported on two edges is shown in Fig. 5.29. The plate is divided into 16 identical rectangular plate elements (Appendix A) of size 0.35 by 0.30 m. Two models are considered. One is derived to generate the data that is used as an input to the updating procedure and the second model that is simplified and used in the updating. The first model is not reduced since it should possibly well describe the dynamics of the plate. For the input data only the translational degrees of freedom are extracted to build the input mode shapes. The precise plate FE model has 25 translations and 50 angles of rotation, a total of 75 degrees of freedom. The boundary conditions are selected so that the nodes at the free sides of the plate (along the longer plate side of length L) have no restrictions on translations or angles. The nodes at the sides that are freely supported have zero translations and free angles of rotation. The full model is not reduced according to the boundary conditions but the stiffness coefficients corresponding to the zero translations are chosen as very large numbers. The calculations of the natural frequencies and mode shapes were conducted for two cases: without the additional mass and with the additional mass placed on element number 5 (Fig. 5.29). The additional weight has been added by increasing the 5th element mass density by 10%, i.e., to 4.5333 kg. The rest of the

elements have the weight of 4.12 kg. The data on material properties are given in example 2.2 of section 2.1.1.

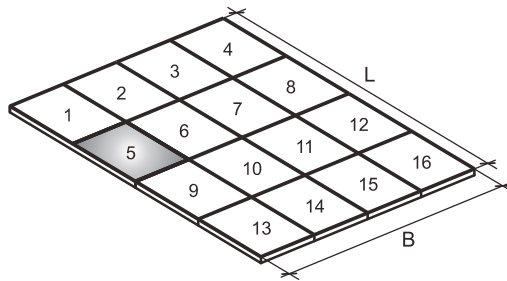
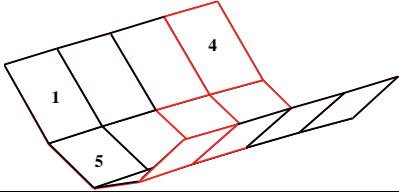
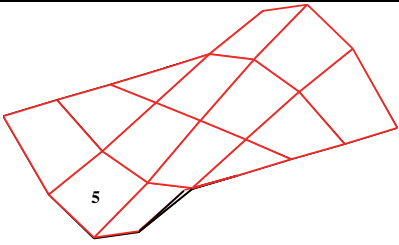
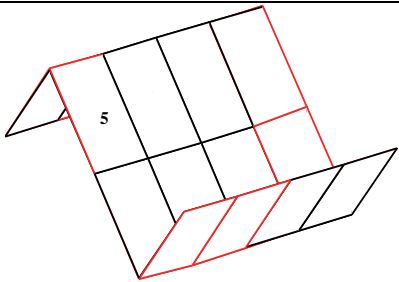
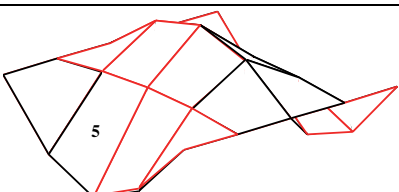


Fig. 5.29. The FE mesh consisting of 16 elements

Table 5.3

Mode shapes with and without additional mass

Mode	NMD [%]	Graphical representation
1	0.567	
2	1.871	
3	2.960	
4	3.783	

The second FE model is applied in the updating algorithm and is reduced since the available measurements on the real plate structure are limited to the translations. Therefore, the angles of rotation are assumed as secondary coordinates and eliminated by IRS method (Appendix B). The degrees of freedom corresponding to zero translations are also reduced by IRS and finally the system is defined only by 15 translational displacements.

The examples of the numerical mode shapes with and without the additional mass are given in Table 5.3. The mode shapes of the plate without the additional mass are plotted with black lines while the modes of the plate with the mass are given in red. The modes are normalized to their maximum value. The presence of the mass does not change the shape of the modes. The NMD criteria (Appendix D) have the values of 0.567% for the difference between the first mode and becomes 3.783% for the fourth modes. A slight difference on the free end of the plate can be seen in the fourth mode (Table 5.3).

The numerical natural frequencies of the plate without the additional mass are given in the second column of Table 5.4. The frequencies of the undamaged plate are called “initial” since they are used in the updating procedure as the initial values at the beginning of the iteration process.

Table 5.4

Natural frequencies of the plate and the frequencies of the updated system

Frequency	“Initial” [Hz]	“Updated” [Hz]	NMD [%]
f_1	6.020	6.004	0.314
f_2	11.703	11.649	0.871
f_3	24.164	23.980	4.96
f_4	27.943	27.854	5.10
f_5	30.795	30.441	9.12
f_6	48.973	48.563	6.81

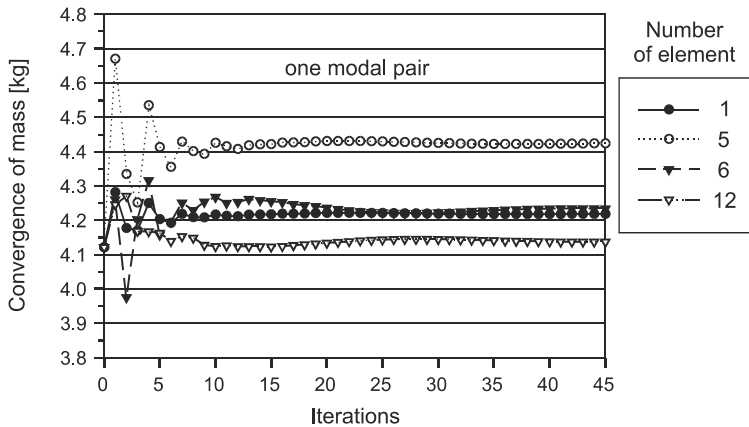


Fig. 5.30. Convergence of the element masses vs. iteration number for one modal pair

The FE updating, in this section, is conducted by sequential procedure described in section 5.4.4. The preliminary computations showed that this method provides the best results also in the case of the plate problem. The updating is conducted on the combinations of the modal pairs. Four combinations are considered, namely, 1st pair, 1st and 2nd, 1st 2nd and 3rd and all four modes together. The convergence of the searched masses of element 2, 7, 13 and 19 are given in Figs. 5.30 and 5.31. The target value of the 5th element mass is 4.5333 kg. The optimization on only one modal pair indicates the difference in mass of the 5th element but its value is incorrect. The iterations on three modal pairs (Fig. 5.31) result in correct mass values of the 5th element, as well as other elements.

In the case of the FE updating on numerical data the results are very good even though the influence of the additional mass on the mode shapes is very small. In such a case it is not necessary to use additional indices, introduced in section 5.3.4, and the results can be presented directly in terms of element masses.

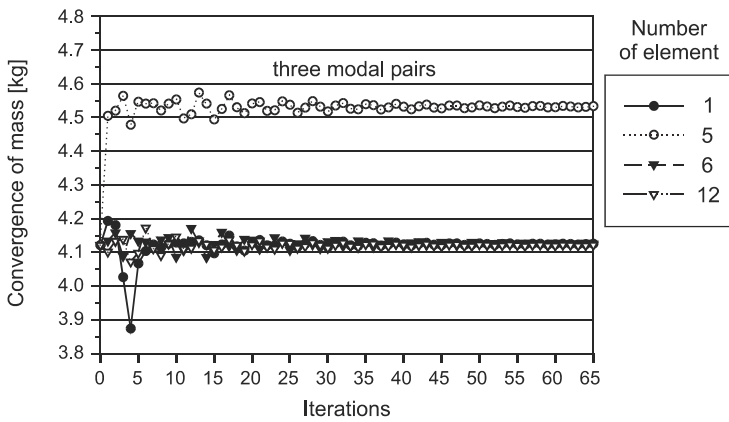


Fig. 5.31. Convergence of the element masses vs. iteration number for three modal pairs

Figs. 5.32, 5.33, 5.34 and 5.35 show the updating results on one, two, three and four modal pairs. The bars in the figures correspond to the finite elements of the plate. The highest values of the element mass in all the cases have been found for the 5th element. The results are summarized in Fig. 5.36 where all the values of the bars can be easily read for all considered cases of the input data.

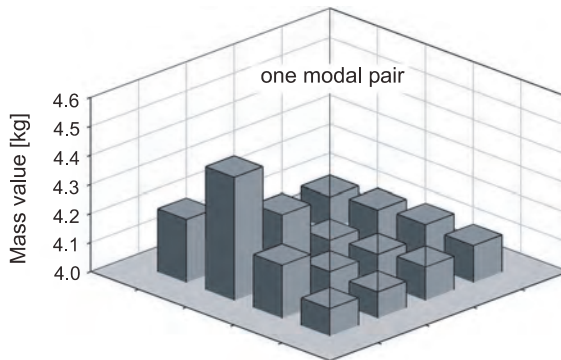


Fig. 5.32. Element mass updating on the first modal pair

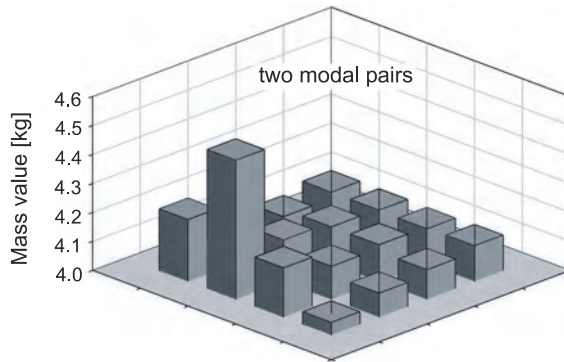


Fig. 5.33. Element mass updating on two modal pairs

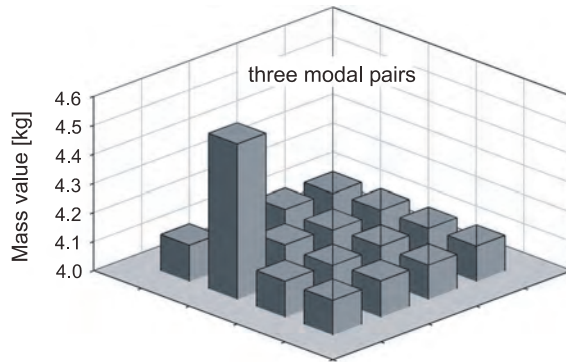


Fig. 5.34. Element mass updating on three modal pairs

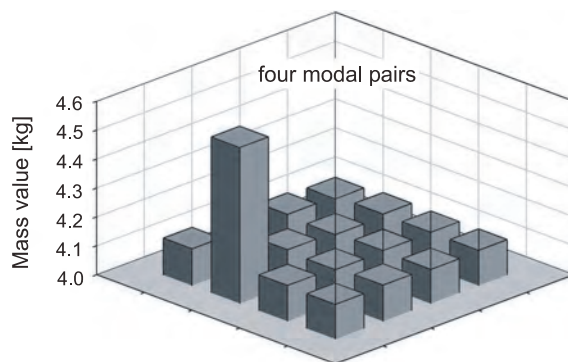


Fig. 5.35. Element mass updating on four modal pairs

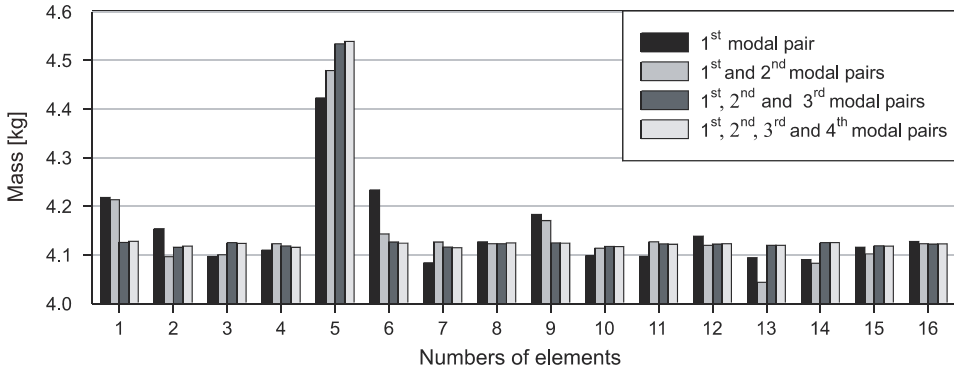


Fig. 5.36. Element mass updating on all considered modal pair combinations

5.5.2. Mass coefficients updating on 36 element FE model

In this section the FE model of the plate modelled by the element of size 20 by 23 cm (Fig. 5.37). The FE model has 147 degrees of freedom (Appendix A). The reduction of the degrees of freedom is conducted by IRS method (Appendix B). The reduced FE model has 35 translational degrees of freedom. The additional mass is located in element 13. The mass of element 13 is 2.799 kg and the mass of the rest of the elements is 1.832 kg. An increase of the mass of 0.968 kg corresponds to the experimental tests presented in the next section.

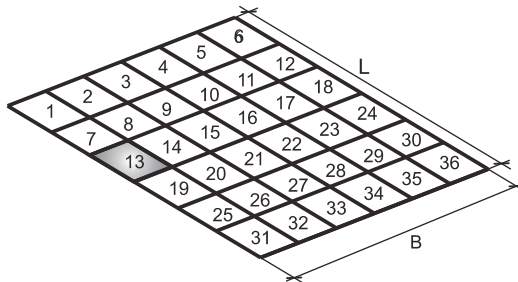


Fig. 5.37. The FE mesh consisting of 36 elements

The natural frequencies of the plate without the additional mass and modeled by 36 elements are given in the second column of Table 5.5. The results of the FE updating of the 36 masses of each element is conducted by the sequential updating procedure on four combinations of modal pairs, i.e., 1st pair, 1st and 2nd, 1st 2nd and 3rd and all four modal pairs. The results of the mass convergence vs. the iteration number is given in Figs. 5.38 and 5.39 for the procedure on two and four modal pairs, respectively. In the case of computations on two pairs the results are not correct. Regarding the optimization on four modal pairs the mass of the element no. 13 reaches the value 2.82 kg while the target value is 2.799 kg. The masses of the remaining elements are also close to their nominal value of 1.8732 kg.

Figs. 5.40, 5.41, 5.42 and 5.43 show the updating results on one, two, three and four modal pairs. The highest values of the element mass in all the cases has been found for the 13th element. It is noted that even though the mass has not been correctly identified, the updating indicates the location of the additional mass (Fig. 5.40). The results on four modal

pairs (Fig. 5.43) show that the value of the mass of element 13 is correctly calculated. The averaging effect of the combination of several modal pairs helps to obtain the correct results. However, in real structures the experimental estimation of higher modes is more difficult. The higher modes contained more information on the local damage but at the same time other factors may strongly influence their identification precision.

Table 5.5

Natural frequencies of the plate and the frequencies of the updated system

Frequency	“Initial” [Hz]	“Updated” [Hz]	NMD [%]
f_1	6.015	5.932	1.571
f_2	11.733	11.430	4.53
f_3	24.135	24.025	6.29
f_4	28.327	27.746	10.97
f_5	31.064	30.857	12.49
f_6	50.045	49.722	7.00

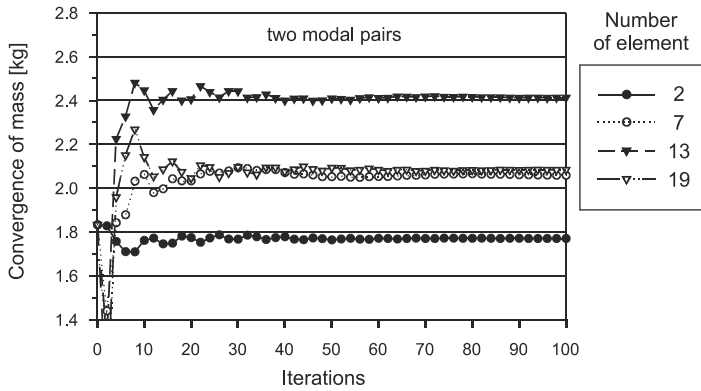


Fig. 5.38. Convergence of the element masses vs. iteration number for two modal pairs

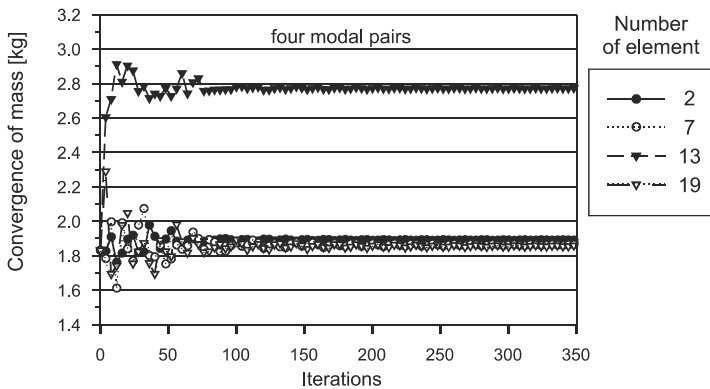


Fig. 5.39. Convergence of the element masses vs. iteration number for four modal pairs

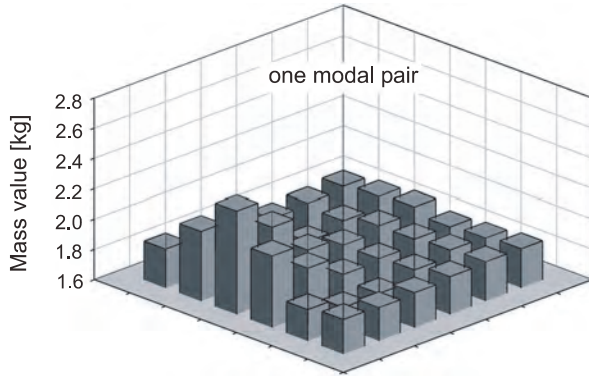


Fig. 5.40. Element mass updating on the first modal pair

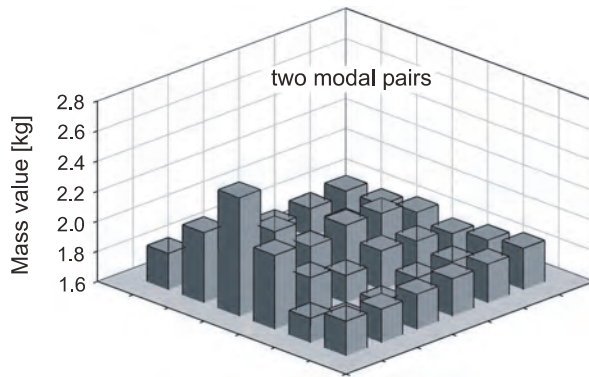


Fig. 5.41. Element mass updating on two modal pairs

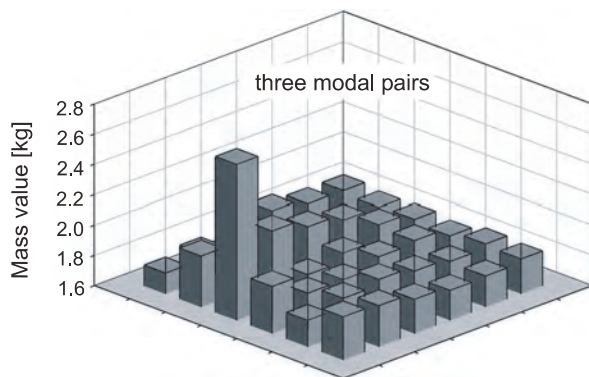


Fig. 5.42. Element mass updating on three modal pairs

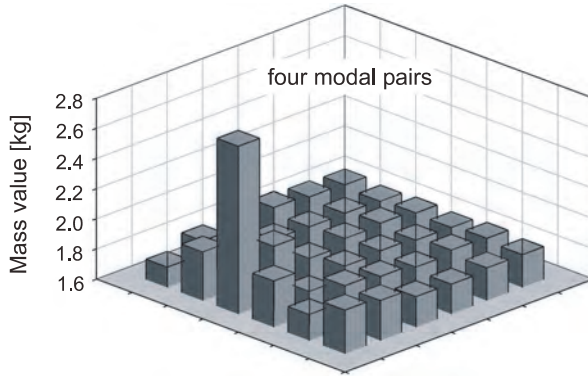


Fig. 5.43. Element mass updating on four modal pairs

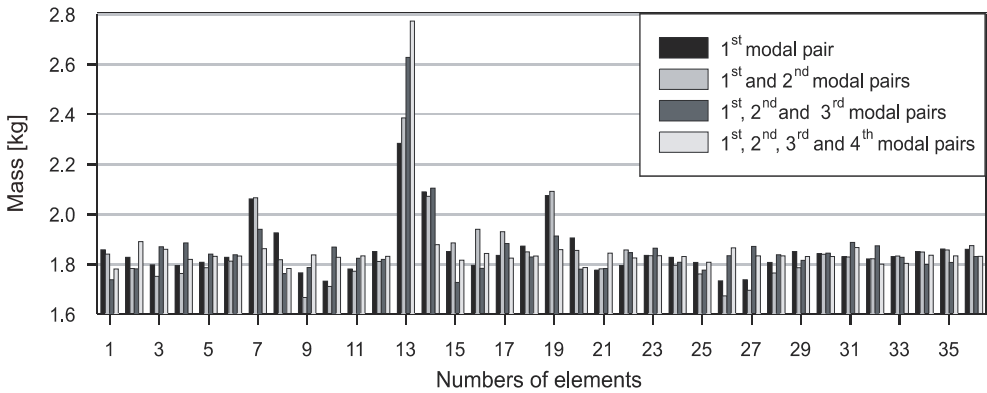


Fig. 5.44. Element mass updating on all considered modal pair combinations

5.6. FE model updating in plate on experimental data

The steel plate experimental setup is shown in the example 2.2 in Chapter 2 in Fig. 2.4. The data acquisition equipment, as well as the experimental procedure is given in Chapter 3 (section 3.1.2). In this section both the forced vibration tests were conducted. The sweep tests were conducted by actuator VEB RFT Messelektronik, Germany, type 11073 and the force acting on the plate was measured using the force sensor PCB W208C04.

The numbering of the finite element of the FE model with mesh of 4×4 is given in Fig. 5.45. An additional mass of 0.968 kg is located between element 5 and 9. The location of the additional mass is denoted by a big black dot.

Table 5.6

Analytical and experimental values of plate natural frequencies

Initial values	FEM solution	Measured values	
		No add. mass	With add. mass
$E\bar{I}^3$ 26.25 kNm	f_1 6.176	6.170	6.100
ν 0.333	f_2 11.29	11.240	11.02
ρ 7.85 t/m ³	f_3 25.26	23.400	23.42

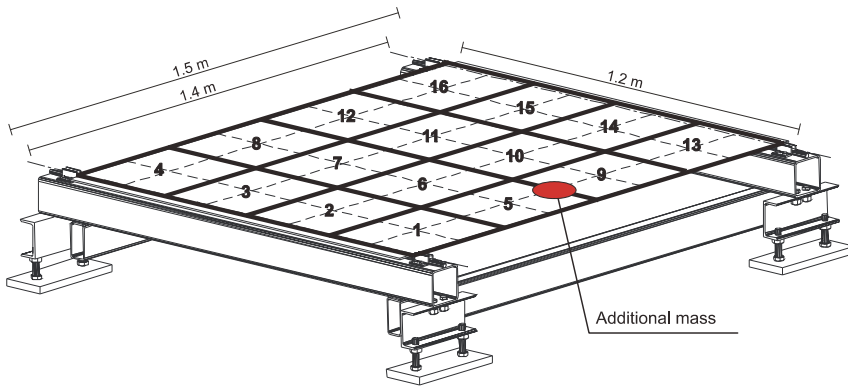


Fig. 5.45. The plate modelled with 16 finite elements

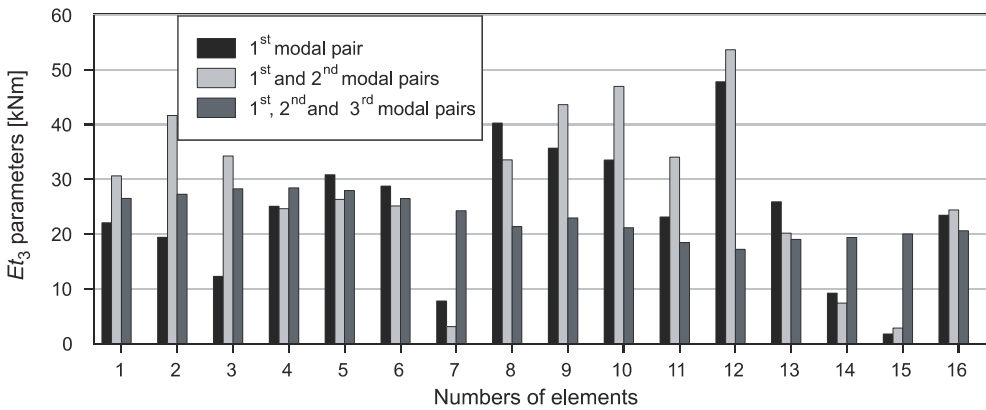


Fig. 5.46. The updated parameters by the sequential updating procedure

The measured natural frequencies of the plate with and without the additional mass are given in Table 5.6. The effect of the mass is observable on the plate natural frequencies.

The FE updating is conducted for 16 element FE model that is reduced to 15 translational degrees of freedom by IRS method (see previous section). The initial values for the updating procedure with the corresponding numerical natural frequencies are presented in Table 5.6. The results of the optimization by the sequential updating procedure

on three combinations of the input data are given in Fig. 5.46. None of the conducted calculation results in a correct indication of the additional mass that should have a larger value of element mass 5 and 9.

The comparison between the numerical and experimental mode shapes for the case without and with the additional mass for the first, second and third mode is given in Figs. 5.47, 5.48 and 5.49. The black lines denotes the numerical modes and the red colour corresponds to the experimental data. In general the values of NMD indicate a very good agreement between the numerical and the experimental eigenvectors. The highest value of NMD of 9.944% is for the third mode without the additional mass. The fit between the third modes with the additional mass has very low NMD of 1.349%. Even though the modes are estimated on several recorded signal through the H_2 estimator, the experimental higher modes have local errors visible on the sides of the plate.

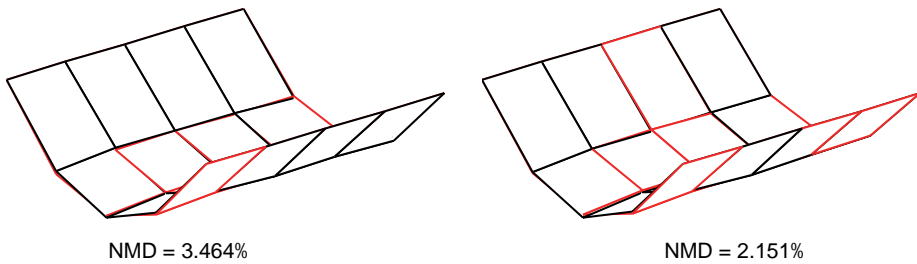


Fig. 5.47. Comparison between the first numerical and experimental modes for a plate without mass and with the additional mass

A direct identification of the additional mass is possible on the numerical data. However, in the case of the experimental mode shapes the study of the mean values of the used input data combinations and application of the proposed damage index (section 5.3.4) is hereafter conducted.

The updating results together with the mean values are given in Fig. 5.50. In this case the global updating procedure is used. Despite the application of different possible updating algorithms the results of the updating are not correct. The largest mean value is for the 4th element which is not loaded by the additional mass. The bars corresponding to the 5th and 9th element have smaller values than most of the presented elements.

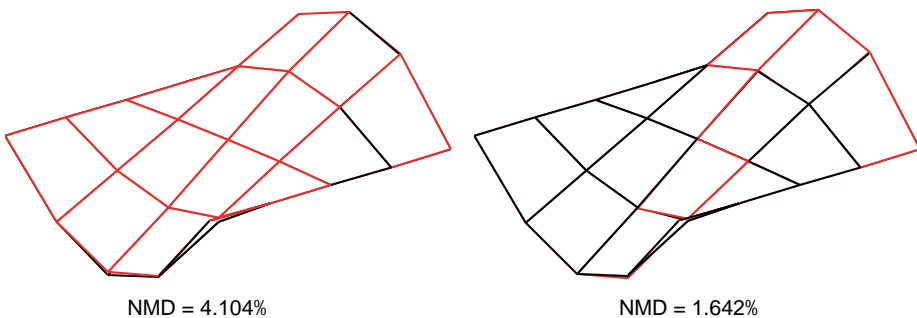


Fig. 5.48. Comparison between the second numerical and experimental modes for plate without mass and with the additional mass

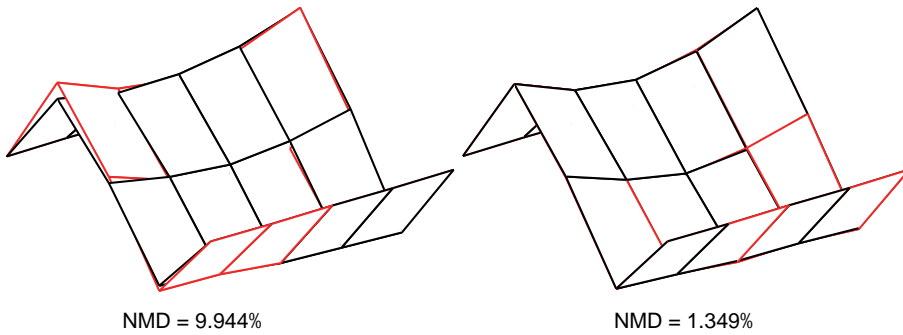


Fig. 5.49. Comparison between the third numerical and experimental modes for plate without mass and with the additional mass

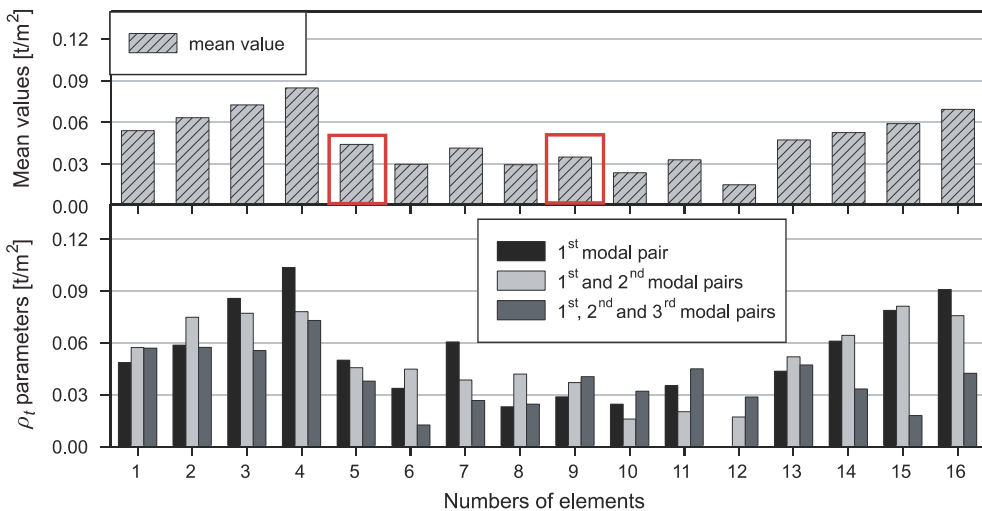


Fig. 5.50. The updated parameters with global updating procedure

The application of the damage index, useful in all presented in this book cases, is given in Fig. 5.51. The results from the sequential procedure are used. The information on mean values and the correctness between the numerical and experimental modes do not improve the updating results. The mean index value is negative for the 5th element indicating that the mass of the element decreased. The mean value of the index for element number 9 is close to zero. The largest positive mean index value is for element 13.

The updating of the plate element masses on the experimental modal pairs failed. The reason is due to the additional errors in the experimental mode estimation. The most appropriate mode shapes were determined by the sweep tests. In these experiments 9 accelerometers were moved around the plate with the actuator attached in one location. The total mass of 9 sensors is slightly more than 1 kg which is more than the additional mass. The sensors located in lines during the experiments changed the natural frequencies and the mode shapes in each series and the final experimental modes are different than the real modes of the steel plates. This differences are not important from the visual point of view but are crucial for the sensitive updating process.

Another source of the errors are the boundary conditions. The simply supported plate laid on the bars. However, the plate is not perfectly attached to the supports. Fig. 5.52 shows the measurements conducted directly above the support. The graphs correspond to the first and the second plate support and the lines correspond to the first five modes. The results are given for the experimental mesh with 64 nodes (8x8 elements). It is clearly visible that three corners of the plate oscillate, and therefore, are not attached to the supports. The imperfections of the plate curvatures are not essential for the general characteristics of the experimental modes but in case of the updating problem the algorithm tries to fit the experimental data into the incorrect FE model. The presented discussion intends to show how difficult the updating on in situ data is and how important it is to correctly identify the FE model as well as the experimental mode shapes.

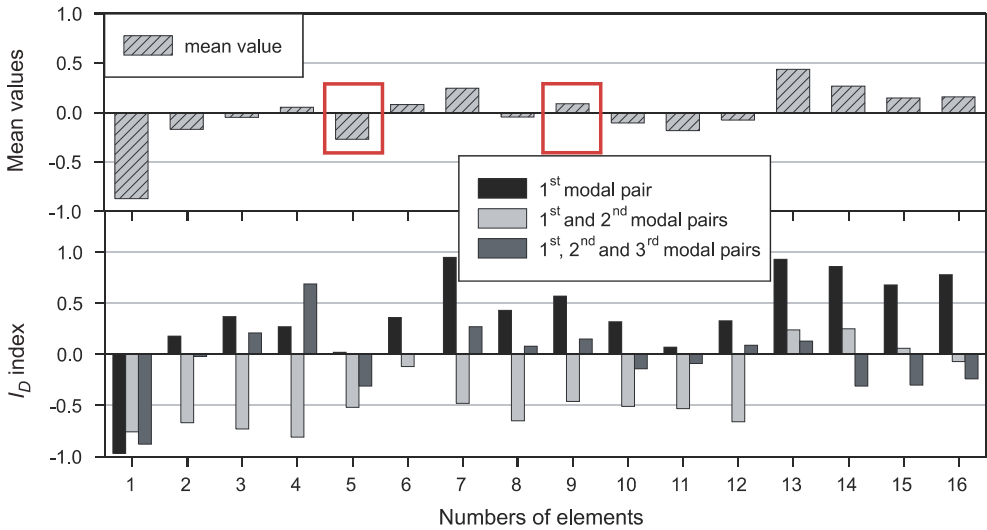


Fig. 5.51. The updated parameters with sequential updating procedure

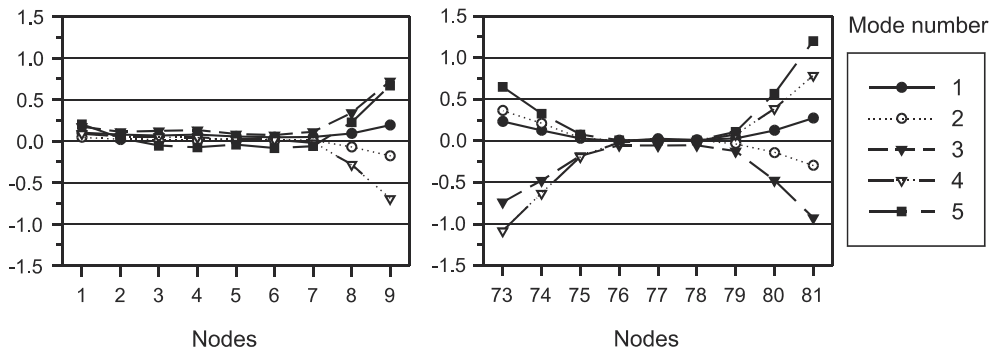


Fig. 5.52. The values of the mode shapes for two supported edges of the plate

5.7. Conclusions

The FE updating on the experimental mode shapes improves the possibility of proper identification of FE stiffness and mass coefficients. The examples of the cantilever beam and the simply supported plate show that the additional information stored in mode shapes can be effectively used.

The proposed sequential procedure improves the updating results and the combination of input modal pairs with the additional damage index helps to extract the information of the damage location.

The detailed study on the steel plate FE updating indicates that updating on the numerical data can be successfully conducted on small and large FE models. However, the research on the experimental data confirmed the common knowledge that the errors resulting from the modelling assumptions and measurement precision significantly limit the applicability of the FE updating.

Multilevel damage detection neural system on mode shapes of plate structure

The previous chapters have shown that the process of damage identification based on experimental data or in situ measurements has many limitations. In fact, if a precise determination of the experimental mode shapes is not possible, the detection of the damage location cannot be successfully conducted. Therefore, the so called soft computing methods are hereafter proposed. In these methods the search for the damage location is facilitated by the application of a neural network system.

The artificial neural networks are used in high performance aircraft control systems, in weapon steering, facial recognition, electronic code sequence prediction, integrated circuit chip layout, process control, financial analysis of corporate bond rating or credit-line usage, breast cancer cell analysis, speech recognition, speech compression, and many others (Demuth and Beale 2002). The applicability of the so called “soft computing” has also been also studied for damage detection in engineering structure. The localization and recognition of the ships damage have been considered by, e.g., Zubaydi et al. (2002). The applicability of the neural networks in bridges has been studied by, e.g., Barai and Padney (1997) as well as Yeung and Smith (2005). The artificial neural networks (ANN) have been applied in helicopters (Cabell et al. 1998), joints in steel structures (Yun et al. 2001) and even in the analysis of the crates of beverages (Zacharias et al. 2004).

Various researches are suggested using different signals as inputs to the ANN: the ultrasonic signals (Okafor and Dutta 2001, natural frequencies (Sahin and Shenoj 2003, Waszczyszyn and Ziemiański 2001, Zapico et al. 2003) or vibration responses (Barai and Padney 1997, Kao and Hung 2003, Yam et al. 2003).

There is a vast literature on the types of possible neural based systems that can be applicable in damage detection problems. A systematic presentation of the soft computational inverse techniques in nondestructive evaluation is given, e.g., by Liu and Han (2003). The most often used artificial neural network, is the so called backpropagation network. Its application in civil engineering field has been studied, among others, by Kuźniar and Waszczyszyn (2002) or Hoła and Schabowicz (2005). The main advantage of the backpropagation ANN is its simplicity (Freeman 1994).

In this book the strategy for use of a multilevel neural system is presented. The simple backpropagation network with three layers is considered. The natural frequencies and mode shapes are used as the inputs to the ANN system. Two types of dynamic testes are considered and they correspond to two levels of the system precision. First level is based on ambient vibration and modes estimated through Stochastic Subspace Identification method, while the second level is based on detailed modes obtained from impact and sweep test. The intension of using the ambient vibration tests as an introductory stage in damage location is due to the fact that ambient tests can be very easily conducted on many civil engineering structures. If the ambient test indicates the presence of a damage, the second

stage of the more expensive dynamic tests can be initiated. Both stages of the method are based on artificial neural system. The damage in this chapter is simulated by an additional mass placed on the upper surface of the steel plate.

6.1. Experimental study

The experimental model of the plate has already been shown in Fig 2.4 and its description is given in section 3.2.3.1. Fig 6.1 gives the numbers corresponding to the locations of the additional mass. The configuration of the measurement equipment has been described in section 3.2.3.1.

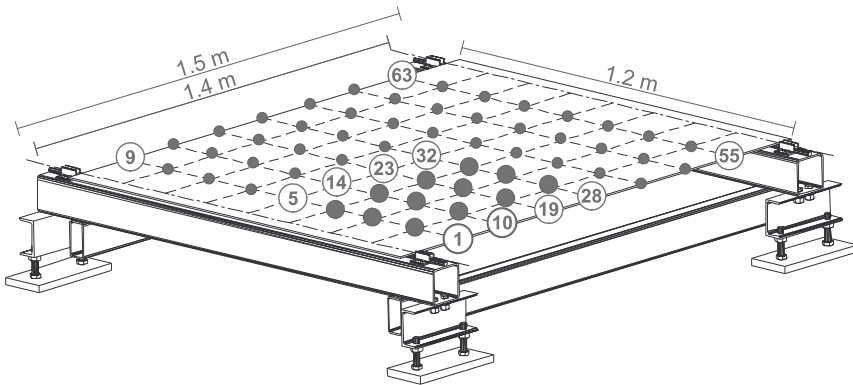


Fig. 6.1. Location of the measurement location and positions of the additional mass

Two cases of mass distribution were considered. In case 1 there was no additional mass and in case 2 the additional mass of 5.62 kg was placed at points numbered from 1 to 5, from 14 to 18, from 19 to 23 and from 32 to 36 (Fig. 6.1). The additional mass used in this chapter is different from the mass used in studies in Chapter 5. The points of the additional load application are marked by big black dots.

The experiments were conducted on ambient vibration tests, as well as on impulse and sweep tests.

6.1.1. Ambient vibration test

The plate vibrations were excited by the people walking on the sidewalk near the laboratory building, cars passing on the nearby university street and students working in the laboratory. The ambient vibration measurements were conducted during the rush hours. The total number of 63 channels of acceleration responses were recorded in 6 data setups (11 measurement points each). Two consecutive data measurement series had one common sensor location for comparison purposes. The reference sensors were carefully determined in each data set to obtain the best results. Each measurement consisted of 131072 points (during 256 seconds), and was down-sampled at the frequency of 128 Hz. An example of the measurements taken during the ambient tests is presented in Fig. 6.2. The acceleration peaks reached of up to 0.4 m/s^2 and were induced by accidental activities of the students and technicians in the laboratory.

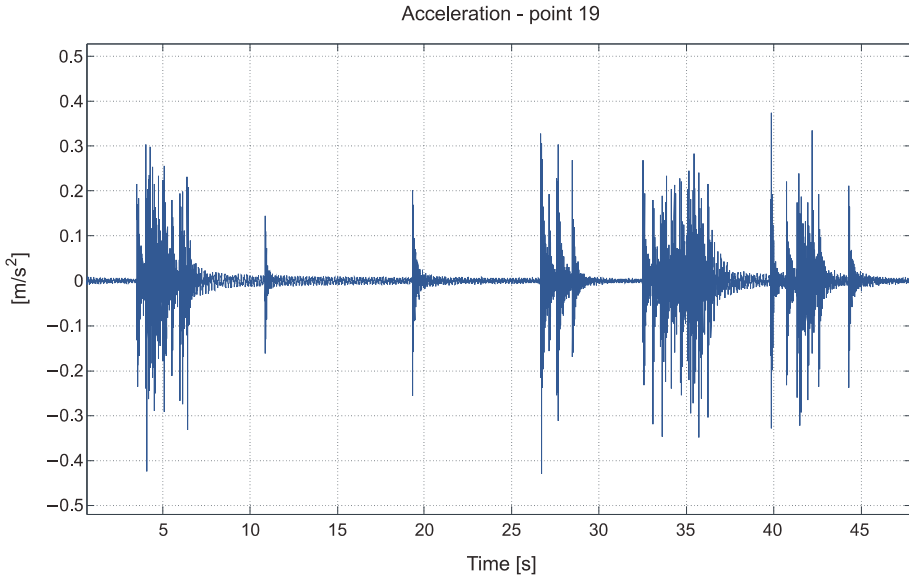


Fig. 6.2. Acceleration signal from ambient vibrations

6.1.2. Forced vibration test

Two types of the vibration excitation were applied, namely, impact loading and linear motor actuator. Dynamic pulse loads were applied using a modal hammer (PCB Piezotronics type 086C03). The plate was subjected to a dynamic pulse load applied at 63 equally spaced points on the surface while response measurements were made at 1 point. In the case of sweep test the actuator was placed at point 2 below the plate and the measurements were conducted at 63 locations. Fig. 6.3. shows an electro-magnetic linear motor (VEB RFT Messelektronik, type 11073, Germany) used in the forced dynamic tests. The exciting force measurements were made by force sensor PCB W208C04 presented in Fig. 6.3. The excitation frequency, for the sweep test, changed from 0 to 200 Hz with the step 0.1 Hz a second.



Fig. 6.3. The electro-magnetic actuator VEB RFT Messelektronik and force sensor PCB W208C04

6.2. Modal parameter identification

6.2.1. Ambient vibration test

The main difficulties in the identification process by Stochastic Subspace Identification method are: proper estimation of the model order and reliable detection of the spurious modes (section 3.2.2). Stabilization diagrams were constructed to reflect the stability of the identified modes of the steel plate. Variation of the estimated modal properties is common in the identification on the noisy experimental data and in this case two additional criteria were proposed

$$\begin{aligned}\Delta\omega &= \omega_{i+1} - \omega_i < 0.01, \\ \Delta\xi &= \xi_{i+1} - \xi_i < 0.02.\end{aligned}\quad (6.1)$$

The first criteria imposes constrain on the change in the system frequencies while the second one on variation of the damping ratios.

6.2.2. Forced vibration tests

The mode shapes are derived from the plate accelerance FRF, $\mathbf{H}(s)$ whose coefficients can be computed by equation (2.96). The standard form of the single frequency response function is

$$h_{ij}(i\omega) = \sum_{k=1}^m \frac{a_{ij}^k}{(i\omega - p^k)} + \frac{a_{ij}^{k*}}{(i\omega - p^{k*})}, \quad (6.2)$$

where the residual values a_{ij}^k , a_{ij}^{k*} and poles p^k , p^{k*} are complex conjugate pairs. The number of poles is denoted by N . However, it is convenient to express function (6.2) in terms of the variables that have a physical meaning. Equation (6.2) can be expressed by

$$h_{ij}(i\omega) = \sum_{k=1}^m \frac{-2a_{ij}^k \omega_r^k \sqrt{1 - (\xi^k)^2}}{\omega^2 + i2\xi^k \omega_r^k \omega - (\omega_r^k)^2} = \frac{-2\rho_{rij}^k \xi^k (\omega_r^k)^2}{\omega^2 + i2\xi^k \omega_r^k \omega - (\omega_r^k)^2}, \quad (6.3)$$

where ρ_{rij}^k denotes the peak response of the transform function, ξ^k is a modal damping ratio and ω_r^k is the resonance frequency of the k -th mode. The difference between residual values a_{ij}^k in equation (6.2) and (6.3) is that the values in (6.2) are expressed in complex form ($a = \text{Re} + i\text{Im} = a^{\text{Re}} + ia^{\text{Im}}$) while the value in (6.3) is just the imaginary part of a_{ij}^k . If the damping ratio is less than 1, the real part a^{Re} of each a_{ij}^k coefficient is much less than the imaginary part. Consequently, the coefficients in equation (6.3) are nothing more than imaginary part a^{Im} . The relation between a_{ij}^k and ρ_{rij}^k for resonant frequency is given by

$$a_{ij}^k = \frac{\rho_{rij}^k \xi^k (\omega_r^k)^2}{\sqrt{1 - (\xi^k)^2}}. \quad (6.4)$$

Estimation of the resonant frequencies and identification of mode shapes from the imaginary part of frequency response function is conducted for case 1 and twenty times for case 2.

The parameters ρ_{rij}^k , ξ^k and ω_r^k are determined by the Lavenberg – Marquardt optimization algorithm (LMA). At the beginning of the optimization algorithm, the plate natural frequencies ω_r^k and coefficients ρ_{rij}^k are computed from the maxima of the experimental transfer functions. The performance index for LMA is defined as follows

$$\mathfrak{J} = \min_{\omega} \frac{1}{2} \left\| F(\omega, h_{ij}(i\omega)) - h_{ij}^p(\omega) \right\|_2^2 = \frac{1}{2} \sum_{n=1}^q \left(F(\omega, h_{ij}(i\omega)_n) - h_{ij}^p(\omega)_n \right)^2, \quad (6.5)$$

where $h_{ij}(i\omega)$ denotes the approximation of the imaginary part of FRF (6.3), $h_{ij}^p(\omega)$ is the measurement data FRF and q is a number of samples of ω . The optimization is repeated for the iteratively changed initial conditions for each value ρ_{rij}^k .

6.3. Neural network system

6.3.1. Backpropagation algorithm

The neural networks are commonly used to solve problems where the solutions cannot be determined in terms of the exact solution. The simplest neural networks are built from neural cells arranged in layers. The input layer takes the data, processes it and passes it through to the neurons in the next layers. The AN response “comes out” from the neural network in the output layer. It is assumed that there is no connection between neurons in the same layer and each neuron of certain layer receives inputs only from the previous layer (e.g., Demuth and Beale 2002). The neural network “knowledge” about the problem is stored in weights associated with neurons.

The most often used teaching technique is called backpropagation. The method requires a set of inputs that are known as target values. The aim is to find the most appropriate weights corresponding to the neurons that can simulated the target values. The input samples are fed through the network numerous cycles and they are compared with the targets until the network recognizes the relationship between the inputs and outputs. One transmission of the signals and backpropagation of the errors is called an epoch. The forward pass through the network is the propagation of the signal from the input to the output. The actual response of the network is computed. The teaching is based on backward pass where the errors between the actual and target values travels from the outputs to the inputs indicating the necessary changes in the weights. The sum of errors of all the neurons must be minimized. The backpropagation algorithm is presented in detail in many papers and books, for example, by Bow (2002), Freeman (1994) and Hu and Hwang (2002).

The net functions of the hidden and output layer are given in the form

$$net_m^{h(p)} = \sum_{r=1}^R w_{mr}^h z_r^{(p)} + b_m^h, \quad (6.6)$$

$$net_k^{o(p)} = \sum_{m=1}^M w_{km}^o j_m^{(p)} + b_k^o, \quad (6.7)$$

where R denotes number of neurons in input layer and M is a number of neurons in hidden layer. The superscript p refers to a p^{th} input pattern and b is a bias. In the following example the sigmoid function is selected to relate the input from the m^{th} hidden layer neuron to the output layer neuron. The logarithmic sigmoid function can be written as

$$i_m^{(p)} = f_m^h \left(net_m^{h(p)} \right) = \frac{1}{1 + e^{-net_m^{h(p)}}}. \quad (6.8)$$

In this book the hyperbolic tangent sigmoid function is used,

$$i_m^{(p)} = f_m^h \left(net_m^{h(p)} \right) = \frac{1}{1 + e^{-2net_m^{h(p)}}} - 1. \quad (6.9)$$

In the presented ANN application, the output for the output layer neurons is given as an identity function

$$o_k^{(p)} = f_k^o \left(net_k^{o(p)} \right) = n_k^{o(p)}. \quad (6.10)$$

The error of the ANN prediction is defined as

$$E^{(p)} = \frac{1}{2} \sum_{k=1}^K \left(d_k^{(p)} - o_k^{(p)} \right)^2, \quad (6.11)$$

where K denotes the number of neurons in an output layer and $d_k^{(p)}$ is a known target. The global error can be expressed as a sum of errors of all patterns:

$$E = \sum_{p=1}^P E^{(p)}, \quad (6.12)$$

where P denotes the number of all patterns. Inserting equation (6.10) into equation (6.11) gives

$$E^{(p)} = \frac{1}{2} \sum_{k=1}^K \left(d_k^{(p)} - f_k^o \left(net_k^{o(p)} \right) \right)^2. \quad (6.13)$$

The gradient $E^{(p)}$ with respect to the weights of the output layer is

$$\begin{aligned} \frac{\partial E^{(p)}}{\partial w_{km}^o} &= - \left(d_k^{(p)} - o_k^{(p)} \right) \frac{\partial f_k^o \left(net_k^{o(p)} \right)}{\partial \left(net_k^{o(p)} \right)} \frac{\partial \left(net_k^{o(p)} \right)}{\partial w_{km}^o} = \\ &= - \left(d_k^{(p)} - o_k^{(p)} \right) f_k^{o'} \left(net_k^{o(p)} \right) i_m^{(p)}, \end{aligned} \quad (6.14)$$

whereas the gradient $E^{(p)}$ with respect to the weights of the hidden layer is

$$\frac{\partial E^{(p)}}{\partial w_{mr}^h} = - f_m^{h'} \left(net_m^{h(p)} \right) z_r^{(p)} \sum_{k=1}^K \left(d_k^{(p)} - o_k^{(p)} \right) f_k^{o'} \left(net_k^{o(p)} \right) w_{km}^o. \quad (6.15)$$

Finally, equations for weights update for both output and hidden layers, are found to be

$$w_{km}^o(t+1) = w_{km}^o(t) - \eta \frac{\partial E^{(p)}}{\partial w_{km}^o}, \quad (6.16)$$

$$w_{mr}^h(t+1) = w_{mr}^h(t) - \eta \frac{\partial E^{(p)}}{\partial w_{mr}^h}, \quad (6.17)$$

where t is iteration step and η denotes a learning rate. The weight at step $t+1$ is computed by subtracting from the weight at step t , the increment determined as a partial derivative of the error

with respect to the corresponding weight. It is assumed that the learning rate is the same in all neurons in all layers. The learning rate controls speed of computation convergence, i.e., small rate results in large number of iterations and problems with reaching the stopping criteria, while large learning rate may lead to the non convergent process (Demuth and Beale 2002).

The optimization procedure can be conducted by many variations of the numerical realization of the backpropagation algorithms like gradient descent algorithms with momentum, conjugated gradient algorithms or quasi-Newton algorithms, etc. In this study a variant of conjugated gradient algorithm called the scaled conjugate gradient method is used. Common gradient based methods modify the weights in the direction of the negative gradient. However, use of the performance function in the direction where it is decreasing most rapidly is not necessary accompanied by the fastest convergence (Demuth and Beale 2002). The fastest convergence can be obtained by search performed along the conjugate direction. The applied, in the following example, conjugated gradient algorithm has the ability to modify the step size at each iteration Moller (1993). This feature allows to avoid the time consuming line-search per learning iteration.

6.3.2. Architecture

The used network (Fig. 6.4) consists of four layers: input layer, two hidden layers and one output layer. The hyperbolic tangent sigmoid function was selected for the hidden layers and the linear transfer function was selected for the output layer. Input of the neural network is a 192-elements vector consisting of the first, second and third natural frequencies and first, second and third mode shapes. The first hidden layer has 80 neurons whereas the second hidden layer has 5 neurons. These numbers were chosen based on trial and effort simulations. The 2-element output indicates the presence of damage and the additional mass position.

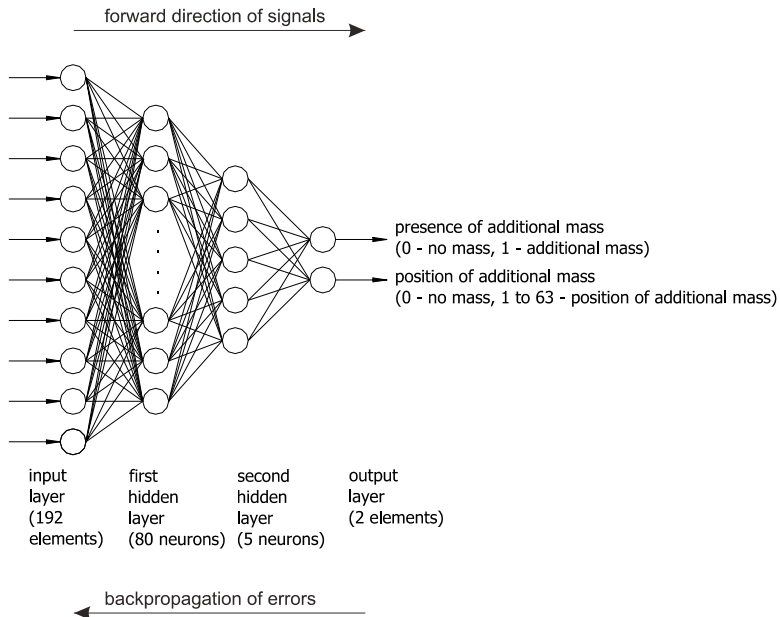


Fig. 6.4. Acceleration signal from ambient vibrations

6.4. Results

The natural frequencies determined from the dynamic tests are shown in Table 6.1. The frequencies obtained from both types of the tests are in very good agreement. The mode shapes identified from the ambient and forced vibrations for the case with and without mass are given in Fig. 6.5. The modes obtained from the ambient tests have irregular surfaces indicating the presence of noise. The modes computed from the forced vibration tests are smooth and very similar to the theoretical mode shapes (Chapter 2).

Table 6.1

Natural frequencies of the lowest three modes

Frequency	Ambient vibrations		Forced vibration tests	
	case 1	case 2	case 1	case 2
f_1 [Hz]	6.179	5.611	6.17	5.63
f_2 [Hz]	11.533	10.054	11.24	10.06
f_3 [Hz]	23.550	23.215	23.40	23.15

To show the difficulty of the model order selections in SSI method the stabilization diagram for the plate considered is given in Fig. 6.6. The “+” marks indicate the cases when both criteria (6.1) are fulfilled, “o” depicts the results when only the frequency criterion is satisfied and the letter “k” shows the cases when only the damping condition is fulfilled. The results in Fig. 6.6 show that only the first few frequencies can be identified. It is noted that the lowest three frequencies, considered in the neural network, are obtained in a very stable way with a large number of “+” marks.

The natural frequencies and the mode shapes, also from the numerical simulations were used as the inputs to the neural network. The FE model of the plate has been described in Chapter 5 and Appendix A. The 63 considered positions of the additional mass are depicted in Fig. 6.1. Additionally the neural system was trained on the experimental data for mass location at 10 different points and for the experimental data without an additional mass. The total number of input patterns used for training was 75. A detailed register of the input component data is presented in Table 6.2.

Table 6.2

Patterns for training of neural network

Input patterns (frequencies and mode shapes)	Number of patterns
numerical without mass	1
numerical with mass in point 1 to 63	63
experimental without mass (from forced vibration test)	1
experimental with mass in points 2,4,14,16,18,20,22,32,34,36 (from forced vibration test)	10
total	75

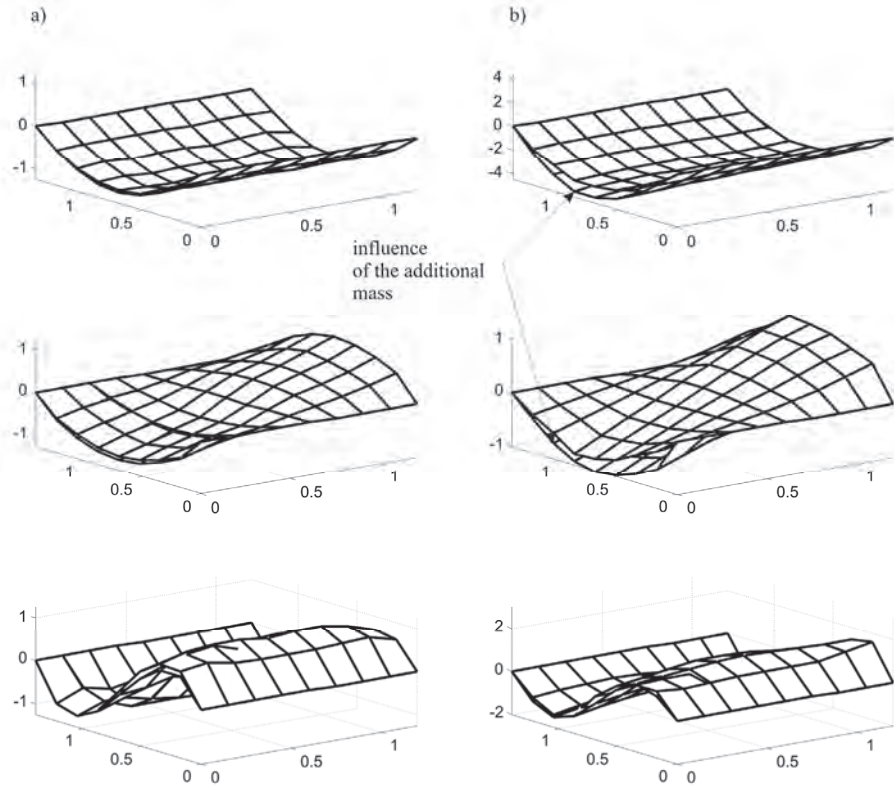


Fig. 6.5. Experimentally determined first two mode shapes without and with additional mass:
 a) Ambient vibration tests, b) Forced vibration tests

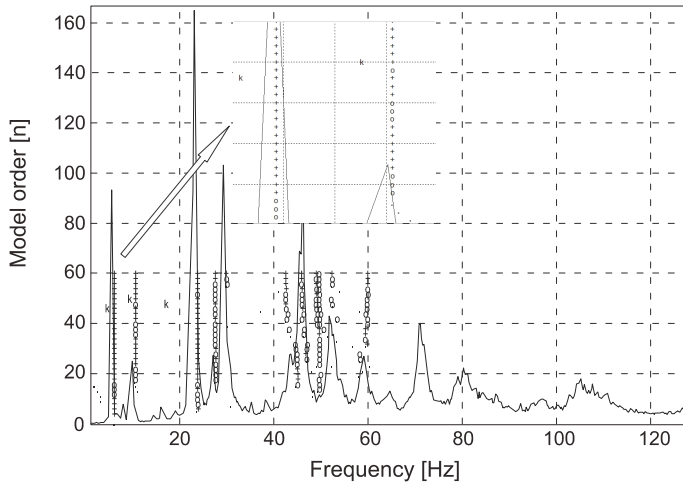


Fig. 6.6. Stabilization diagram

To demonstrate the feasibility of the prediction of the mass presence and its position prediction, the new patterns were fed into the trained neural network. The frequencies and mode shapes from the ambient and forced vibration tests, given in Table 6.3, were used as inputs to the network.

Table 6.3

Patterns for testing of neural network

Input patterns (frequencies and mode shapes)	Number of patterns
experimental without mass (from ambient vibration test)	1
experimental with mass in points 15, 28 (from ambient vibration test)	2
experimental with mass in points 1,3,5,15,17,19,21,23,35 (from forced vibration test)	9
total	12

The results of the neural network prediction of mass presence and its position are given in Fig. 6.7. In the case of data from the ambient vibration test as well as the data from forced vibration test the prediction of mass presence is very clear for all patterns. However, the information of mass location is in a good agreement with the actual values only for a 5 patterns.

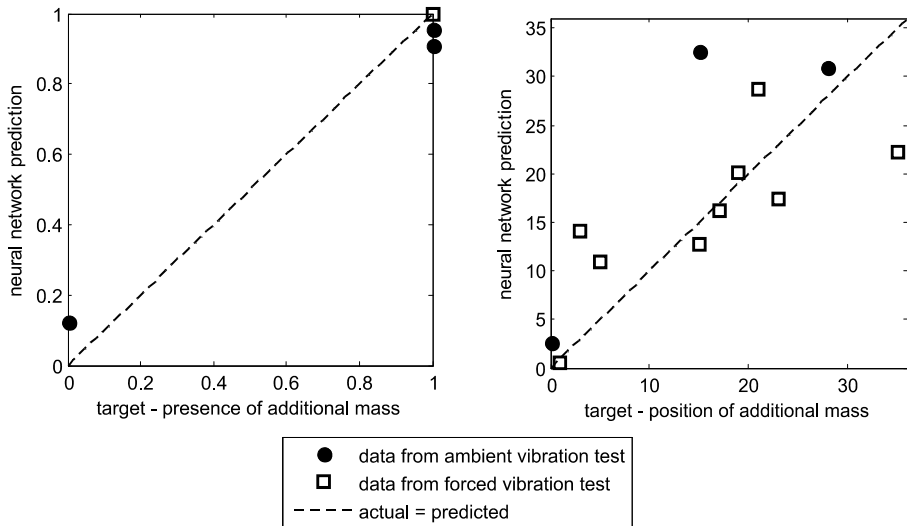


Fig. 6.7. Neural network predicted values of defect presence and its location

The artificial neural network techniques belong to the class of so-called soft computing and the ANN can predict mass position only with a certain probability. Nevertheless, the ANN predictions are relatively good. A detailed results are given in Table 6.4 and 6.5.

Table 6.4

Neural network predictions of the additional mass presence

Presence of mass	Ambient test			Forced test								
Actual	0	1	1	1	1	1	1	1	1	1	1	1
NN predicted	0.12	0.95	0.91	1.00	1.00	1.00	1.00	1.00	1.00	1.00	1.00	1.00

Table 6.5

Neural network predicted versus actual mass location

Position of additional mass	Ambient test			Forced test								
Actual	0	15	28	1	3	5	15	17	19	21	23	35
NN predicted	2.6	32.6	30.9	0.5	14.1	10.9	12.7	16.2	20.0	28.7	17.5	22.2

6.5. Conclusions

In this chapter the ambient vibration damage detection is combined with the damage localization technique based on the neural network system. The proposed approach is tested on plate natural frequencies and mode shapes determined from the experimental vibration tests and numerical simulations.

The trained neural network system can effectively identify the presence of the additional mass and can predict the mass location based on the mode shapes extracted from the forced vibration tests. The neural network tested on the ambient mode shapes can recognize the presence of the mass but the quality of the input data is insufficient to provide the mass location.

Practical applications of the studied damage detection strategy needs time consuming forced vibration tests to create the neural network expert system. However, once the system is created, simple and quick ambient vibration measurements of the structure can be conducted to give quick estimation of the structure health.

Acknowledgements

I wish to express my deep gratitude to Dr. Magdalena Rucka for her help, encouragement and support as well as passion in solving the scientific problems of damage detection. The gratitude should be extended to MSc Michał Hirsz and MSc Marcin Dudek, my Ph. D. students . Without their contribution this book could not be completed.

The support of the Head of the Structural Mechanics and Bridge Department, Prof. Jacek Chrościelewski, is gratefully acknowledged. I would like to thank all the members of my Department. Thanks are extended to all the Ph. D. and Master students whom I had the fortune to supervise.

The discussions with Prof. Zbigniew Zembaty and merciless comments from Prof. Paweł Kłosowski have considerably improved the important elements of this book. Their contribution is acknowledged. The final touch in the editorial work has been given by Associate Prof. Robert Jankowski and Stanisław Lipecki.

I am also grateful to the Faculty of Civil and Environmental Engineering Board: Prof. Hanna Obarska-Pempkowiak, Prof. Jerzy M. Sawicki, Associate Prof. Ireneusz Kreja, Prof. Jacek Tejchman, Dr. Marek Jasina, Dr. Arkadiusz Ostojski, Dr. Rafał Ossowski and Marek Lubowicki for their support and understanding, particularly, in my final work on the book. I am very thankful for the hundreds of annoying questions about the completeness of this book raised by the Head of the Dean's office, Mrs. Bożena Lorbiecka. I am very thankful to all the people, not mentioned here, who kept my work going on.

Finally I would like to thank my wife, Anita, for endless encouragement and time to work, as well as to my daughter, Sara and the twins Daria and Szymek for releasing me from reading evening stories during the last two months before publishing the book. I should also admit that our German Shepherd, Pit, involuntarily resigned from most of his everyday walks.

The book reports the research financed by the MNiSW grant N506 065 31/3149 entitled: "Multilevel damage detection system in engineering structures". The grant has been obtained, scientifically guided and supervised by author. Support obtained in this project considerably helped to complete Ph.D thesis of Michał Hirsz and Marcin Dudek.

Krzysztof Wilde

References

- Abdel-Ghaffar A. M.: Ambient vibration studies of Golden Gate bridge, I: Suspended structure. *Journal of Engineering Mechanics*, ASCE, 111(4), 1985, 463–482.
- Abdel-Ghaffar A. M., Housner G. W.: Ambient vibration tests of suspension bridge. *Journal of Engineering Mechanics Division*. ASCE, 104(5), 1978, 983–990.
- Abdelghani M., Goursat, M., Biolchini T.: On-line modal monitoring of aircraft structures under unknown excitation. *Mechanical Systems and Signal Processing* 13 (6), 1999, 839–853.
- Allemang R. J., Brown D. L.: A Correlation Coefficient for Modal Vector Analysis. 1th International Modal Analysis Conference (IMAC I), Orlando, Florida, November 1982, 110–116.
- Barai S. V., Padney P. C.: Time-delay neural networks in damage detection of railway bridges. *Advanced in Engineering Software*; 28(1), 1997, 1–10.
- Baruch M.: Optimization procedure to correct stiffness and flexibility matrices using vibration data. *IEEE Transactions on Aerospace and Electrical Systems*, AES-19(5), 1978, 711–729.
- Baruch M., Bar-Itzhack I. Y.: Optimal Weighted Orthogonalization of Measured Modes. *AIAA Journal*, 16(4), 1978, 346–351.
- Basu B., Gupta V. K.: Stochastic seismic response of single-degree-of-freedom systems through wavelets. *Engineering Structures* 22(12), 2000, 1714–1722.
- Berman A., Nagy E. J.: Improvement of large analytical modes using test data. *AIAA Journal*, 21(8), 1983, 1168–1173.
- Biswas M., Panday A. K., Samman M. M.: Diagnostic experimental spectral/modal analysis of a highway bridge. *The international Journal of Analytical and Experimental Modal Analysis*. 5(1), 1990, 33–42.
- Boggess A., Narcowich F. J.: *A First Course in Wavelets with Fourier Analysis*. Beijing: Publishing House of Electronics Industry 2002.
- Bow S.-T.: *Pattern Recognition and Image Preprocessing*. New York: Marcel Dekker Inc. 2002.
- Brownjohn J. M. W., Dumanoglu A. A., Severn R. T., Blakeborough A. B.: Ambient vibration survey of the Bosphorus Suspension Bridge. *Earthquake Engineering and Structural Dynamics* 18(2), 1989, 263–283.
- Brownjohn J. M. W., Dumanoglu A. A., Severn R. T., Taylor C. A.: Ambient vibration measurements of the Humber Suspension Bridge and comparison with calculated characteristics. *Proceedings Institution of Civil Engineers, Part 2*, 83, 1987, 561–600.
- Cabell R. H., Fuller C. R., O'Brien W. F.: Neural network modeling of oscillatory loads and fatigue damage estimation of helicopter components. *Journal of Sounds and Vibration* 209(2), 1998, 329–342.
- Catbas F. N., Aktan A. E.: Vibration testing of a long span bridge: Objectives and challenges. *Proceedings of 17th IMAC, Vol. 1*, 1999, 166–173.
- Cawley P., Adams R. D.: The location of defects in structures from measurements natural frequencies. *Journal of Strain Analysis* 14 (2), 1979, 49–57.

- Chan Y. T.: Wavelet basics. Boston – Dordrecht – London: Kluwer Academic Publishers 1995.
- Chang C.-C., Chen L.-W.: Damage detection of a rectangular plate by spatial wavelet based approach. *Applied Acoustic* 65(12), 2004, 819–832.
- Chang C.-C., Chen L.-W.: Vibration damage detection of a Timoshenko beam by spatial wavelet based approach. *Applied Acoustics* 64(12), 2003, 1217–1240.
- Chmielewski T., Zembaty Z.: *Podstawy dynamiki budowli*. Warszawa: Arkady 1998.
- Chopra A. K.: *Dynamics of structures*. Upper Saddle River. New Jersey: Prentice Hall 2001.
- Chróścielewski J.: Analiza numeryczna płyt uźebrowanych w zakresie nieliniowości geometrycznej i materiałowej metodą elementów skończonych (FEM analysis of stiffened plates with geometric and material nonlinearities). Rozprawa doktorska. Politechnika Gdańska, Wydz. Budownictwa Lądowego 1983.
- Clough R. W., Penzien J.: *Dynamics of structures*. McGraw-Hill Inc. 1993.
- Cuhna A., Caetano E, Delgado R.: Dynamic tests on large cable-stayed bridge. *Journal of Bridge Engineering*. 6(1), 2001, 54–62.
- Daubechies I.: *Ten lectures on wavelet*. Philadelphia: Society for Industrial and Applied Mathematics 1992.
- Demuth H., Beale M.: *Neural networks toolbox*. The MathWorks Inc. 2002.
- Doebling S. W., Farrar C. R., Prime M. B., Shevitz D. W.: *Damage Identification and Health Monitoring of Structural and Mechanical Systems From Changes in Their Vibration Characteristics: A Literature Review*, Los Alamos National Laboratory Report LA-13070-MS, May 1996.
- Douka E., Loutridis S., Trochidis A.: Crack identification in beams using wavelet analysis. *International Journal of Solid and Structures* 40(13–14), 2003, 3557–3569.
- Douka E., Loutridis S., Trochidis A.: Crack identification in plates using wavelet analysis. *Journal of Sound and Vibration* 270(1–2), 2004, 279–295.
- Dudek M.: Identyfikacja parametrów dynamicznych konstrukcji mostowych na baize drgań wywołanych obciążeniem środowiskowym. Rozprawa doktorska, Politechnika Gdańska, Wydział Inżynierii Lądowej i Środowiska, 2008.
- Farrar C. R., James III G. H.: System identification from ambient vibration measurements on a bridge. *Journal of Sound and Vibration*, 205(1), 1997, 1–18.
- Farrar C. R., Doebling S. W.: *Damage detection. Field Applications to Large Structures* 1998.
- Flores-Santiago O., Link M.: *Localization Techniques for Parametric Updating of Dynamic Mathematical Models*. International Forum on Aeroelasticity and Structural Dynamics, Strasbourg, France, May 1993.
- Fox R., Kapoor M.: Rate of Change of Eigenvalues and Eigenvectors. *AIAA Journal*, 6, 1968, 2426–2429.
- Freeman J. A.: *Simulating neural networks with Mathematica*. Addison-Wesley Publishing Company Inc. 1994.
- Friswell M. I., Mottershead J. E.: *Finite Element Model Updating in Structural Dynamics*. Kluwer Academic Publishers 1995.
- Gentile A., Messina A.: On the continuous wavelet transforms applied to discrete vibrational data for detecting open cracks in damaged beams. *International Journal of Solid and Structures* 40(2), 2003, 295–315.
- Ghoshal A., Sundaresan M. J., Schulz M. J., Pai P. F.: Structural health monitoring techniques for wind turbine blades. *Journal of Wind Engineering and Industrial Aerodynamics* 85 (3), 2000, 309–324.

- Glabisz W.: Pakietowa analiza falkowa w zagadnieniach mechaniki. Wrocław: Oficyna Wydawnicza Politechniki Wrocławskiej 2004.
- Gurley K., Kareem A.: Application of wavelet transforms in earthquake, wind and ocean engineering. *Engineering Structures* 21(2), 1999, 149–167.
- Guyan R. J.: Reduction of Stiffness and Mass Matrices. *AIAA Journal*, 3(2), 1965, 380.
- Ho B. L., Kalman R. E.: Effective construction of linear state-variable models from input/output functions”, *Regelungstechnik*, Tom 14, Nr 12, 1996, 545–548.
- Hirsz M., Wilde K.: Identification of plate dynamic parameters for structural health monitoring. The 8th SSTA Conference “Shell Structures: Theory and Applications”, Gdańsk – Jurata, Poland, 12–14 October 2005.
- Hirsz M.: Finie element model updating on experimental model parameters. *Rozprawa doktorska*, Politechnika Gdańska, Wydział Inżynierii Lądowej i Środowiska, 2008.
- Hoła J., Schabowicz K.: New technique of nondestructive assessment of concrete strength using artificial intelligence. *NDT&E International* 38(4), 2005, 251–259.
- Hong J.-C., Kim Y. Y., Lee H. C., Lee Y. W.: Damage detection using Lipschitz exponent estimated by the wavelet transform: applications to vibration modes of a beam. *International Journal of Solid and Structures* 39(7), 2002, 1803–1846.
- Hou Z., Noori M., Amand R. S.: Wavelet-based approach for structural damage detection. *Journal of Engineering Mechanics* 126(7), 2000, 677–683.
- Hu Y. H., Hwang J.-N.: *Handbook of neural networks signal processing*. CRC Press LLC 2002.
- Huang N. E.: The empirical mode decomposition and the Hilbert spectrum for nonlinear and non-stationary time series analysis, *Proceedings of Royal Society of London*, No. 454, 1998, 903–995.
- Idichandy V. G., Ganapathy C.: Modal parameter for structural integrity of fixed offshore platforme, *Experimental Mechanics*, 30(4), 1990, 382–391.
- Irons B. M.: Structural Eigenvalues Problems: Elimination of Unwanted Variables. *AIAA Journal*, Vol. 3, May 1965, 961–962.
- Juang J. N.: *Applied System Identification*. New Jersey: PTR Prentice-Hall Inc. 1994.
- Juang J. N., Pappa R. S.: An eigensystem realization algorithm for modal parameter identification and model reduction”, *Journal of Guidance, Control, and Dynamics*, nr 8 (5), 1985, 620–627.
- Kaiser G.: *A Friendly Guide to Wavelets*. Boston–Basel–Berlin: Birkhauser 1994.
- Kalman R. E.: A new approach to linear filtering and prediction problems. *Transaction of the ASME – Journal of Basic Engineering*, 82 (seria D), 1960, 35 – 45.
- Kao C. Y., Hung S.-L.: Detection of structural damage via free vibration responses generated by approximating artificial neural networks. *Computer & Structures* 81(28–29), 2003, 2631–2644.
- Kato M., Shimada S.: Vibration of PC bridge during failure process. *Journal of Structural Engineering*, ASCE, 112(7), 1986, 1692–1703.
- Kim H., Melhem H.: Damage detection of structures by wavelet analysis. *Engineering Structures* 26(3), 2004, 347–362.
- Kim J. T., Stabbs N.: Improved damage identification method based on modal information. *Journal of Sound and Vibration* 252(2), 2002, 223–238.
- Kim J.-T., Ryu Y.-S., Cho H.-M., Stabbs N.: Damage identification in beam-type structures: frequency-based method vs mode-shape-based method. *Engineering Structures* 25(1), 2003, 57–67.
- Kokot S., Zembaty Z.: Reconstruction problem of reinforced concrete beams under harmonic excitations, *Key Engineering Materials*, Trans Tech Publications Ltd., Vol. 347, 2007, 691–696.

- Kucharski T.: Systemy pomiarów drgań mechanicznych. Warszawa: Wydawnictwa Naukowo-Techniczne 2002.
- Kung S. Y.: A new identification and model reduction algorithm via singular value decomposition, Proceedings of the 12th Asilomar Conference on Circuits, Systems and Computers, Pacific Grove, California, 1978, 705–714.
- Kuźniar K., Waszczyszyn Z.: Neural analysis of vibration problems of real flat buildings and data pre-processing. *Engineering Structures* 24(10), 2002, 1327–1335.
- Lardies J., Gouttebroze S.: Identificatin of modal parameters using the wavelet transform. *International Journal of Mechanical Sciences* 44(11), 2002, 2263–2283.
- Lieven N. A., Waters T. P.: Error Location Using Normalised Cross Orthogonality. Proceeding of the 12th International Modal Analysis Conference (IMAC XII), Honolulu, Hawaii, U.S.A. 1994, 761–764.
- Lieven N. A.: Spatial Correlation of Mode Shapes, the Coordinate Modal Assurance Criterion. The 6th International Modal Analysis Conference (IMAC VI), Kissimmee, Florida, February 1988, 690–695.
- Lin R. M., Lim M. K., Du H.: Improved inverse eigensensitivity method for structural analytical model updating. *Transactions of the ASME, Journal of Vibration and Acoustic*, Vol. 117, 1995, 192–198.
- Link M.: Updating of Analytical Models – Procedures and Experience. Conference on Modern Practice in Stress and Vibration Analysis, Sheffield, England, April 1993, 35–52.
- Liu G. R., Han, W.: *Computational inverse techniques in nondestructive evaluation*, CRC Press LLC 2003.
- Loutridis S., Douka E., Trochidis A.: Crack identification in double-cracked beams using wavelet analysis. *Journal of Sound and Vibration* 277(4–5), 2004, 1025–1039.
- Maia N. M. M., Silva J. M. M.: *Theoretical and experimental modal analysis*. Baldock – Hertfordshire: Research Studies Press Ltd. 1997.
- Mallat S., Hwang W. L.: Singularity detection and processing with wavelets. *IEEE Transaction on Information Theory* 38(2), 1992, 617–643.
- Mallat S., Zhong S.: Characterization of signals from multiscale edges. *IEEE Transaction on Pattern Analysis and Machine Intelligence* 14(7), 1992, 710–732.
- Mallat S.: *A wavelet tour of signal processing*. Academic Press 1998.
- Mazurek, D. F. and DeWolf, J. T. 1978. Experimental study on bridge monitoring technique. *Journal of Structural Engineering*. ASCE. 116(9), 2532–2549.
- McConnell K. G.: *Vibration Testing: Theory and Practice*. New York: John Wiley and Sons, Inc. 1995.
- Meirovitch L.: *Dynamics and control of structures*. New York: John Wiley and Sons, Inc. 1990.
- Meirovitch L.: *Fundamentals of vibrations*. Mc Graw Hill 2001.
- Melhem H., Kim H.: Damage detection in concrete by Fourier and wavelet analyses, *Journal of Engineering Mechanics* 129(5), 2003, 571–577.
- Messina A.: Detecting damage in beams through digital differentiator filters and continuous wavelet transforms. *Journal of Sound and Vibration* 272(1–2), 2004, 385–412.
- Meyer Y.: *Wavelets. Algorithms and Applications*. Philadelphia: Society for Industrial and Applied Mathematics 1993.

- Mirza M. S., Ferdjani O., Hadj-Arab A., Joucdar K., Khaled A., Razaqpur A. G.: An experimental study of static and dynamic responses of prestressed concrete box girder bridges, *Canadian Journal of Civil Engineering*, 17(3), 1990, 481–493.
- Misiti M., Misiti Y., Oppenheim G., Poggi J.-M.: *Wavelet toolbox*. The MathWorks Inc. 2000.
- Moller M. F.: A scaled conjugated gradient algorithm for fast supervised learning. *Neural Networks* 6(4), 1993, 525–533.
- Mottershead J. E., Friswell M. I.: Model Updatind in Structural Dynamics: A Survey. *Journal of Sound and Vibration*, 167(2), 1993, 347–375.
- Nichols J. M.: Structural health monitoring of offshore structures using ambient vibrations. *Applied Ocean Research* 25 (3), 2003, 101–114.
- Niedostatkiewicz M., Rucka M., Wilde K.: Application of time-frequency methods for analysis of dynamic silo flow. The 8th SSTA Conference “Shell Structures: Theory and Applications”, Gdańsk – Jurata, Poland, 12–14 October 2005, Londyn: Balkema 2005, 393–397.
- Niedostatkiewicz M., Tejchman J.: Experimental and theoretical studies on resonance dynamic effects during silo flow. *Powder Handling and Processing*, 15, 1, 2003, 36–42.
- O’Callahan J. C.: A Procedure for an Improve Reduced System (IRS) Model. 7th International Modal Conference, Las Vegas, January 1989, 17–21.
- O’Callahan J. C., Avitabile O., Rieme, R.: System Equivalent Reduction Expansion Process. 7th International Modal Conference, Las Vegas, January 1989, 29–37.
- Okafor A. C., Dutta A.: Optimal ultrasonic pulse repetition rate for damage detection in plates using neural networks. *NDT&E International* 34(7), 2001, 469–481.
- Omenzetter P., Brownjohn J. M. W., Moyo P.: Identification of unusual events in multi-channel bridge monitoring data. *Mechanical Systems and Signal Processing* 18 (2), 2004, 409–430.
- Omenzetter P., Wilde K., Fujino Y.: Study on passive deck-flaps flutter control system on full bridge model. I: Theory, *Journal of Engineering Mechanics ASCE*, Vol. 128, No. 3, 2002a, 264–279.
- Omenzetter P., Wilde K., Fujino Y.: Study on passive deck-flaps flutter control system on full bridge model. II: Theory, *Journal of Engineering Mechanics ASCE*, Vol. 128, No. 3, 2002b, 280–286.
- Ovanesova A. V., Suárez L.E.: Application of wavelet transform to damage detection in frame structures. *Engineering Structures* 26(1), 2004, 39–49.
- Overschee P., De Moor B.: *Subspace Identification for Linear Systems. Theory, Implementation, Applications*. Kluwer Academic Publishers 1996.
- Pai P.F., Young L.G.: Damage detection of beams using operational deflection shapes. *International Journal of Solid and Structures* 38(18), 2001, 3161–3192.
- Pandey A. K., Biwas M., Samman M. M.: Damage detection from changes in curvature mode shapes. *Journal of Sound and Vibration* 145(2), 1991, 321–332.
- Paz M.: Dynamic Condensation. *AIAA Journal*, Vol. 22, May 1984, 724–727.
- Quek S.-T., Wang Q., Zhang L., Ang K.-K.: Sensitivity analysis of crack detection in beams by wavelet technique. *International Journal of Mechanical Sciences* 43(12), 2001, 2899–2910.
- Ranjith P, Baby P. C, Joseph P.: ECG analysis using wavelet transform: application to myocardial ischemia detection. *ITMB-RBM* 24(1), 2003, 44–47.
- Rucka M.: Wavelet analysis in detection and localization of damage in engineering structures. *Rozprawa doktorska. Politechnika Gdańska, Wydz. Inżynierii Lądowej i Środowiska* 2005.
- Rucka M., Wilde K.: Application of continuous wavelet transform in vibration based damage detection method for beam and plates. *Journal of Sound and Vibration* 297, 2006b, 536–550.

- Rucka M., Wilde K.: Application of wavelet analysis in damage detection and localization. Gdańsk: Wydawnictwo Politechniki Gdańskiej 2007.
- Rucka M., Wilde K.: Crack identification using wavelets on experimental static deflection profiles. *Engineering Structures* 28(2), 2006a, 279–288.
- Rucka M., Wilde K.: Damage location in beam and plate structures by wavelet analysis of experimentally determined mode shapes. *Key Engineering Materials* 293–294, 2005a, 313–320.
- Rucka M., Wilde K.: Lokalizacja uszkodzeń konstrukcji belkowych za pomocą badań dynamicznych i analizy falkowej. *Inżynieria i Budownictwo* 6, 2005b, 333–335.
- Rucka M., Wilde K.: Numerical simulation of damage detection in rectangular plate by two-dimensional wavelet transform. *International Workshop on simulations in urban engineering*, Gdańsk, Poland 2004, 205–208.
- Rucka M., Wilde K.: *Dynamika budowli z przykładami w środowisku MATLAB®*. Wydawnictwo Politechniki Gdańskiej, 2008.
- Sahin M., Sheno R. A.: Quantification and localization of damage in beam-like structures by using artificial neural networks with experimental validation. *Engineering Structures* 25(14), 2003, 1785–1802.
- Salane H. J., Baldwin J. W.: Identification of modal properties of bridges. *Journal of Structural Engineering*. ASCE. 116(7), 1990, 2008–2021.
- Savage. R. J., Hewlett. P. C.: A new NDT method for structural integrity assessment. *NDT International* 11, 1978, 61–66.
- Siringoringo D. M., Fujino Y.: System identification of suspension bridge from ambient vibration response. *Engineering Structures*. 30(2), 2008, 462–477.
- Sivannarayana N., Reddy D. C.: Biorthogonal wavelet transforms for ECG parameters estimation. *Medical Engineering & Physics* 21(3), 1999, 167–174.
- Slavič J., Simonovski I., Boltežar M.: Damping identification using a continuous wavelet transform: application to real data. *Journal of Sound and Vibration* 262(2), 2003, 291–307.
- Sohn H., Farrar C.R., Hemez F. M., Shunk D. D., Stinemates S. W., Nadler B. R., Czarnecki J. J.: *A Review of Structural Health Monitoring Literature from 1996 – 2001*, Los Alamos National Laboratory report LA-13976-MS, 2004.
- Srinivasen M. G., Kot C.: Effects of damage on the modal parameters of a cylindrical shell 10th International Modal Analysis Conference, San Diego, California, 1992, 529–535.
- Strang G., Nguyen T.: *Wavelets and Filter Banks*. Wellesley: Wellesley-Cambridge Press 1996.
- Struzik R. S.: Wavelet methods in (financial) time-series processing. *Physica A* 296(1–2), 2001, 307–319.
- Sun. X., Hardy H. R.: An investigation on applicability of modal analysis as nondestructive evaluation method in geotechnical engineering. 10th International Modal Analysis Conference. San Diego, California. 1, 1992, 9–19.
- Szymczak C., Tomaszewska A.: O diagnostyce budowli na podstawie pomiarów drgań *Inżynieria i Budownictwo*, R. 63, nr 11, 2007, 579–582.
- Tejchman J.: Silo-quake – measurements, a numerical polar approach and a way for its suppression, *Thin-Walled Structures*, 31/1–3, 1998, 137–158.
- Wang Q., Deng X.: Damage detection with spatial wavelets. *International Journal of Solid and Structures* 36(23), 1999, 3443–3468.
- Wang W. J., McFadden P. D.: Application of wavelets to gearbox vibration signals for fault detection. *Journal of Sound and Vibration* 192(5), 1996, 927–939.

- Waszczyszyn Z., Ziemiański L.: Neural networks in mechanics of structures and materials – new results and prospects of application. *Computer & Structures* 79(22-25), 2001, 2261–2276.
- Waters T. P.: Finite Element Model Updating Using Measured Frequency Response Function. Ph.D. Thesis, Department of Aerospace Engineering, University of Bristol, U.K. 1995.
- Wei F-S.: Structural dynamic model modification using vibration test data. *AIAA Journal*, 28(1), 1990, 175–177.
- West W. M.: Illustration of the Use of Modal Assurance Criterion to Detect Structural Changes in an Orbiter Test Specimen, in *Proc. Air Force Conference on Aircraft Structural Integrity*, 1984, 1–6.
- Wilde K., Hirsz M., Dudek M., Rucka M.: Experimental study on multilevel damage detection strategy for plate structures, *Fourth World Conference on Structural Control and Monitoring*, San Diego, USA, 2006, 1–8.
- Wilde K.: Passive aerodynamic control of wind induced instabilities in long span bridges. *Seria Monografie nr 30*. Gdańsk: Wydawnictwo Politechniki Gdańskiej 2002.
- Wilde K., Fujino Y., Masukawa J.: Time domain modeling of bridge deck flutter *Journal of Structural Engineering/Earthquake Engineering*, Japanese Society of Civil Engineers, July 1996, Vol. 13, 93s–104s.
- Wilde K., Fujino Y.: Aerodynamic control of bridge deck flutter by active surfaces, *Journal of Engineering Mechanics*, American Society of Civil Engineers, Vol. 124, No. 7, 1998, 718–727.
- Wilde K., Rucka M., Tejchman J.: Silo music – Mechanism of dynamic flow and structure interaction, *Powder Technology*, doi: 10.1016/j.powtec.2007.11.08
- Yam L. H., Yan Y. J., Jiang J. S.: Vibration-based damage detection for composite structures using wavelet transform and neural identification. *Composite Structures* 60(4), 2003, 403–412.
- Yeung W. T., Smith J. W.: Damage detection in bridges using neural networks for pattern recognition of vibration signatures. *Engineering Structures* 27(5), 2005, 685–698.
- Yuen M. M. F.: A numerical study of the eigenparameters of damaged cantilever. *Journal of Sound and Vibration* 103(3), 1985, 301–310.
- Yun C.-B., Yi J.-H., Bahng E. Y.: Joints damage of framed structures using a neural networks technique. *Engineering Structures* 23(5), 2001, 425–435.
- Zacharias J., Hartmann C., Delgado A.: Damage detection on crates of beverages by artificial neural networks trained with finite-element data. *Computer methods in applied mechanics and engineering* 193(6–8), 2004, 561–574.
- Zapico J. L., González M. P., Worden K.: Damage assessment using neural networks. *Mechanical Systems and Signal Processing* 17(1), 2003, 119–125.
- Zembaty Z., Kowalski M., Pospisil S.: Dynamic identification of a reinforced concrete frame in progressive states of damage, *Engineering Structures* 28, 2006, 668–681.
- Zembaty Z., Kowalski M.: Dynamic identification of a model of brick masonry building, *Archives of Civil Engineering*, XLVI, No. 1, 2000, 107–136.
- Zieliński T.: *Cyfrowe przetwarzanie sygnałów. Od teorii do zastosowań*. Warszawa: WKŁ 2006.
- Zienkiewicz O. C., Taylor. R. L.: *The Finite Element Method*, Vol. 1, 4th ed. London: McGraw-Hill 1988.
- Zubaydi A., Haddara M. R., Swamidas A. S. J.: Damage identification in a ship's structure using neural networks. *Ocean Engineering* 29(10), 2002, 1187–1200.

Finite elements of beam and plate

The FEM leads to the dynamic models of engineering structures described by a discrete set of matrix equations. The properties of a continuous structure are represented in terms of mass, stiffness and damping matrices. The mass and stiffness matrices are assembled from the contribution of the individual finite elements with simple shapes and in the most common applications the damping matrix is assembled as a combination of the mass and stiffness matrices. Each finite element possesses a mathematical formula which is associated with a simple geometrical description. The process of the structure division into such simple elements is called discretization. Element edges are defined when nodal points are connected by unique polynomial curve or surface. The well known formulated types of elements in the FEM are beams, plates and shells. The variational formulation of the FEM can be considered as the extension of the Ritz method.

The general formulation of the element mass and stiffness matrices can be presented in the form

$$\mathbf{M}^e = \int_{-1}^1 \int_{-1}^1 \int_{-1}^1 \mathbf{N}^T \rho \mathbf{N} \det(\mathbf{J}) d\xi_1 d\xi_2 d\xi_3, \quad (\text{A.1})$$

$$\mathbf{K}^e = \int_{-1}^1 \int_{-1}^1 \int_{-1}^1 \mathbf{B}^T \mathbf{D} \mathbf{B} \det(\mathbf{J}) d\xi_1 d\xi_2 d\xi_3, \quad (\text{A.2})$$

where \mathbf{N} is the matrix of shape functions (shape matrix), ρ represents mass density, \mathbf{B} is the matrix of shape functions derivatives, \mathbf{J} is the Jacobian matrix which defines relationship between the local and global coordinates $dx dy dz = \det(\mathbf{J}) d\xi_1 d\xi_2 d\xi_3$ for isoparametric elements. In this book two types of finite elements will be used: one-dimensional Euler beam and quadrilateral plate element with four nodes. The finite element stiffness and mass matrices are aggregated into the global stiffness and mass matrices that together with the selected damping matrix define the dynamic system in so called Spatial Model.

A.1. One-dimensional Eulerian beam element in 2D space

The stiffness matrix of one-dimensional Euler beam element (Fig. A.1) can be obtained either from the differential equation of the beam bending deformation line or with use of standard FEM procedure resulting in the approximation of such line. This beam element has two nodes i and k . Each node has two degrees of freedom: the translation v and the angle of rotation φ . The length of the element is denoted by L and the cross section area is A . In this case equation (A.1) and (A.2) in the local coordinates can be simplified to the forms

$$\mathbf{M}^e = \rho A \int_0^L \mathbf{N}(x)^T \mathbf{N}(x) dx, \quad (\text{A.3})$$

and

$$\mathbf{K}^e = EI \int_0^L \mathbf{N}''(x)^T \mathbf{N}''(x) dx, \quad (\text{A.4})$$

where E denotes Young's modulus, I denotes moment of inertia with respect to the z axis and EI is the bending rigidity. The solutions of equations (A.3) and (A.4) are the following matrices,

$$\mathbf{M}^e = \begin{bmatrix} 156 & 22L & 54 & -13L \\ 22L & 4L^2 & 13L & -3L^2 \\ 54 & 13L & 156 & -22L \\ -13L & -3L^2 & -22L & 4L^2 \end{bmatrix} \frac{\mu L}{420}, \quad (\text{A.5})$$

$$\mathbf{K}^e = \begin{bmatrix} 12 & 6L & -12 & 6L \\ 6L & 4L^2 & -6L & 2L^2 \\ -12 & -6L & 12 & -6L \\ 6L & 2L^2 & -6L & 4L^2 \end{bmatrix} \frac{EI}{L^3}. \quad (\text{A.6})$$

where the μ is the weight distribution on the length of the element.

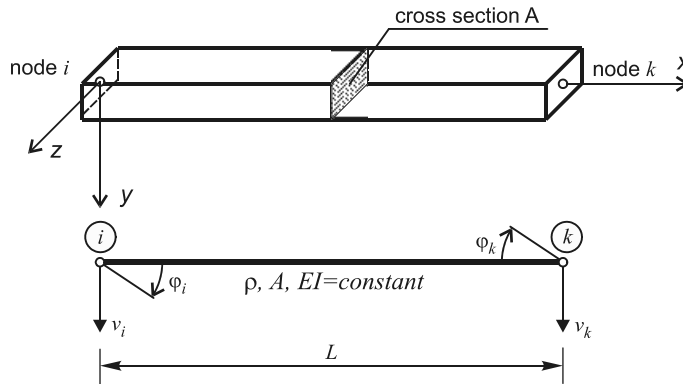


Fig. A.1. One dimensional beam element

The element matrices \mathbf{M}^e and \mathbf{K}^e are assembled into the global \mathbf{M} mass and stiffness \mathbf{K} matrices

$$\mathbf{K} = \mathbf{A}_{e=1}^{Ne} \mathbf{K}^e, \quad \mathbf{M} = \mathbf{A}_{e=1}^{Ne} \mathbf{M}^e. \quad (\text{A.7})$$

A.2. Plate finite element

The rectangular plate element is shown in Fig. A.2. The length of one side is denoted by a and the perpendicular side is b . The element poses four nodes (i, j, k and l) and each node has a three degrees of freedom: translation w and two angles of rotation θ_x and θ_y .

which are the derivatives of translation w . Therefore, there are 12 degrees of freedom per element. The interpolation functions are bi-cubic polynomials and the element achieves C^1 continuity. The coefficients of the element mass and stiffness matrices has been presented by Zienkiewicz and Taylor (1972, the 4th edition in 1998). In this book the derivation presented by Chróścielewski (1983) has been adopted.

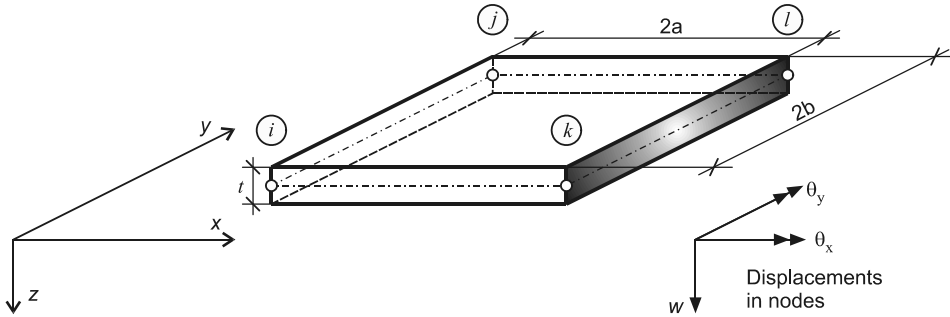


Fig. A.2. Rectangular plate element

In this case equations (A.1) and (A.2) in the local coordinates can be simplified to the formulas,

$$\mathbf{M}^e = \int_0^{2a} \int_0^{2b} \mathbf{N}^T \rho \mathbf{N} dx dy, \tag{A.8}$$

and

$$\mathbf{K}^e = \int_0^{2a} \int_0^{2b} \mathbf{B}^T \mathbf{D} \mathbf{B} dx dy. \tag{A.9}$$

If the t (thickness of the plate) and ρ (mass density) are constant the equation (A.8) and (A.9) can be express in the form

$$\mathbf{M}^e = \rho t \{ \mathbf{C}^{-1} \}^T \left(\int_0^{2a} \int_0^{2b} \mathbf{P}^T \mathbf{P} dx dy \right) \mathbf{C}^{-1}, \tag{A.10}$$

and

$$\mathbf{K}^e = \{ \mathbf{C}^{-1} \}^T \left(\int_0^{2a} \int_0^{2b} \mathbf{Q}^T \mathbf{D} \mathbf{Q} dx dy \right) \mathbf{C}^{-1}, \tag{A.11}$$

and the matrix \mathbf{C} is defined by Zienkiewicz and Taylor (1998).

The stiffness matrix of the rectangular plate element can be describe in the partial form as

$$\mathbf{K}^e = \frac{1}{60ab} \mathbf{L} \{ D_x \mathbf{K}_1^e + D_y \mathbf{K}_2^e + D_1 \mathbf{K}_3^e + D_{xy} \mathbf{K}_4^e \} \mathbf{L}, \tag{A.12}$$

where D_x , D_y , D_{xy} and D_1 are the components of the elasticity matrix \mathbf{D} for the orthotropic plate

Model reduction methods

To verify the FE model of an existing engineering structure with the in situ measurements, it is necessary to modify the models degrees of freedom. The response of the structure is, in general, measured at the accessible chosen locations. The number of the measurement points is limited. Practically it is possible to record only the translational response, while most of the common FE models include also rotational degrees of freedom. In addition the frequency range of the measurements is limited due to limitations on number of sensors and the data acquisition systems. Thus, only limited natural frequencies and mode shapes can be verified by FE model. In most cases the experimental data are incomplete in comparison to the numerical results. To conduct the FE model verification it is necessary to perform a reduction of the numerical model.

The most common way of FE model reduction is elimination of “not important” degrees of freedom called secondary or slave coordinates while remaining degrees of freedom necessary for correct descriptions of the structure dynamics. The “important” degrees of freedom are called the primary or master coordinates. The purpose of the model reduction is to eliminate the largest number of secondary degrees such as the reduced model can be precisely updated on the available experimental data. The most popular methods for model reduction are presented in the following sections.

B.1. Static Reduction (Guyan Reduction)

One of the oldest and most popular reduction methods is static reduction introduced by Guyan (1965) and Irons (1965). This is the simplest reduction method in finite element modeling. The equations of motion for the undamped system subjected by forces acting on the master coordinates can be written in the partial form as

$$\begin{bmatrix} \mathbf{M}_{mm} & \mathbf{M}_{ms} \\ \mathbf{M}_{sm} & \mathbf{M}_{ss} \end{bmatrix} \begin{Bmatrix} \ddot{\mathbf{x}}_m \\ \ddot{\mathbf{x}}_s \end{Bmatrix} + \begin{bmatrix} \mathbf{K}_{mm} & \mathbf{K}_{ms} \\ \mathbf{K}_{sm} & \mathbf{K}_{ss} \end{bmatrix} \begin{Bmatrix} \mathbf{x}_m \\ \mathbf{x}_s \end{Bmatrix} = \begin{Bmatrix} \mathbf{P}_m \\ \mathbf{0}_s \end{Bmatrix}. \quad (\text{B.1})$$

Variables m and s describe the chosen matrix partition on master and slave degrees of freedom. Neglecting the inertia terms for the second part of equation it can be written equation which may be used to eliminate the slave degrees of freedom

$$\mathbf{K}_{sm} \mathbf{x}_m + \mathbf{K}_{ss} \mathbf{x}_s = \mathbf{0}_s. \quad (\text{B.2})$$

All the coordinates can be related to the master coordinates by using the equation,

$$\begin{Bmatrix} \mathbf{x}_m \\ \mathbf{x}_s \end{Bmatrix} = \begin{bmatrix} \mathbf{I} \\ -\mathbf{K}_{ss}^{-1} \mathbf{K}_{sm} \end{bmatrix} \mathbf{x}_m = \mathbf{T}_s \mathbf{x}_m, \quad (\text{B.3})$$

where \mathbf{T}_s denotes the static transformation matrix which can be defined from the equation (B.3) as

$$\mathbf{T}_s = \begin{bmatrix} \mathbf{I} \\ -\mathbf{K}_{ss}^{-1}\mathbf{K}_{sm} \end{bmatrix}. \quad (\text{B.4})$$

The reduced mass and stiffness matrices are then given by

$$\mathbf{M}_R = \mathbf{T}_s^T \mathbf{M} \mathbf{T}_s \quad \text{and} \quad \mathbf{K}_R = \mathbf{T}_s^T \mathbf{K} \mathbf{T}_s. \quad (\text{B.5})$$

The Guyan reduction is exact only at the zero frequency and other techniques should be applied in cases involving dynamic effects due to inertia forces in the structure. As the excitation frequency increases, the inertia terms neglected in equation (B.2) become more significant. In general, finite element models prefer to use the consistent mass matrices. In the case when only the stiffness matrix is reduced by static condensation and the mass matrix is calculated as lumped mass matrix, the lowest frequencies of the reduced model are more exact.

B.2. Dynamic Reduction

The dynamic reduction or dynamic condensation, proposed by Paz (1984), is very similar to the static condensation. These methods depend directly on the original Guyan method for the static condensation and, as a consequence, the eigensolution provides acceptable values only for a few lowest modes left in the reduced problem. By the modification of the Guyan's condensation method, the dynamic reduction reproduces the exact response of a structure at arbitrary chosen frequency ω_0 . If one of the natural frequencies of the system solution is chosen, the system will be reduced perfectly only at the chosen frequency. The centre frequency, in the range of interest, is one choice. It is also possible to select the characteristic frequency by weighted distance geometric approach. Equation (B.3) is modified and the new transformation is given by

$$\begin{Bmatrix} \mathbf{x}_m \\ \mathbf{x}_s \end{Bmatrix} = \begin{bmatrix} \mathbf{I} \\ -(\mathbf{K}_{ss} - \omega_0^2 \mathbf{M}_{ss})^{-1} (\mathbf{K}_{sm} - \omega_0^2 \mathbf{M}_{sm}) \end{bmatrix} \{\mathbf{x}_m\} = \mathbf{T}_d \mathbf{x}_m. \quad (\text{B.6})$$

The transformation matrix in this case is given by

$$\mathbf{T}_d = \begin{bmatrix} \mathbf{I} \\ -(\mathbf{K}_{ss} - \omega_0^2 \mathbf{M}_{ss})^{-1} (\mathbf{K}_{sm} - \omega_0^2 \mathbf{M}_{sm}) \end{bmatrix}. \quad (\text{B.7})$$

To obtain reduced mass and stiffness matrices the similar expression to equation (B.5) is used.

B.3. Improved Reduced System (IRS)

The Improved Reduced System technique develops Guyan's method to include a contribution from the slave inertias. The transformation matrix in this technique used to generate the slave coordinates from the master coordinates is given by O'Callahan, (1989),

$$\mathbf{T}_i = \mathbf{T}_s + \mathbf{SMT}_s\mathbf{M}_R^{-1}\mathbf{K}_R, \quad (\text{B.8})$$

where \mathbf{M}_R and \mathbf{K}_R are reduced mass and stiffness matrices obtained from static condensation and \mathbf{S} is expressed as

$$\mathbf{S} = \begin{bmatrix} \mathbf{0} & \mathbf{0} \\ \mathbf{0} & \mathbf{K}_{ss}^{-1} \end{bmatrix}. \quad (\text{B.9})$$

B.4. System Equivalent Reduction Expansion Process (SEREP)

The System Equivalent Reduction Expansion Process (O'Callahan et al., 1989) uses the complete finite element eigenvectors to produce the transformation matrix \mathbf{T}_u . The numerical eigenvectors are separated into master and slave coordinates and can be written as

$$\boldsymbol{\phi} = \begin{bmatrix} \boldsymbol{\phi}_{mm} & | & \boldsymbol{\phi}_{ms} \\ \boldsymbol{\phi}_{sm} & | & \boldsymbol{\phi}_{ss} \end{bmatrix}. \quad (\text{B.10})$$

The transformation matrix in this case is defined as follows

$$\mathbf{T}_u = \begin{bmatrix} \mathbf{I} \\ \boldsymbol{\phi}_{sm} \boldsymbol{\phi}_{mm}^{-1} \end{bmatrix}. \quad (\text{B.11})$$

The reduced mass and stiffness matrices may be obtained in a similar way to equation (B.5). The reduced numerical system has exactly the same lower eigenfrequencies as the full model and the quality of the results is insensitivity to the selection of the full system degrees of freedom that are kept in the reduced model.

Signal processing

The experimental modal analysis is not possible without the signal processing. The techniques used to improve the signals for the purpose of modal parameters extraction has been developed over the past 100 year, however, the development of quick and cheap PC computers allowed the digital signal processing to be used in every experiment currently conducted in the all world.

The most popular transform method is the Fourier Transform (FT). It provides a frequency representation of the signal i.e., gives information which frequency components with what amplitude exist in the signal. The Fourier transform is a tool for the analysis of the stationary signals. For the nonstationary signals, where the time localization of spectral components is required, there is a need for transformations giving the time-frequency representation.

The possibility of sequential analysis of short segments of an original signal by Fourier transform has been proposed by Gabor. He assumed that this short fragments of the signal are stationary and they can be transformed separately using a window function. The so called window is moved along the signal and the FT transformation is repeated. Gabor's adaptation, called the Windowed Fourier Transform (WFT), maps a signal into a two-dimensional function of time and frequency. The main disadvantage of the WFT is the application of the same window for the analysis of the entire signal. Jean Morlet and Alex Grossman for the first time proposed to use variable window and called the suggested transform by the name "wavelet". Using the windowed Fourier transform they discovered that keeping the window fixed might not give the best results for the selected signals. In view of this development the Wavelet Transform (WT) uses a variable window function for analyzing different frequency bands. The wavelet transform can measure the time-frequency variation of spectral components with variable time-frequency resolution.

The time-frequency analysis can be also conducted by so called empirical modal decomposition performed by the Hilbert-Huang transform (Huang, 1998). The method breaks the signal into the intrinsic mode functions and residues that can be very useful in signal analysis and, for example, in trend elimination.

C.1. Fourier transform

C.1.1. Fourier series

In 1808, French mathematician, Joseph Fourier showed that any periodic motion (Fig. C.1) can be represented by a superposition of sinusoidal vibration

$$p(t) = a_0 + \sum_{n=1}^{\infty} a_n \cos(2\pi f_n t) + \sum_{n=1}^{\infty} b_n \sin(2\pi f_n t), \quad (\text{C.1})$$

where $p(t)$ is time signal, f_n denoted frequency in Hz, a_0, a_n, b_n are the Fourier coefficients given by

$$a_0 = \frac{1}{T} \int_0^T p(t) dt, \quad a_n = \frac{2}{T} \int_0^T p(t) \cos(2\pi f_n t) dt, \quad b_n = \frac{2}{T} \int_0^T p(t) \sin(2\pi f_n t) dt. \quad (\text{C.2})$$

Relationship between the frequency f_n measured in Hz and circular frequency ω_n in rad/s is as follows

$$\omega_n = 2\pi f_n. \quad (\text{C.3})$$

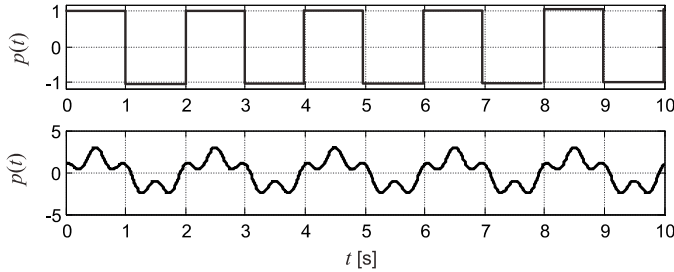


Fig. C.1. Periodic signals

Fourier series can decompose the signal into components of frequencies, which are the multiple of the fundamental frequency

$$f_n = nf, \quad \omega_n = n\omega \quad (\text{C.4})$$

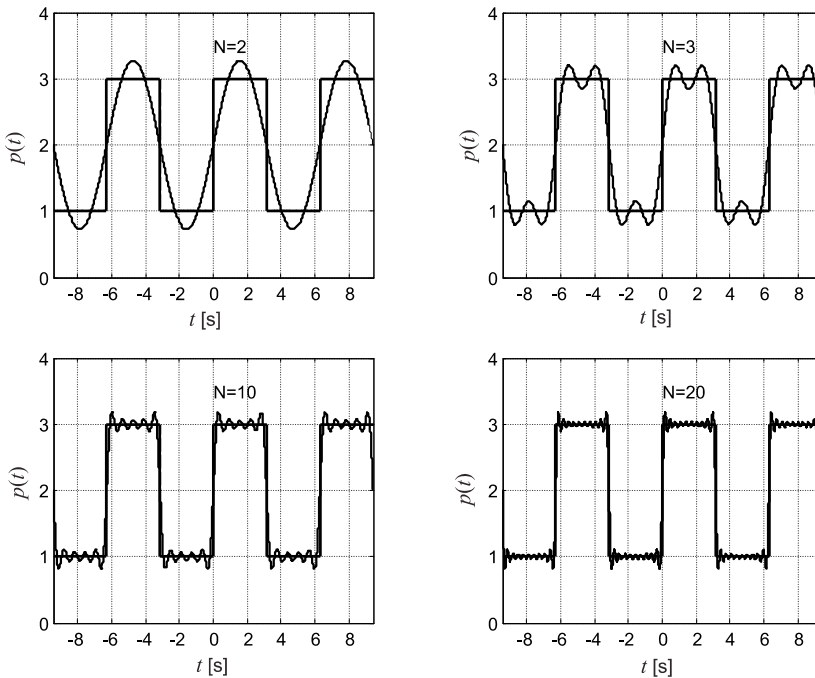


Fig. C.2. Rectangular periodical signal and its representation by the Fourier series for $N = 2, 3, 10, 20$

Rectangular signal and its representation by the Fourier series is given in Fig. C.2. The Fourier series are represented by 2, 3, 10 and 20 terms.

The Fourier series in the form of (C.1) can be rewritten into the exponential form. The exponential form is shorter and easier to mathematic calculations. Making use of the relationship between the exponential and trigonometrical functions

$$\begin{aligned} e^{in\omega t} &= \cos(n\omega t) + i \sin(n\omega t), \\ e^{-in\omega t} &= \cos(n\omega t) - i \sin(n\omega t), \end{aligned} \quad (C.5)$$

sinusoidal and cosinusoidal functions can be expressed by

$$\begin{aligned} \cos(n\omega t) &= \frac{e^{in\omega t} + e^{-in\omega t}}{2}, \\ \sin(n\omega t) &= \frac{e^{in\omega t} - e^{-in\omega t}}{2i}. \end{aligned} \quad (C.6)$$

Inserting (C.6) into equation (C.1) exponential form of the Fourier series can be obtained

$$\begin{aligned} p(t) &= a_0 + \sum_{n=1}^{\infty} \frac{a_n}{2} (e^{in\omega t} + e^{-in\omega t}) + \sum_{n=1}^{\infty} \frac{b_n}{2i} (e^{in\omega t} - e^{-in\omega t}) = \\ &= a_0 + \sum_{n=1}^{\infty} \frac{1}{2} (a_n - ib_n) e^{in\omega t} + \sum_{n=1}^{\infty} \frac{1}{2} (a_n + ib_n) e^{-in\omega t} = \\ &= a_0 + \sum_{n=1}^{\infty} P_n e^{in\omega t} + \sum_{n=1}^{\infty} P_{-n} e^{-in\omega t} = \sum_{n=0}^{\infty} P_n e^{in\omega t} + \sum_{n=1}^{\infty} P_{-n} e^{-in\omega t} = \sum_{n=-\infty}^{\infty} P_n e^{in\omega t}, \end{aligned} \quad (C.7)$$

where

$$\begin{aligned} P_n &= \frac{1}{2} (a_n - ib_n) = \frac{1}{2} \left(\frac{2}{T} \int_0^T p(t) \cos(n\omega t) dt - \frac{2i}{T} \int_0^T p(t) \sin(n\omega t) dt \right) = \\ &= \frac{1}{T} \int_0^T p(t) e^{-in\omega t} dt, \\ P_{-n} &= \frac{1}{2} (a_n + ib_n) = \frac{1}{2} \left(\frac{2}{T} \int_0^T p(t) \cos(n\omega t) dt + \frac{2i}{T} \int_0^T p(t) \sin(n\omega t) dt \right) = \\ &= \frac{1}{T} \int_0^T p(t) e^{in\omega t} dt. \end{aligned} \quad (C.8)$$

Finally the Fourier series in the exponential form can be expressed by

$$p(t) = \sum_{n=-\infty}^{\infty} P_n e^{in\omega t}, \quad P_n = \frac{1}{T} \int_0^T p(t) e^{-in\omega t} dt. \quad (C.9)$$

C.1.2. Fourier integral

The Fourier transform can be thought of as a continuous form of the Fourier series and it is defined as (e.g. Boggess and Narcowich 2002, Mallat 1998)

$$F(\omega) = \int_{-\infty}^{+\infty} f(t)e^{-i\omega t} dt, \quad (\text{C.10})$$

where $F(\omega)$ denotes the Fourier coefficients that are the amplitudes of each sinusoidal wave $e^{-i\omega t}$, ω is a circular frequency measured in units of radians per second and t is time. Relation between the circular frequency ω and the frequency f measured in cycles per second is $\omega = 2\pi f$. The Fourier coefficient $F(\omega)$ is obtained by multiplying the time signal $f(t)$ by the complex exponential $e^{-i\omega t}$ at certain frequency ω and integration over time domain. If the signal contains the frequency component ω , the product has large value. Otherwise, when the signal does not contain the frequency component ω the product yields zero. Fig. C.3 shows the Fourier transform plane.

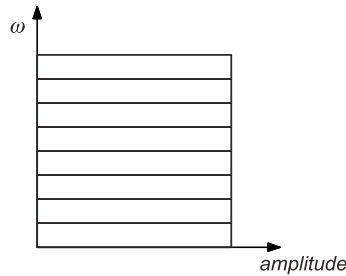


Fig. C.3. Fourier transform plane

C.1.3. Discrete Fourier transform

The Discrete Fourier Transform (DFT) was developed due to application of discrete signals. Continuous signal can be converted into a discrete using an analogue-to-discrete converter every t_s resulting N samples (Fig. C.4). The sampling frequency is given by

$$f_s = \frac{1}{t_s}. \quad (\text{C.11})$$

The signal is periodic with the period T

$$T = Nt_s, \quad (\text{C.12})$$

and the fundamental frequency can be expressed by

$$f_0 = \frac{1}{T} = \frac{1}{N\Delta t} = \frac{f_s}{N} \quad (\text{C.13})$$

The frequency f_n is given by the formula

$$f_n = f(n) = nf_0 \quad (\text{C.14})$$

The discrete Fourier Transform is derived from the Fourier integral

$$X(f) = \int_{-\infty}^{\infty} x(t)e^{-i2\pi ft} dt, \quad (\text{C.15})$$

and it has the form

$$X(n) = \sum_{k=0}^{N-1} x(k)e^{-i2\pi ft} = \sum_{k=0}^{N-1} x(k)e^{-i2\pi n f_0 k t_s} = \sum_{k=0}^{N-1} x(k)e^{-i2\pi n \frac{1}{N} k t_s}. \quad (\text{C.16})$$

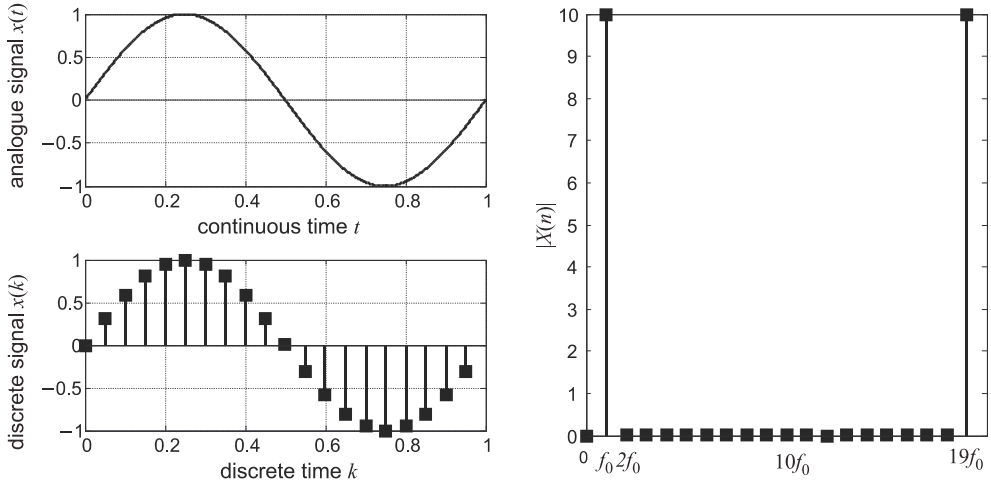


Fig. C.4. Continuous signal and its discrete representation (a); DFT of discrete signal (b) (after Rucka and Wilde 2008)

Finally, the DWT is described by the equation

$$X(n) = \sum_{k=0}^{N-1} x(k)e^{-\frac{i2\pi nk}{N}}. \quad (\text{C.17})$$

To accelerate the DFT, the fast Fourier transform (FFT) algorithm can be applied. Equation (C.17) can be divided into two parts

$$\begin{aligned} X(n) &= \sum_{k=0}^{N-1} x(k)e^{-\frac{i2\pi nk}{N}} = \sum_{k=0}^{N/2-1} x(2k)e^{-\frac{i2\pi n(2k)}{N}} + \sum_{k=0}^{N/2-1} x(2k+1)e^{-\frac{i2\pi n(2k+1)}{N}} = \\ &= \sum_{k=0}^{N/2-1} x(2k)e^{-\frac{i2\pi n2k}{N}} + e^{-\frac{i2\pi n}{N}} \sum_{k=0}^{N/2-1} x(2k+1)e^{-\frac{i2\pi n(2k)}{N}} \end{aligned}, \quad (\text{C.18})$$

$$W_N = e^{-\frac{i2\pi}{N}}, \quad (\text{C.19})$$

$$X(n) = \sum_{k=0}^{N/2-1} x(2k)W_N^{2nk} + W_N^n \sum_{k=0}^{N/2-1} x(2k+1)W_N^{2nk}. \quad (\text{C.20})$$

The example of time signal and its Fourier transform performed by the FFT algorithm is given in Fig. C.5.

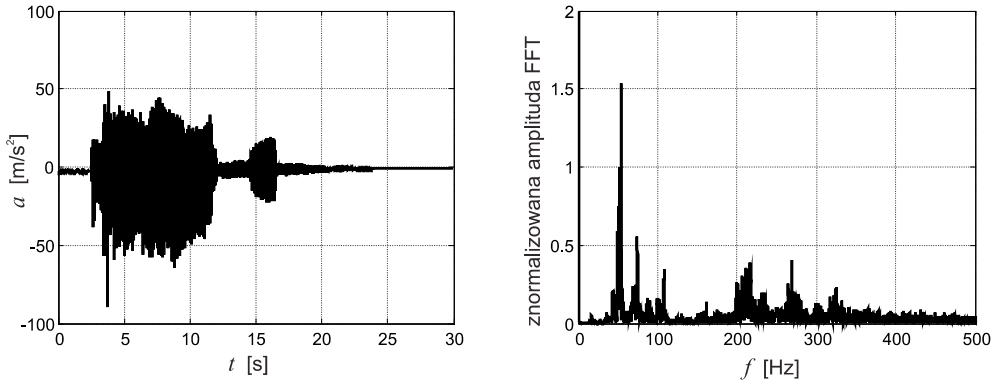


Fig. C.5. Vibration of a silo in the time and frequency domain

C.2. Windowed Fourier Transform

The Windowed Fourier Transform (WFT) maps time domain signal into the two-dimensional function of time and frequency (Kaiser 1994), as shown in Fig. C.6

$$Sf(u, \zeta) = \int_{-\infty}^{+\infty} f(t)g_{u,\zeta}^*(t)dt = \int_{-\infty}^{+\infty} f(t)g(t-u)e^{-i\zeta t} dt. \tag{C.21}$$

The window $g_{u,\zeta}(t)$ can be real as well as complex-valued. The term $g_{u,\zeta}^*(t)$ denotes complex conjugated. The signal $f(t)$ is multiplied by the window function $g_{u,\zeta}(t)$ modulated at the frequency $\omega = \zeta$ and then transformed by Fourier technique. The window is sequentially moved along the signal and the computation of Fourier coefficients is repeated. The window time interval σ_t and frequency interval σ_ω are fixed and are the same for all the considered signal samples and frequencies. Therefore, the Windowed Fourier Transform gives the same resolution across the time-frequency plane (see Fig. C.6).

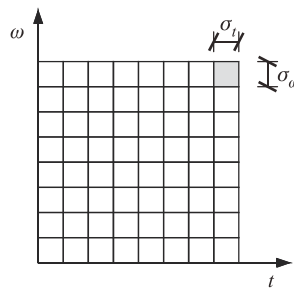


Fig. C.6. WFT in the time-frequency plane

The frequency resolution and the time resolution in the wavelet transform are interconnected. In fact, all functions, including window functions, obey the Heisenberg uncertainty principle. The notion states that the sharp localization in time and frequency are mutually exclusive. Thus, in the case of Windowed Fourier Transform it is impossible to find out exactly what spectral component exist at what exact instance of time, in fact the information is smeared. It is impossible to simultaneously reduce a time width and increase

frequency resolution during the WFT coefficients computation. Using the concept of Heisenberg uncertainty Chen (1995) showed that the area of a rectangle having a time width σ_t and a frequency width σ_ω is at least

$$\sigma_t \sigma_\omega \geq \frac{1}{2} \quad (\text{C.22})$$

The size of the window controls the resolution in the time and frequency of the WFT. The use of wavelets requires to compromise a good time resolution (narrow window) with poor frequency resolution, or on the other hand, good frequency resolution (wide window function) implies poor time localization (Chan 1995).

The example of the windowed Fourier transform of the silo vibrational signal (Fig. C.5) is given in Fig. C.7. The discharge process resulted in changes of the mass of the considered dynamic system. Therefore, the analysis used a technique for non-stationary signals and took into account the parameter variation in frequency and time. In this case, the signal processing was conducted by the windowed Fourier transform with the Gaussian function chosen for the window function $g(t)$.

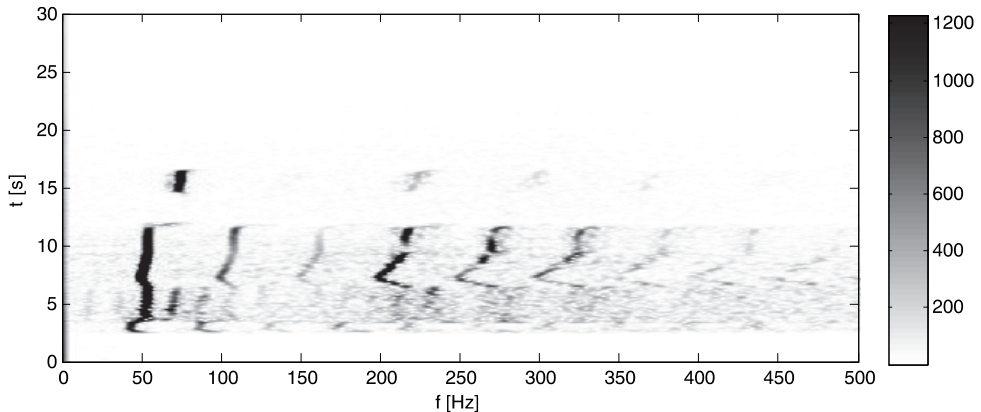


Fig. C.7. Windowed Fourier transform of a silo vibrations

C.3. Wavelet transform

The wavelet transforms provide an additional representation of the nonstationary signal in frequency and time. They are alternatives to the Fourier transform rather than its replacement. For a given signal $f(t)$, where the variable t is time, the continuous wavelet transform (CWT) is obtained by integration of the product of the signal function and the wavelet functions (e.g. Białasiewicz 2000, Chan 1995, Mallat 1998) in the following form

$$Wf(u, s) = \frac{1}{\sqrt{s}} \int_{-\infty}^{+\infty} f(t) \psi^* \left(\frac{t-u}{s} \right) dt, \quad (\text{C.23})$$

where $\psi^*(t)$ is the complex conjugate of the wavelet function and s denotes the scale parameter. $Wf(u, s)$ is called the wavelet coefficient for the wavelet $\psi_{u,s}(t)$. It is noted that the scale is not the frequency in the sense of the Fourier transform. The scale used in wavelet transforms has similar meaning as a scale used in maps, i.e., the global view of the prob-

lem can be seen with high scales whereas low scales allow to analyse details. Wavelets precisely identify high frequency components using short time intervals and detect low frequencies with longer time windows. Following the Heisenberg uncertainty principle, wavelets (Fig. C.8) keep the resolution box area constant while the time width σ_t and scale σ_ω are changed. Each box represents equal portion of the time-frequency plane.

The relationship between a scale and frequency cannot be defined in a precise sense. Misiti et al. (2000) suggested the formula, for computation of pseudo-frequency f_c corresponding to a wavelet scale, in the following form

$$f_a = \frac{f_c T}{s}, \quad (\text{C.24})$$

where f_c denotes the centre frequency of a wavelet in Hz and T is a sampling period.

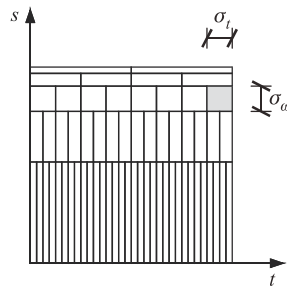


Fig. C.8. WT in the time-scale plane

The example of the wavelet transform of the silo vibrational signal (Fig. C.5) is given in Fig. C.9.

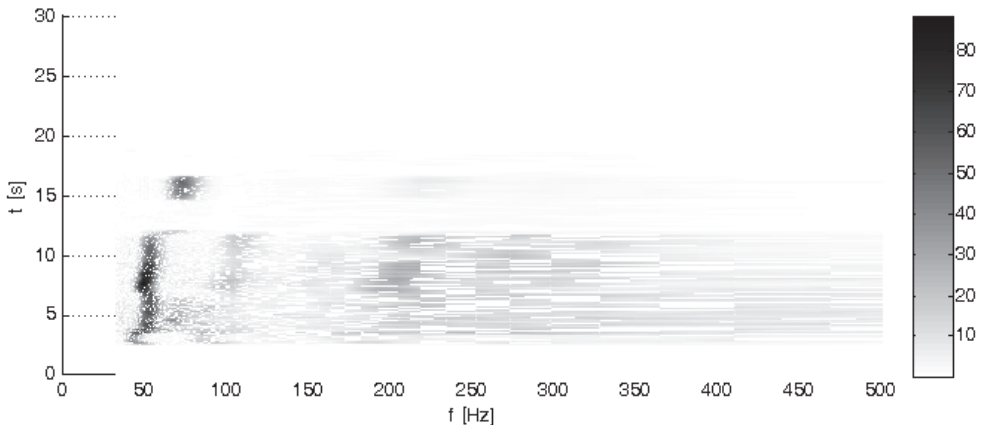


Fig. C.9. Wavelet transform of a silo vibrations

C.4. Hilbert transform

The Hilbert transform has been introduced to the signal processing theory by Denis Gabor by application of the complex Euler formula,

$$e^{iz} = \cos(\mathbf{z}) + i \sin(\mathbf{z}). \quad (\text{C.25})$$

Any signal can be presented in complex form as,

$$\mathbf{y}(t) = \mathbf{u}(t) + i\tilde{\mathbf{u}}(t), \quad (\text{C.26})$$

where $\mathbf{y}(t)$ is an analytical signal and $\tilde{\mathbf{u}}(t)$ is a Hilbert transform of $\mathbf{u}(t)$ according to the formula,

$$\tilde{\mathbf{u}}(t) = \mathbf{H}[\mathbf{u}(t)] = \frac{1}{\pi} \int_{-\infty}^{\infty} \frac{\mathbf{u}(\tau)}{t - \tau} d\tau = \mathbf{u}(t) * \frac{1}{\pi t}. \quad (\text{C.27})$$

The Hilbert transform is a convolution of signal $\mathbf{u}(t)$ and function $1/\pi t$. The transform can be considered as the filter that shifts the phases by $-\pi/2$ without changing the spectral amplitudes. Thus, equation (C.27) can be written in the form,

$$\mathbf{y}(t) = \mathbf{u}(t) + i\tilde{\mathbf{u}}(t) = \mathbf{A}(t)e^{i\theta(t)}, \quad (\text{C.28})$$

where the amplitude at time t is given by

$$\mathbf{A}(t) = |\mathbf{y}(t)| = \sqrt{\mathbf{u}^2(t) + \tilde{\mathbf{u}}^2(t)}, \quad (\text{C.29})$$

and phases are

$$\theta(t) = \arctan\left(\frac{\tilde{\mathbf{u}}(t)}{\mathbf{u}(t)}\right). \quad (\text{C.30})$$

The circular frequency at time t is

$$\omega(t) = \frac{d\theta}{dt}. \quad (\text{C.31})$$

The instantaneous circular frequency has been given by Zieliński (2005). The instantaneous frequency is a function of time and is convenient to characterize the non stationary signals.

C.5. Hilbert- Huang transform (HH transform)

The Hilbert-Huang transform is also referred to as Empirical Modal Decomposition EMD (Huang, 1998). The concept states that the signal can be decomposed into the time-frequency domain through the Hilbert transform. In theory, the EMD components should separate the phenomena occurring in different time scales. Each component of the EMD is called the Intrinsic Mode Function (IMF). As modes, the IMFs satisfy two criteria:

1. The IMF may only have one zero between successive extremes.
2. The IMF must have zero "local mean."

The computation of the IMFs which satisfy the above criteria and sum to create the signal goes as follows. A candidate for the highest-frequency IMF is determined by first fitting a cubic spline through all local maxima to create an upper envelope. A lower envelope is constructed in the same manner. Together, the envelopes form a candidate for the time-varying amplitude of the IMF. However, we want to ensure that the component

function will have negligible local mean. The practitioner has another choice here in deciding the threshold above which the process will not accept a candidate IMF. If the average value of the two envelopes does not fall uniformly within the threshold value of zero, we subtract the mean from the envelopes. The construction is repeated until the second criterion is satisfied. The result of this inner loop produces the first IMF. Subtraction of the IMF from the original signal gives the difference called the residue. The construction of an IMF is now repeated for the residual signal. This EMD procedure is repeated until the residue is either constant or monotone. This final residue should reveal any trend that exists in the data.

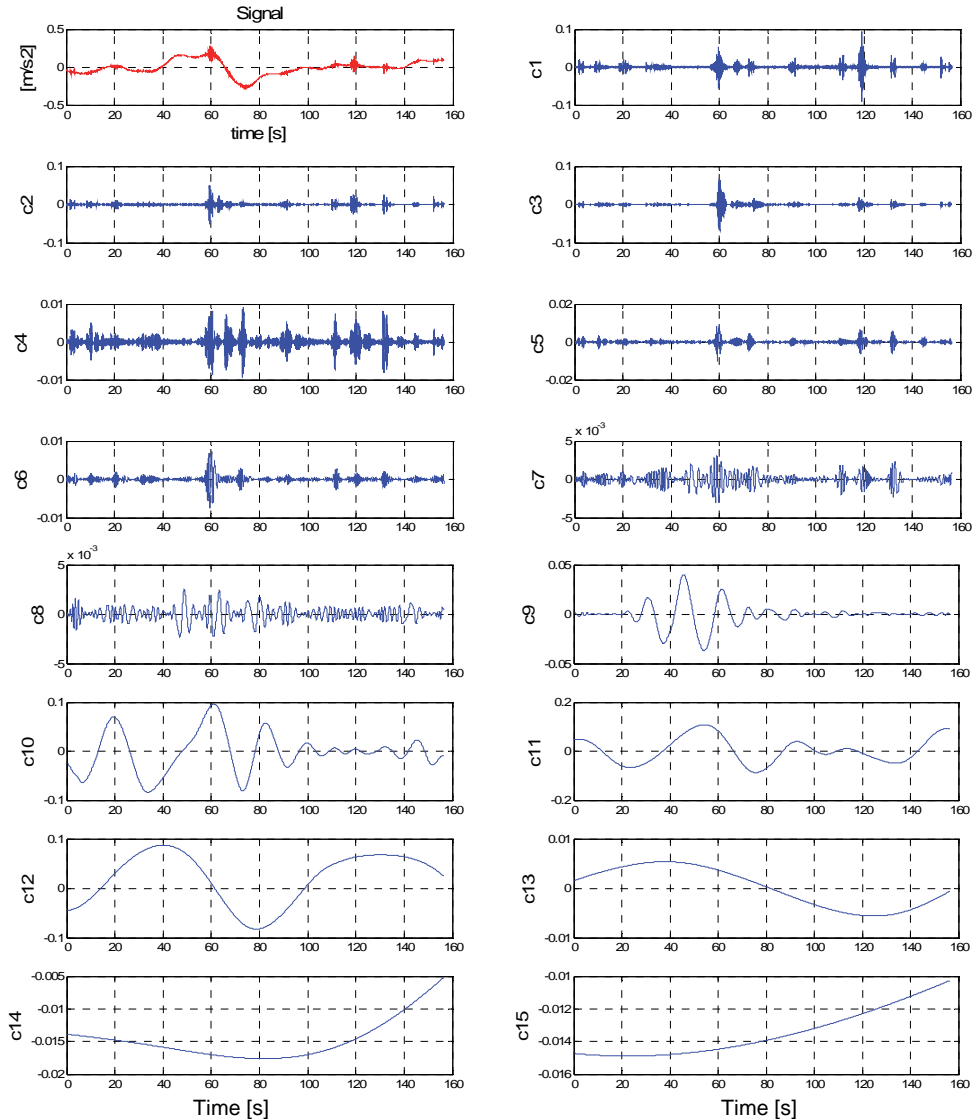


Fig. C.10. The acceleration signal and the IMF's of the HH transform

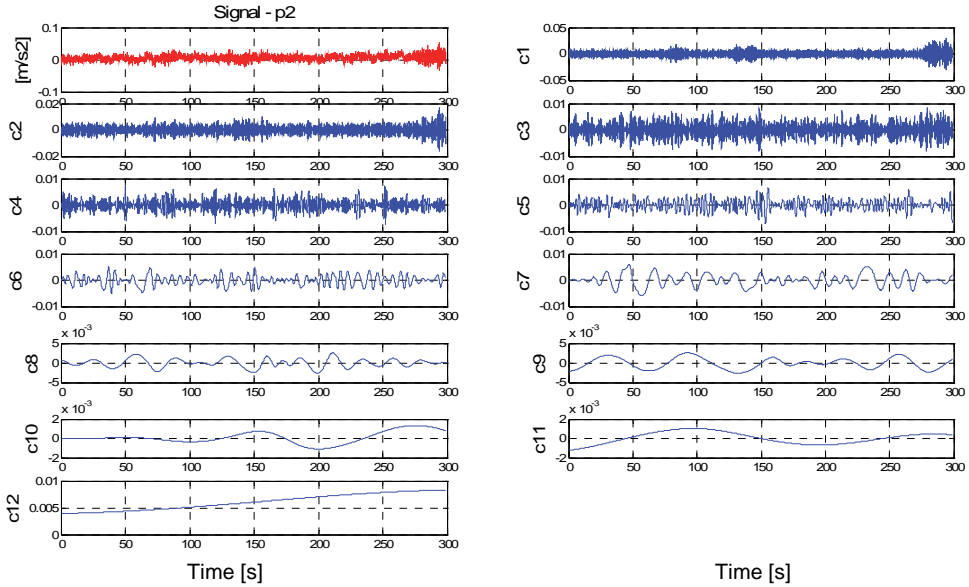


Fig. C.11. The IMFs of signal from cable stayed bridge in Gdańsk

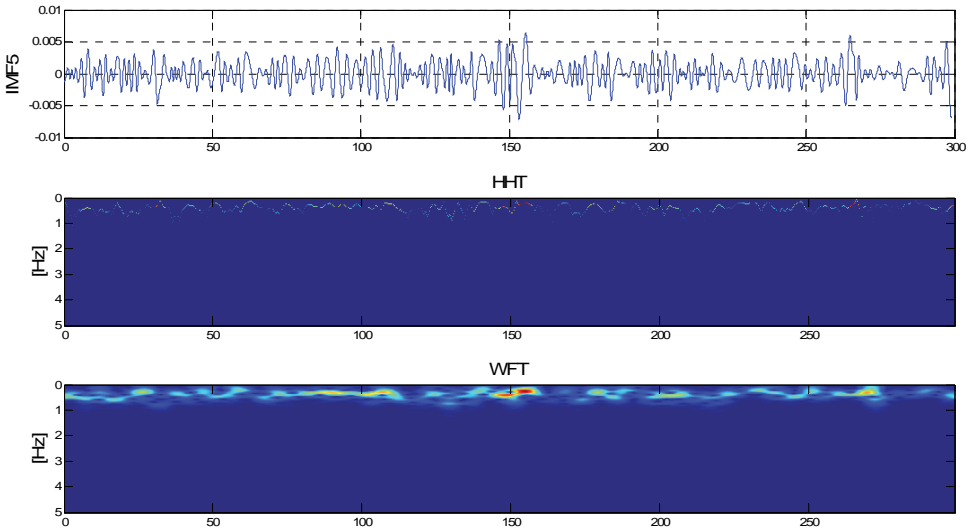


Fig. C.12. The IMF (a), HH transform (b) and Windowed Fourier Transform of 5th IMF (c)

The sifting leading to computation of the HH transform can be summarized in the following points:

1. Selection of the local minima and maxima of the signal $X(t)$.
2. Computation of the mean value, $m_1(t)$, of the local maxima and minima.
3. Computation of the shifted response as $h_1(t) = X(t) - m_1(t)$.
4. The shifted response, $h_1(t)$, is considered as the input signal to the HH transform for the next level computations.

5. Let the $h_{11}(t)$ be the average value of the envelope of the component $h_1(t)$ as $h_{11}(t) = h_1(t) - m_{11}(t)$.
6. The computation at steps 1 to 5 can be repeated k times, i.e., $h_{1k}(t) = h_{1(k-1)}(t) - m_{1k}(t)$.
7. The IMF function is the component $c_1 = h_{1k}$. The residue is $r_1(t) = X(t) - c_1(t)$.
8. The steps from 1 to 7 are repeated j times. After the j computations the residua are

$$\begin{aligned} r_1(t) - c_2(t) &= r_2(t) \\ \vdots & \\ r_{j-1}(t) - c_j(t) &= r_j(t) \end{aligned} \quad (\text{C.32})$$

9. Criteria for the end of the decomposition is (Huang, 1998)

$$SD = \sum_{t=0}^T \frac{|h_{1(k-1)}(t) - h_{1k}(t)|^2}{h_{1(k-1)}^2(t)} < 0,3. \quad (\text{C.33})$$

The examples of the HH transform application are given on the example of the signals recorded during ambient vibration tests in the composite bridge in Żukowo, Gdańsk described in section 3.2.3.2 (Fig. C.10).

The IMF computed by HH transform of the signal measured at the cable-stayed bridge in Gdańsk at the location of the tower are given in Fig. C.11. The time frequency presentation of the 5th IMF together with the Windowed Fourier transform is given in Fig. C.12.

Eigenvectors validation criteria

The comparison of the experimental and numerical frequencies (eigenvalues) can be calculated by the simple relative error formula. In the case of mode shapes, however, the statement about how close the experimental modes are to its corresponding numerical eigenvectors is much more complicated. The first difficulty is the fact that the natural frequencies and mode shapes in the experimental data must relate to the same mode. It is crucial that the eigenfrequency and eigenvector must be paired correctly. Sometimes it can happen that the accelerometer is placed at node which magnitude is near zero so the eigenfrequency may be estimated correctly but the mode shape not. Caution must be undertaken which modes are compared. In structures with more complicated geometry many modes can look similar and it must be remembered that the FE model has lots of modelling assumptions like, for example, an unrealistic boundary conditions. It is important to define which component of the eigenvector is dominant and whether it matches the dominant component of the experimental mode. Another problem is the mode shape scaling. The estimated mode shapes usually have different magnitude than analytical eigenvectors. Those problems can be addressed in the following sections devoted to mode shape validation criteria.

D.1. Modal Assurance Criterion (MAC)

The Modal Assurance Criterion (Allemang and Brown 1982) is the most common means for comparing the experimental and analytical mode shapes. The coefficient MAC is very easy to apply. The value of the MAC between an experimental mode ϕ_{mi} and an analytical mode ϕ_{aj} is defined as follows:

$$\text{MAC}_{ij} = \frac{|\phi_{mi}^T \phi_{aj}|^2}{(\phi_{aj}^T \phi_{aj})(\phi_{mi}^T \phi_{mi})}. \quad (\text{D.1})$$

The value of this coefficient is between 0 and 1. The MAC does not require an estimate of the system matrices and can be computed for the experimental data with incomplete degrees of freedom or the numerical eigenvectors from the reduced FE model. The next advantage of the MAC is that the modes may be complex.

D.2. Normalized Cross Orthogonality (NCO)

The NCO comparison technique is based on the orthogonality condition. The NCO between a measured mode ϕ_{mi} and an analytical mode ϕ_{aj} is defined as

$$NCO_{ij} = \frac{|\phi_{mi}^T M \phi_{aj}|^2}{(\phi_{aj}^T M \phi_{aj})(\phi_{mi}^T M \phi_{mi})} \quad (D.2)$$

The NOC_{ij} is a real number bounded between 0 and 1, like the MAC coefficient. For the selected experimental and analytical modes the NCO value is close to 1 when the modes are similar or correlated. If modes are uncorrelated, the NCO values are much smaller from 1. Computation of the NCO can be performed only for the real modes.

In the case when the modes are not necessarily mass normalised the MAC and NOC criteria can also be used (Lieven 1988, Friswell and Mottershead 1995). In some papers the NOC criteria was called COMAC and was used for error localization (e.g., Lieven et. al. 1994).

D.3. Normalized Modal Difference (NMD)

The Normalized Modal Difference criterion has been proposed by Waters (1995). The NMD can be defined using the MAC coefficient and can be written as

$$NMD_{ij} = \sqrt{\frac{1 - MAC_{ij}}{MAC_{ij}}}. \quad (D.3)$$

The meaning of the NMD is the average value of the errors of each degrees of freedom between two compared modes. For example, if 5% error is introduced by each degree of freedom the value of the NMD equals 0.05. The NMD is more sensitive to differences between mode shapes than the MAC.

D.4. Modal Scale Factor (MSF)

The Modal Scale Factor (Allemang and Brown, 1982) solves, among other things, the mode shape scaling problem. Measured mode shapes obtained from the FRF may have different magnitudes than analytical eigenvectors. The Modal Scale Factor (MSF) is defined as

$$MSF_i = \frac{\phi_{ar}^T \phi_{mi}}{\phi_{mi}^T \phi_{mi}}. \quad (D.4)$$

Usually the analytical eigenvectors are mass normalised. The mass distribution of the real structure is unknown so the mode shapes may not be scaled consistently. Normalizing the measured mode shapes by the analytical mass matrix and premultiplying by MSF results in consistent scaling of the measured mode shape. The Modal Scale Factor is also useful when the measured and analytical mode shapes are 180° out of phase.

D.5. Mode Singular Value (MSV) criterion

The Mode Singular Value criterion has been proposed by Juang (1994). The MSV is used in as a criterion for the selection of the system minimum realization in the ambient based identification methods. The formulation of the MSV is conducted for estimates of the dynamic system decrived by the discrete state space formulation in the modal form,

$$\begin{aligned}\mathbf{x}_m(k+1) &= \hat{\mathbf{A}}\mathbf{x}_m(k) + \hat{\mathbf{B}}_m \mathbf{u}(k) \\ \mathbf{y}(k) &= \hat{\mathbf{C}}_m \mathbf{x}_m(k)\end{aligned}\quad (\text{D.5})$$

Where $\mathbf{x}_m(k+1)$ is a vector of modal discrete degrees of freedom at time step $k+1$, $\mathbf{u}(k)$ is the input vector and $\mathbf{y}(k)$ is the output vector. The modal matrix is of the form $\hat{\mathbf{A}}$, has the form

$$\hat{\mathbf{A}} = \begin{bmatrix} \hat{\lambda}_1 & & & 0 \\ & \hat{\lambda}_1^* & & \\ & & \ddots & \\ & & & \hat{\lambda}_n \\ 0 & & & & \hat{\lambda}_n^* \end{bmatrix}, \quad (\text{D.6})$$

and consists of the discrete complex conjugate eigenvalues of the system. The matrices $\hat{\mathbf{B}}_m$ and $\hat{\mathbf{C}}_m$ can be divided in to the vectors corresponding to the system eigenvalues, i.e.,

$$\hat{\mathbf{B}}_m = \begin{bmatrix} \hat{\mathbf{b}}_1 \\ \hat{\mathbf{b}}_2 \\ \vdots \\ \hat{\mathbf{b}}_n \end{bmatrix}, \quad (\text{D.7})$$

and

$$\hat{\mathbf{C}}_m = [\hat{\mathbf{c}}_1 \quad \hat{\mathbf{c}}_2 \quad \dots \quad \hat{\mathbf{c}}_n]. \quad (\text{D.8})$$

The MSV criterion is defined as

$$\text{MSV}_i = \sqrt{|\hat{\mathbf{c}}_i| \left(1 + |\hat{\lambda}_i| + |\hat{\lambda}_i^2| + \dots + |\hat{\lambda}_i^{l-2}| \right) |\hat{\mathbf{b}}_i|}, \quad (\text{D.9})$$

where l is a number of the Markov parameters used in the formulation. The coefficient MSV_i provides the information on the contribution of the particular mode to the total response impulse response of the system. If the particular mode is negligible in the system response the MSV coefficient is close to zero.

WYDAWNICTWO POLITECHNIKI GDAŃSKIEJ

Wydanie I. Ark. wyd. 11,3, ark. druku 12,25, 66/513

Druk: Przedsiębiorstwo Prywatne *W/B* Piotr Winczewski
ul. Sobieskiego 14, 80-216 Gdańsk, tel. 058 341 99 89